A novel way to measure the rheology of liquids

By

Abdulrahman Jasim Al-Behadili

Submitted in accordance with the requirements for the degree of

Doctor of Philosophy

The University of Canterbury

Mechanical Engineering Department

2018

Abstract

Many liquid samples do not easily lend themselves to standard rheometry techniques. Consequently, it is important to find a novel way of measuring the rheology of liquids without using a rheometer.

This thesis explores the rheology measurement of Newtonian and non-Newtonian fluids by monitoring the effect of flow perturbation on the free surface velocity. A dam-break problem was considered, in which the release of a gate initially separating two fluid pools of different depths was performed. Three different liquids were used to implement the experiment, namely silicone oil, aqueous glycerol, and molasses. By seeding the free surface with buoyant particles, the flow velocity was measured using particle tracking velocimetry. A mathematical model based on the lubrication approximation for fluids with a power-law rheology was developed. This model was validated against a similarity solution, which could be obtained for the spreading of a gravity current under its own weight, and by neglecting surface tension.

The parametric identification of the rheological parameters was validated with synthetic data. Subsequently, the identification procedure was tested with noisy synthetic dataset and was found to be valid even when up to 40% noise was added to the ideal dataset. Minimizing the difference between the free surface velocity fields obtained numerically and those measured experimentally enabled the identification of rheological parameters. The methodology was tested on silicone oil, aqueous glycerol, and molasses, and the results were compared with the rheometer measurements. We found that the silicone oil and the aqueous glycerol were Newtonian, whereas the molasses were non-Newtonian. Moreover, the power-law model worked precisely with Newtonian fluids. Consequently, the Ellis rheological model was suggested. The model was validated against a Navier–Stokes solver. The identification process of the rheological parameters mentioned above was repeated with the same validation and testing procedures in terms of the Ellis model. The parametric identification results in terms of the Ellis model matched closer with the rheometer data compared to the power law model for the molasses.

Finally, the parametric identification of the rheological parameters of both the power-law and Ellis models were based on the lubrication approximation. The lubrication approximation is an approximation form of the Navier–Stokes equations. The difference between the two models was

calculated using the reconstructed rheological parameters of the fluids used. We found that the difference between the lubrication approximation and the Navier–Stokes equations was influenced by the inertia effects and the aspect ratio. This implies the lubrication approximation cannot accurately predict the dynamics of the flow when the inertia effects are high. When the aspect ratio is significant, the lubrication approximation cannot accurately capture the behaviour of the dam-break flow configuration. An extension of this part is the non-dimensionalisation of the lubrication approximation and the Navier–Stokes equations based on the power law initially, followed by the Ellis model. The non-dimensionalisation process was implemented by substituting scale variables into the lubrication approximation and the Navier–Stokes equations, where dimensionless expressions for both models including the Reynolds, Froude, and Bond numbers were obtained. Here, an important aspect is the effect of using the range of dimensionless numbers that agree between the two models. The results show that the compatibility is better with the Reynolds number of approximately 1 and an aspect ratio of up to 0.02.

The following papers and conference, based on sections of this thesis, have appeared or published under review.

-Morris, S., Sellier, M. and AL-Behadili, A.J.M. (2017). Comparison of lubrication approximation and Navier–Stokes solutions for dam-break flows in thin films.

- AL-Behadili, A.J.M., Sellier, M., Nokes, R., Moyers, M. and Geoghegan, P.H. (2017). Rheology Based On Free Surface Velocity. Submitted under review in Inverse Problem in Science and Engineering.

- Sellier, M., AL-Behadili, A.J.M. and Morris, S. (2017). *Rheometry based of free surface velocity for the dam-break problem*. In: The 8th Biennial Australian Colloid & Interface Symposium (ACIS), Sydney, Australia. Pages 1-22.

- Sellier, M., AL-Behadili, A.J.M. Hewett, J. and Devaud, L. (2017). *Spreading laws of gravity current and their application to lava viscometry*. In: Viscoplastic Fluids Workshop: From Theory to Applications, Rotorua, New Zealand.

Acknowledgments

All thanks are due to **Allah** for his mercy, blessing and assistance in preparing this work. I would like to express my deepest thanks for the man who gave me advice, help, support and never gave me up, in spite of the mistakes I made. He always put me back on the right track to the safe way, my supervisor Dr. Mathieu Sellier.

I would state my gratitude to my associated supervisors Professor Roger Nokes (Civil Engineering) and Dr. Miguel Moyers Gonzalez (Department of Mathematics and Statistics) for their feedback and their support.

Many thanks to all the technical staff in Mechanical and Civil departments. They help me in providing the materials for the experimental part of this work.

I would also like to thank my family, who always encouraging me to do the best and making me more enthusiastic for this work.

Finally, I am proud of my wife Zahraa Al-Sahlanee for her company, support and patience. She was the only person who carry the responsibility for taking care of our sons Rawan & Azez throughout more than a year. In spite of she was sick, she have been deciding to travel from Baghdad to Christchurch to accompany me in New Zealand. When she arrived to Christchurch, my motivation in studying go up significantly.

Contents

List of Figures

namely (a) 0.01, (b) 0.013, (c) 0.015 and (d) 0.02. Dashed line represents dimensionless Navier-Stokes solution (NS) and solid line represents dimensionless lubrication approximation (LA)

Figure 7.19: Dimensionless film thickness as a function of dimensionless horizontal distance in terms of the Ellis model at five different dimensionless time and four different aspect ratios, namely, (a) 0.01, (b) 0.013, (c) 0.015 and (d) 0.02. Dashed line represents dimensionless Navier-Stokes solution (NS) and solid line represents dimensionless lubrication approximation (LA)

List of Tables

Nomenclature

Bk	..... Control parameters
Bo	..... Bond number
Ca	..... Capillary number
d	..... Diameter
d_p	..... Diameter of the particle
e	..... Amount of added noise
E	..... Random values were taken between -1 and +1
F_g	..... Gravity force
Fr	..... Froude number
g	..... Acceleration
h	..... Fluid film thickness
h_c	..... Computed data
h_{exp}	..... Experimental data
$\tilde{h}$	..... Dimensionless fluid film thickness
H_g	..... Height of fluid in upstream side of the tank
H_1	..... Initial height of fluid in downstream side of the tank
H_0	..... Height scale of the fluid domain
k	..... Consistency factor
L	..... Length of the domain of the tank
L_g	..... Length of the domain in upstream side of the tank
L_1	..... Length of the domain in downstream side of the tank
L_0	..... Length scale of the fluid domain
n	..... Flow behaviour index
n_c	..... Flow behaviour index of the Carreau model
OF	..... Objective function
p	..... Fluid pressure

$\tilde{p}$ ..... Dimensionless fluid pressure

P_0 ..... Pressure scale variable

pr ..... Percentage of the added noise

Q ..... Fluid flux

Re ..... Reynolds number

t ..... Time

$\tilde{t}$ ..... Dimensionless time

T ..... Torque

T_0 ..... Time scale variable

x, y, z ..... Cartesian coordinates

$\tilde{x}, \tilde{z}$ ..... Cartesian dimensionless coordinates

X ..... Similarity variable

x_N ..... Front position of the gravity current

u ..... x-component of fluid velocity

$\tilde{u}$ ..... x-component of fluid dimensionless velocity

u_c ..... Computed free surface velocity

u_m ..... Measured free surface velocity

U_0 ..... Fluid velocity scale variable

v ..... y-component of fluid velocity

V ..... Fluid volume

w ..... z-component of fluid velocity

$\tilde{w}$ ..... z-component of fluid dimensionless velocity

Wd ..... Tank width

Abbreviations

fps ..... Frame per second

GEA ..... Global Engineering Alliance

IDT ..... Integrated design tools

LA ..... Lubrication approximation

MCR ..... Modular Compact Rheometer

MMS ..... Method of manufactured solutions

NS ..... Navier-Stokes

PTV ..... Particle Tracking Velocimetry

Greek symbols

α ..... The shear thinning parameter

δ_a ..... Absolute error

δ_B ..... Boundary layer thickness

δ_c ..... Calculated value

δ_r ..... Relative error percentage

δ_t ..... True value obtained from Rheometer

δ_u ..... Relative error percentage

ψ ..... Similarity function

ε ..... Aspect ratio

$\dot{\gamma}$ ..... Shear rate

$\dot{\boldsymbol{\gamma}}$ ..... Rate of deformation tensor

λ ..... The characteristic time

λ_s ..... The time scale

μ ..... Viscosity

$\widetilde{\mu}$ ..... Dimensionless viscosity

μ_0 ..... Viscosity at zero shear rate

μ_∞ ..... Viscosities at high shear rate

ρ ..... Fluid density

ρ_p ..... Particle density

σ ..... Fluid surface tension

τ ..... Shear stress

τ_s ..... Relaxation time of the particle

$\tau_{1/2}$ ..... Shear stress at which the viscosity is $\mu_0/2$

θ ..... Inclination angle

ω ..... rotational velocity

Chapter 1

Introduction & Literature review

Contents

1.1 Motivation

In a flow bounded by a free surface, perturbations induced by boundary or initial conditions are transferred to the fluid free surface and induce free surface velocity variations. This transfer is dependent on the rheology of the fluid. This study explores the hypothesis that the free surface velocity field is a signature of the fluid rheology and therefore the fluid rheology can be inferred indirectly by measuring the free surface velocity field. Typically, a rheometer is used to measure the rheology of fluids. However, standard rheometers produce low quality results or do not work when the sample is extremely hot (lava), dangerous (nuclear wastes), in too small a quantity (aerosol particles), or inaccessible (remotely observed flows on other planets).

Figure 1.1: Lave (left) and aerosol particles (right) Sellier, AL-Behadili et al. (2017)

In this thesis, we investigate a **novel way to measure the rheology of fluids** by studying only the free surface velocity.

1.2 Rheology

Rheology is the study of the deformation and flow of substances Barnes, Hutton et al. (1989). Rheology is described by a constitutive law that relates the deformation rate to the applied stress. Newtonian fluids such as water exhibit a linear relationship between shear stress and shear rate. However, this relationship is nonlinear for non-Newtonian fluids, such as molasses, xanthan gum and ketchup as shown in Figure 1.2.

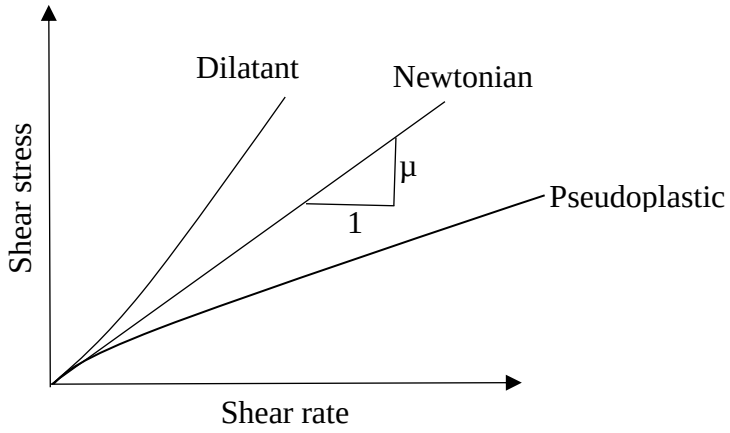

Figure 1.2: Flow curves for Newtonian and non-Newtonian fluids Sochi (2010)

Non-Newtonian fluids are divided into several types, such as shear thinning (pseudoplastic) and shear thickening (dilatant). The fluid behaves as shear thinning when the viscosity decreases with increasing shear rate. The fluid behaves as shear thickening when the viscosity increases with increasing shear rate. The behaviour of fluids are represented by constitutive laws. Three common non-Newtonian rheological models are described in the following sections Sochi (2010):

A) Power-law model

The power-law model, which is called the Ostwald de Waele model is considered the simplest. The power law expresses the viscosity μ in terms of the shear rate $\dot{\gamma}$ and has two parameters: the consistency factor (k) and the flow behavior index (n).

$$\mu = k\,\dot{\gamma}^{n-1}\,. \qquad (1.1)$$

Based on Equation (1.1), if $n < 1$, the fluid is shear-thinning or pseudo-plastic; if $n > 1$ the fluid is shear-thickening or dilatant; if $n = 1$ the fluid behaviour is Newtonian. Figure 1.3 shows the viscosity as a function of shear rate for a power-law model on logarithmic scales.

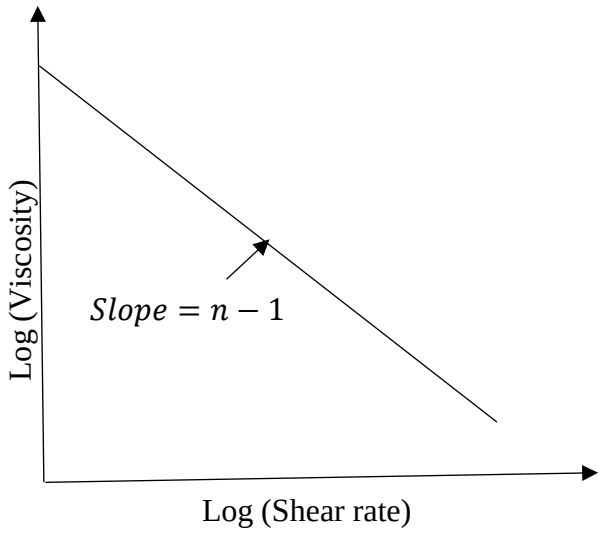

Figure 1.3: Viscosity as a function of shear rate for a power law model on logarithmic scales Sochi (2010)

B) Ellis model

The Ellis, also called the slight variant model, includes three parameters, namely, the viscosity at zero shear μ_0, shear stress $\tau_{1/2}$ at which the viscosity is $\mu_0/2$, and shear thinning parameter α. The following expression is used to calculate the viscosity μ according to the Ellis model:

$$\frac{1}{\mu} = \frac{1}{\mu_0}\left(1 + \left|\frac{\tau}{\tau_{1/2}}\right|^{\alpha-1}\right). \qquad (1.2)$$

In this equation, α is an indicial parameter related to the power-law index by $\frac{1}{n}$. One drawback of this model is that when a fluid experiencing low shear, the calculated viscosity may be under predicted Myers (2005).

The Ellis model shows a good agreement with the Carreau model. This model gives good results when using many different fluids with high shear rate Myers (2005).

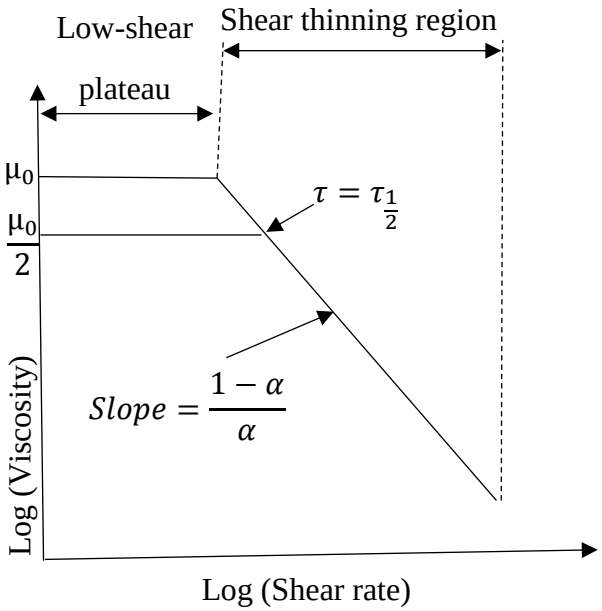

Figure 1.4: Viscosity versus shear rate for the Ellis model on logarithmic scales Sochi (2010).

C) Carreau model

The Carreau model expresses the viscosity in terms of shear rate and has four free parameters. The governing equation for this model takes the following form:

$$\mu = \mu_\infty + (\mu_0 - \mu_\infty)[1 + \lambda^2\dot{\gamma}^2]^{(n_c-1)/2}, \tag{1.3}$$

where $\mu_\infty$and μ_0 are the limiting viscosities at high and low shear rates, respectively; λ is the characteristic time; $\dot{\gamma}$ is the shear rate, and n_c is the flow behaviour index of the Carreau model Myers (2005).

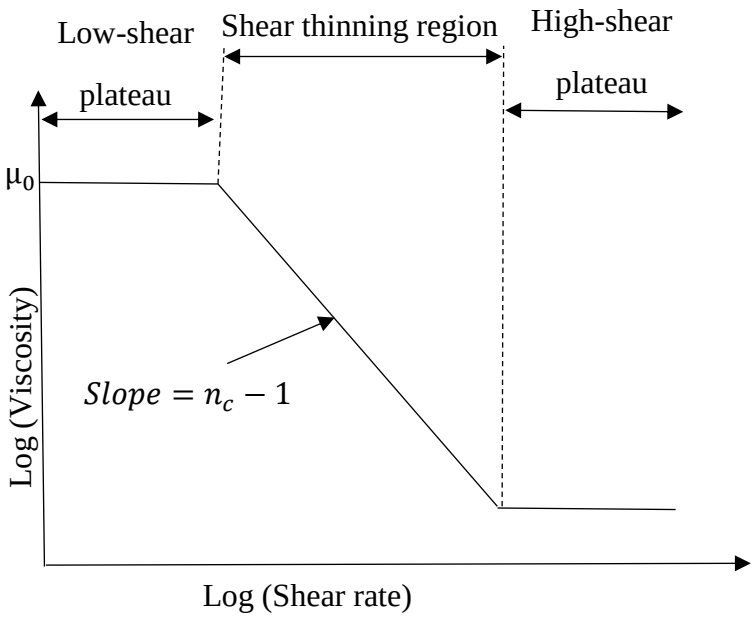

Figure 1.5: Viscosity versus shear rate for the Carreau model on logarithmic scales Sochi (2010).

In general, both the three parameters of the Ellis model and the four parameters of the Carreau model offer more flexibility than the two parameters of the power law in describing the rheology of the fluids. The drawback is that the identification of more parameters is required.

1.3 Rheometry

Currently, the classical way of measuring fluid viscosity is by using rheological instruments. These instruments are divided into two types, according to their geometry, rotation type, and tube type. The rotational types include the parallel plate, and the cone and plate instruments. The tube types include the pipe, high pressure capillary, and glass capillary, as shown in Figure 1.6.

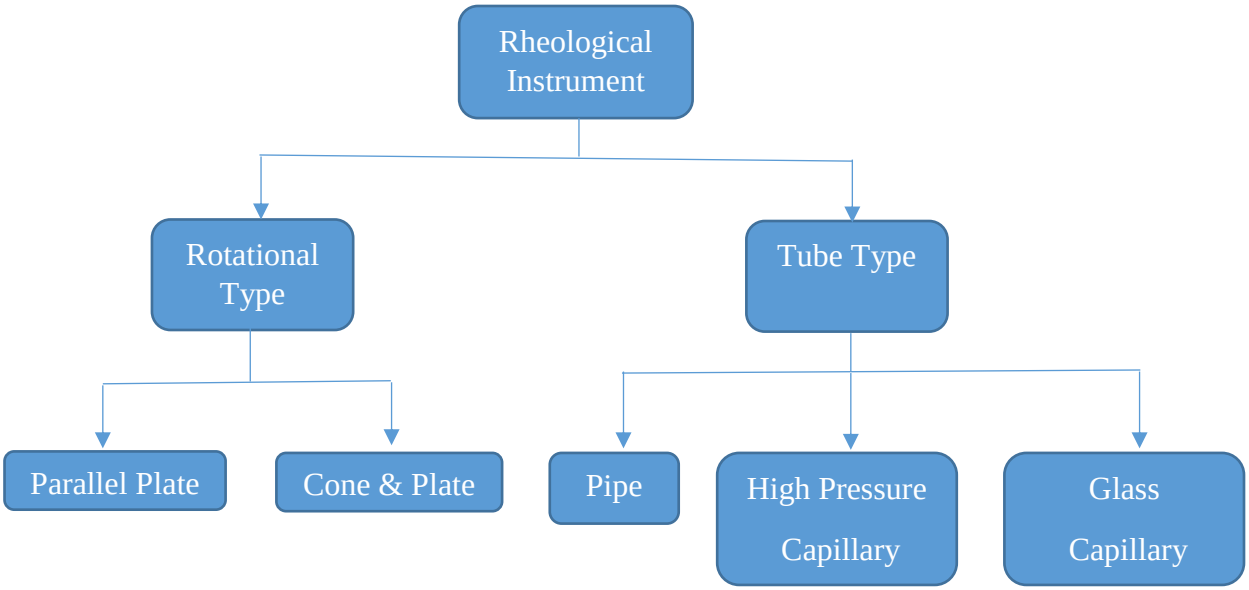

Figure 1.6: Rheological instruments classification Steffe (1996)

The rotational instruments have two different functions: (i) the controlled stress mode, which can analyse the material at very low shear rates and investigate the yield stress, and (ii) the controlled shear rate mode. The high pressure capillary works with high shear rates, whereas the glass capillary is only used for Newtonian fluids because their shear rates vary during fluid discharge.

The purpose of the rotational motion is to measure the displacement and load arising in the fluid. The displacement is then converted to a strain rate and the load is converted to stress. Typically, the output rheological parameters of the rheometer are normalized by the input amplitude. Both the step input of the shear rate and the transient normal stress are used to describe rheological parameters H. Ewoldt, T. Johnston et al. (2014).

A viscometer includes a rotating solid cylinder immersed inside a container of fluid. The type that experiences a resistant force against the direction of rotation is called the coaxial cylinder viscometer. The relationship between the resistance force and the speed of rotation gives a measurement of the fluid viscosity Wazer and R (1963). In Figure 1.7, T is the torque and ω is the rotational velocity. The fluid sample is squeezed between the upper and lower plates.

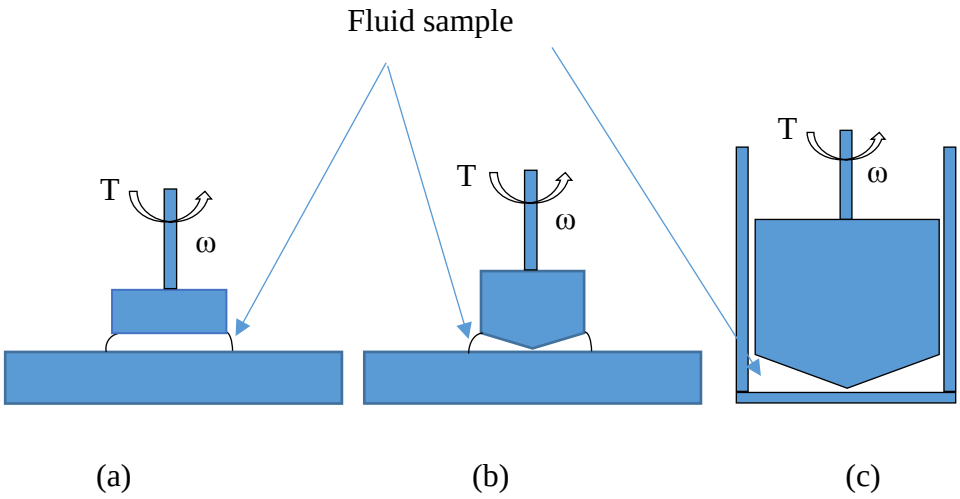

Figure 1.7: Viscosity measurement devices: (a) two-parallel-plate rheometer, (b) cone-and-plate rheometer, and (c) coaxial cylinder viscometer Steffe (1996)

1.4 Hypothesis and thesis work

The free surface velocity field is a signature of the fluid rheology; therefore, the fluid rheology can be inferred indirectly by measuring the free surface velocity field. It implies that the rheology of a fluid can be measured by studying only the free surface velocity. To test this hypothesis, the following methodology is implemented:

- A free surface flow is generated in the lab; the dam-break problem will be considered in the forthcoming chapters.
- The corresponding free surface velocity is measured.
- A constitutive law is assumed to describe the rheology of the liquid (this constitutive law involves a limited number of parameters).
- A numerical model is developed to represent the free surface flow
- The parameters are identified by minimizing the difference between the measured and modelled data.

1.5 Literature review

A) Measuring free surface velocity

Several studies have investigated the behaviour of free surface flow. Recently, Sellier and Panda (2017) stated that the free surface velocity of a fluid can be measured using particle image velocimetry (PIV) or particle tracking velocimetry (PTV) techniques. These techniques are commonly used to measure flow velocity. A sequence of flow images is analysed to extract the velocity field. In both techniques the velocity is calculated from the displacement of the particles and the time steps between each subsequent picture Sokoray-Varga and Józsa (2008).

PTV is different from PIV in the way displacement is calculated. PIV depends on linking the intensity field of two subsequent image frames. A dense particles seeding is needed to extract the velocity field whereby the measurement is based on the Eulerian principle. However, for the PTV technique, the particles in each frame are individually tracked and identified for successive image frames whereby the measurement is based on the Lagrangian principle Fu, Biwole et al. (2015) and Dark (2017).

A two-dimensional PIV technique is used to calculate the free surface velocities of water Eswaran, Singh et al. (2011). The experiment is implemented using an excited tank with low frequency to generate unsteady low-steepness waves. Small floating tracer particles are used over the fluid free surface to track the movement of the fluid Eswaran, Singh et al. (2011). The free surface velocity was also measured Kanemura, Kondo et al. (2008) using PIV to track the pattern of the free surface waves. Sokoray-Varga and Józsa (2008) used the PTV technique to measure the free surface velocity of water in a channel. The measurement procedure relies on the illumination of the tracer particles floating in the plane of the water free surface.

The large-scale particle image velocimetry (LSPIV) technique was used by Meselhe, Peeva et al. (2004) to calculate the free surface velocity for low velocity and shallow water flows. Two major differences between PIV and LSPIV are (i) PIV covers a smaller area compared to LSPIV, and (ii) the lighting system required to implement LSPIV is inexpensive compared to that required for PIV. By using the LSPIV technique, the free surface velocity was extracted by tracking the tracer particles floating on the water surface. The results show that LSPIV is suitable for measuring the lower values of the free surface velocities. In the current work, the PTV technique was chosen over PIV/LSPIV to measure the free surface velocity for several reasons. Firstly, PIV would

require a light sheet which precisely overlaps the free surface which was thought to be challenging. Secondly, the PIV method requires specialist, expensive equipment in comparison to PTV. Finally, PTV expertise was available in the supervisory team through Prof R. Nokes and the Stream PTV software he developed.

B) Measurements of the rheology of liquids

The rheological behaviour of fluids can be measured with many different techniques. For example, Longo, Di Federico et al. (2015) considered the spreading of a gravity current. The rheological parameters were identified by comparing the position of the gravity current front which is measured experimentally and predicted theoretically using a similarity solution analogous to that of Sayag and Worster (2012). Three types of fluids were used: corn-starch mixed with water to obtain a shear-thickening fluid (n >1), a mixture of water, ink and glycerol to obtain a Newtonian fluid (n =1) and xanthan gum which was mixed with the Newtonian fluid to obtain a shear-thinning fluid (n <1), n is the flow behavior index. Recently, Renbaum-Wolff, Grayson et al. (2013) developed a new technique to measure the viscosity of small aerosol particles, which cannot be measured with standard rheometry techniques. The principle of this technique is to deposit a droplet of material approximately on a substrate and pierce it with a sharp needle. The time required for the droplet to relax to its equilibrium shape can be related to the viscosity. The mathematical models were first tested against data from the literature for the closure of a hole in a continuous thin film, then experimentally demonstrated for droplets of polybutene oil Sellier, Grayson et al. (2015).

McKinley and Tripathi (2000) improved a technique for measuring the rheology of the fluid that was used in the past by Basilevsky, Entov et al. (1990). This technique is based on the concept of the capillary rheometer. The improved process was performed by squeezing a fluid droplet between two plates and then pulling the plates apart to generate a thinning filament. Measuring the rate at which this filament thins can be used to estimate the rheology of the fluid. The rheological properties of the fluid can be estimated by comparing the evolution of the diameter to the result of a one-dimensional model used to describe the filament. This technique was associated with the fibre dynamics which were described by Eggers (1997).

Another technique was implemented by Matta and Tytus (1990) and developed further by Anna, Rogers et al. (1999). This technique involves stretching a fluid bridge sandwiched between two

parallel plates and monitoring the velocity of the upper plate. The imposed velocity of the upper plate is exponential. It has been found that the viscosity of a fluid can be evaluated using the rheometer through the shape recovery of a stretched drop. This can be achieved by comparing the computed time obtained from solving the mathematical solution for the experimental data with that obtained experimentally.

C) Inferring rheology from free surface data

Here, the free surface data is assumed to be an important parameter that can be used to reconstruct the unknown variables. Recently, Sellier (2016) reviewed the literature in which free surface data is used to reconstruct the unknown fluid properties, such as the density, surface tension, and viscosity for Newtonian fluids, and the parameters of an assumed constitutive law for non-Newtonian fluids.

Subsequently, Martin and Monnier (2015) demonstrated that by using the free surface velocity measurement techniques, the rheology of a fluid that falls from an inclined surface can be estimated. Figliuzzi, Jeulin et al. (2012) described a method for estimating the rheology of paint. This method is based on determining the film surface topography at fixed time intervals. Moran and Yeung (2004) have shown that the viscosity of a fluid through the shape recovery of a stretched drop can be evaluated. This can be achieved by relating the shape relaxation time computed experimentally to that calculated numerically using the Stokes equations.

Free surface data was used to estimate the viscosity as described by Moran, Yeung et al. (2003). In addition, free surface velocity was used to evaluate the rheometry by evaluating the aspect ratio of a fluid filament, whereby the viscosity limit is obtained using a natural time scale Rodd, Scott et al. (2005).

In general, fluid velocity can be used to reconstruct rheological parameters. Park, Hong et al. (2007) and Bandulasena, Zimmerman et al. (2011) evaluated the rheological parameters using an inverse problem approach. Park, Hong et al. (2007) measured the fluid velocity inside a straight channel. Subsequently, they solved the governing partial differential equations with the experimental data obtained and implemented the inverse problem process. The velocity field was measured PIV. The solution obtained from the inverse problem approach allows for the evaluation of the unknown rheological parameters.

D) Solving the inverse problem

The inverse problem technique is used to identify the unknown fluid properties or flow conditions. Unknown fluid properties can be reconstructed by using the free surface data. An example of these properties are the fluid density, surface tension, the viscosity for Newtonian fluids and parameters related with the constitutive laws for non-Newtonian fluids. In this case, the measured free surface flow data can be used to indirectly obtain the unknown fluid properties. To solve the inverse problem, it is important to describe the mathematical model, which includes governing equations such as lubrication approximation and Navier–Stokes equations. The full details with derivations of the lubrication approximation from Navier–Stokes were described by Oron and Bankoff (1997), Spurk and Aksel (2008) and Craster and Matar (2009).

The model parameters must be identified after describing the mathematical model. These parameters are minimising the objective function, which can be written as:

$$OF(h_c, Bk) = \frac{1}{2} \int \left(h_c - h_{exp}\right)^2 dx + regularization\ terms \tag{1.4}$$

In equation (1.4), the term h_c represents the computed data, while h_{exp} represents the experimental data. A global minimum of the objective function is then found and this corresponds to the unknown model parameters. The regularization terms in equation (1.4) was explained with details by Engl, Hanke et al. (1996), Aster, Borchers et al. (2011) and Hasanoğlu and Romanov (2017).

The inverse problem approach can be used to evaluate the potential flow pattern of the ice sheet as mentioned by Rignot, Mouginot et al. (2011). This approach was based on the flow regimes and the quality of the free surface data, which were used to predict the ice sheet motion in the Antarctic region. The inverse problem approach was also improved by Nascimento, Naccache et al. (2010) by measuring the pressure drop beside the fluid flow velocity, which is aids in evaluating the fluid rheological properties.

1.6 Thesis outline

In this thesis, a novel method is developed to measure the rheology of a fluid from the free surface velocity. The main idea of the current work is to reconstruct the fluid rheological parameters from the measured free surface velocity. The flow configuration investigated is the dam-break problem.

The rheological parameters are identified by minimising the difference between the model and experimental results.

The current work includes three different fronts: experimental, analytical, and numerical. The dam-break classical flow configuration was used and is described in Chapter 2. Three fluids were tested in the experiments, namely silicone compound oil, aqueous glycerol, and molasses. The aim of the experiments was to obtain the free surface velocity fields using PTV.

Analytically, the lubrication approximation equations were derived after neglecting the inertia terms from the Navier–Stokes equations. First, the viscosity was defined according to the power-law rheological model as indicated in Chapter 3.

In Chapter 4, the numerical analysis and the numerical setup are described with the relevant results and verifications. In Chapter 5. The numerical analysis was implemented with the experimental results to reconstruct the rheological parameters for silicone oil, glycerol, and molasses. Furthermore, the results were compared with both the Navier–Stokes and the rheometer data. The Ellis model is then used to obtain the rheological parameters of non-Newtonian fluid (molasses) as indicated in Chapter 6.

Finally, in Chapter 7, a comparison of the lubrication approximation and Navier–Stokes equations was performed for both Newtonian and non-Newtonian fluids. First, the comparison was executed using the dimensional form for the two models lubrication approximation and the Navier–Stokes. Next, the comparison was performed using the dimensionless forms of the lubrication approximation and Navier–Stokes equations for the power-law and Ellis models, respectively. This allows for a more general comparison.

1.7 Key contribution

The contribution of this thesis is to measure the rheology of a fluid without using a rheometer. A novel method was implemented to calculate the rheology of a fluid by measuring its free surface velocity. The free surface velocity is measured using PTV and an image processing system. Mathematical expressions of the free surface velocity were derived for two different rheological models. Each rheological model was based on the Navier–Stokes and the lubrication approximation equations. The measured and computed free surface velocities were used in a parametric identification process with a wide range of rheological parameters. The minimized

mismatch between the measured and computed free surface velocities led to the identification of the fluid rheology.

Chapter 2

Experimental Apparatus and Velocimetry Method

Contents

2.1 Experimental apparatus

The aim of this experimental investigation was to measure the free surface velocity of a fluid in order to reconstruct its rheological properties using the parameter identification solution as described in Chapter 5. The classical dam-break flow was used to achieve this goal.

2.1.1 Tank

The experimental tank (made from Plexiglass) and its initial free surface condition, is shown in Figure 2.1. The outside dimensions included a width of 524 mm, a length of 940 mm, and a height of 262 mm with a 12-mm thickness on each side of the tank. The tank included an interior vertical gate.

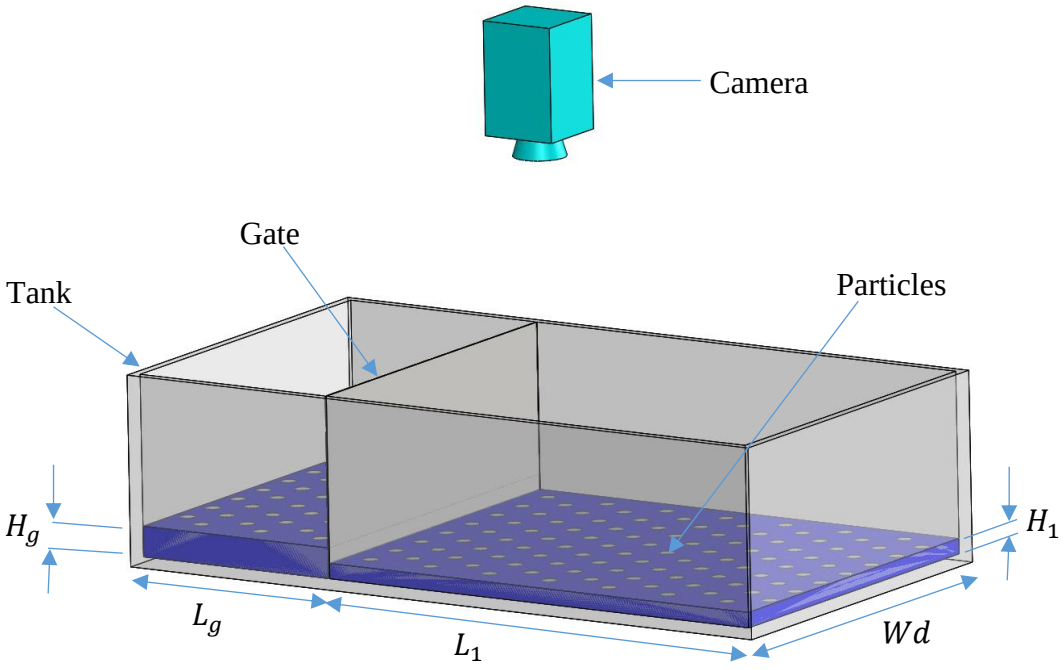

Figure 2.1: Experimental setup- not to scale

In Figure 2.1, $L_g = 280$ mm, $L_1 = 636$ mm, and Wd=524 mm. The height of the fluid in the upstream and downstream sides of the tank, H_g and H_1 respectively, is indicated in Section 2.1.5.

The gate was a vertical stainless steel sheet that was 255 mm high, 511 mm deep and 1 mm thick (the dimensions were checked using a digital Vernier). The space between the gate and the tank walls was filled with foam rubber to avoid leakage. The tank was placed inside a dark space on identical double blocks of wood. To ensure that the tank was horizontal, a spirit level was used with an accuracy of 1 mm/m. A black rubber sheet was placed over the bottom of the tank to obtain a black background to facilitate the identification of the white beads (see Section 2.1.2). Grease was applied on the contact sides of the gate to prevent friction with the tank's sides. The tank had an open top and a drain hole was made at the bottom of the tank. This hole was located near one of the corners furthest from the gate (see Figure 2.2). The system was drained with a manual ball valve.

To measure the initial thickness of the fluid inside the tank, a point gauge with 0.1 mm accuracy was used and was placed on a mobile table. The volume of the fluid on each side of the gate was measured using a beaker.

The tank was placed in a dark area to avoid external light. A cuboid structure, built from angle irons covered with a black cloth was used to provide the dark space. The cuboid structure was 3 m high, 1 m deep, and 1.5 m long.

2.1.2 Polystyrene white beads

White polystyrene beads, with a diameter of 1 mm and a specific gravity of 1.05 Kim, Hong et al. (2014), were used as drogue particles. The small size of the particles ensured that the particles did not affect the flow. Furthermore, they were light, and were therefore buoyant. Because they follow the streamlines of the fluid, the beads were spread on the surface of the fluid to track their motion. The relaxation time, τ_s of the particle, which represents the time response of the particle to the fluid acceleration, is given by the Stokes time equation,

$$\tau_s = \frac{\rho_p \, {d_p}^2}{18 \, \mu}, \tag{2.1}$$

where, d_p is the diameter of the particle, ρ_p is the particle density, μ is the viscosity of the fluid, and τ_s is the relaxation time of the particle. The relaxation time is 1.42×10^{-4} s for the silicone oil, with a viscosity of 0.41 Pa·s as shown in Figure 2.4. Consequently, the time scale λ_s, which represents the ratio between a relaxation time τ_s and an experimental time t_{exp}, is 3.15×10^{-6},

which is much less than one. The smaller time scale values are desirable because it implies that the particles behave closer to the surface fluid flow.

In terms of particle colour, it is important to ensure that the colour of the particles used is in contrast with both the tank bottom and the fluid used in order to recognise them clearly. In particular, the white particles ensured that the particles were clearly identified against the black background. A sieve with a fine mesh was used to spread the white beads uniformly over the free surface of the fluid.

It is evident that the properties of the beads such as size, colour, and density play a crucial role for any tracking system. Both the size and density affect the relaxation time of the particle as described in equation (2.1). The particle diameter must be as small as possible, such that the particles can track the fluid by following the streamlines of the flow.

2.1.3 Camera (IDT X3 model)

Images were captured with a 1280 H × 1024 V pixel Studio Motion Pro X3 high speed camera with a 55-mm lens attached. The high-speed camera with a maximum rate of 1040 fps (frames persecond) used in the experiment was placed directly above the tank at a height of 1.8 m above the free surface, as shown in Figure 2.1. A frame rate of 30 fps was used. It corresponds to the lowest possible frame rate for the camera but was sufficient for the slow flow motion of the fluids used. Furthermore, the camera must be as far from the tank as possible to reduce parallax. The camera was set on a special frame that included two protractors: one for the vertical angle and the other for the horizontal angle. Both the camera setup and the lighting system contributed to the intensity recorded by the camera. Thus, if the light intensity recorded by the camera is too high, the intensity of the pixel within the particles is higher than the saturated level and is not acceptable Nokes (2014).

One of the settings used for the camera was the exposure time. The exposure time was changed until the picture with a high quality at 3000 microseconds was obtained. The selected exposure time enables the user to see the particles and freeze them during their motion. Moreover, the exposure time was chosen to ensure that the particles' intensities were less than the saturated level.

The camera was also used to obtain the pixel scale ratio. This ratio is important to convert the pixel of the images to millimetres. To obtain the value of the scale from pixel to a physical coordinate

(in millimetre), the best way is by capturing a picture of a ruler placed over the bottom of the tank, and then convert the pixels to millimetres.

2.1.4 Lighting system

The lighting system was required to provide a clear contrast between the particles and the background. The light source for this system was a bank of fluorescent lights (Phillips 58W/865). Four fluorescent light tubes were placed on two sides of the tank, 10 cm from the tank walls (two tubes on each side). To ensure a uniform light intensity in the tank, the light from the fluorescent tubes was diffused by placing 3 mm white Acrylic sheets along two sides of the tank, as shown in Figure 2.2.

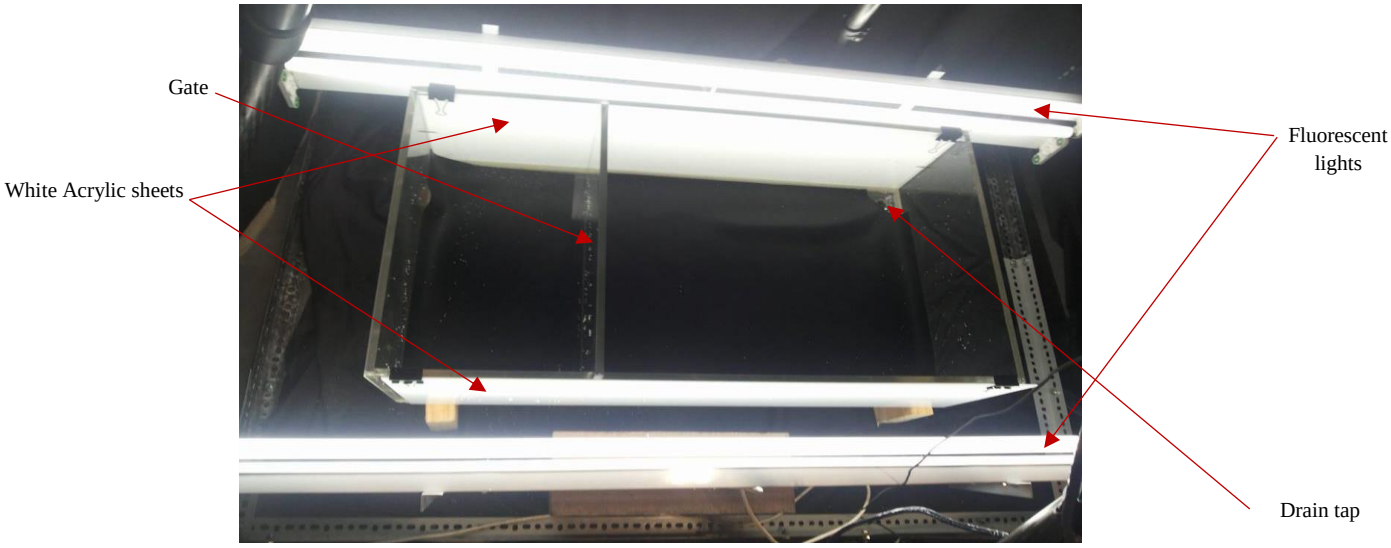

Figure 2.2: Tank and lighting system of the experimental configuration (off-centre view from above the tank)

2.1.5 Tested fluids

Three different fluids were used in the experiments. All three fluids have a viscosity higher than that of water. Some of these fluids were transparent such as the silicone compound oil and aqueous glycerol. Consequently, the black background of the tank produced a good contrast with the light reflected from the white beads. The other fluid used was molasses and as this fluid was dark, it

provided contrast with the white particles. The fluids used in the experiment are discussed in the following sections.

A) Silicone compound oil

A highly viscous silicone compound oil was used. The viscosity of the silicone compound oil used was 350 times that of water. The viscosity, surface tension and the density of the silicone oil used are 0.35 Pa·s, 0.021 N/m, and 970 kg/m^3, respectively Corporation (2006). The supplier of this fluid is Macron fine chemicals & JT baker (New Zealand agent).

B) Aqueous glycerol

The second fluid used was aqueous glycerol. The fluid concentration was 99% (99% glycerol and 1% water). The viscosity of the aqueous glycerol used, 1.15 Pa·s at 20 ^{o}C, was higher than that of the silicone compound oil. The density and the surface tension were 1257 kg/m^3 and 0.062 N/m, respectively. The supplier of this fluid is Thermo Fisher Scientific New Zealand Limited.

C) Molasses

The third fluid was the molasses. Black strap molasses was purchased from the company GEA Wiegand in New Zealand. This fluid was very viscous with density 1450 kg/m^3 and surface tension 0.05 N/m Miller and Pike (1993). The rheological parameters were measured as indicated in Chapters 5 and 6, respectively.

The fluid height in both the upstream H_g and downstream H_1 sides of the tank for all the fluids used in the current work is shown in Table 2.1.

Fluid	$\boldsymbol{H_g}$ **m**	$\boldsymbol{H_1}$ **m**
Silicone compound oil	0.019	0.009
Aqueous glycerol	0.026	0.010
Molasses	0.020	0.008

Table 2.1: Upstream and downstream experimental values

The heights of the upstream and the downstream were selected to generate sufficient flow for visualization and for measuring the fluid flow over a finite time.

2.2 Description of PTV system and Streams software

Particle tracking velocimetry (PTV) was used to extract the free surface velocity from the images captured by the camera. PTV is a process in which individual particles are tracked within a fluid. For the purposes of this study, the Streams software package Nokes (2014) was used. PTV includes four steps: image capture and processing, particle identification, particle matching between frames, and velocity field generation. PTV systems produce particle-based velocity data that must be interpolated onto an Eulerian grid.

Streams is a PTV and an image processing system. This program is designed to facilitate flow visualization and to track the particles within the fluid.

To be more familiar with the Streams software, one should read the three manuals, namely Streams Version 2.03 System Theory and Design, Streams Version 2.03 User's Guide: Core Objects, and Streams Version 2.03 User's Guide: Field objects Nokes (2014). Some of the key Streams concepts are briefly discussed below.

2.2.1 Image sequence

In Streams, the image sequence represents the starting point of the image processing. The image sequence includes a series of images. These images are captured with a constant time step that should be short enough to facilitate particle matching. Large particle displacements between frames can render particle matching more difficult. The pixel scale (mm/ pixel) must be specified when an image sequence is created.

To obtain the value of the scale from pixel to a physical coordinate (in millimetre), the best way is by capturing a picture of a ruler placed over the bottom of the tank.

2.2.2 Particle Identification Process

The particle identification process is used to identify the particles within each frame to obtain a list of particles with their physical properties such as size, shape, and intensity. Furthermore, this process identifies the particle location. Some errors had occurred in the calculation of the particle position. For example, some particles were not identified due to the poor intensity of the pixels within the particles. In some cases, a bubble was identified as a particle when it was illuminated by the light, and a larger particle might be identified as two particles.

The particle identification algorithm locates the size and position of particles within the image. The algorithm was to identify the position of particles in case the intensity of any pixel within the image exceeds the threshold intensity. This algorithm considered the Gaussian intensity distribution of each particle (in both horizontal and vertical directions). The particle record object analyses the pixel intensity matrix of each image. The algorithm identified particles using an intensity threshold. Subsequently, the centre of mass of the identified pixels were captured.

The calculated pixel scale was 0.353 mm/pixel with ±0.5 pixel, which represents the worst assumed accuracy of the identified pixel Whittaker (2013). This causes a potential displacement error of ±0.17 mm. At the capture rate of 30 fps for the silicone oil and aqueous glycerol cases, this leads to a velocity error of ±5.1 mm/s. The capture rate was 6 fps for the molasses, which leads to ±1.02 mm/s error in the velocity. Consequently, the error in the velocity measured is 8 % for silicone oil, 5.1 % for glycerol and 12 % for molasses.

2.2.3 Particle Records

The Particle Records are the second object in the object list of the Streams software. They represent the complete video recorded from the image sequence process. The outcome of the particle identification process is the particle record, which is simply a record of the particles identified in each frame.

2.2.4 PTV analysis

Particle tracking velocimetry (PTV) is based on the recording of fluid motion by tracking small particles in the fluid. The velocity can be calculated from measuring the time step between frames,

and the displacement of particles between frames. The velocity calculated by the PTV analysis represents the velocity of the centre of mass for each particle.

$$u(x,t) = \frac{\Delta x(x,t) \pm [0.5, 0.25\ pixel]}{\Delta t}\ (\frac{mm}{s}). \quad (2.2)$$

In equation (2.2), u is the particle velocity, Δx is the particle displacement between the frames, and Δt is the time step. The velocity calculated from equation (2.2) is the Lagrangian velocity and is applied for each particle between the frames. These velocities were obtained from the movement of the particles that were matched between frames, based on a central difference approximation. The Lagrangian velocities obtained are then interpolated onto a rectangular grid to obtain the Eulerian velocity field.

The PTV image processing includes an important part related to the particle matching between frames. An optimisation algorithm was used in this matching process to select the best matches between particles based on the lowest cost (in terms of distance). In Streams the position of the particles is calculated in each frame. For example, the position of the particles in Figure 2.3 is calculated in frame I and II, then the distance can be calculated. If the particle doesn't move then the distance is zero and that will considered in the optimisation algorithm.

In particular, each match was based on the cost within the PTV analyses. Figure 2.3 describes the particles match procedure between frames. This figure represents two subsequent frames, I and II, of which each frame includes five particles. Five matches are possible for particle B within frame II. An optimisation algorithm is used to find the particle within II that is the best match for particle B. This process is repeated for all the particles within frame I, and the matches with the lowest total cost are selected by the optimisation algorithm Dark (2017), Nokes (2014) and Whittaker (2013).

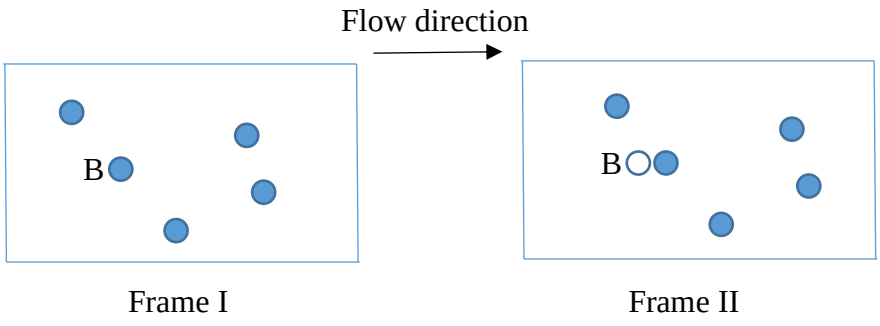

Figure 2.3: Particle matching process between two frames

The main point of the matching process is to identify particles from one frame to the next. The match percentage could be as high as 95% for good quality free surface data Nokes (2014).

2.3 The experimental procedure

The experiment was performed in the workshop of the Mechanical Engineering Department at the University of Canterbury. The experimental procedures are as follows:

1- Water was placed inside the tank after each experiment to ensure no leakage from the tank. The gate was placed inside the tank and was sealed tightly to ensure no leakage from its edges. At the conclusion of this stage, the drain system (as described in Section 2.1.1) was opened to remove the water from the tank such that the tank is ready for the experiment.

2- A ruler was placed inside the tank to calculate the pixel to millimetres conversion factor.

3- The fluid used in the experiment was then prepared. The depth of the fluid inside the tank was measured using a point gauge. The fluid must be placed in both the upstream and downstream ends of the tank but in different quantities to obtain different fluid levels across the gate.

4- The polystyrene beads were scattered over the surface of the fluid uniformly to avoid coalescence between particles.

5- The camera must start recording the motion from the initial state and the particles were ensured to be stationary before opening the gate.

6- The gate must be pulled to allow the fluid to flow from the high level to the low level.

7- In the current experiments, 1500 frames were captured for the silicone oil and glycerol cases, and 2500 frames for the molasses case due to the difference in fluid viscosity.

8- Finally, the drain tap must be opened to drain the fluid used.

2.4 Fluid rheology

The rheology of the silicon compound oil and aqueous glycerol were measured using a Rheometer MCR 301.

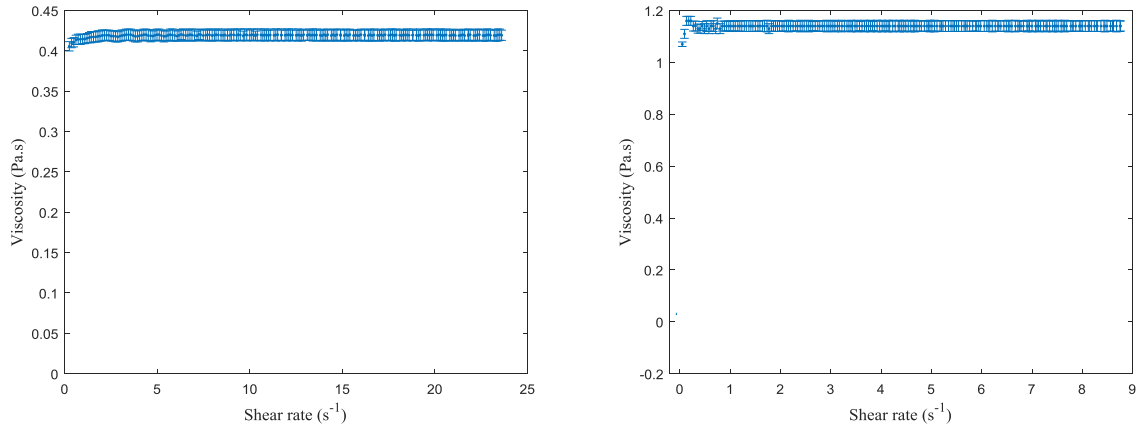

(a) (b)

Figure 2.4: Experimental data of viscosity vs. shear rate measured using Rheometer MCR 301 for (a) silicone oil (μ =0.41 Pa·s) and (b) aqueous glycerol (μ = 1.14 Pa·s)

Figure 2.4 illustrates the average of three experimental data sets for the viscosity at room temperature (20 °C) plotted against the shear rate for both the silicone compound oil and glycerol. The number of data points which were used to measure the viscosity by the Rheometer MCR 301 was 200 and the fix time between each measurements was 1 s. The used MCR was a rotational type and has good temperature control and sensitivity across a range of viscosities. It consists of upper plate with the shear area that is deflected by the shear force, and the resulting deflection is measured. The lower plate is stationary. The liquid samples must adhere to both plates and not slip or slide along them. The assumption is made that the sample deforms homogenously over the entire gap. Measurements were taken using MCR301 rheometer with a Direct Strain Oscillation (DSO) option, which enables strain-controlled oscillatory tests to be carried out at the smallest torques

and deflection angles. Temperature was controlled using a Peltier temperature controlled unit PTD 200 and a Peltier control hood in order to minimise temperature gradients within the samples.

The error bars of the rheometer data were computed on the shear rate, fluid viscosity and standard deviation for all the dataset obtained from repeating the experiment three times. It is clear that both fluids behave as Newtonian fluids within the above-mentioned shear rate range.

The same rheometer, MCR 301 and the same number of data points were used to measure the viscosity of the molasses. The results are shown Figure 2.5.

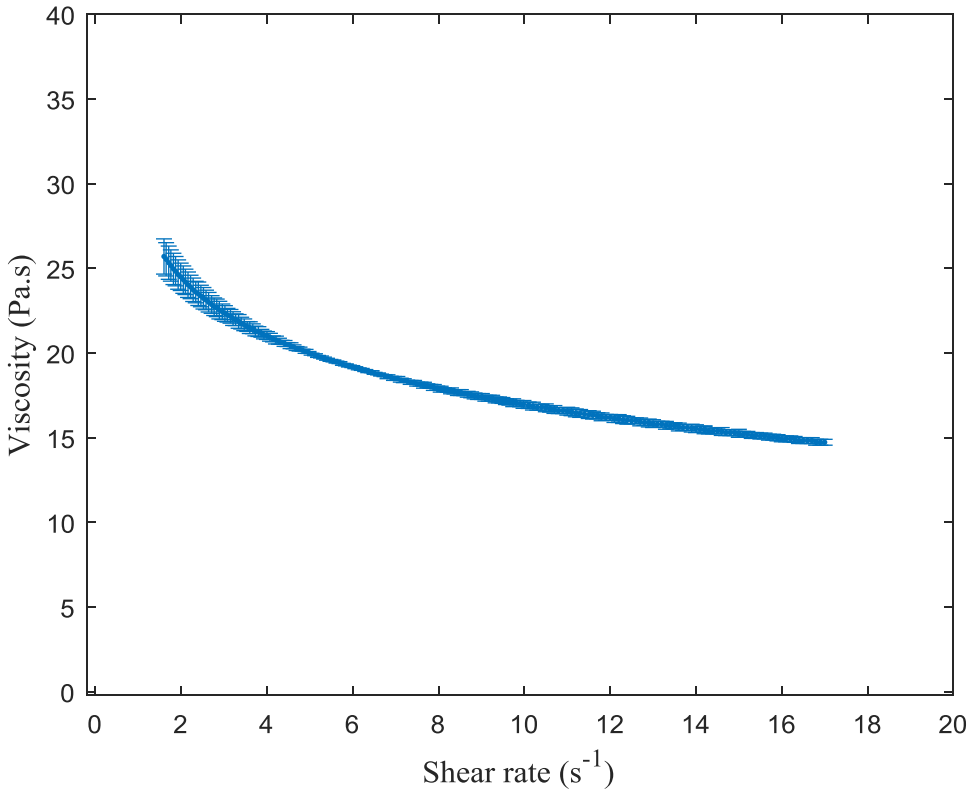

Figure 2.5: Viscosity of molasses, the non-Newtonian fluid used in the experiments, as measured using Rheometer MCR 301

From Figure 2.5, it is clear that the molasses behave as a non-Newtonian fluid within the above-mentioned shear rate range (1.5 s^{-1} to 17 s^{-1}). The rheological parameters of the molasses are as indicated in Chapter 5 in terms of the power-law model, and in Chapter 6 in terms of the Ellis model. The best fit rheological parameters for the molasses were obtained using a Matlab code which solves the non-linear least square problem to fit the rheometer data by varying the two

power-law parameters or the three Ellis model parameters. The results from the data fitting code was n =0.76 & k =28.8 Pa.s^n in terms of the power-law model and $\alpha = 1.6$, $\tau_{1/2}$=271 Pa and μ_0=37.4 Pa.s in terms of the Ellis model.

2.5 Repeatability

The repeatability of the free surface velocity measurement is discussed in this section. The time step between frames was 0.03 s and the mm/pixel scale for both the x and y axes was 0.353. Each experiment was repeated three times under the same conditions to obtain the average value. The following figures show the velocity profiles for the three experiments using the silicone compound oil.

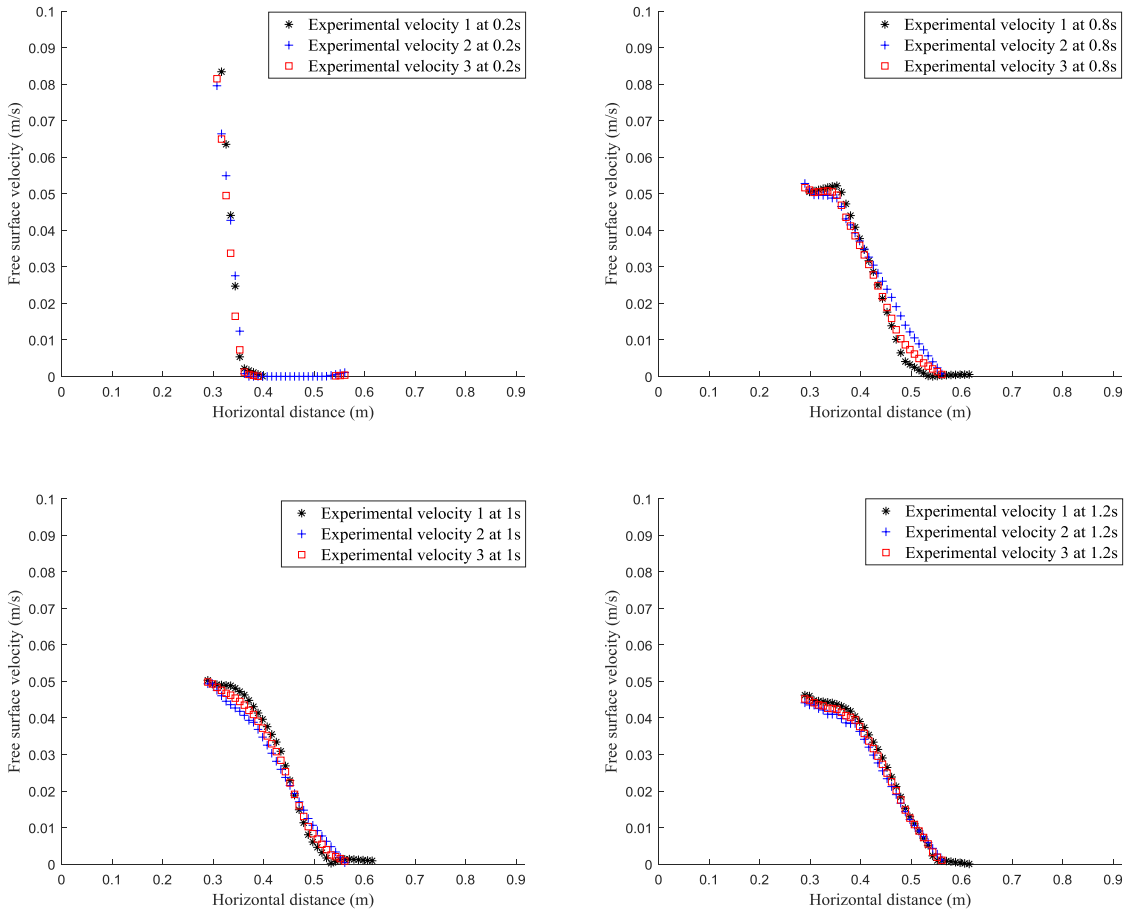

Figure 2.6: Comparison between three experiments at different times, namely $t = 0.2$ s, $t = 0.8$ s, $t = 1$ s and $t = 1.2$ s.

Figure 2.6 shows the free surface velocity profile for three experiments at four different times. It is clear that the velocity profile was not exactly the same for each experiment. These slight differences could be attributed to a few reasons. First, the measurement of the fluid level had an accuracy of 0.1 mm. The second reason could be due to the speed of gate removal, as the time step of the experiment was small at 0.03 s. If the time to remove the gate was inaccurate, for example by 0.1 s, then the timing would be off by three frames.

Chapter 3

The mathematical models

Contents

3.1 Model based on Navier–Stokes

The Navier–Stokes equations express the conservation of mass and momentum. For a non-Newtonian incompressible fluid in the Cartesian coordinate, the Navier–Stokes equations and the related sketch are given as,

$$\rho\left(\frac{\partial u}{\partial t}+u\frac{\partial u}{\partial x}+w\frac{\partial u}{\partial z}\right)=-\frac{\partial p}{\partial x}+\frac{\partial}{\partial x}\left(\mu\frac{\partial u}{\partial x}\right)+\frac{\partial}{\partial z}\left(\mu\frac{\partial u}{\partial z}\right), \tag{3.1}$$

$$\rho\left(\frac{\partial w}{\partial t}+u\frac{\partial w}{\partial x}+w\frac{\partial w}{\partial z}\right)=-\frac{\partial p}{\partial z}+\frac{\partial}{\partial x}\left(\mu\frac{\partial w}{\partial x}\right)+\frac{\partial}{\partial z}\left(\mu\frac{\partial w}{\partial z}\right)+\rho g\ , \tag{3.2}$$

$$\frac{\partial u}{\partial x}+\frac{\partial w}{\partial z}=0. \tag{3.3}$$

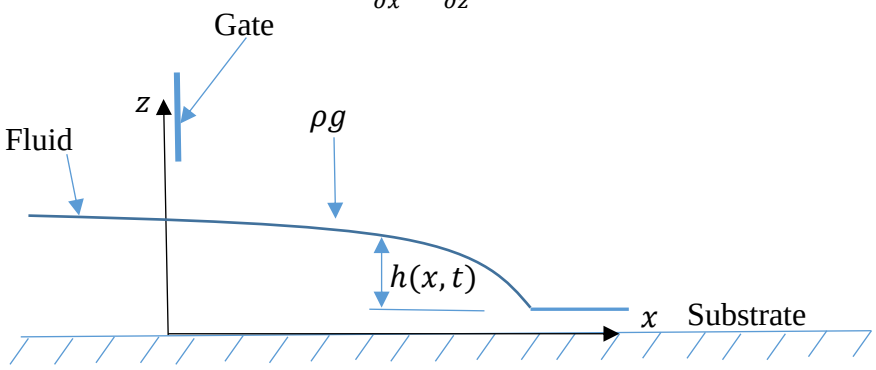

Figure 3.1: Sketch of the problem with notations

where u, w is the fluid velocity in the x and z directions respectively; ρ, μ, and g are the density, viscosity, and acceleration of the fluid, respectively. With a suitable rheological model for μ, these equations can be applied to non-Newtonian flows.

3.2 Model based on the lubrication approximation

The lubrication equations are an approximation of the Navier–Stokes equations for which the inertia terms are neglected, and a small aspect ratio ε is assumed. The aspect ratio is the ratio between a characteristic film thickness and a characteristic length scale in the flow direction. Thus,

the height and length scale of the problem are defined as $H_0 = \frac{H_1+H_g}{2}$ and $L_0 = L_1 + L_g$, respectively, as shown Figure 2.1of the tank diagram, and the aspect ratio is $\varepsilon = \frac{H_0}{L_0}$.

A possible rheological model for non-Newtonian fluids is the **power-law model.** The power-law model expresses viscosity in terms of the shear rate and has two parameters: the consistency factor (k, Pa·s^n) and the flow behaviour index (n, dimensionless). Some models are valid within a specific range of the rheological parameters. For example, a mathematical model based on the power law was investigated by Noble and Vila (2013). This model describes the flow of a thin film for power-law fluids and is valid when the behaviour index is greater than 0.5.

According to the power-law model, the rheology of fluid is given by

$$\mu = k\,|\dot{\gamma}|^{n-1}\,. \tag{3.4}$$

In equation (3.4), $\dot{\gamma}$ is the shear rate obtained from the rate of the deformation tensor $\dot{\boldsymbol{\gamma}}$, which is given by

$$\dot{\boldsymbol{\gamma}} = \nabla u + \nabla u^T = \begin{pmatrix} u_x & u_y & u_z \\ v_x & v_y & v_z \\ w_x & w_y & w_z \end{pmatrix} + \begin{pmatrix} u_x & v_x & w_x \\ u_y & v_y & w_y \\ u_z & v_z & w_z \end{pmatrix} = \begin{pmatrix} 2u_x & u_y + v_x & u_z + w_x \\ u_y + v_x & 2v_y & v_z + w_y \\ u_z + w_x & v_z + w_y & 2w_z \end{pmatrix}. \tag{3.5}$$

Here, we consider a two dimensional problem where the solution is independent of the y coordinate and the film thickness is a function of the horizontal distance and time $h(x,t)$. Therefore,

$$\dot{\boldsymbol{\gamma}} = \begin{pmatrix} 2u_x & u_z + w_x \\ u_z + w_x & 2w_z \end{pmatrix}, \tag{3.6}$$

In which the shear rate is the magnitude of the rate of the deformation tensor,

$$\dot{\gamma} = \sqrt{\frac{1}{2}(\dot{\boldsymbol{\gamma}} : \dot{\boldsymbol{\gamma}})}\,. \tag{3.7}$$

To derive the lubrication approximation with a small aspect ratio ε, both the velocity gradient in the x–direction, $\frac{\partial u}{\partial x}$ and the velocity component in the z–direction, w are negligible due to the small aspect ratio. Consequently, $\frac{\partial u}{\partial z}$ dominates in equation (3.6), which leads to

$$u_z \gg u_x \, , u \gg w,$$

$$\dot{\gamma} = \left|\frac{\partial u}{\partial z}\right|.$$

Moreover, for a low Reynolds number and a unidirectional flow, equations (3.1), (3.2) and (3.3) reduce to

$$\frac{\partial p}{\partial x} = \frac{\partial}{\partial z}\left(\mu \frac{\partial u}{\partial z}\right), \tag{3.8}$$

$$\frac{\partial p}{\partial z} = -\rho g. \tag{3.9}$$

Equation (3.8) can be integrated as follows:

$$\mu \frac{\partial u}{\partial z} = \frac{\partial p}{\partial x}\,(z) + C_1.$$

The appropriate boundary condition should then be applied to obtain the value of the constant C_1. The free surface is shear-free and therefore,

$$\frac{\partial u}{\partial z} = 0 \ \text{ on } \ z = h, \tag{3.10}$$

which leads to

$$C_1 = -\frac{\partial p}{\partial x}\, h.$$

Substituting equation (3.4) for the viscosity gives

$$k \left|\frac{\partial u}{\partial z}\right|^{n-1} \frac{\partial u}{\partial z} = \frac{\partial p}{\partial x}\,(z-h). \tag{3.11}$$

The term $(z-h)$ is negative or zero because ($0<z<h$) and both the shear-thinning and shear-thickening cases need to be considered to avoid imaginary roots. Consequently, we take the absolute value for both sides of equation (3.11) to yield

$$\left|\frac{\partial u}{\partial z}\right|^{n} = \frac{1}{k}\left|\frac{\partial p}{\partial x}\right|\,(h-z)\,,$$

$$\left|\frac{\partial u}{\partial z}\right| = \left(\frac{1}{k}\right)^{\frac{1}{n}} \left|\frac{\partial p}{\partial x}\right|^{\frac{1}{n}} (h-z)^{\frac{1}{n}}. \tag{3.12}$$

The term $\frac{\partial u}{\partial z}$ is always positive because $\frac{\partial u}{\partial z}$ is an increasing function of (z). Integrating equation (3.12) with respect to z gives

$$u = \frac{-n}{n+1}\left(\frac{1}{k}\right)^{\frac{1}{n}} \left|\frac{\partial p}{\partial x}\right|^{\frac{1}{n}} (h-z)^{\frac{n+1}{n}} + C_2, \tag{3.13}$$

For a viscous fluid, the no-slip condition is applied and is given by

$$u = 0, z = 0, \tag{3.14}$$

which allows for the identification of C_2 as follows,

$$C_2 = \frac{n}{n+1}\left(\frac{1}{k}\right)^{\frac{1}{n}}\left|\frac{\partial p}{\partial x}\right|^{\frac{1}{n}}(h)^{\frac{n+1}{n}}.$$

Substituting C_2 into equation (3.13) gives

$$u = \frac{n}{n+1}\left(\frac{1}{k}\right)^{\frac{1}{n}}\left|\frac{\partial p}{\partial x}\right|^{\frac{1}{n}}\left[(h)^{\frac{n+1}{n}} - (h-z)^{\frac{n+1}{n}}\right]. \tag{3.15}$$

By applying the conservation of mass equation in terms of the evolution of the free surface $h(x,t)$, the following expressions are obtained, which shows the relationship between the film thickness and the fluid flux Q.

$$\frac{\partial h}{\partial t} + \frac{\partial Q}{\partial x} = 0, Q = \int_0^h u\, dz,$$

$$\frac{\partial h}{\partial t} + \frac{\partial}{\partial x}\left(\int_0^h u\, dz\right) = 0. \tag{3.16}$$

Substituting equation (3.15) into equation (3.16) to obtain an equation for the film thickness gives

$$\frac{\partial h}{\partial t} + \frac{n}{2n+1}\left(\frac{1}{k}\right)^{\frac{1}{n}}\frac{\partial}{\partial x}\left[\left|\frac{\partial p}{\partial x}\right|^{\frac{1-n}{n}}\frac{\partial p}{\partial x}\, h^{\frac{2n+1}{n}}\right] = 0. \tag{3.17}$$

The free surface velocity can be obtained by substituting $z = h$ in equation (3.15):

$$u_s = \frac{n}{n+1}\left(\frac{1}{k}\right)^{\frac{1}{n}}\left|\frac{\partial p}{\partial x}\right|^{\frac{1}{n}}(h)^{\frac{n+1}{n}}. \tag{3.18}$$

Integrating equation (3.9) with respect to z and applying the pressure condition at the free surface $p\ (z = h) = -\sigma \frac{\partial^2 h}{\partial x^2}$ gives

$$p(z) = \rho g\ (h - z) - \sigma\ \frac{\partial^2 h}{\partial x^2}, \tag{3.19}$$

where σ is the fluid surface tension and the term $\rho g\ z$ disappears when taking the gradient as in equation (3.17). Both equations (3.17) and (3.19) represent the lubrication approximation equations which are the approximation form of the Navier–Stokes equations. The lubrication approximation equation is only valid for a small aspect ratio, as indicated by many researchers such as Craster and Matar (2009), Leal (2007) and Oron and Bankoff (1997).

3.3 Model validation

3.3.1 Two dimension gravity current under its own weight

Equation (3.17) was solved using the similarity solution of the non-linear time-dependent equation by neglecting the surface tension as derived by E.Herbert (1982) and Halfar (1983) and used by Sayag and Worster (2012). The authors have solved the non-linear time-dependent lubrication approximation equation using the similarity solution technique. Subsequently, they found a mathematical expression for the fluid film thickness $h(x, t)$ related to the gravity current flow configuration as shown in Figure 3.2. Furthermore, the similarity solution includes a mathematical expression that allows for the measurement of the front current $x_N(t)$ with the related spreading time t. The mathematical expression of the front current includes the fluid rheological parameters.

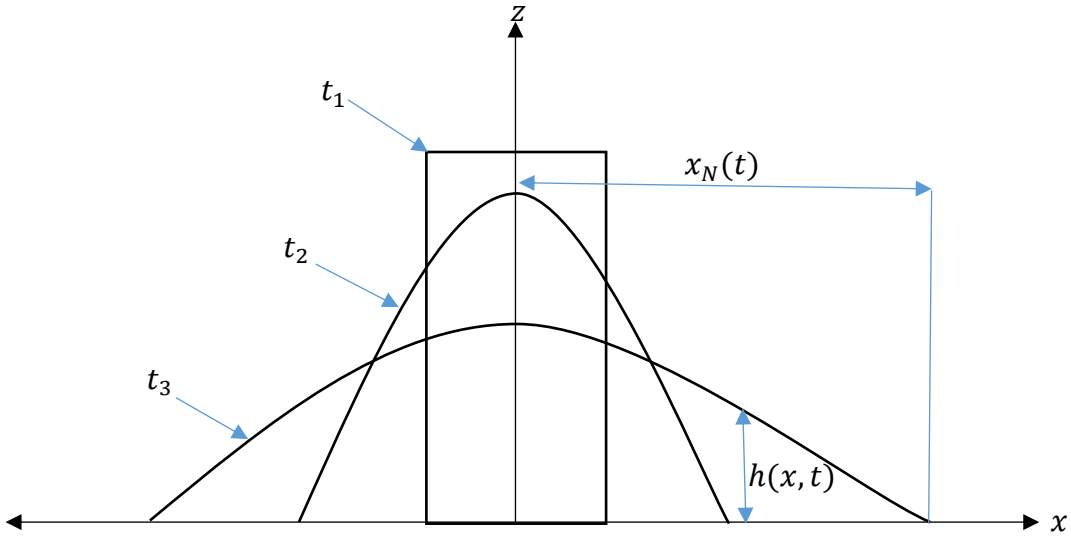

Figure 3.2: Evolution of film thickness distribution for the gravity current flow configuration and notation for the spreading of an infinite liquid strip

In Figure 3.2, $h(x,t)$ is the fluid film thickness and t_1 is the initial time. In this section, equation (3.17) and equation (3.19) were solved after neglecting the surface tension in COMSOL Multiphysics using a smoothed rectangle function (rect1(x)) describing the initial free surface level for the gravity current classical flow. To obtain the similarity solution for equation (3.17), the following volume constraint needs to be considered:

$$V = \int_0^{x_N(t)} h\, dx, \tag{3.20}$$

where V is the constant fluid volume and $x_N(t)$ is the front position of the gravity current. Then, assuming a similarity solution in the form of equation (3.17) and introducing it in the partial differential equation, followed by solving the resulting ordinary differential equation, the film thickness is expressed as Sayag and Worster (2012)

$$h(x,t) = \xi_N^{\frac{n+1}{n+2}}\, V\, b^{-1}\, t^{\frac{-n}{2n+3}}\, \psi(X), \quad X = \frac{\xi}{\xi_N}, \tag{3.21}$$

where $\psi(X)$ is the similarity function and X is the similarity variable.

$$\xi = x\, b^{-1} t^{\frac{-n}{2n+3}}, \tag{3.22}$$

$$b = \left[\frac{n}{2n+1}\left(\frac{\rho g}{k}\right)^{\frac{1}{n}} V^{\frac{n+2}{n}}\right]^{\frac{n}{2n+3}}.$$

Then, $h(x,t)$ is obtained from equation (3.21) and the position of the current front $x_N(t)$ can be determined as follows:

$$x_N(t) = \xi_N\, b\; t^{\frac{n}{2n+3}}. \tag{3.23}$$

The position of the current front is affected by the fluid rheology, time, and volume of the flowing fluid Longo, Di Federico et al. (2015). According to Sayag and Worster (2012), $\psi(X)$ is given by

$$\psi(X) = \left[\frac{n+2}{n+1}\left(\frac{n}{2n+3}\right)^{n}(1 - X^{n+1})\right]^{\frac{1}{n+2}}, \tag{3.24}$$

where

$$\xi_N = \left[\frac{2}{n+1}\left(\frac{n+2}{n+1}\right)^{\frac{1}{n+2}}\left(\frac{n}{2n+3}\right)^{\frac{n}{n+2}}\frac{\Gamma\left(\frac{n+3}{n+2}\right)\Gamma\left(\frac{1}{n+1}\right)}{\Gamma\left(\frac{n+3}{n+2}+\frac{1}{n+1}\right)}\right]^{-\frac{n+2}{2n+3}}. \tag{3.25}$$

Equation (3.23) can, in theory, be used to find the rheological parameters for a gravity current of a power-law fluid. Indeed, plotting the natural log of the front position against the natural log of time should give a straight line, the slope of which will be $\frac{n}{2n+3}$, which means that the power-law exponent can be calculated once the slope is known. For example, if we measure the position of the current as a function of time for a fluid with $n = 0.5$, $k = 20.28$ Pa·s^n, $\rho = 1500$ kg/m^3, and $V = 5 \times 10^{-4}$ m^3, the following figure is obtained:

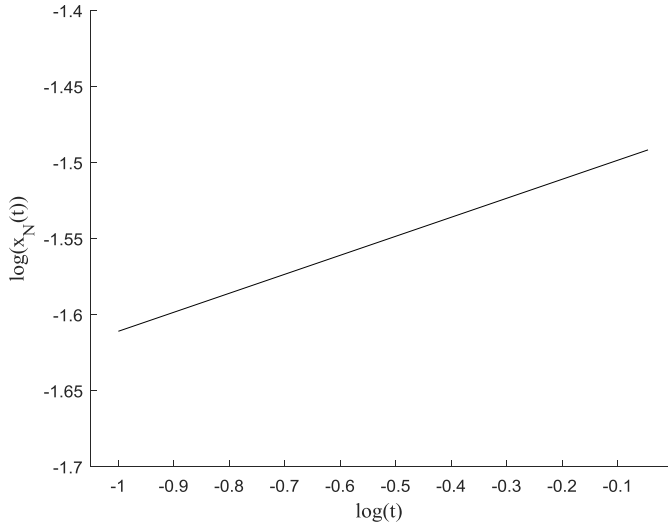

Figure 3.3: Log($x_N(t)$) as a function of log(t) of a non-Newtonian fluid for a two dimension equation

In Figure 3.3, the same flow behaviour index n can be recovered from the slope of the line. The equation of the line is $\log x = 0.125 \log t - 1.486$. The slope of the line is 0.125, which means $n = 0.5$. The consistency factor k can be calculated after substituting the fluid density, volume, and n in equation (3.23), which gives 20.28 Pa·s^n.

To validate the similarity solution which exists for the lubrication approximation of a gravity current flow configuration, the film thickness $h(x,t)$ can be determined numerically and analytically. A finite element solver, COMSOL 5.0 Multiphysics, was used to numerically solve equations (3.17) and (3.19). The analytical solution of equation (3.21) was computed using MATLAB. In COMSOL, the geometry represented a horizontal interval of 0.916 m length, which represents the length of our test rig (see Section 2.1.1) and was divided into 200 quadratic elements. This interval involves a zero flux at the ends ($\frac{\partial p}{\partial x} = 0$ and $\frac{\partial h}{\partial x} = 0$ at both $x = 0$ and $x = L$). The boundary conditions represented shear-free at the free surface and no-slip on the bottom of the domain. The smooth and continuously differentiable rectangle flow function was used to describe the initial fluid free surface of the gravity current flow configuration. For both simulations the values of n,k, and V were chosen to be 0.5, 20.28 Pa·s^n, and 5×10^{-4}m^3, respectively. The

comparison between the numerical results obtained using COMSOL and the similarity solution was implemented by neglecting the surface tension and is shown in Figure 3.4.

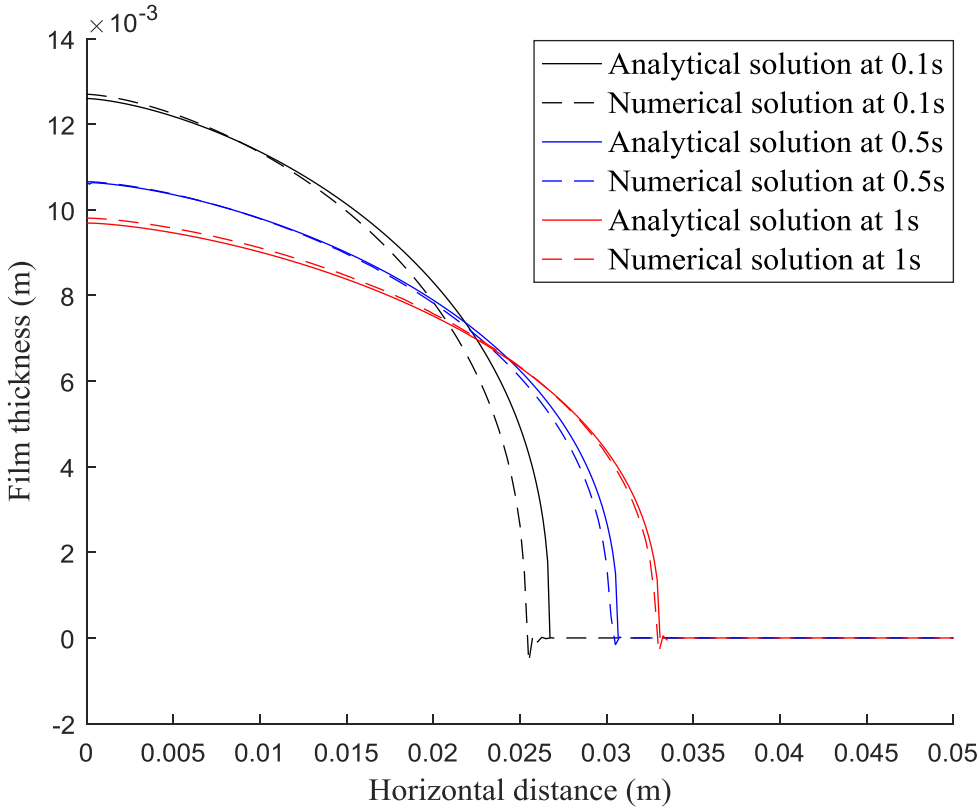

Figure 3.4: Film thickness h as a function of the position x calculated using COMSOL and the similarity solution of equation (3.21)

Figure 3.4 shows that the analytical and numerical solutions of the time-dependent lubrication approximation are very close and the small difference at the earliest time step can be attributed to the Dirac impulse function that was assumed for the analytical solution, whereas a finite fluid depth H_0 has to be imposed as the initial condition in COMSOL. In addition, an overshoot in the front region occurred in the numerical solution due to the slope of the rectangle flow function that was used to describe the initial free surface. The initial values used in the numerical set up was zero for p, $\frac{\partial p}{\partial t}$ and $\frac{\partial h}{\partial t}$. While, the initial value of h was rect1(x).

3.3.2 Axisymmetric equations (spreading of a liquid puddle)

The derivation above is considered for the two-dimensional lubrication equations (spreading of an infinite liquid strip or planar flow). Next, we consider the axisymmetric spreading of a gravity current as shown in Figure 3.5.

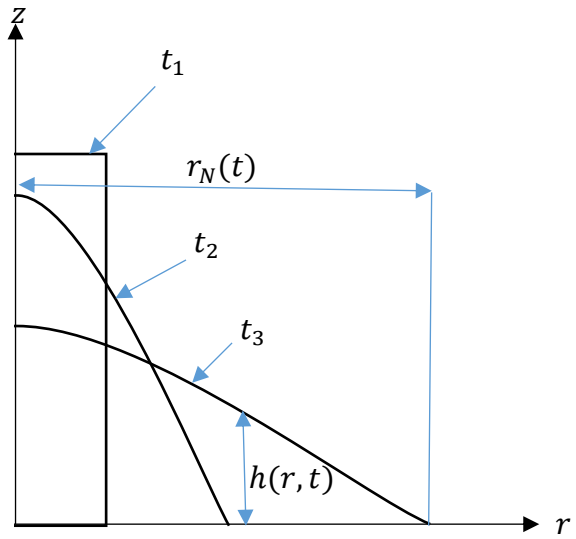

Figure 3.5: Evolution of film thickness distribution for the gravity current flow configuration and notation for the spreading of a liquid puddle

In Figure 3.5, $h(r,t)$ is the fluid film thickness and t_1 is the initial time. It is important to transform the Cartesian coordinate into a cylindrical coordinate using a mathematical transformation expression:

$$x = r\cos\theta \text{ and } y = r\sin\theta\,.$$

Substituting the expressions above into equation (3.8) yields

$$\frac{\partial p}{\partial r} = \frac{\partial}{\partial z}\left(\mu\frac{\partial u}{\partial z}\right). \tag{3.26}$$

Integrating (3.26), yields

$$\mu \frac{\partial u}{\partial z} = \frac{\partial p}{\partial r}\,(z) + C_1.$$

According to the shear-free condition on the fluid free surface, $z = h$ and $\frac{\partial u}{\partial z} = 0$, which leads to $C_1 = -\frac{\partial p}{\partial r}\,h$. Substituting equation (3.4) into equation (3.26) yields

$$k\,\left|\frac{\partial u}{\partial z}\right|^{n-1}\frac{\partial u}{\partial z} = \frac{\partial p}{\partial r}\,(z-h).$$

Similar to Section 3.2,

$$k\left|\frac{\partial u}{\partial z}\right|^{n} = \left|\frac{\partial p}{\partial r}\right|\,(h-z), \tag{3.27}$$

$$\left|\frac{\partial u}{\partial z}\right| = \left(\frac{1}{k}\right)^{\frac{1}{n}}\left|\frac{\partial p}{\partial r}\right|^{\frac{1}{n}}\left((h-z)\right)^{\frac{1}{n}}. \tag{3.28}$$

Integrating equation (3.28) yields

$$u = \frac{-n}{n+1}\left(\frac{1}{k}\right)^{\frac{1}{n}}\left|\frac{\partial p}{\partial r}\right|^{\frac{1}{n}}\left((h-z)\right)^{\frac{n+1}{n}} + C_2\,.$$

Then, at $z = 0, u = 0$, which means $C_2 = \frac{n}{n+1}\left(\frac{1}{k}\right)^{\frac{1}{n}}\left|\frac{\partial p}{\partial r}\right|^{\frac{1}{n}}(h)^{\frac{n+1}{n}}$. Substituting the C_2 obtained in the equation above for u yields

$$u = \frac{n}{n+1}\left(\frac{1}{k}\right)^{\frac{1}{n}}\left|\frac{\partial p}{\partial r}\right|^{\frac{1}{n}}\left[(h)^{\frac{n+1}{n}} - (h-z)^{\frac{n+1}{n}}\right]. \tag{3.29}$$

Substituting equation (3.29) into the conservation of mass for axisymmetric flow in terms of the evolution of the free surface $h(r,t)$ of fluid gives

$$\frac{\partial h}{\partial t}+\frac{1}{r}\frac{\partial}{\partial r}\left(r\int_0^h u\,dz \right)=0. \tag{3.30}$$

Substituting equation (3.29) into (3.30) followed by integration with respect to z yields

$$\frac{\partial h}{\partial t}+\frac{n}{2n+1}\left(\frac{1}{k}\right)^{\frac{1}{n}}\frac{1}{r}\frac{\partial}{\partial r}\left[r\left|\frac{\partial p}{\partial r}\right|^{\frac{1-n}{n}}\frac{\partial p}{\partial r}\,h^{\frac{2n+1}{n}}\right]=0. \tag{3.31}$$

Similar to Section 3.3.1, equation (3.31) can be solved using the similarity solution as derived by E.Herbert (1982), Halfar (1983) and used by Sayag and Worster (2012). The volume constant is given by

$$V=2\pi\int_0^{R_N(t)} rh\,dr. \tag{3.32}$$

The similarity solution mentioned by Sayag and Worster (2012) is expressed as

$$h(r,t)=\xi_N^{\frac{n+1}{n+2}}\,V\,b^{-2}\,t^{\frac{-2n}{3n+5}}\,\psi(X), \tag{3.33}$$

where, $\xi=r\,b^{-1}t^{\frac{-n}{3n+5}}$ and $X=\frac{\xi}{\xi_N}$. Hence,

$$b=\left[\frac{n}{2n+1}\left(\frac{\rho g}{k}\right)^{\frac{1}{n}}V^{\frac{n+2}{n}}\right]^{\frac{n}{3n+5}}. \tag{3.34}$$

Therefore, $R_N(t)=\xi_N\,b\;t^{\frac{n}{3n+5}}$, (3.35)

According to (Sayag and Worster 2012), $\psi(X)$ is given by

$$\psi(X) = \left[\frac{n+2}{n+1}\left(\frac{n}{3n+5}\right)^{n}\left(1 - X^{n+1}\right)\right]^{\frac{1}{n+2}}, \tag{3.36}$$

where

$$\xi_N = \left[\frac{2\pi}{n+1}\left(\frac{n+2}{n+1}\right)^{\frac{1}{n+2}}\left(\frac{n}{3n+5}\right)^{\frac{n}{n+2}}\frac{\Gamma\left(\frac{n+3}{n+2}\right)\Gamma\left(\frac{2}{n+1}\right)}{\Gamma\left(\frac{n+3}{n+2}+\frac{2}{n+1}\right)}\right]^{-\frac{n+2}{3n+5}}. \tag{3.37}$$

Similar to Section 3.3.1, the rheological parameters for the axisymmetric flow can be calculated from the slope $\frac{n}{3n+5}$ of equation (3.37) in a log–log plot. In this section, a fluid with $n = 0.1$, $k =$ 5.7 Pa·s^n, $\rho = 1500$ kg/m^3, and $V = 5 \times 10^{-4}$ m^3 was considered and the resulting front position as a function of time is shown in Figure 3.6.

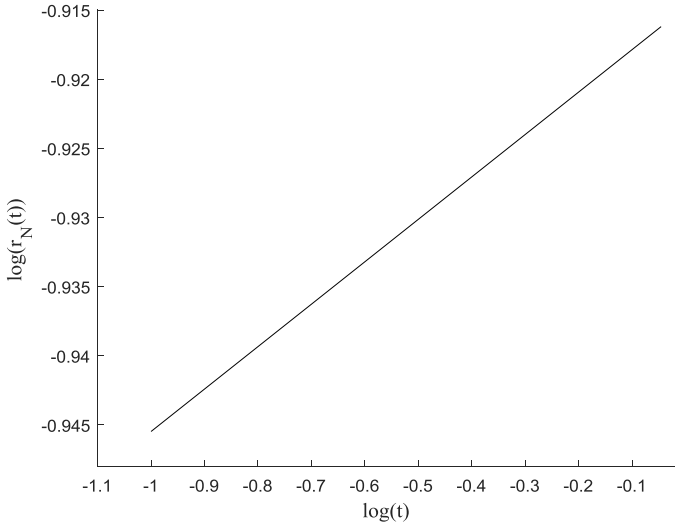

Figure 3.6: Log($r_N(t)$) as a function of log(t) of a non-Newtonian fluid for an axisymmetric equation

In Figure 3.6, the same flow behaviour index n can be obtained from the slope of the line. The equation of the fitted line is $\log r = 0.0307\ \log t - 0.914$. The slope of the line is 0.0307, which means $n = 0.1$ for the fluid used and k can be obtained after substituting the fluid density, volume, and n in equation (3.35), which gives 5.7 Pa·s^n.

To verify equation (3.33), the film thickness obtained from equation (3.33) can be compared with that obtained by Sayag and Worster (2012). The authors have used xanthan gum with density 1500 kg/m^3 and volume 5×10^{-4} m^3 as a working fluid to achieve the axisymmetric gravity currents of power-law fluids over a rigid horizontal surface. The rheological parameters results of the above-mentioned work were n =0.1 and k =5.7 Pa·s^n. The outcomes from the comparison is shown in Figure 3.7.

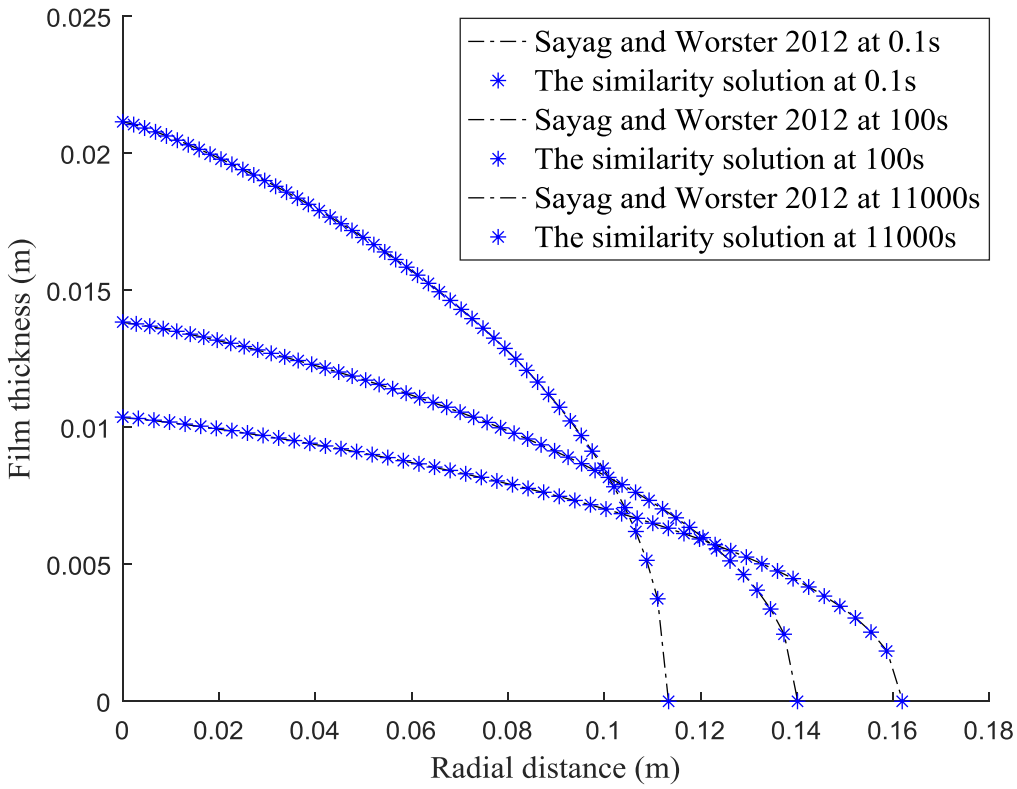

Figure 3.7: Liquid film thickness as a function of radial distance for three different times

Figure 3.7 shows very good agreement between the results of the current similarity solution and that obtained by Sayag and Worster (2012). The three curves above show how the film thickness and wetting front change with respect to time. Initially, the film thickness and the radial distance is more than 0.02 m and 0.1 m, respectively. Subsequently, the gravity current becomes shallower and covers a wider surface area.

Chapter 4

The numerical methods

Contents

4.1 Numerical solution for the lubrication approximation equations

In this section, we aim to solve two different problems numerically: the dam-break problem and the two-dimension gravity current over a wetted surface problem as shown in Figure 4.1.

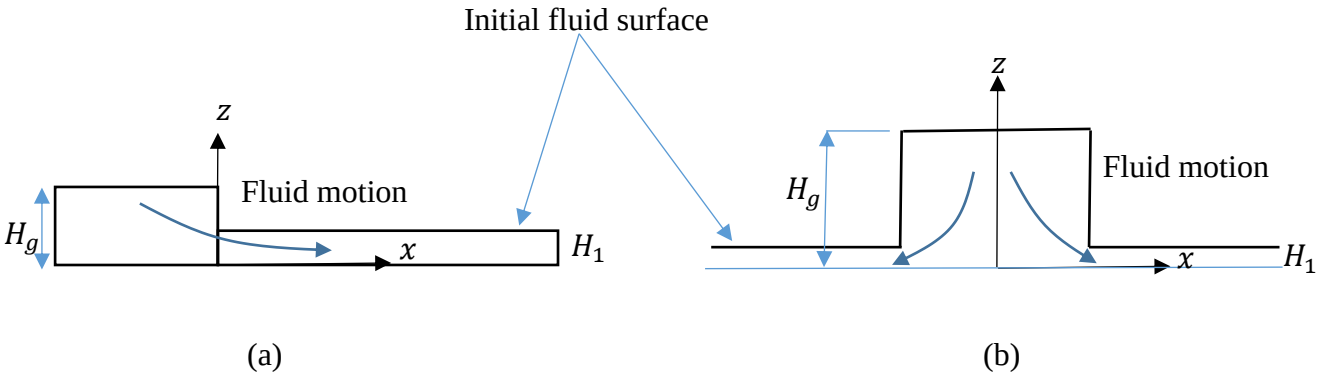

Figure 4.1: Sketch of two different flow problems: (a) dam-break problem and (b) two dimension gravity current over a wetted surface problem

The lubrication approximation are partial differential equations describing the fluid film thickness $h(x,t)$ and the fluid pressure $p(x,t)$. The boundary conditions applied are no-slip at $z = 0$ and stress-free at $z = h$. The lubrication approximation are adapted to include the effect of some rheological models such as the power-law model. These equations were discretized using the finite element method, which was solved using COMSOL Multiphysics.

This software can solve a wide range of partial differential equations. In this project, we aim to solve equations (3.17) and (3.19) using the coefficient form partial differential equation module from COMSOL. The lubrication approximation equations included two dependent variables, namely the fluid film thickness h and the fluid pressure p. To solve the lubrication approximation equations with COMSOL, equations (3.17) and (3.19) are rewritten in the standard form solved by COMSOL and the coefficients are matched:

$$e_a \frac{\partial^2 \boldsymbol{u}}{\partial t^2} + d_a \frac{\partial \boldsymbol{u}}{\partial t} + \nabla.\left(-c\,\nabla \boldsymbol{u} - \boldsymbol{\alpha u} + \boldsymbol{\gamma}\right) + \boldsymbol{\beta}.\,\nabla \boldsymbol{u} + a\boldsymbol{u} = \boldsymbol{f}, \boldsymbol{u} = [h, P]^T. \qquad (4.1)$$

In equation (4.1), e_a, $d_a, c, \boldsymbol{\alpha}, \boldsymbol{\gamma}, \boldsymbol{\beta}, a$, and $\boldsymbol{f}$ are the coefficients required from the partial differential equations. The geometry represents a horizontal interval divided into quadratic elements; the total length was 0.916 m and the number of quadratic elements was 200. This interval involves a zero flux boundary condition at the ends ($\frac{\partial p}{\partial x} = 0$ and $\frac{\partial h}{\partial x} = 0$ at both $x = 0$ and $x = L$). The initial values used in the numerical set up was zero for p, $\frac{\partial p}{\partial t}$ and $\frac{\partial h}{\partial t}$. While, the initial value of h was step1(x), which represents the step flow function.

In both equations (3.17) and (3.19) the coefficients of the dependent variables $h(x,t)$ and $p(x,t)$ were matched with the coefficients in equation (4.1) as shown in Table 4.1.

Coefficients of equation 4.1	Coefficients of $h(x,t)$ Equation 3.17/3.19	Coefficients of $p(x,t)$ Equation 3.17/3.19
e_a	0/0	0/0
d_a	1/0	0/0
c	0/- σ	0/0
$\boldsymbol{\alpha}$	0/0	0/0
$\boldsymbol{\gamma}$	$\frac{n}{2n+1}\left(\frac{\left\|\frac{\partial p}{\partial x}\right\|}{k}\right)^{\frac{1}{n}} h^{\frac{2n+1}{n}}$	0
$\boldsymbol{\beta}$	0/0	0/0
a	0/- ρ g	0/1
$\boldsymbol{f}$	0	0

Table 4.1: The coefficient match of equation (4.1) in COMSOL

The fluid parameters must first be indicated to implement the numerical solution of the lubrication approximation equations. These parameters must include the fluid properties and the domain dimensions, which were used in the experiment as shown in Table 4.2.

Parameters		
Name	Value	Description
L	0.916 m	Domain length
ρ	970 $\frac{kg}{m^3}$	Fluid density
g	9.81 $\frac{m}{s^2}$	Acceleration
σ	0.0211 $\frac{N}{m}$	Fluid surface tension
H_1	0.009 m	Initial thickness of the liquid at the downstream region of the flow
k	0.5 Pa·s^n	Consistency factor
n	0.9	Flow behaviour index

Table 4.2: Parameters used in COMSOL Multiphysics

Next, the initial fluid free surface must be described by choosing the step flow function or the rectangle flow function from the model builder, according to the flow configuration as shown in Figure 4.1.

In the following sections, we describe two different numerical solutions of the lubrication approximation in terms of the flow configurations.

4.1.1 Numerical solution of the dam-break problem

The step function was used to describe the liquid free surface in the dam-break problem. The fluid flows gradually from the high level (upstream) to the low level (downstream) of the tank. The step function includes two smoothed corners that affect fluid flow initially due to the high curvature around the corners.

According to Figure 4.2, $h(x,t)$ represents the liquid film thickness and the maximum height of the film can be expressed as $h(x,t) + H_1$.

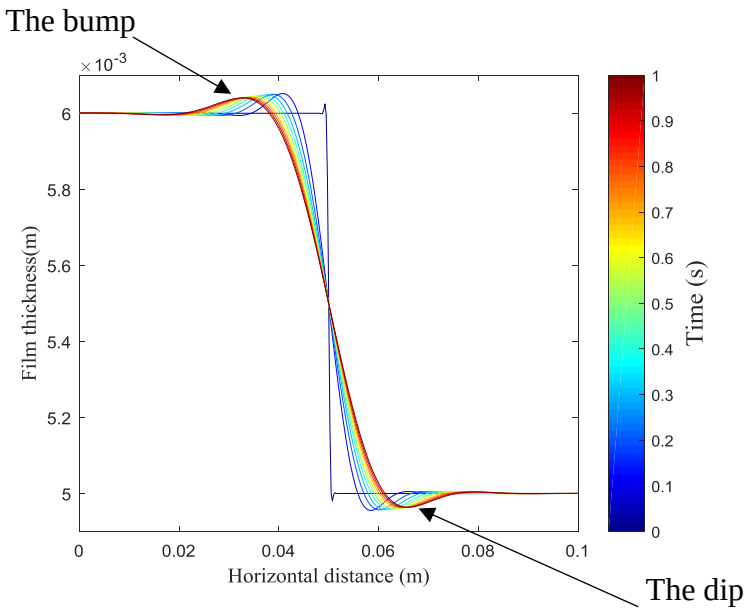

Figure 4.2: Evolution of the film thickness distribution for the dam-break problem. The time interval between each curve is 0.1 s, the parameters were: $L = 0.1$ m, $\rho = 1000$ Kg/m^3, $\sigma = 0.7$ N/m, $H_1 = 0.005$ m, $n = 0.4$, and $k = 60$ Pa·s^n

The computational domain for Figure 4.2 was a line interval of length 0.1 m, which was divided into 200 quadratic elements. It is evident that there is a "bump" on the thick side of the film and a "dip" on the thin side as observed by McGraw, Jago et al. (2011). The dip and bump appearing in the film thickness profile are due to the effect of the surface tension measuring 0.7 N/m. When surface tension was set to zero, the following figure is obtained:

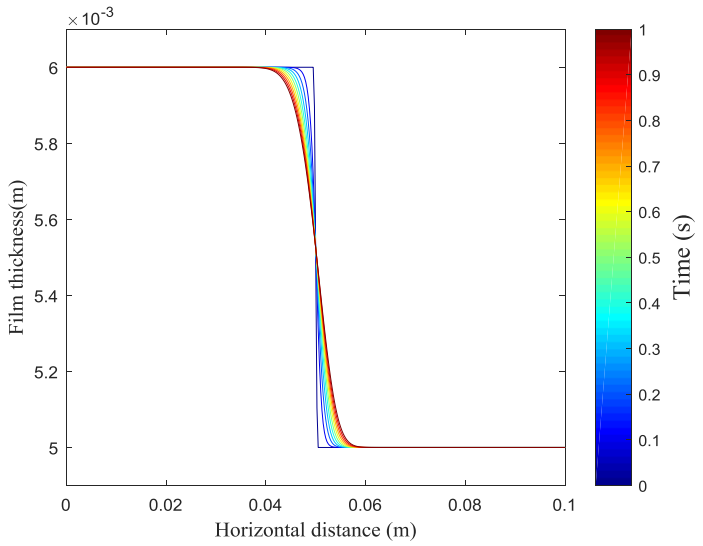

Figure 4.3: Evolution of the film thickness distribution with zero surface tension for the dam-break problem. The time interval between each curve is 0.1 s, the parameters used are the same as in Figure 4.2

In both Figure 4.2 and Figure 4.3, the film profile looks like the "stepped film" of the dam-break problem, in which it flattens (the curvature decreases) and flows along the wide distance with increasing simulation time McGraw, Salez et al. (2012).

4.1.2 Numerical solution of the two dimension gravity current over a wetted surface problem

The rectangle function was used to describe the initial fluid surface in the two dimension symmetrical fluid motion over a wetted surface flow configuration as shown in Figure 4.4. The film thickness height $h(x,t)$ represents the vertical distance between the crest of the rectangle function and the initial thickness of the liquid H_1.

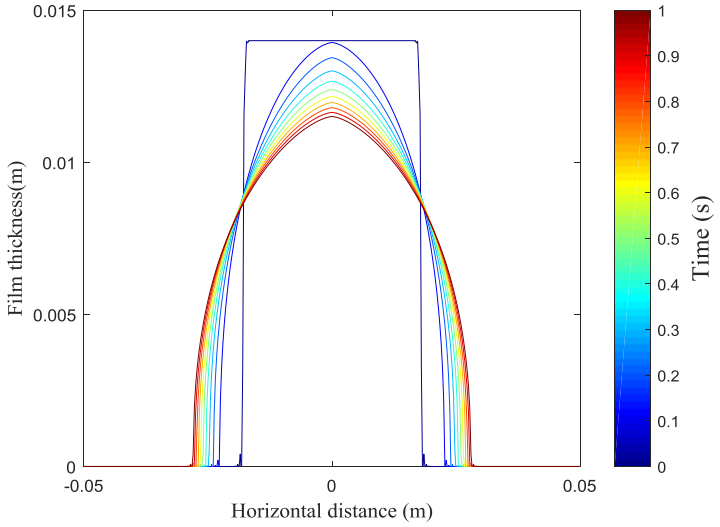

Figure 4.4: Evolution of the film thickness distribution for the two dimension gravity current over a wetted surface problem. The time interval between each curve is 0.1 s, the parameters used are the same as in Figure 4.2

In Figure 4.4, the computational domain was a line interval of length 0.1 m, which was divided into 200 quadratic elements. The volume of the fluid used was 5×10^{-4} m^3.

4.2 Numerical solution of free surface velocity equation

The lubrication approximation equations were solved to obtain the fluid film thickness h and the fluid pressure p. These computed values were used to calculate the fluid free surface velocity by applying equation (3.18). The velocity profiles obtained were described in Sections 4.2.1 and 4.2.2.

4.2.1 Velocity profile of dam-break problem

In this section, equation (3.18) was used to obtain the velocity profile for the dam-break problem. The software COMSOL was used to obtain the velocity profile with the same numerical setup indicated in Section 4.1.1.

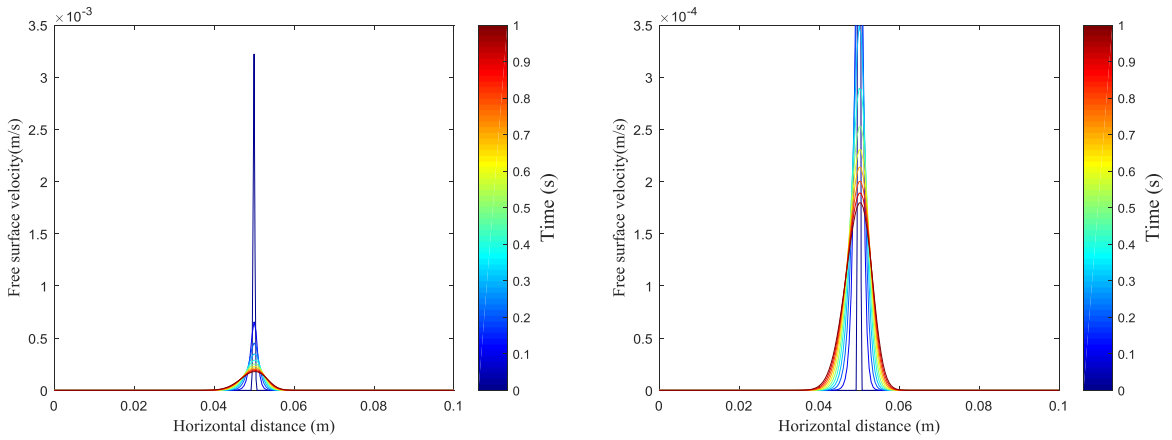

Figure 4.5: Evolution of the free surface velocity distribution for the dam-break problem. The time interval between each curve is 0.1 s and the parameters are the same as in Figure 4.2

Figure 4.5 illustrates the free surface velocity profile for the dam-break problem. The velocities are at early times were greater than those at later times. This occurs because the fluid flow rate is associated to the fluid free surface slope. Initially, the free surface slope was high. Consequently, the earliest free surface velocities were the highest.

4.2.2 Velocity profile of the two dimension gravity current over a wetted surface problem

Similar to Section 4.2.1, the free surface velocity profile was calculated using equation (3.18). However, in Section 4.2.1 the initial free surface of the fluid was described using the step flow profile. In this Section, the rectangle flow profile was used to describe the initial fluid free surface.

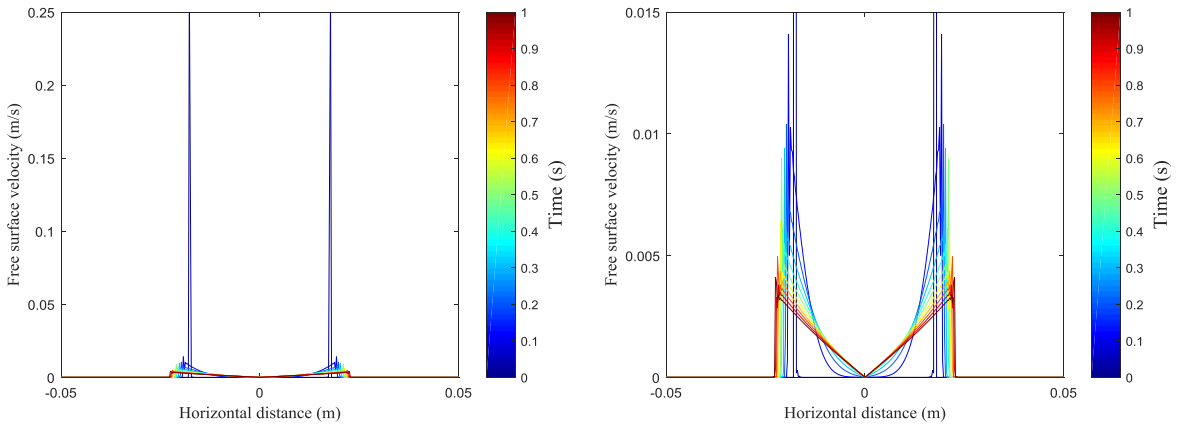

Figure 4.6: Evolution of the free surface velocity distribution for the two-dimension gravity current over a wetted surface problem. The time interval between each curve is 0.1 s, the parameters are the same as in Figure 4.1 with $V = 5 \times 10^{-4}$ m^3

As evident in Figure 4.6, the velocity profile has an axial symmetry around the z–axis, as expected, because the rectangular geometry of the domain is symmetrical. Therefore, it reaches the maximum value around the top corners due to the small curvature.

4.3 Navier–Stokes solver

The Navier–Stokes equations are used to model Newtonian or non-Newtonian flows depending on which rheological law is selected. COMSOL uses the Finite Element Method. The two-phase flow moving mesh interface of COMSOL was used to simulate the traversing fluid in the dam-break problem. The full incompressible Navier–Stokes equations were solved in a domain that was deformed by the moving surface of the fluid using the Arbitrary Lagrangian Eulerian (ALE) method. This method describe the moving of mesh based on both the Lagrangian and Eulerian algorithms. The ALE attempts to combine the advantages of both algorithms and minimise their disadvantages as far as possible. In addition, the ALE method allows the mesh to conform to the evolving fluid domain as the free surface transforms over time.

The Winslow mesh smoothing technique was used for propagating the mesh deformation throughout the domain. The geometry for the computational domain was composed of two adjacent rectangles (representing the tank in two dimensions), with dimensions as shown in Figure 4.8. The initial free surface of the fluid was composed of the top edges of the domain, and the

sharp corners at $x = 0$ mm were smoothed with 2-mm fillets, in order to avoid discontinuities of the free surface slope. The domain was discretised with an unstructured mesh consisting of 1735 triangular elements. The simulation was initialised with $u = 0$ m/s and $p = 0$ Pa throughout the domain. The boundary conditions prescribed for the fluid phase were (i) no-slip on the base of the tank, (ii) Navier slip on the two ends of the tank, and (iii) an external fluid interface for the free surface. Lastly, for the boundary conditions imposed on the mesh: (i) the base of the tank was fixed in the z-direction, (ii) the two ends of the tank were fixed in the x-direction, and (iii) no constraints were imposed on the mesh displacement at the free surface. A contact angle of 90° was imposed on the two end corners of the free surface. Moreover, a ramp function $rm(t)$ was used to ramp the gravity body force to ease solution convergence. The ramp function was applied over 8.3×10^{-3} s, as shown in Figure 4.7.

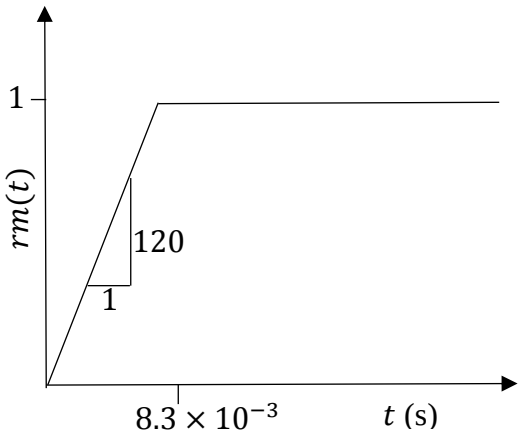

Figure 4.7: Ramp function used in simulations

In Figure 4.7, the slope gives an indication of the time required from the start of the simulation until it reaches the full gravity force. The gravity force F_g, which arose due to the volume of the fluid, is $F_g = \rho\ g\ rm(t)$. A transition zone of size 0.005 s was used to smooth out the beginning and end of the ramp function profile in order to avoid simulation crash.

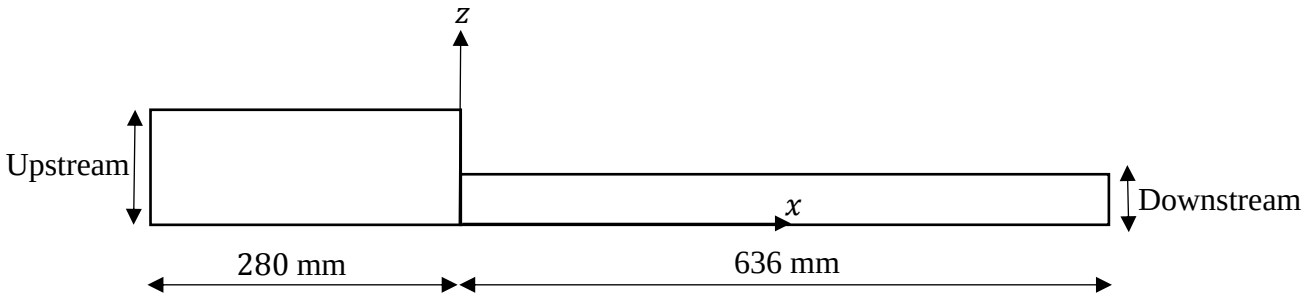

Figure 4.8: Geometry for simulations

The heights of the upstream and downstream were selected to generate sufficient flow for visualization and for measuring the fluid flow over a finite time (as explained in Chapter 2).

4.4 Parameter identification

Parameter identification was performed by implementing a parametric study and minimizing the mismatch between the measured and computed free surface velocity. To measure the mismatch, the following objective function OF was defined for N times in the experimental data:

$$OF(n,k) = \sum_{i=1}^{N} 0.5 \int_{0}^{L} \left(u_c(x, t = i\Delta t) - u_m\,(x, t = i\Delta t)\right)^2 dx\,. \tag{4.2}$$

Where u_m is the measured free surface velocity obtained from the experiment and u_c is the computed velocity obtained from the lubrication approximation (equation 3.18). N is the number of the experimental times at which the free surface velocity field was selected. Consequently, a wide range of n $(0 < n \leq 2)$ and k $(0 < k \leq 50)$ was used to calculate the objective function. The optimal results will lead to the minimum value of the objective function; this value means that the convergence between the experimental and the numerical data is optimal or the difference between the solutions is minimal. After obtaining the minimum value of the objective function, the next step is to choose the rheological parameters that correspond to the minimum objective function. Finally, the chosen rheological parameters were compared with the true values obtained from the rheometer measurements to validate the accuracy of the parametric identification solution.

4.4.1 Identification with perfect synthetic data

To test the parametric identification methodology, synthetic experimental data were produced by running COMSOL with k =0.4 Pa·s^n, n =0.7, and applying equation (3.18) with $N = 1$ and $\Delta t = 2$ s. The problem parameters were the same as that indicated in Table 4.2 and the aspect ratio ε was 0.015, which was calculated as indicated in Section 3.2 with H_g and H_1 values from Table 2.1 of the silicone oil. A parametric study was then undertaken to check whether the minimum of the OF had occurred at the correct values of n and k. The following figure shows the contour lines and surface plots of the objective function as a function of the parameters n and k. The solution was implemented with the same numerical setup indicated in Section 4.1.1. However, the domain length was 0.916 m instead of 0.1 m to represent the length of our test rig (see Section 2.1.1). A step flow function was used to describe the initial fluid surface profile (a subset of the data that is close to the solution is shown here).

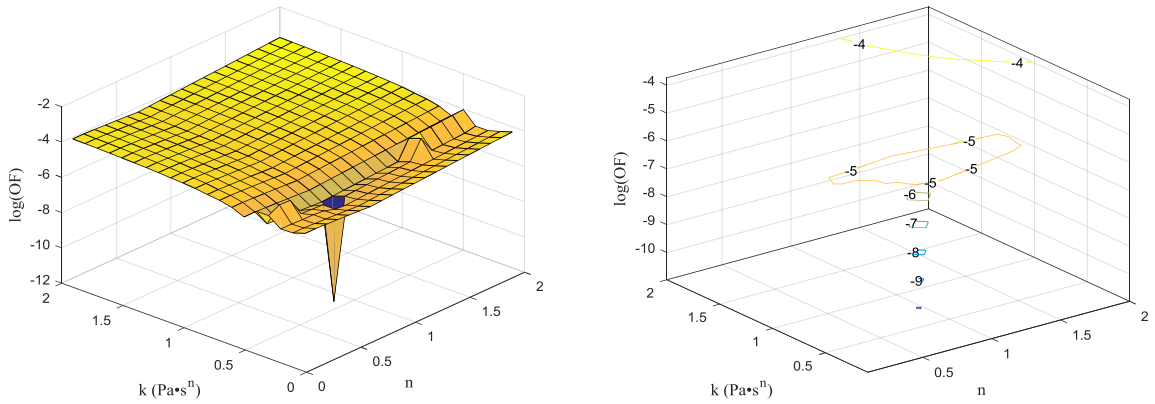

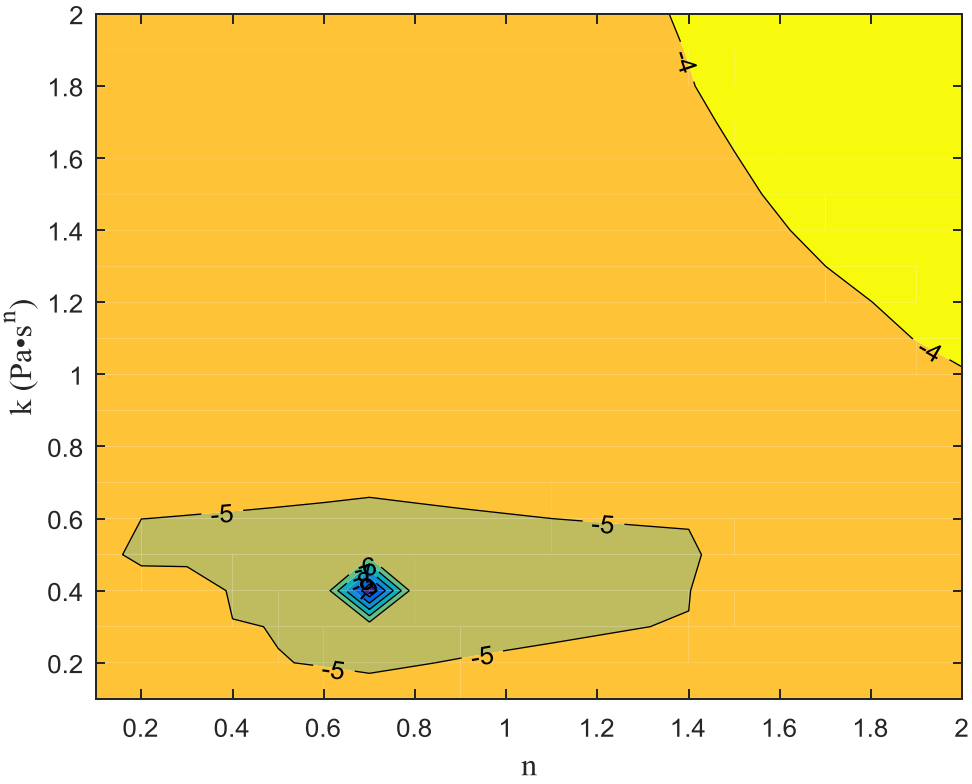

Figure 4.9: Contour lines and surface of the objective function with respect to the rheological parameters obtained from the solution of the parameter identification problem with perfect synthetic data obtained from the lubrication approximation solver

In Figure 4.9, the global minimum value of the objective function is 1.06×10^{-11} m^3/s^2 at n = 0.7±0.1 and k = 0.4±0.1 Pa·s^n. The results above indicate that the solution of the parameter identification problem is valid and, more importantly, a unique minimum exists, which indicates that the parameters can be identified in principle.

The synthetic data above were generated using the lubrication approximation solver. Another synthetic experimental dataset was produced by running COMSOL with k = 0.5 Pa·s^n and n = 1.5, and $N = 1$ at $\Delta t = 2$ s using the two-dimensional Navier–Stokes solver. The numerical setup was the same as that indicated in Section 4.3 with 0.015 aspect ratio and the problem parameters were according to Table 4.2. The results, again, show the existence of a global minimum and the

successful identification of the parameters as the values n = 1.5±0.1 and k = 0.5±0.1 Pa·s^n were recovered.

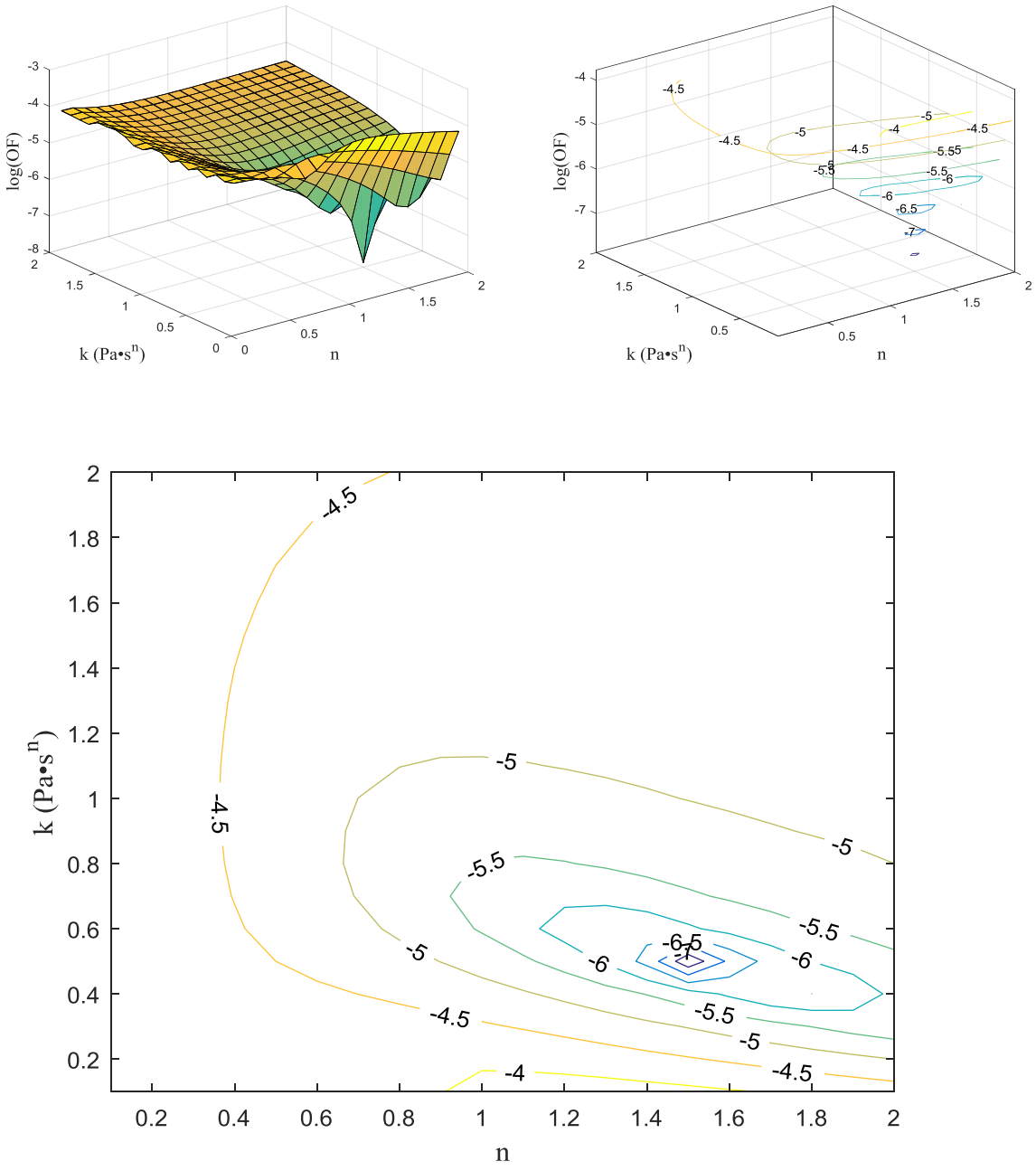

Figure 4.10: Contour lines and surface of the objective function with respect to the rheological parameters obtained from the solution of the parameter identification problem with perfect synthetic data obtained from the two-dimensional Navier–Stokes solver

4.4.2 Identification with noisy synthetic data

The previous results have illustrated that the proposed strategy was capable of reconstructing the rheological parameters from an ideal data set for the free surface data. However, experimental data is typically affected by noise. A sensitivity analysis provides information about the robustness of the proposed method. Previous studies have used the sensitivity analysis to understand the robustness of the results, as in the works of Winkelmann, Martin et al. (2011), Sellier and Panda (2016) and Heining and Sellier (2016). Consequently, the parameter identification process was next tested with noisy synthetic dataset created from the lubrication model by running the COMSOL with n = 0.7, k = 0.4 Pa·s^n, and $N = 1$ at $\Delta t = 2$ s. Artificial uniform distribution noise was added to the synthetic experimental data and then the parameter identification process was repeated with the same numerical setup, i.e. of 0.916 domain length, as mentioned in Section 4.1.1. The OF in equation (4.2) can be rewritten to include the noise component:

$$OF(n,k) = \sum_{i=1}^{N} 0.5 \int_{0}^{L} (u_c(x, t = i\Delta t) - (u_m(x, t = i\Delta t) + e))^2 \, dx \, . \tag{4.3}$$

The amount of noise (e) in equation (4.3) is defined as

$$e = (u_{max} - u_{min}) * E * pr \, , \tag{4.4}$$

where, u_{max} and u_{min} represent the maximum and minimum values of the free surface velocity, respectively; pr is the percentage of the added noise; and the random values -1 $\leq$ $E \leq$ +1. The identification procedure is found to be valid even when up to 40% noise is added to the ideal dataset, which validates the robustness of the results.

Figure 4.11 shows the contour plots of the objective function with respect to the rheological parameters obtained for two cases: the first is without added noise and the second is with 40% added noise (a subset of the data that is close to the solution is shown here).

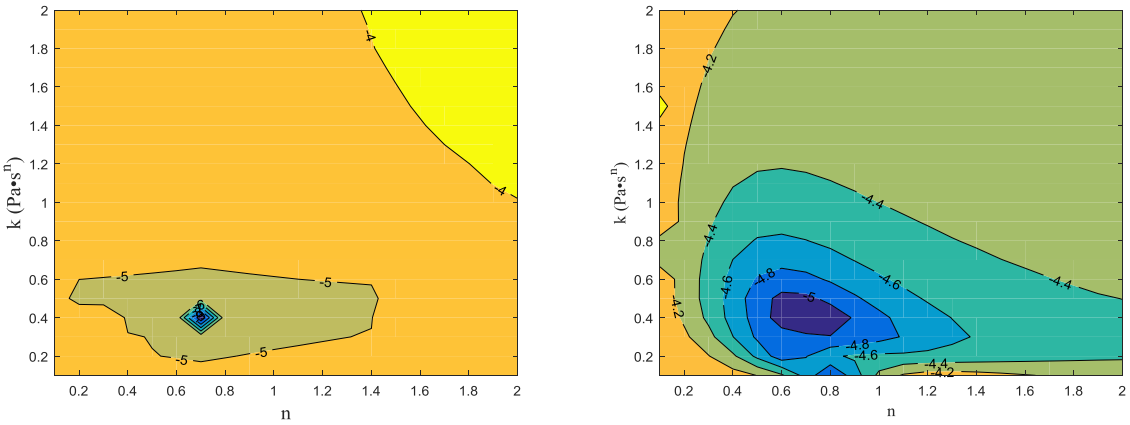

Figure 4.11: Contour lines of the objective function with respect to the rheological parameters for two cases, the first is without added noise (left) and the second is with added 40% noise (right), with k =0.4 Pa·s^n, n =0.7

The identification with experimental data will be explained in Chapter 5.

Chapter 5

Results and Discussion

Contents

5.1 Experimental results for silicone compound oil

The area inside the tank which was captured by the camera for all the experiments is shown in Figure 5.1.

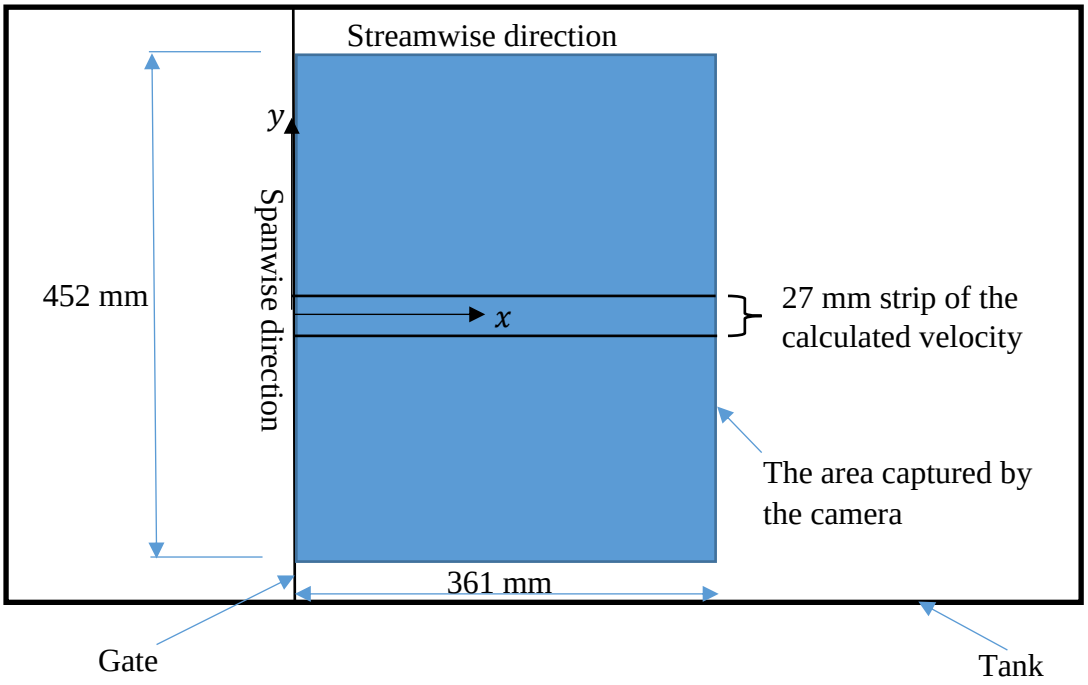

Figure 5.1: Sketch of the area captured by the camera

In the first experiment using silicone oil, we found that the average match percentage rate of the particles was 97.5%. This percentage gives an indication about the quantity of particles recognized by the software Streams and is used to calculate the velocity fields. Non-matched particles cannot be considered for the computation of the velocity field.

Figure 5.2 shows the paths of the particles at the free surface of the silicone oil. Evidently, the paths of particles were almost straight. However, small curves had also appeared, possibly due to the perturbed fluid flow between the gate and the walls.

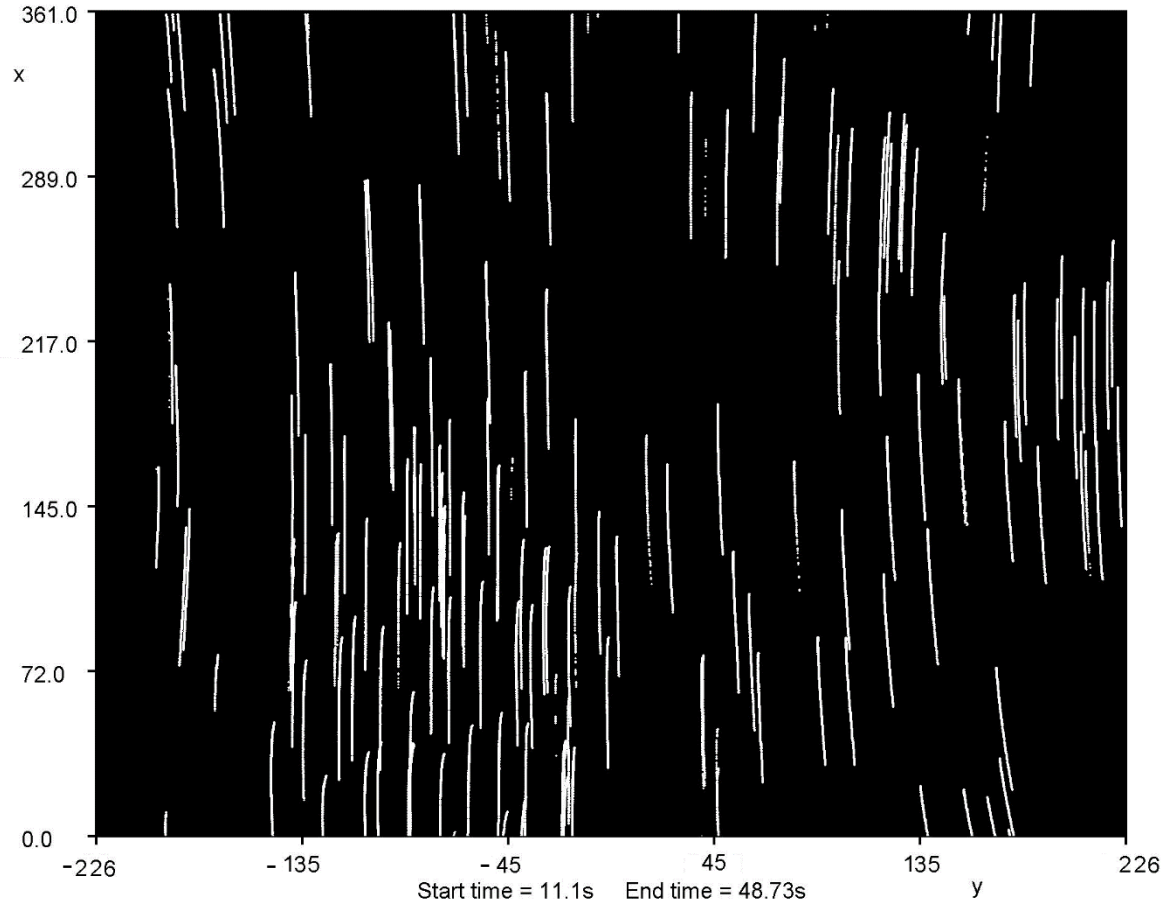

Figure 5.2: Paths of particles at the free surface of the silicone compound oil, where x and y are the horizontal and vertical distances, respectively, in mm. (displayed in Streams)

The velocity vector field can be obtained from the particle record object of Streams and was used to calculate the Eulerian velocity field. In this work, the experimental time step was 0.03 s for the silicone oil, and seven different times between 0.43 s and 2.46 s were chosen in the parameter identification, namely 0.43 s, 0.66 s, 0.93 s, 1.3 s, 1.66 s, 2.06 s, and 2.46 s. Consequently, the objective function defined according to equation (4.2) can be calculated with $N = 7$.

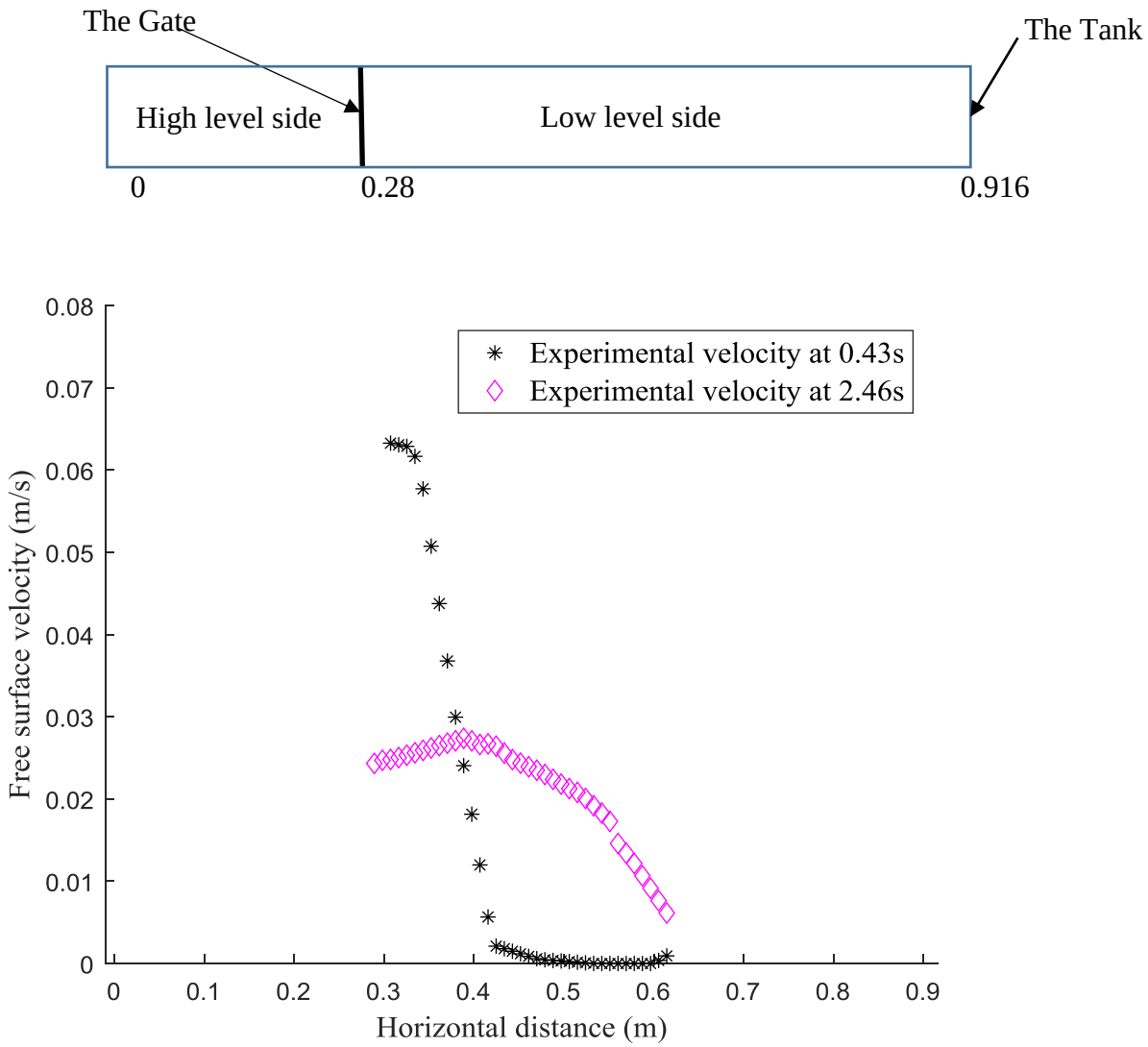

Figure 5.3: Averaged velocity distribution across the flow and along a 2.7-cm width around the tank centreline for the first and last selected periods for silicone oil

Figure 5.3 shows the variation in free surface velocity with the horizontal distance along the tank centreline for two different times (the first and last chosen time for the parametric identification study). This figure clearly shows that at t = 0.43 s the maximum free surface velocity is 0.063 m/s and the velocity decays toward zero away from the gate. At t = 2.46 s, the free surface velocity is bounded between 0.028 m/s and 0.005 m/s along the tank centreline. This implies the fluid free surface velocity became much smaller compared with 0.43 s. Smaller velocity implies higher error in terms of the pixel displacement of the particles as indicated in equation (2.2). The free surface

velocity distribution and the corresponding vector fields are shown in Figure 5.4 for the seven different times.

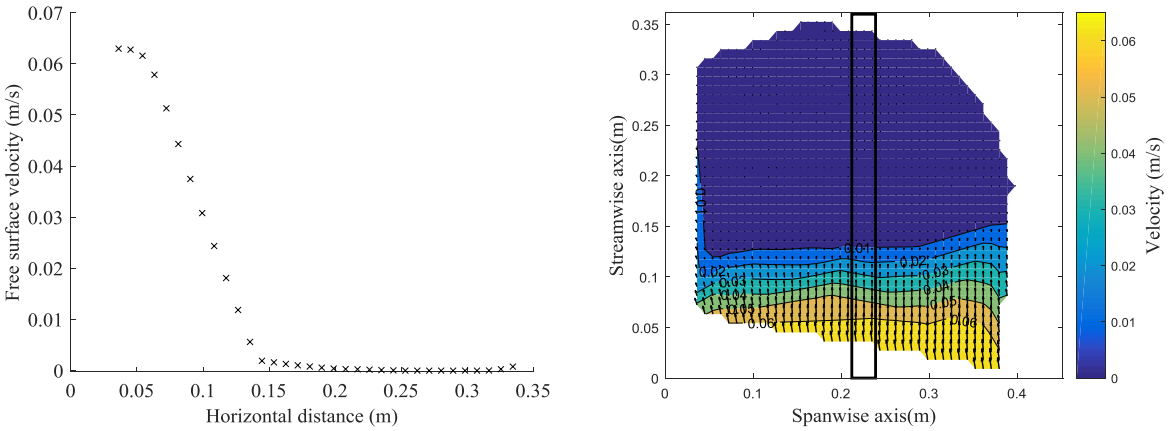

(a)

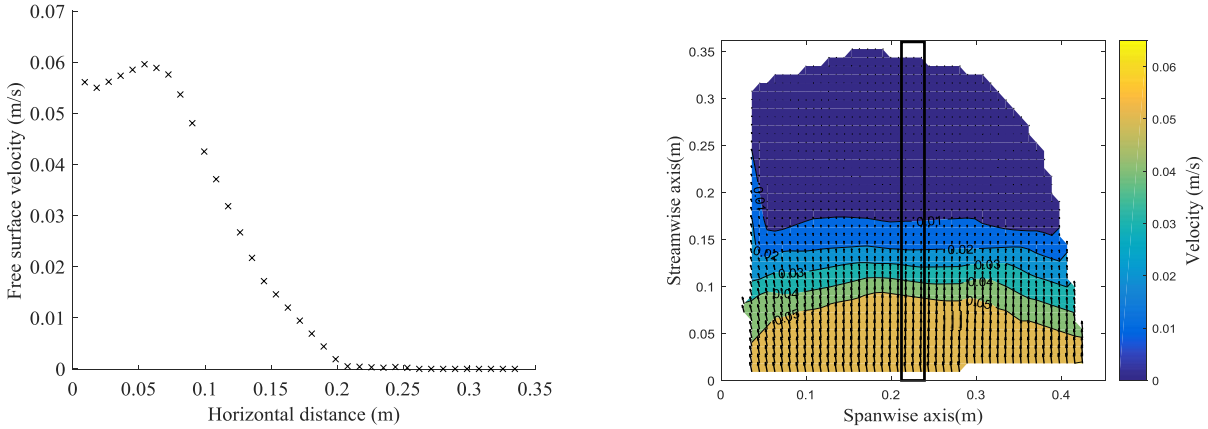

(b)

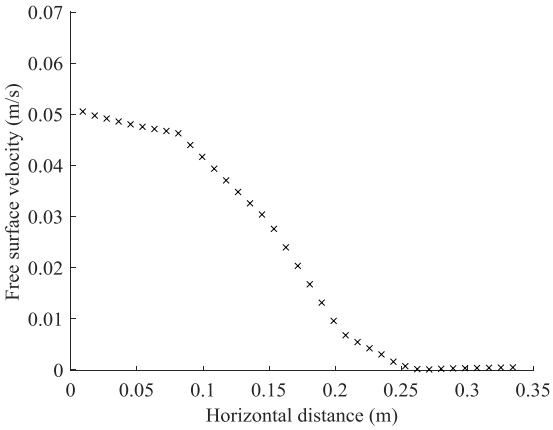
Free surface velocity (m/s)
Horizontal distance (m)

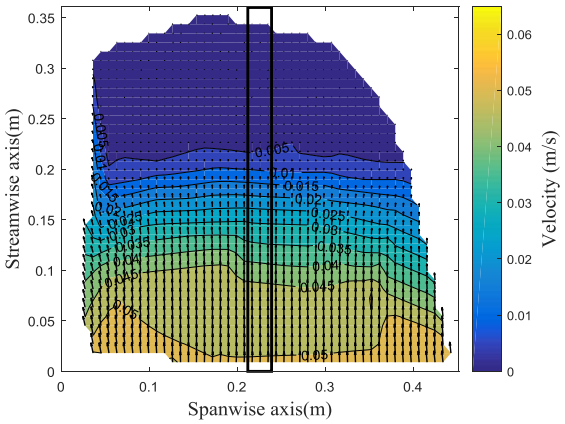
Streamwise axis(m)
Spanwise axis(m)
Velocity (m/s)

(c)

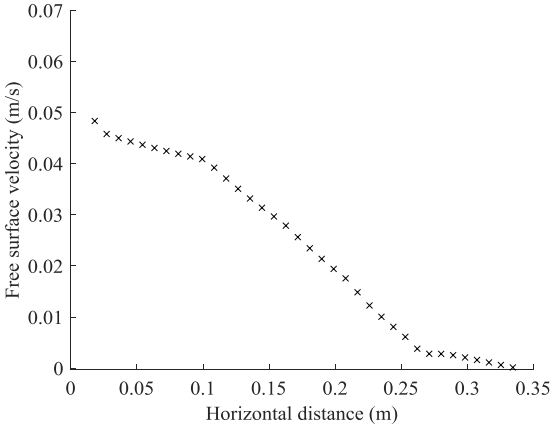
Free surface velocity (m/s)
Horizontal distance (m)

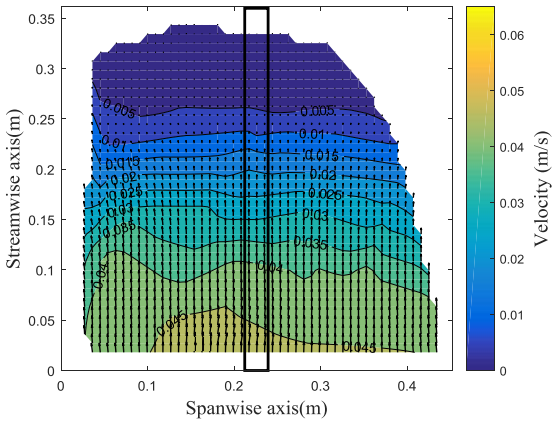
Streamwise axis(m)
Spanwise axis(m)
Velocity (m/s)

(d)

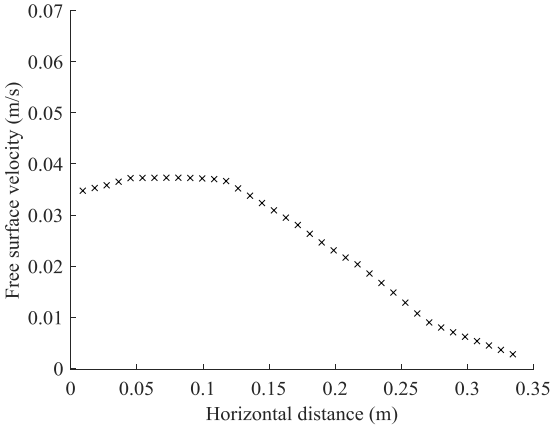
Free surface velocity (m/s)
Horizontal distance (m)

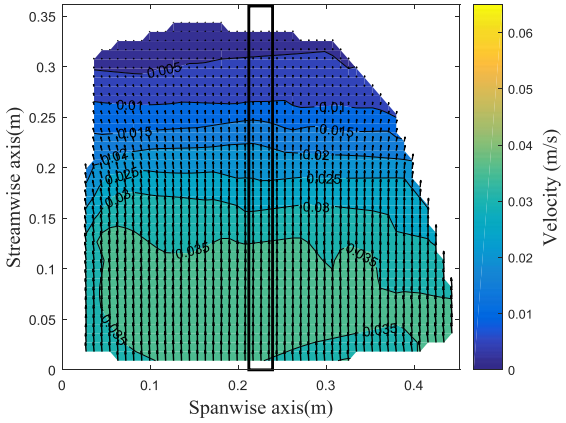
Streamwise axis(m)
Spanwise axis(m)
Velocity (m/s)

(e)

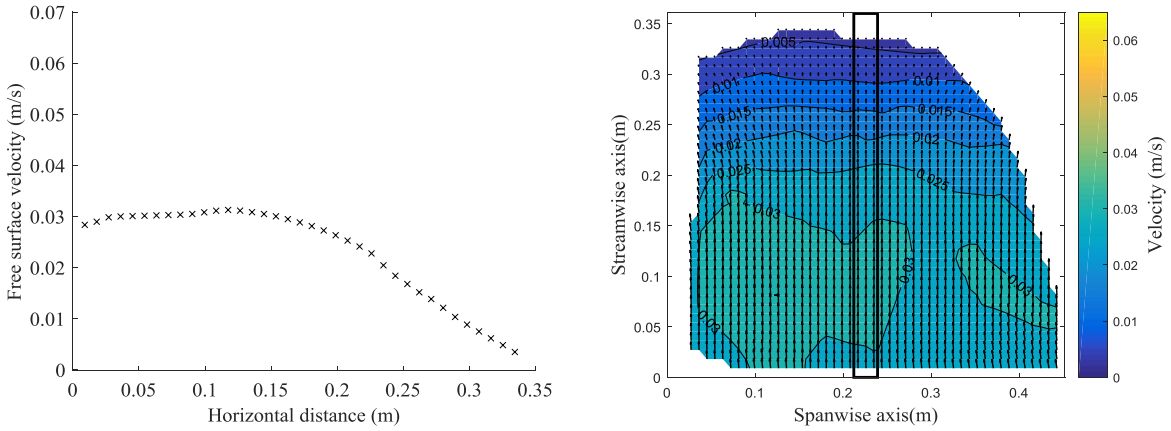

(f)

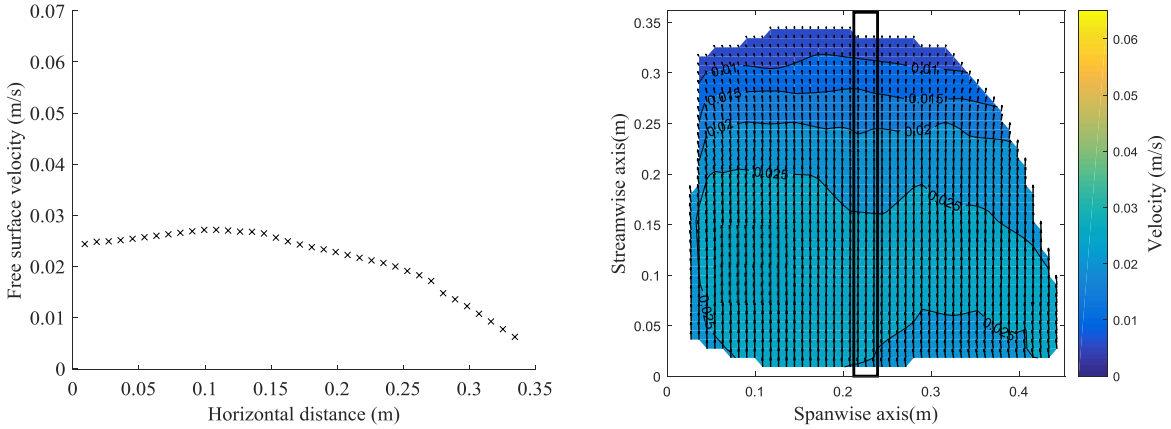

(g)

Figure 5.4: Averaged velocity distribution across the flow and along the 2.7-cm width around the tank centreline of silicone oil (left) and velocity vector field (right) at seven different times, namely (a) 0.43 s, (b) 0.66 s, (c) 0.93 s, (d) 1.3 s, (e) 1.66 s, (f) 2.06 s, and (g) 2.46 s

In Figure 5.4, the area of interest is shown inside a rectangular zone in the velocity vector field. The velocity profile was averaged over a 2.7-cm stripe centre on the centreline of the tank to smooth out any minor interpolation errors arising from the Eulerian velocity calculation within Streams. We disregarded the flow away from the centreline and close to the wall since boundary layer effects tend to curve the particle trajectories. The boundary layer effect can be roughly

calculated with using the worst case; for laminar boundary layers over a flat plate, the Blasius solution to the governing equations of flow gives (Schlichting 1979),

$$\delta_B \approx 0.5 \sqrt{\frac{\mu\, x}{\rho\, u_0}}, \tag{5.1}$$

Where δ_B is the boundary layer thickness, μ the fluid viscosity, ρ the fluid density, x the horizontal distance, and u_0 the free stream velocity. In the case of using silicone oil and considering the lowest flow $u_0 = 0.01$ m/s and a longer distance $x = 0.35$ m, $\delta_B \approx 0.023$ m from each side of the longitudinal walls of the tank. This means that the area of interest is far from the boundary layer effect. Furthermore, it is evident that the free surface velocity decreases slightly when the particles (beads) become further from the gate as shown in Figure 5.4. The velocity magnitude of the flow reduces with time and decays with the distance from the gate, with less than 0.01 m/s in all the times above. During gate removal, eddies arise from shear induced from the gate. These eddies lead to disturbance in the flow of the silicone oil. Consequently, the free surface velocity of silicone oil includes some disturbance. The experimental data does not encompass the entire tank area due to the unmatched particles in some regions of the tank because of unidentified particles, as explained in Section 2.2.2.

5.2 Parameter identification for the silicone compound oil

The parametric identification solution using the experimental data was performed using COMSOL Multiphysics. The computational domain was a horizontal line interval of 0.916-m length and was discretized into 200 quadratic elements with 0.015 film aspect ratio of the silicone oil, which was calculated as indicated in Section 3.2 with H_g and H_1 values from Table 2.1 of the silicone oil. A continuously differentiable step function was used to describe the initial free surface condition, i.e. $h(x, t = 0)$. The boundary conditions applied are no-slip at $z = 0$ and stress-free at $z = h$. The objective function given in equation (4.2) was minimized using an exhaustive grid search with $(0 < n \leq 2)$ and $(0 < k \leq 50)$. We found that the minimum value of the objective function corresponds to n = 0.9±0.1 and k = 0.5±0.1 Pa·s^n for the silicone compound oil as shown in Figure 5.5 (a subset of the data is shown here). The reconstructed rheological parameters of silicone oil above are nearly in line with the expected values shown in Figure 2.4 (a).

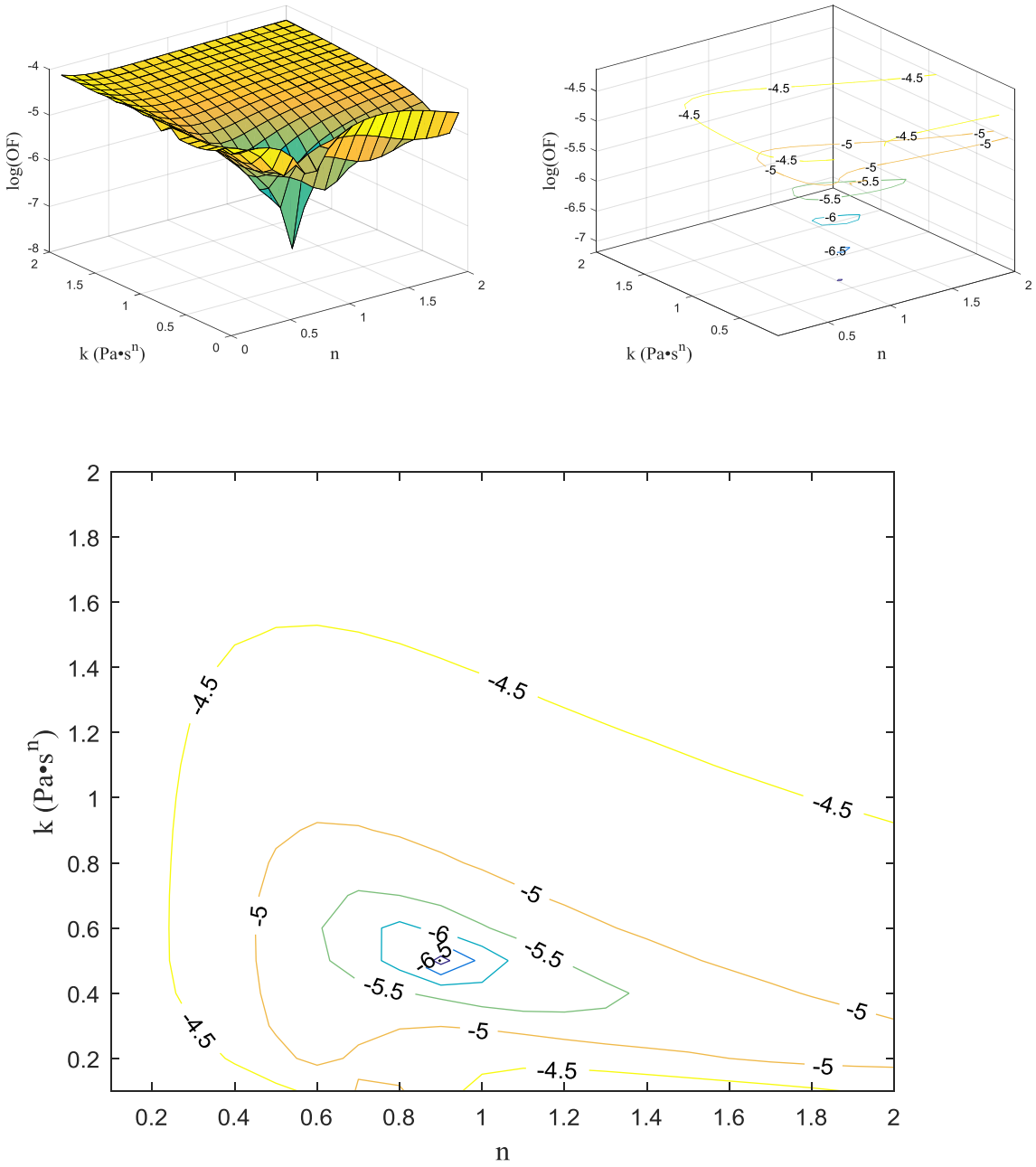

Figure 5.5: Contour lines and surface plot for the log values of the objective function of the reconstructed rheological parameters (silicone oil)

In this section, the computed and experimental free surface velocities are compared. The computed velocities included both the velocity based on the lubrication approximation and Navier–Stokes equations. The purpose of the comparison is to show the compatibility between the measured and

the computed data. In addition, the parametric identification was performed using the lubrication approximation, which is an approximation of the Navier–Stokes equations. Consequently, adding the Navier–Stokes equations can provide a better insight on the compatibility between the free surface velocities. The lubrication approximation and Navier–Stokes velocity profiles were calculated based on the reconstructed rheological parameters of silicone oil (n = 0.9±0.1 and k = 0.5±0.1 Pa·s^n). The computed velocity based on the lubrication approximation was obtained by running COMSOL with a numerical setup identical to that described in Section 5.2. Furthermore, equation (3.18) was used to calculate the free surface velocity. The computed velocity based on the Navier–Stokes equations was obtained by running COMSOL with the Navier–Stokes solver. The numerical setup used to solve the Navier–Stokes equations is the same as that indicated in Section 4.3 with 0.015 film aspect ratio of the silicone oil. The result is shown in Figure 5.6.

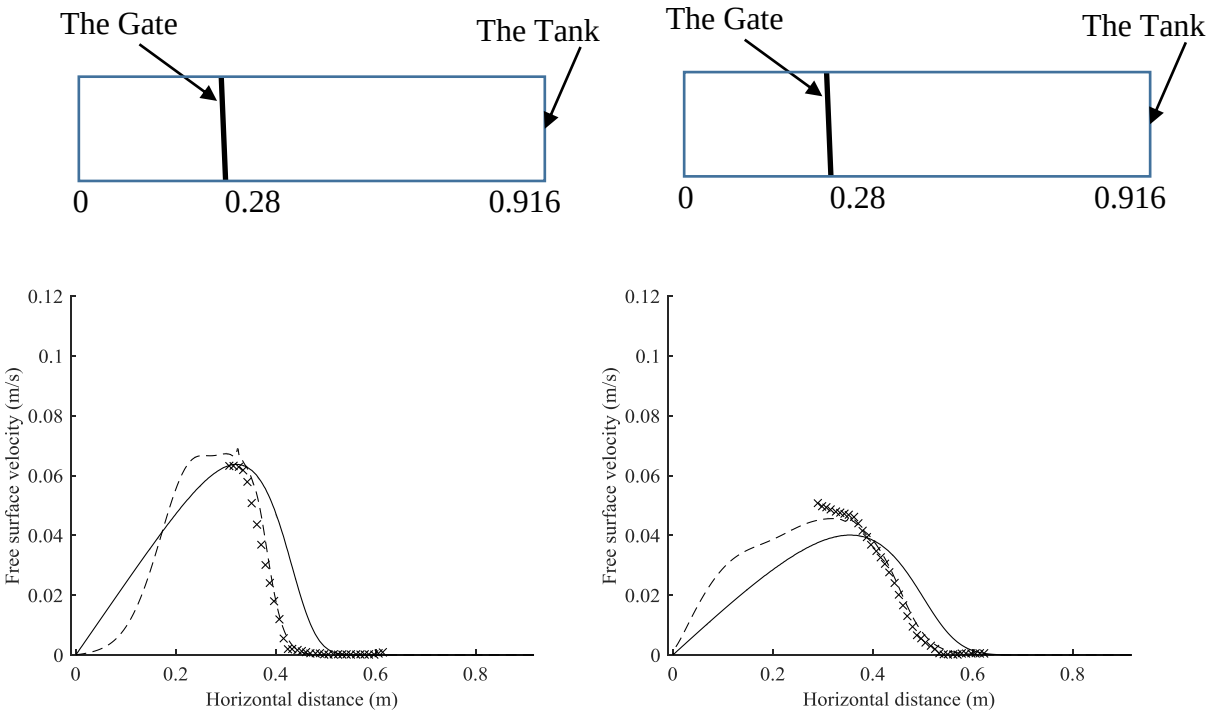

(a) (b)

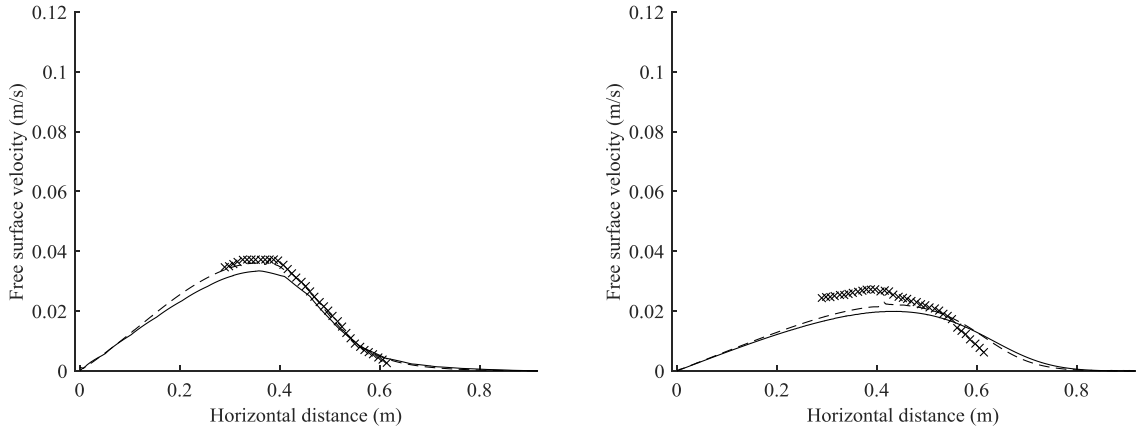

(c) (d)

Figure 5.6: Comparison between the experimental data (crosses), the computed velocity based on the lubrication approximation equations (solid line), and the computed velocity based on the Navier–Stokes equations (dashed line) for silicone oil at four different times: (a) 0.43 s, (b) 0.93 s, (c) 1.66 s, and (d) 2.46 s (only a subset of the times is shown here)

The compatibility between the three different velocity profiles is generally good, as shown in Figure 5.6. The Navier–Stokes velocity profiles contain a small sharp hump at the top due to the high curvature around the step in the free surface. The experimental data is closer to the computed velocity based on the Navier–Stokes equations. However, at 2.46 s, the error becomes larger compared with the measured velocity as indicated in equation (2.2). Furthermore, the power-law model predicts low shear rate cases with low accuracy, as stated by Afanasiev, Münch et al. (2007) and Myers (2005). The difference between the two computed velocities is the highest at early times (0.43 s and 0.93 s) due to the difference in the initial condition, but is mostly because inertia is the highest at early times, which is not accounted for in the lubrication approximation.

From the rheometer data indicated in Figure 2.4(a), it is clear that n =1 and k=0.41 Pa·s^n for the silicone oil used (within the used shear rate range). The shear rate range of silicone oil in the current work was between 1.49×10^{-8} s^{-1} and 4.05 s^{-1}. The shear rate range was computed in COMSOL by post-processing the numerical solution.

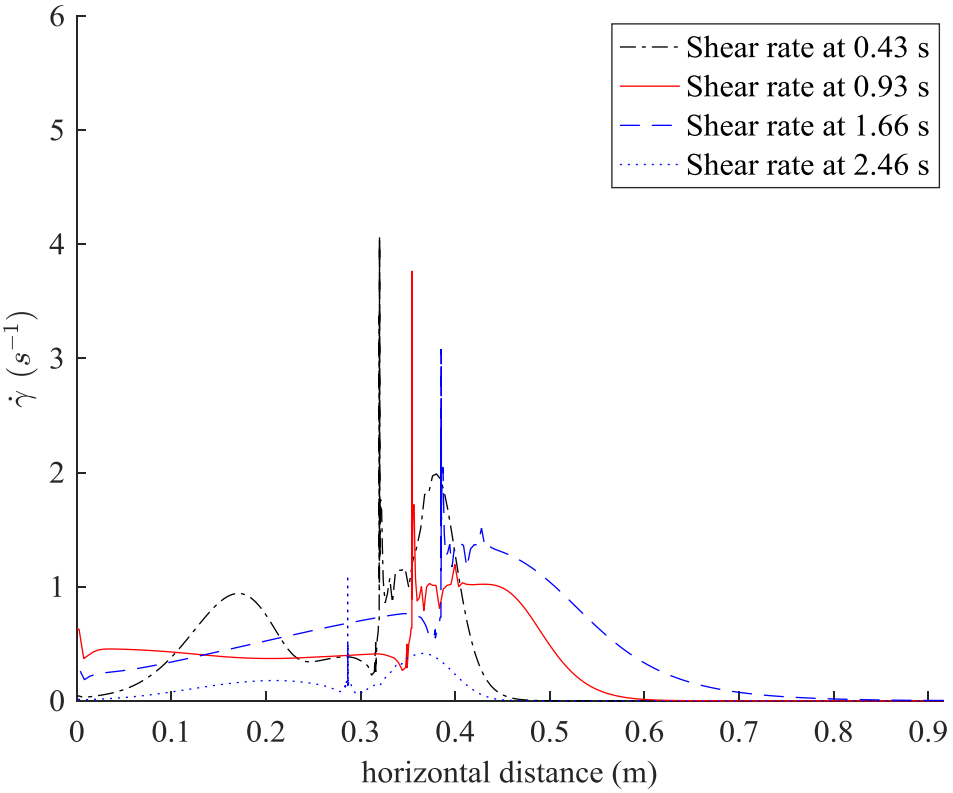

Figure 5.7: Shear rate as a function of horizontal distance at four different times for silicone oil (only a subset of the times is shown here)

The results from the parametric identification solution were n =0.9±0.1 and k=0.5±0.1 Pa·s^n. Consequently, the absolute error and the relative error percentage are 0.1 and 10% for n, 0.09 Pa·s^n and 21.9% for k. These error values were calculated according to the following mathematical expressions:

$$\delta_a = |\delta_t - \delta_c|\,, \tag{5.2}$$

$$\delta_r = \frac{\delta_a}{\delta_t}\ \%. \tag{5.3}$$

In equations (5.2) and (5.3), δ_a is the absolute error, δ_t is the true value measured using the rheometer, δ_c is the calculated value from the parametric identification, and δ_r is the relative percentage error. Most of the errors were due to experimental errors, which were inevitable. One of the errors was from the measurement of the fluid level that had an accuracy of 0.1 mm, and the other was from the measurement of the horizontal level of the test rig that had an accuracy of 1 mm/m. In addition, errors from obtaining the velocity fields occurred due to particle match imperfections. The matches between the particles were not always possible due to the following reasons: (i) some particles in the first frame might have left the light sheet before the second frame was captured, and (ii) a particle in the first frame might have been obscured by another particle in the second frame, or (iii) the particle identification process cannot identify the particle in the second frame Nokes (2014). In addition, errors also arose from the particle identification process as indicated in Section 2.2.2.

Some errors were due to the uncertainty of the model used because the parametric study was based on the lubrication approximation, which is an approximation form of the Navier–Stokes equations. The relative error percentage between the Navier–Stokes equations and the lubrication approximation will be described in more details in Chapter 7.

5.3 Experimental results for aqueous glycerol

The surface tension of aqueous glycerol is higher than that of silicone oil, which implies the low coalescence rate between the particles. This enables the use of more particles compared to the silicone oil experiment (see Figure 5.8). The match percentage at 99.47% in this case was higher than that of the silicone oil.

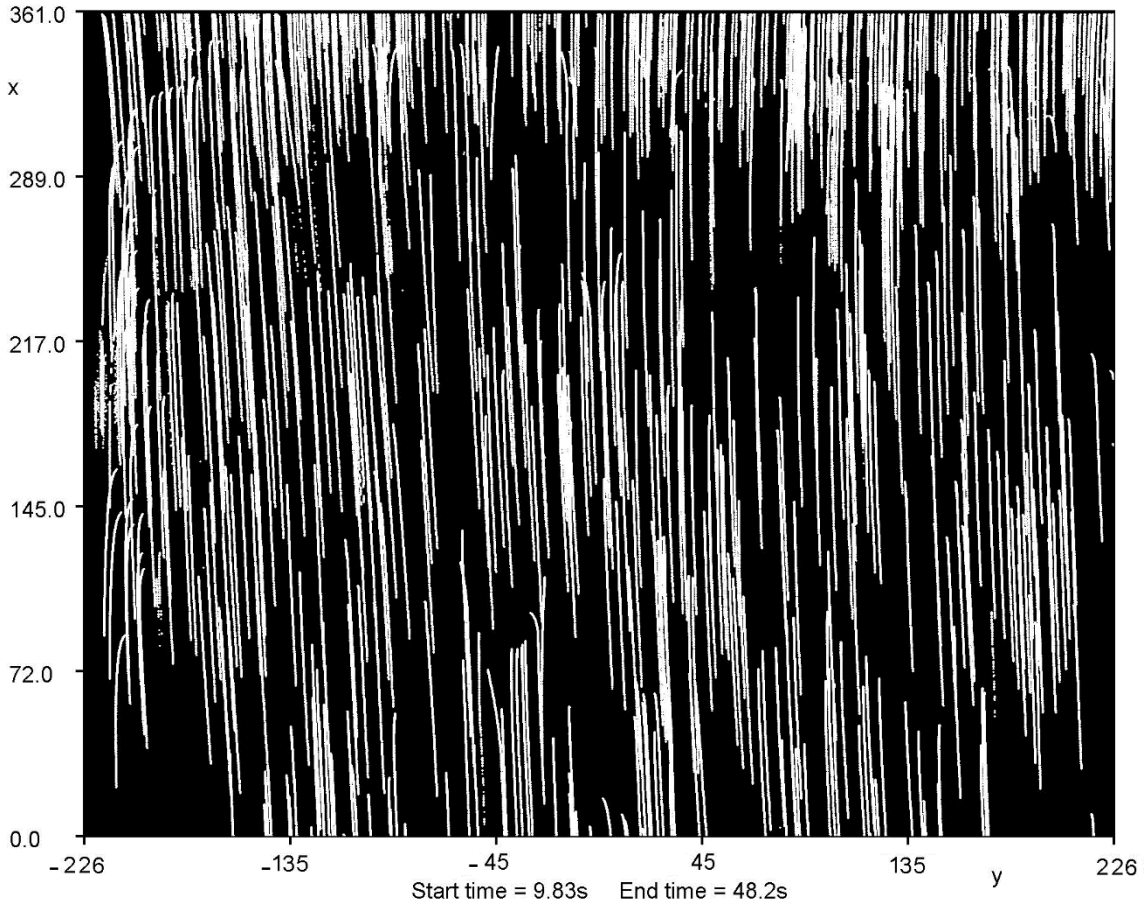

Figure 5.8: Paths of the particles at the free surface of aqueous glycerol, where x and y are the horizontal and vertical distances, respectively, in mm (displayed in Streams)

The velocity vector field and the velocity profile of the aqueous glycerol were calculated from the experimental data. The experimental time step was 0.03 s for the aqueous glycerol case and eight different times were chosen from the experimental data, namely 0.29 s, 0.49 s, 0.99 s, 1.5 s, 1.96 s, 2.46 s, 2.93 s, and 3.56 s. Consequently, the objective function defined according to equation (4.2) can be calculated with N = 8. The velocity magnitude of the flow reduces with time and decays with the distance from the gate with less than 0.02 m/s in all the times above, as shown in Figure 5.9. The velocity vector fields related to these times are shown in Figure 5.9. The area of interest is shown inside a rectangular zone in the velocity vector field as explained in Section 5.1 with $\delta_B \approx 0.063$ m. This means that the area of interest is far from the boundary layer effect.

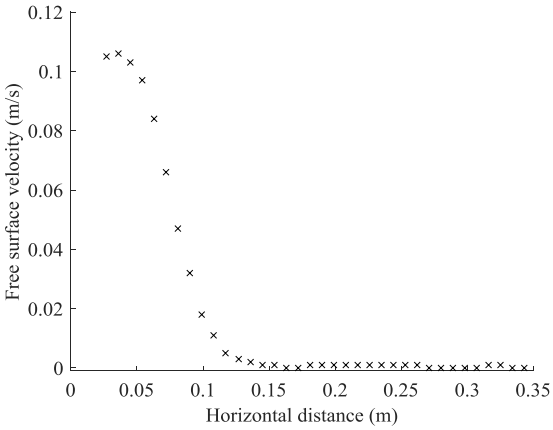
Free surface velocity (m/s)
Horizontal distance (m)

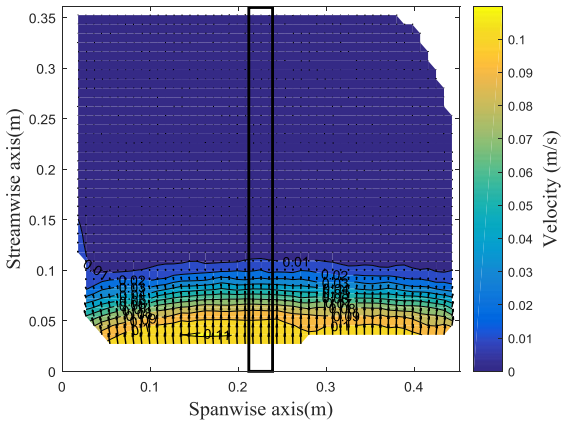
Streamwise axis(m)
Spanwise axis(m)
Velocity (m/s)

(a)

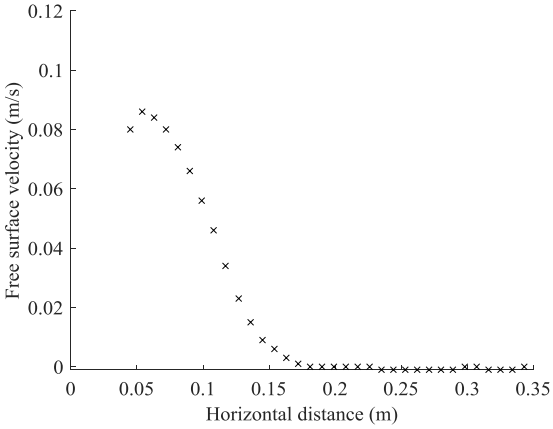
Free surface velocity (m/s)
Horizontal distance (m)

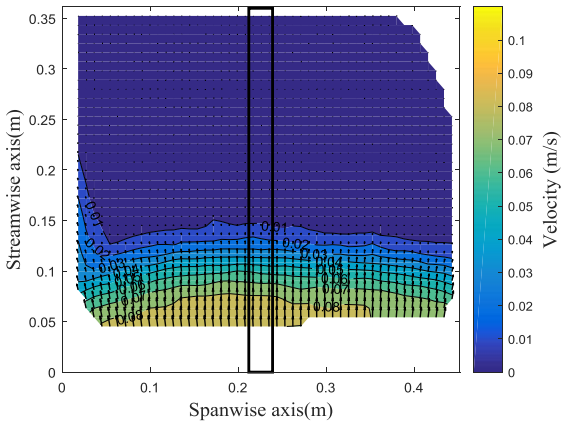
Streamwise axis(m)
Spanwise axis(m)
Velocity (m/s)

(b)

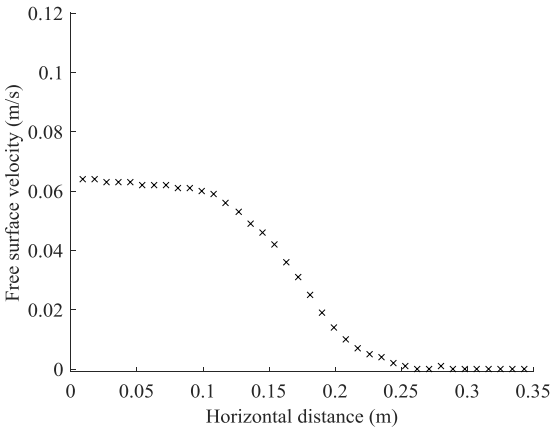
Free surface velocity (m/s)
Horizontal distance (m)

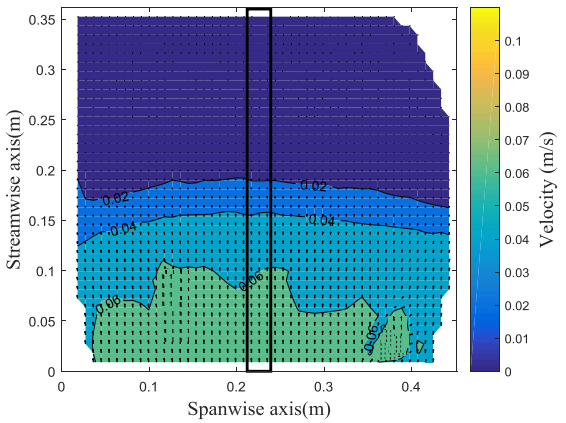
Streamwise axis(m)
Spanwise axis(m)
Velocity (m/s)

(c)

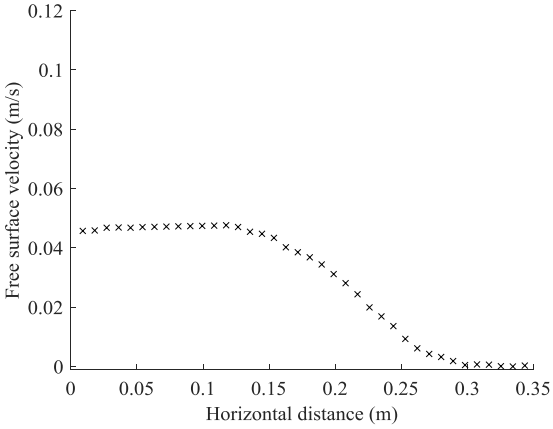
Free surface velocity (m/s)
Horizontal distance (m)

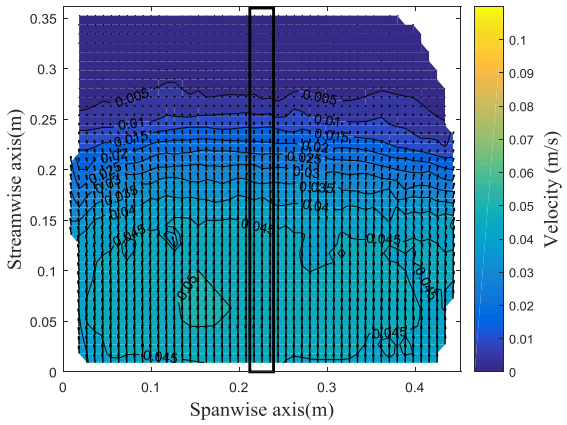
Streamwise axis(m)
Spanwise axis(m)
Velocity (m/s)

(d)

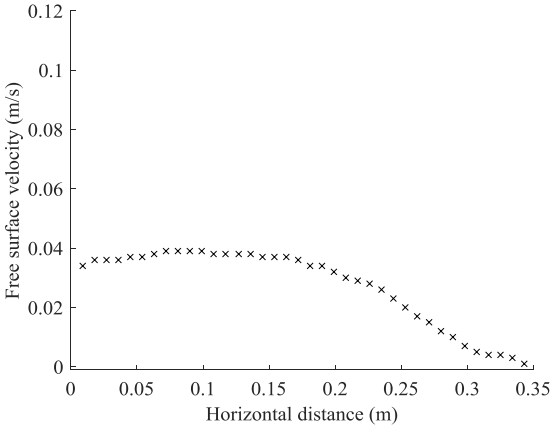
Free surface velocity (m/s)
Horizontal distance (m)

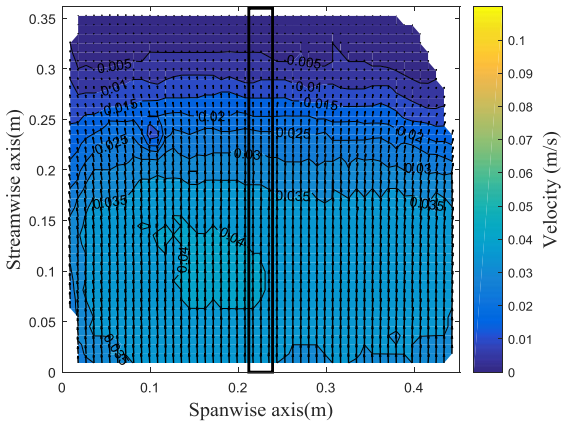
Streamwise axis(m)
Spanwise axis(m)
Velocity (m/s)

(e)

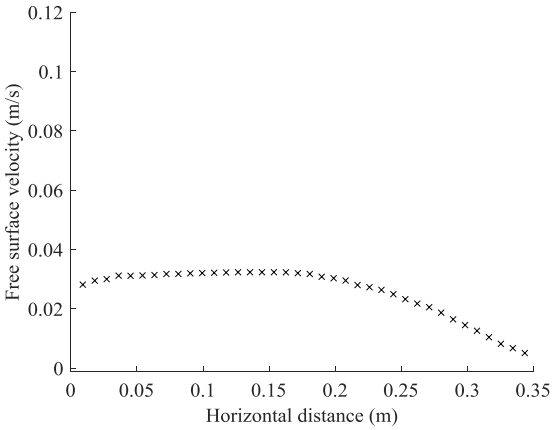
Free surface velocity (m/s)
Horizontal distance (m)

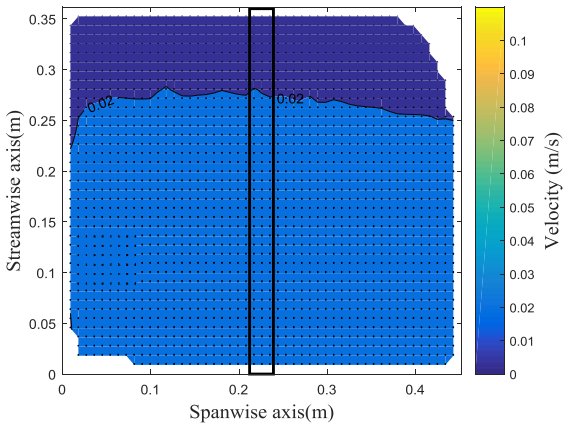
Streamwise axis(m)
Spanwise axis(m)
Velocity (m/s)

(f)

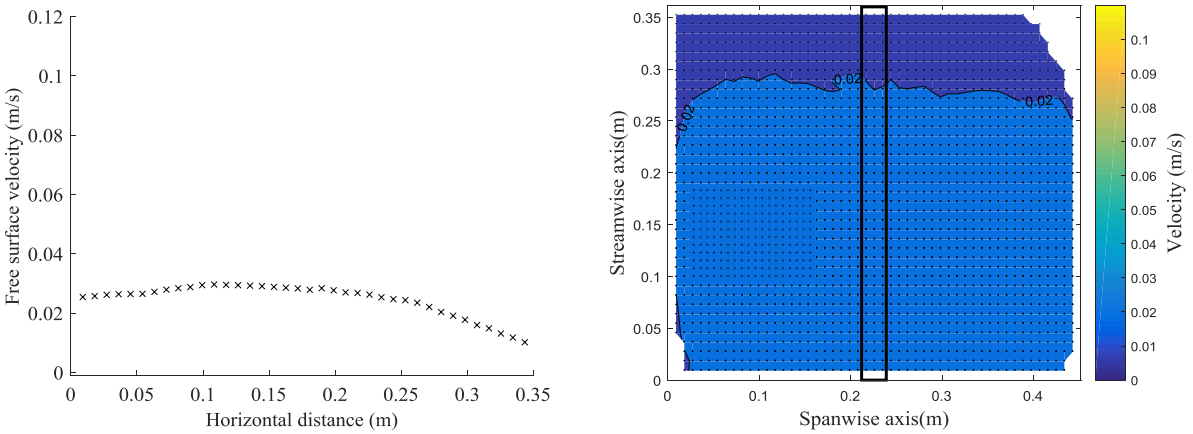

(g)

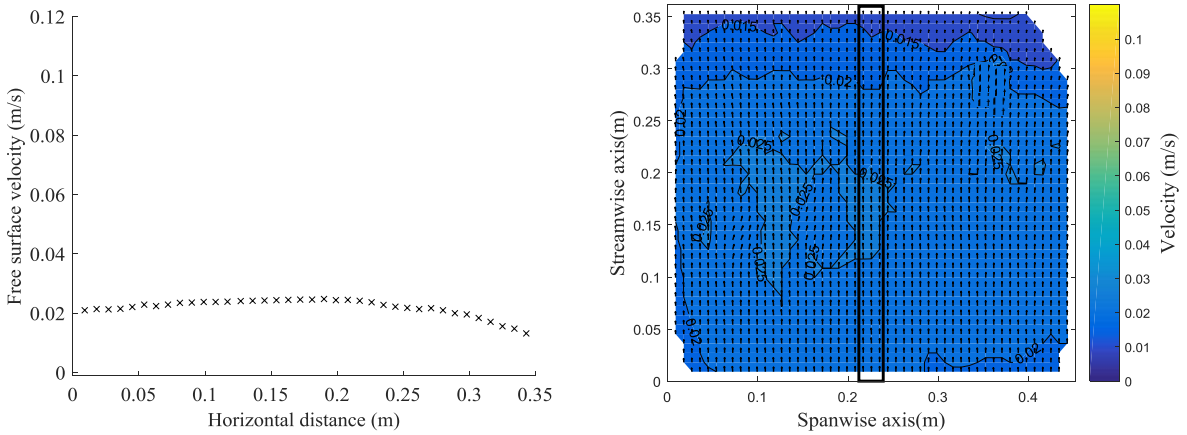

(h)

Figure 5.9: Averaged velocity distribution across the flow and along the 2.7-cm width around the tank centreline of aqueous glycerol (left) and velocity vector fields (right) at eight different times: (a) 0.29 s, (b) 0.49 s, (c) 0.99 s, (d) 1.5 s, (e) 1.96 s, (f) 2.46 s, (g)2.93 s, and (h) 3.56 s

In Figure 5.9, the velocity vector field and the averaged velocity profile behave the same as that shown in Figure 5.4. However, only two differences occur between Figure 5.9 and Figure 5.4: in the aqueous glycerol case, the free surface velocities were higher and the film aspect ratio was 0.019.

5.4 Parameter identification for the aqueous glycerol

In this section, the eight times intervals as mentioned in Section 5.3 were used. The numerical setup and the ranges of the rheological parameters used were as indicated in Section 5.2. However, the values of both H_g and H_1 were selected from Table 2.1 for the aqueous glycerol. After implementing a parametric grid search, we found that n = 1.0±0.1 and k = 1.3±0.1 Pa·s^n led to a minimum of the objective function for the aqueous glycerol, as shown in Figure 5.10 (a subset of the data is shown here). The reconstructed rheological parameters of aqueous glycerol above are nearly in line with the expected values (n = 1 and k = 1.14 Pa·s^n) shown in Figure 2.4 (b).

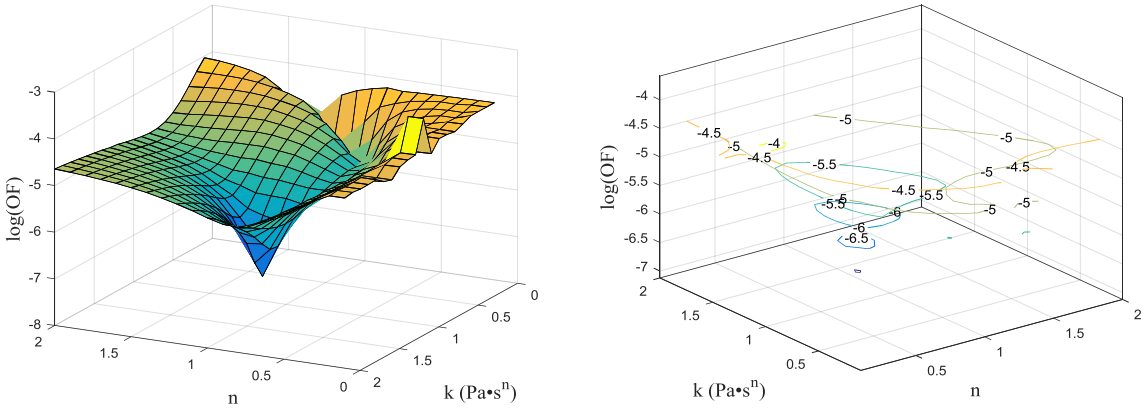

It is clear that there are differences between the reconstructed and the true values of the power-law rheological parameters due to the experimental errors, particles match imperfections and the uncertainty of the used model as described in Section 5.2.

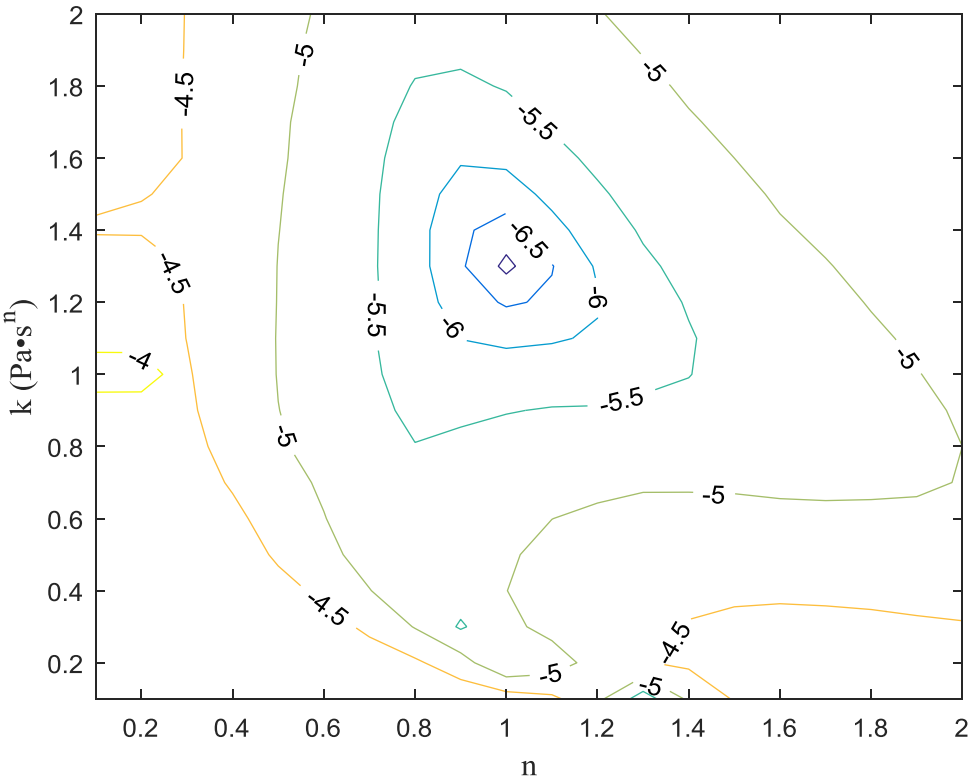

Figure 5.10: Contour lines and surface plot for the log values of the objective function of the rheological parameters for aqueous glycerol

The experimental data were compared with two different computed data, namely the free surface velocity based on the lubrication approximation and those based on Navier–Stokes equations using the reconstructed data (n = 1.0±0.1 and k = 1.3±0.1 Pa·s^n). The model setup for the lubrication approximation solver was the same as that indicated in Section 5.2, using equation (3.18) to obtain the free surface velocity. The numerical setup indicated in Section 4.3 was used for the Navier–Stokes solver to obtain the free surface velocity with 0.019 aspect ratio. The outcomes are shown in Figure 5.11.

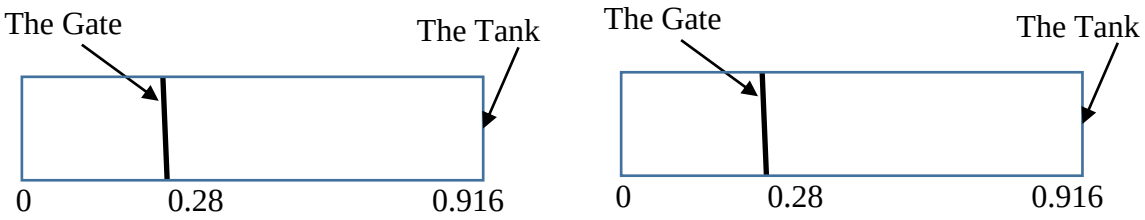
The Gate
The Tank
0
0.28
0.916
The Gate
The Tank
0
0.28
0.916

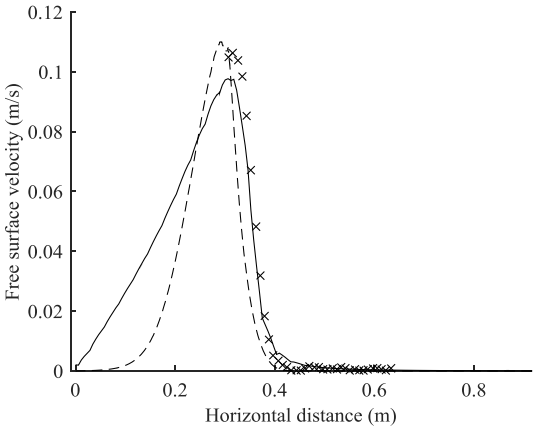
Free surface velocity (m/s)
Horizontal distance (m)

(a)

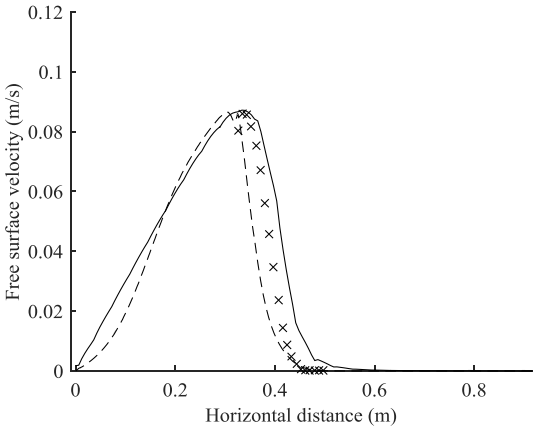
Free surface velocity (m/s)
Horizontal distance (m)

(b)

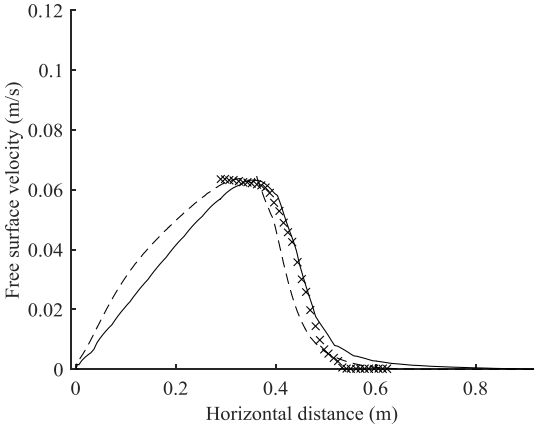
Free surface velocity (m/s)
Horizontal distance (m)

(c)

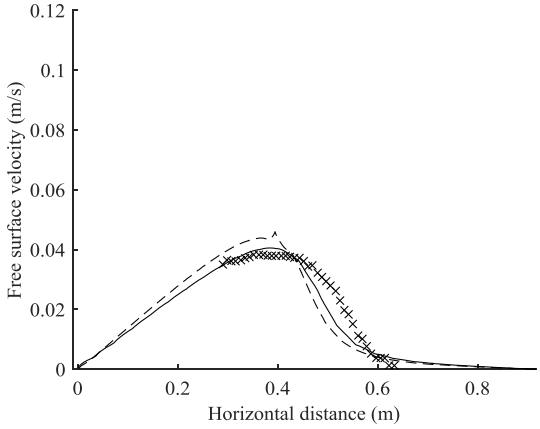
Free surface velocity (m/s)
Horizontal distance (m)

(d)

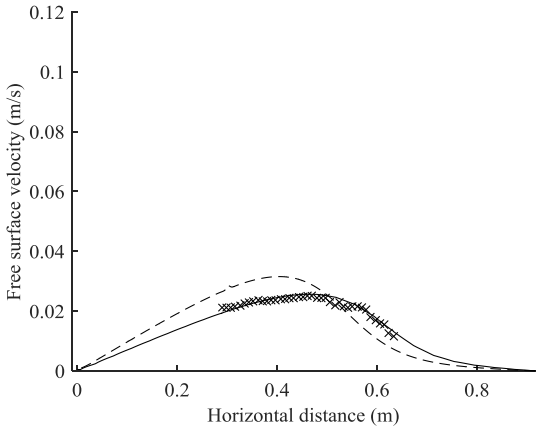

(e)

Figure 5.11: Comparison between the experimental data (crosses), the computed velocity based on the lubrication approximation equations (solid line), and the computed velocity based on the Navier–Stokes equations (dashed line) for aqueous glycerol at five different times: (a) 0.29 s, (b) 0.49 s, (c) 0.99 s, (d) 1.96 s, and (e) 3.56 s.

Figure 5.11 illustrates how the velocity varies along the centreline of the tank for five different times. Generally, the agreement between the velocity profiles is good. However, small differences occur between the velocity profiles because the parameter identification is based on lubrication approximation, which is an approximation of the Navier–Stokes equations. Therefore, the optimal values of the rheological parameters will be for an approximation model. In addition, the difference between Navier–Stokes and the lubrication approximation is due to the fact that the lubrication approximation is an approximation of Navier–Stokes. Furthermore, the differences between the velocity profiles occur also due to experimental and numerical errors, as indicated in Section 5.2.

The measured viscosity of aqueous glycerol was 1.14 Pa·s as indicated in Figure 2.4 (b) and the identified value was 1.3 Pa·s using the parametric identification. Consequently, the absolute error is 0.16 Pa·s, and the relative error percentage is 14%. Similar to Section 5.2, the shear rate range of aqueous glycerol was between 1.52×10^{-8} s^{-1} and 5.3 s^{-1} as shown in Figure 5.12.

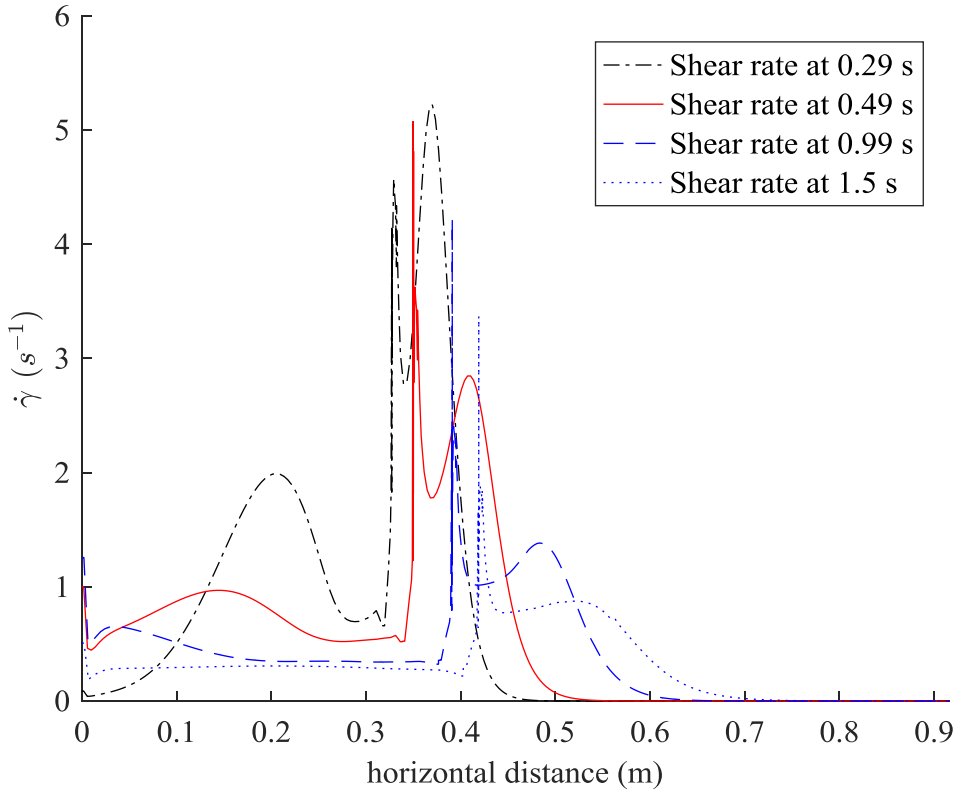

Figure 5.12: Shear rate as a function of horizontal distance at four different times for aqueous glycerol (only a subset of the times is shown here)

In both Sections 5.2 and 5.4, the rheological parameters were calculated using the definition of the objective function, which was described in Section 4.4. The objective function used has dimensions of m^3/s^2. Thus, the dimensionless objective function can be implemented by applying equation (5.4) to test its influence on the results.

$$OF(n,k) = \sum_{i=1}^{N} 0.5 \int_{0}^{L} \left(\frac{u_c^i(x) - u_m^i(x)}{u_m^i(x)} \right)^2 dx. \tag{5.4}$$

Equation (5.4) is applied to reconstruct the rheological parameters of silicone oil and aqueous glycerol with the numerical setup as indicated in Section 5.2 for silicone oil and Section 5.4 for aqueous glycerol. The results are indicated in Table 5.1:

Fluid	OF(dimension form)	OF(dimensionless form)	Rheometer results
silicone oil	$n = 0.9 \pm 0.1$ $k = 0.5 \pm 0.1$ Pa·s^n	$n = 0.9 \pm 0.1$ $k = 0.5 \pm 0.1$ Pa·s^n	$n = 1$ $k = 0.41$ Pa·s^n
aqueous glycerol	$n = 1 \pm 0.1$ $k = 1.3 \pm 0.1$ Pa·s^n	$n = 0.9 \pm 0.1$ $k = 1.4 \pm 0.1$ Pa·s^n	$n = 1$ $k = 1.14$ Pa·s^n

Table 5.1: Rheological parameters in two different objective function definitions

It is evident from Table 5.1 that the difference between the dimension and dimensionless objective function does not significantly affect the identified rheological parameters.

5.5 Experimental results for Molasses

The next experiments were implemented using black strap molasses. The difference in the molasses level across the gate was 12 mm and the corresponding aspect ratio was 0.015, which represent the ratio between a characteristic film thickness and a characteristic length scale in the flow direction. The depth of the molasses was 20 mm on the upstream side and 8 mm on the downstream side. The average match percentage obtained from Stream was 99.31%. The trajectories of the particles are shown in Figure 5.13.

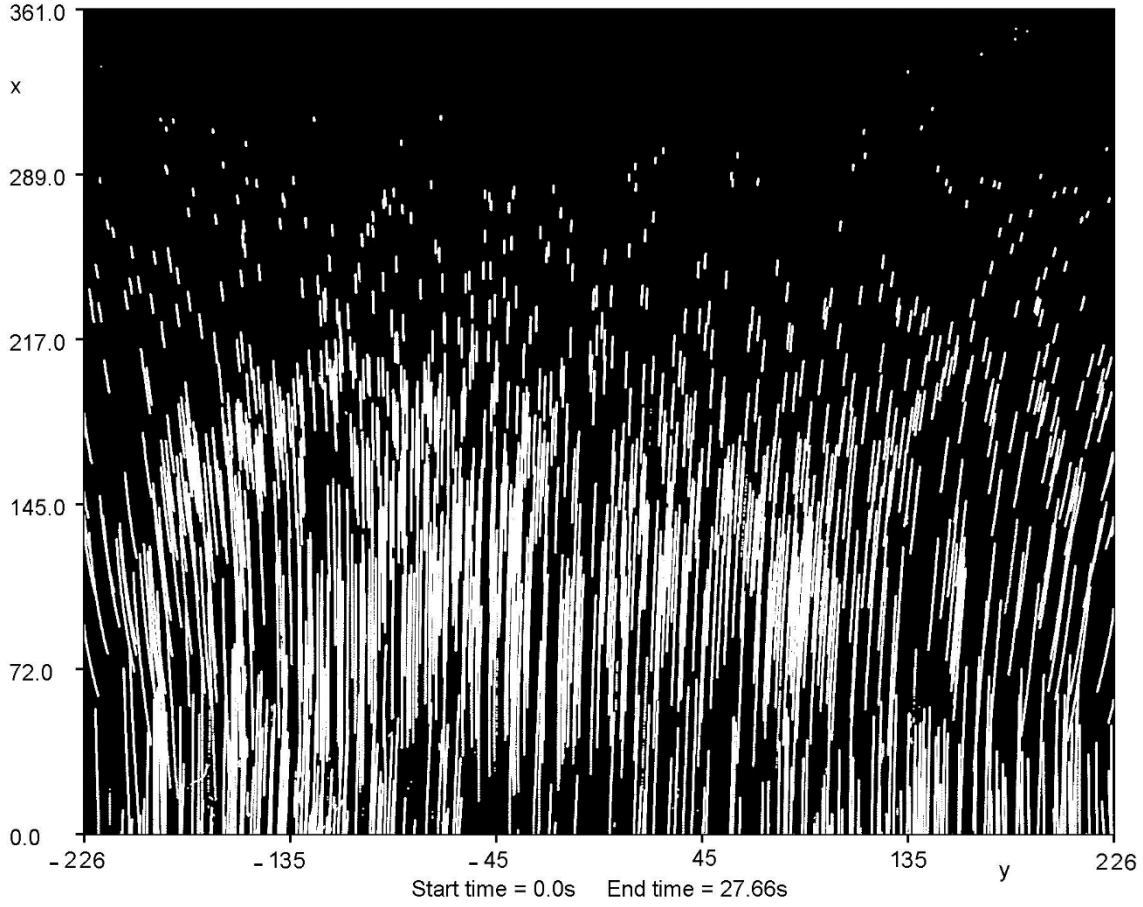

Figure 5.13: Paths of the particles at the free surface for the molasses, where x and y are the horizontal and vertical distances, respectively, in mm.

The velocity vector field and the velocity profile of the molasses are shown in Figure 5.14 at different times. The procedures as those indicated for silicone oil (Section 5.1) and aqueous glycerol (Section 5.3) were applied. However, nine different times were chosen from the experimental data for molasses, namely 0.4 s, 0.6 s, 1.33 s, 1.4 s, 4.13 s, 5.4 s, 6.73 s, 7.73 s, and 12.9 s. Consequently, the objective function defined according to equation (4.2) can be calculated with N = 9. The boundary layer thickness was 0.127 m, which is high but still far from the rectangular zone shown in Figure 5.14. This boundary layer thickness was calculated using the maximum velocity with the corresponding variables of the used molasses.

The experimental time step for the silicone oil and aqueous glycerol was 0.03 s. Much larger time steps had to be used for the molasses to allow sufficient time for the particles to travel a significant

distance because the flow was much slower. A time step of 0.16 s was selected as a good compromise. Consequently, the time step was increased to 0.16 s to minimize the error. Increasing the time step allows the particles to be further apart between frames and therefore allows a more accurate description of the flow field. The following velocity profile and velocity vector field are obtained.

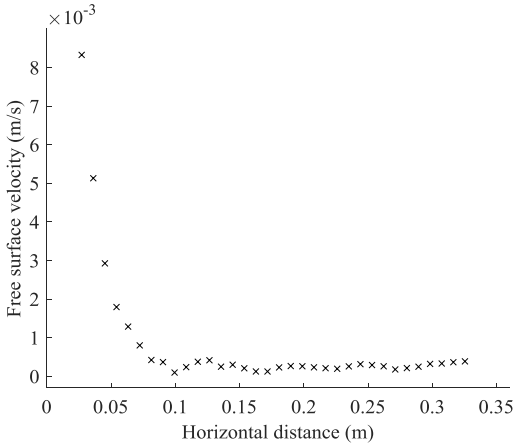

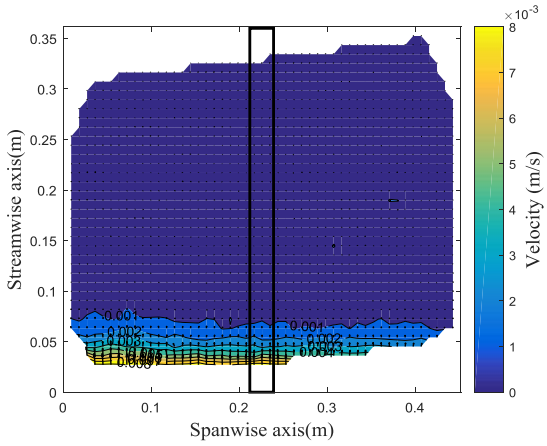

(a)

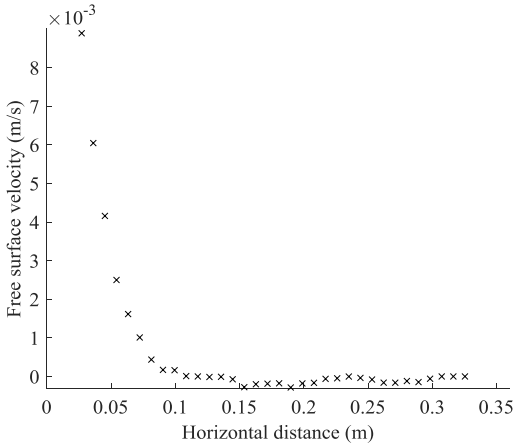

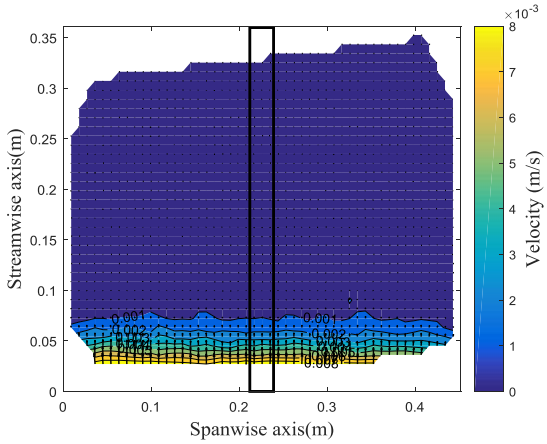

(b)

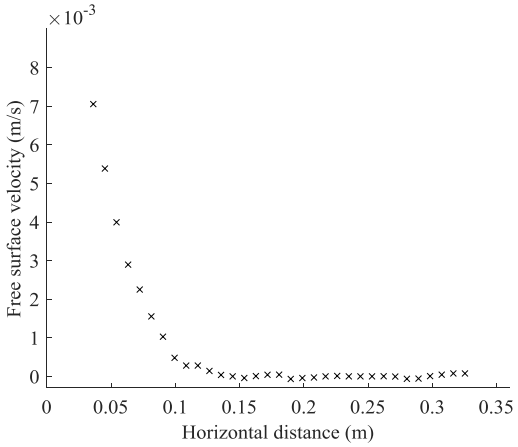
×10^-3
Free surface velocity (m/s)
Horizontal distance (m)

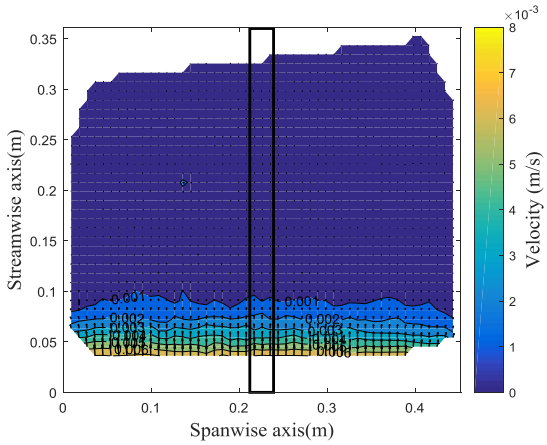
×10^-3
Streamwise axis(m)
Spanwise axis(m)
Velocity (m/s)

(c)

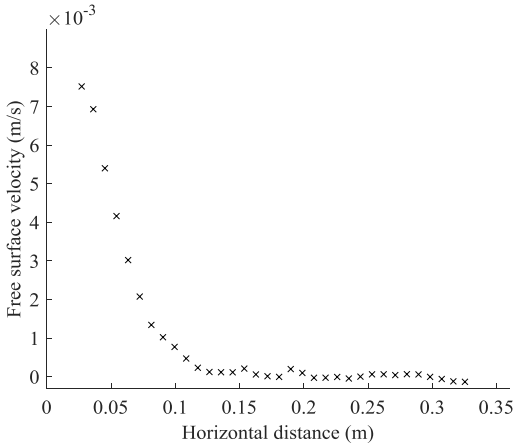
×10^-3
Free surface velocity (m/s)
Horizontal distance (m)

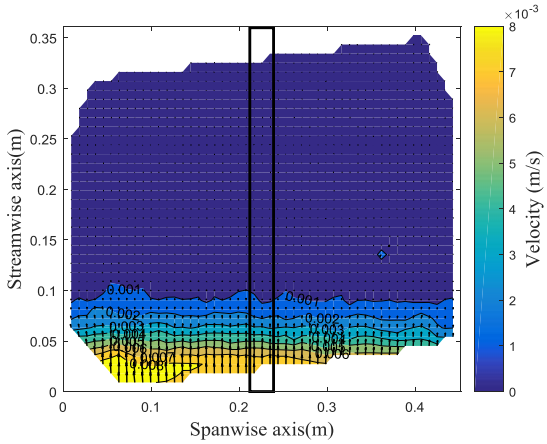
×10^-3
Streamwise axis(m)
Spanwise axis(m)
Velocity (m/s)

(d)

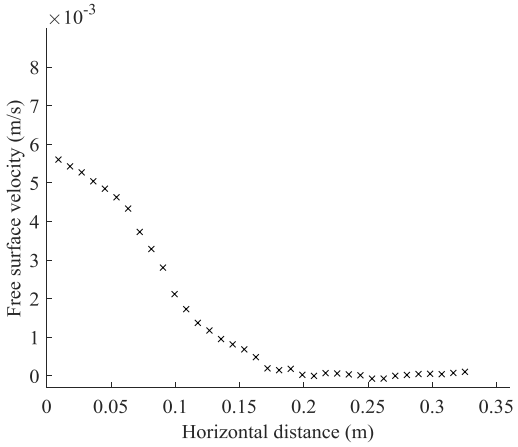
×10^-3
Free surface velocity (m/s)
Horizontal distance (m)

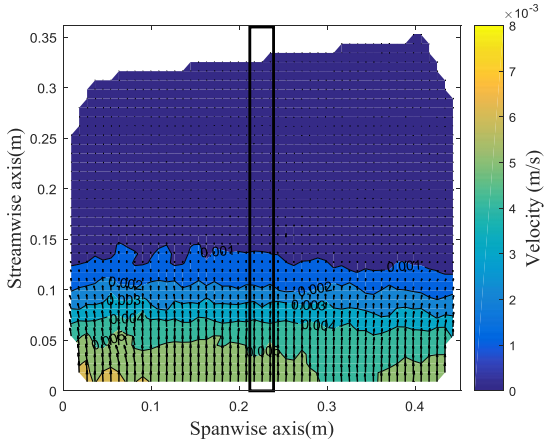
×10^-3
Streamwise axis(m)
Spanwise axis(m)
Velocity (m/s)

(e)

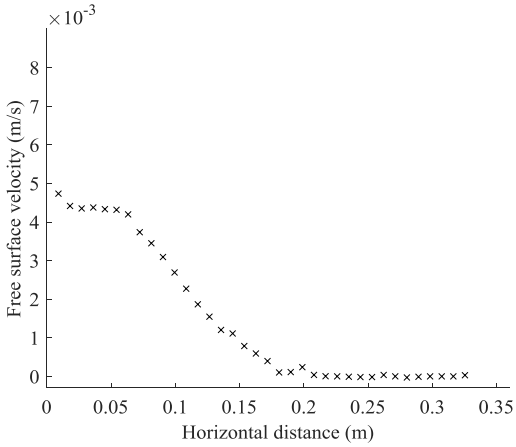
×10^-3
Free surface velocity (m/s)
Horizontal distance (m)

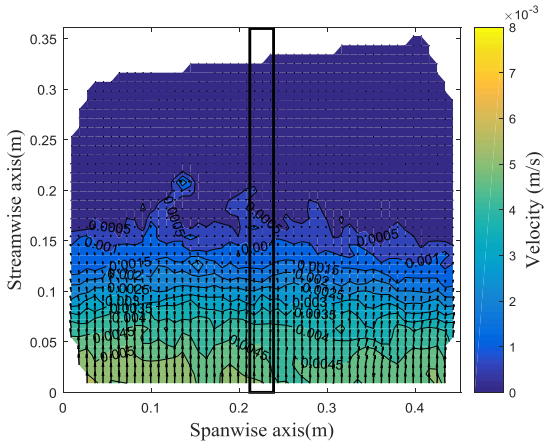
×10^-3
Streamwise axis(m)
Spanwise axis(m)
Velocity (m/s)

(f)

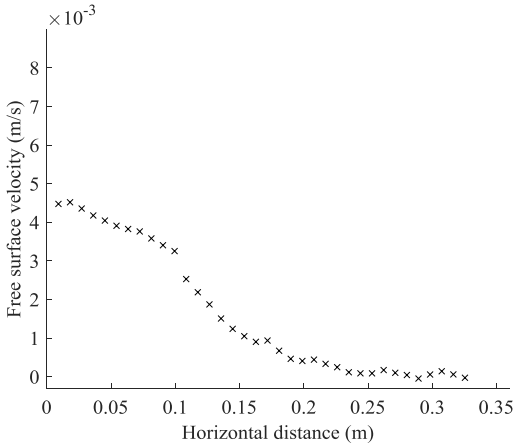
×10^-3
Free surface velocity (m/s)
Horizontal distance (m)

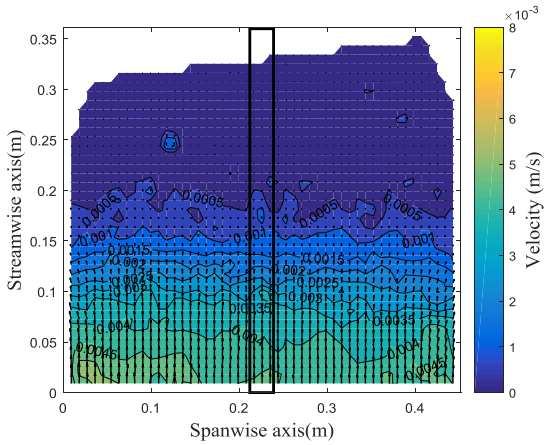
×10^-3
Streamwise axis(m)
Spanwise axis(m)
Velocity (m/s)

(g)

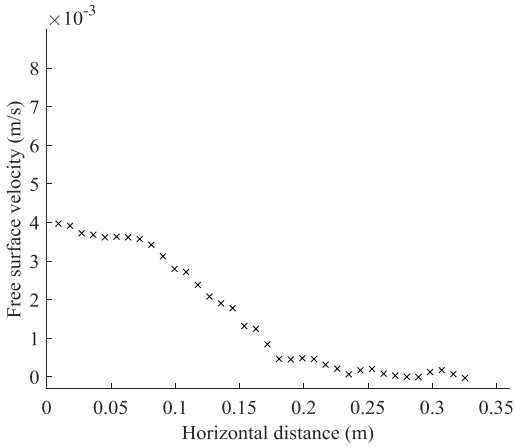
×10^-3
Free surface velocity (m/s)
Horizontal distance (m)

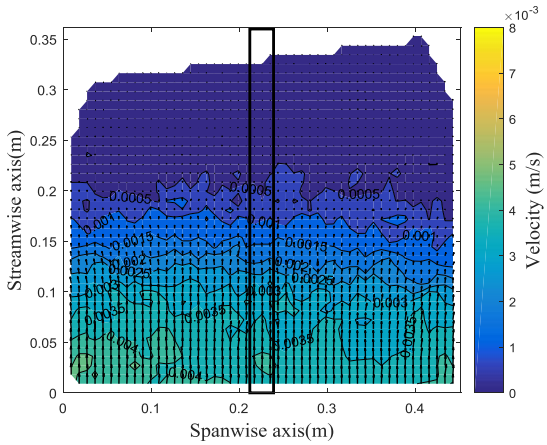
×10^-3
Streamwise axis(m)
Spanwise axis(m)
Velocity (m/s)

(h)

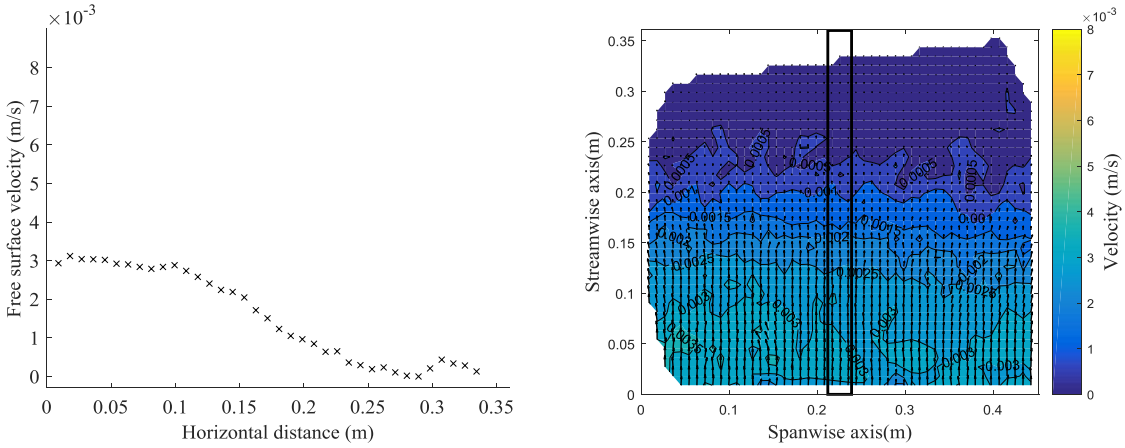

(i)

Figure 5.14: Averaged velocity distribution across the flow and along the 2.7-cm width around the tank centreline of molasses (left) and velocity vector field (right) at nine different times: (a) 0.4 s, (b) 0.6 s, (c) 1.33 s, (d) 1.4 s, (e) 4.13 s, (f) 5.4 s, (g) 6.73 s, (h)7.73 s, and (i) 12.9 s

In Figure 5.14, the velocity vector field and the averaged velocity profile behave the same as that indicated in Sections 5.1 and 5.3. However, the magnitude of the velocities for the molasses was much smaller compare to that of silicone oil and aqueous glycerol. Finally, it is evident that the magnitude of the free surface velocity reduced sharply after opening the gate.

5.6 Parameter identification for the molasses

In this section, the rheological parameters were identified for the molasses using the parametric identification process described previously. The numerical setup is the same as that indicated in Section 5.2. However, the wide ranges of n and k were $(0 < n \leq 2)$ and $(0 < k \leq 100)$, and were used to calculate the objective function; in other words, an exhaustive grid search was performed to locate the minimum. The minimum of the objective function was found for n = 0.7±0.1 and k = 16±1 Pa·s^n for the molasses and the results are presented in Figure 5.14.

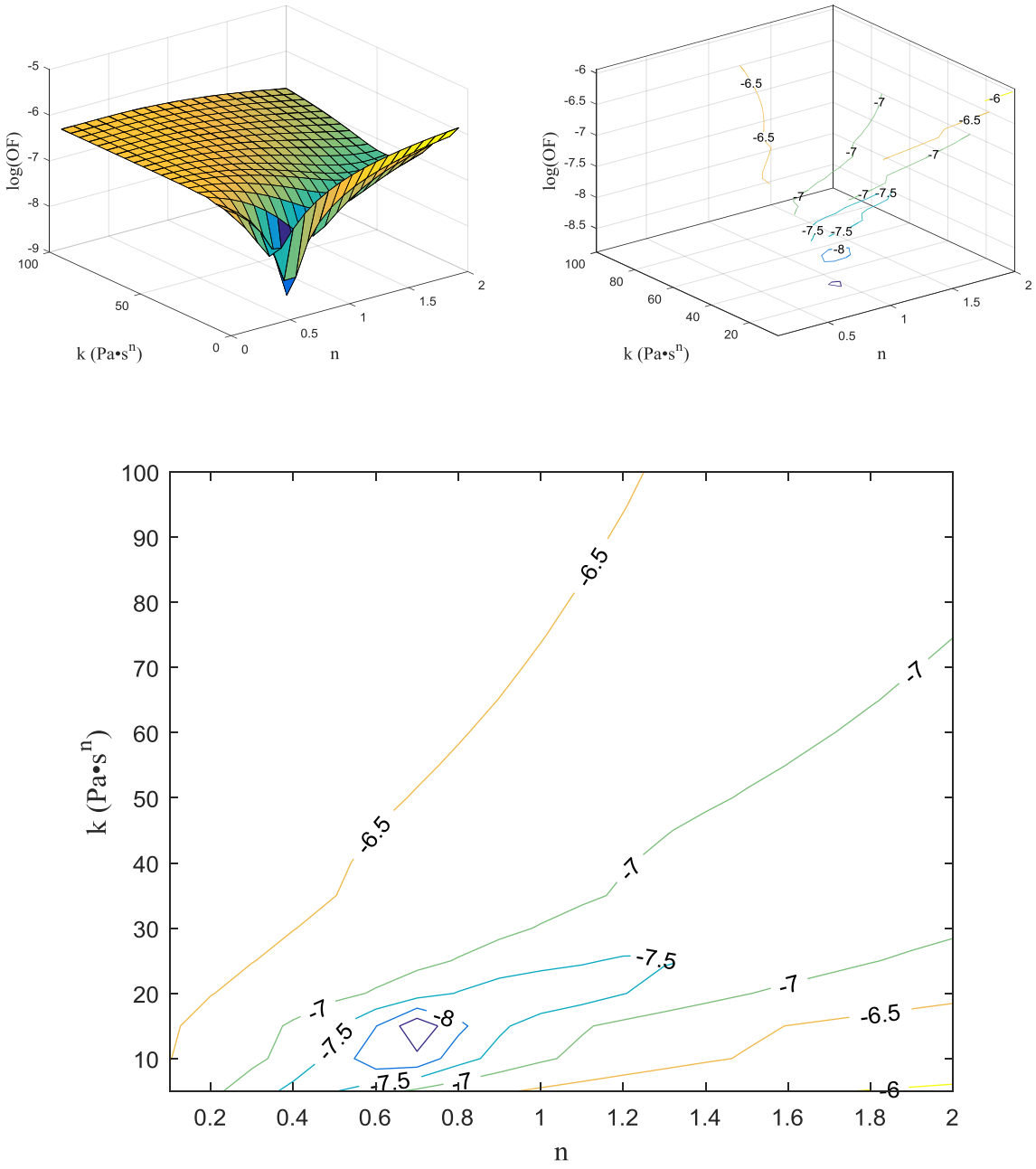

Figure 5.15: Contour lines and surface plot of the log values for the objective function with respect to the rheological parameters (molasses)

Figure 5.16 shows a comparison between three different data, namely experimental data, computed velocity based on the lubrication approximation, and the computed velocity based on the Navier–Stokes equations. The velocity profile is averaged over a 2.7 cm wide strip around the centreline

of the tank and was imported from the Eulerian velocity field by using Streams. The identified rheological parameters for the molasses were used to calculate the computed velocities. The computed velocities based on the lubrication approximation and Navier–Stokes equations were obtained by applying the numerical setup mentioned in Sections 5.2 and 5.4.

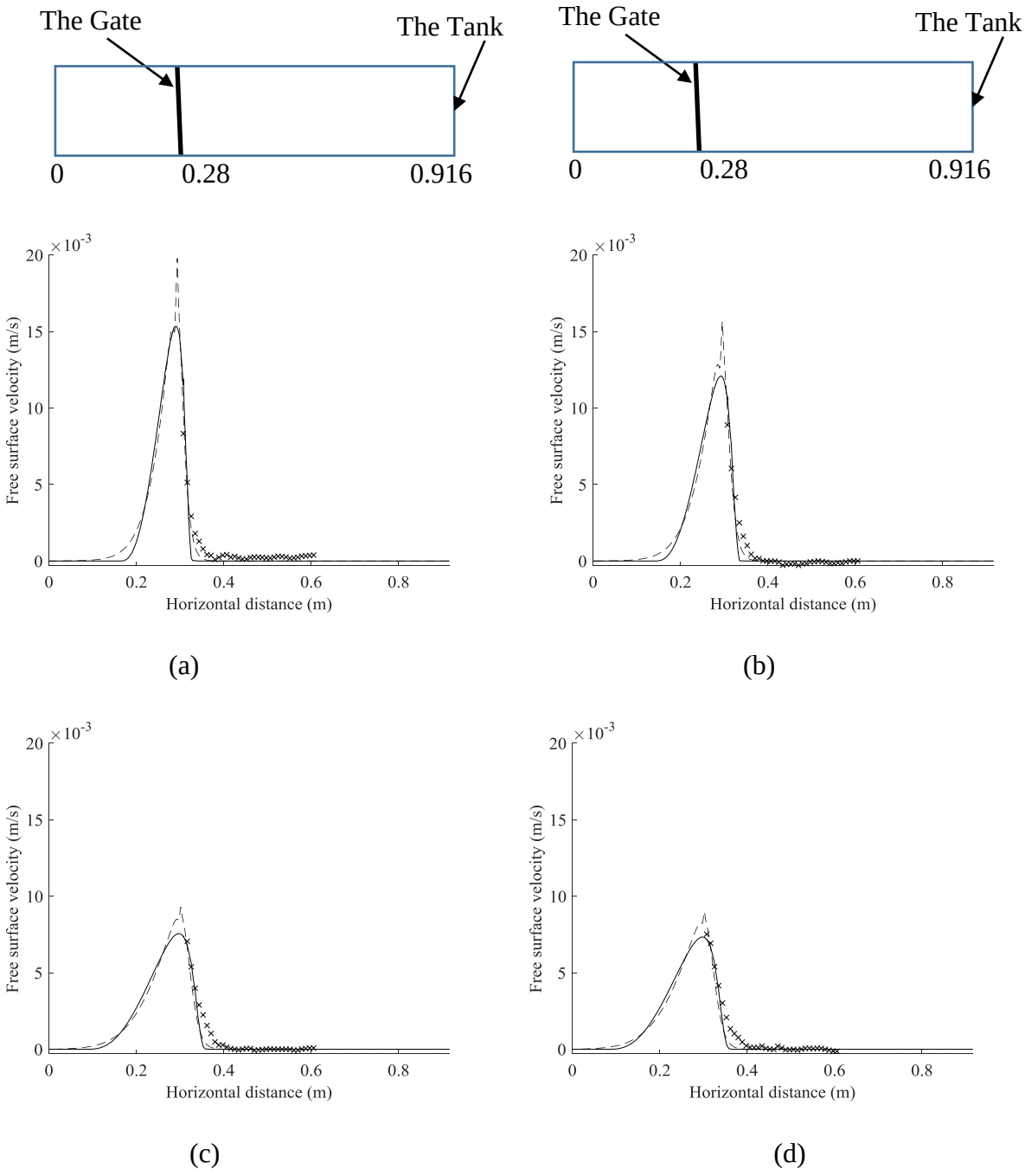

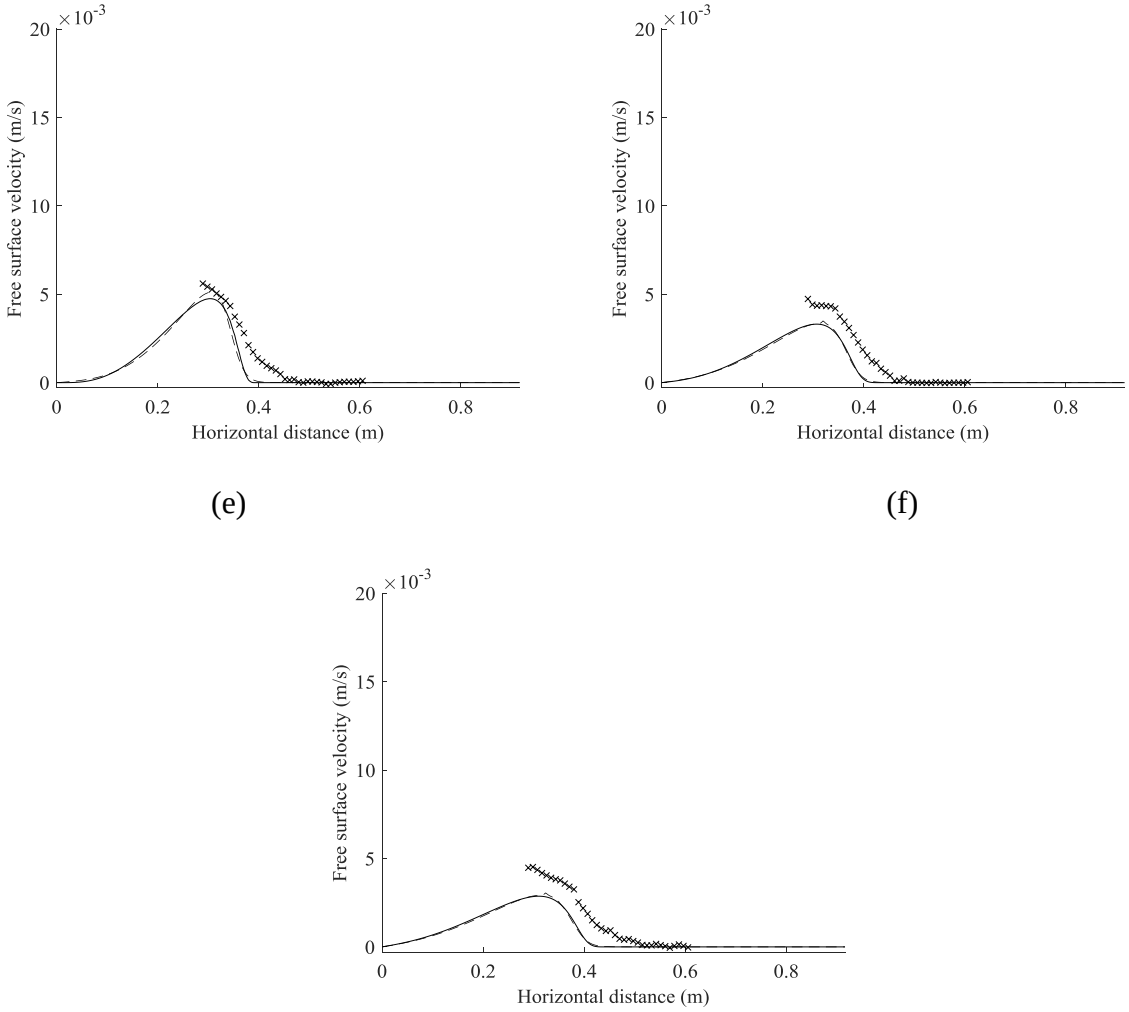

Figure 5.16: Comparison between the experimental data (crosses), the computed velocity based on the lubrication approximation equations (solid line) and the computed velocity based on the Navier–Stokes equations (dashed line) for molasses at a seven different times: (a) 0.4 s, (b) 0.6 s, (c) 1.33 s, (d) 1.4 s, (e) 4.13 s, (f) 5.4 s, and (g) 6.73 s

The justifications for both the agreements and the differences between the velocity profiles in Figure 5.16 are the same as that of Figure 5.11. However, the velocities based on the lubrication approximation under-predicted the ones based on the Navier–Stokes equations because the

lubrication approximation contains several assumptions, yielding an approximation to the Navier–Stokes equations.

The parametric identification results were compared with the rheometer data. The values of the rheological parameters for the molasses are n = 0.7±0.1 and k =16±1 Pa·s^n. These values were substituted into the power-low rheology in equation (3.4) to compare the resulting flow curves.

To obtain the rheological parameters from the rheometer data for the molasses (Figure 2.5), we developed a MATLAB code that identifies the optimal power-law parameters that best matched the rheometer measurements. This code solved the non-linear least square problem to fit the rheometer data by varying the two power-law parameters. The result from the data fitting code was n = 0.76 and k = 28.8 Pa·s^n. Both the rheological parameters from the rheometer and the reconstructed rheological parameters were substituted into equation (3.4) to obtain the flow curve as shown in Figure 5.17.

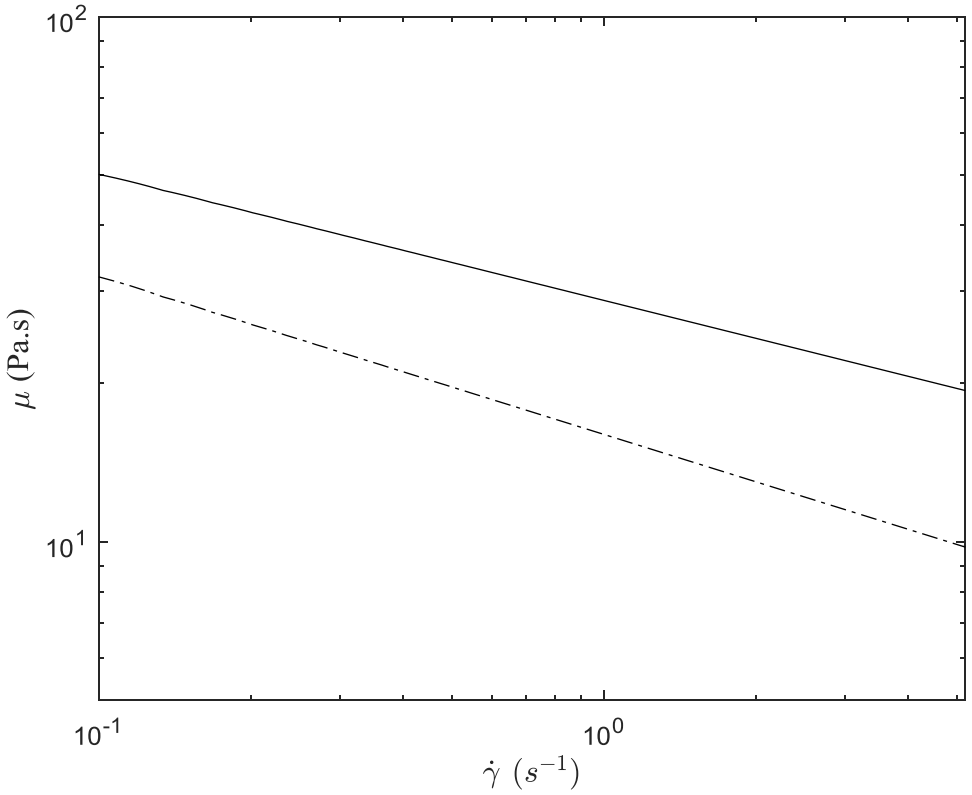

Figure 5.17: Flow curve representing the dynamic viscosity (μ) as a function of shear rate ($\dot{\gamma}$) for the rheometer data (solid line) and the data obtained from the solution of the parametric identification problem (dashed line)

Figure 5.17 shows that the slope is fairly well predicted but the viscosity within the shear rate used contains some errors.

As the difference between the measured velocity and the computed velocity profiles is small, the calculated objective function is not very sensitive to the actual value of the viscosity within the shear rate range indicated in this figure. Consequently, this implies that the power-law model is not a good fit for the molasses in the dam-break classical flow case. The rheology of the molasses was tested by considering the Ellis model, as described in Chapter 6.

Chapter 6

Ellis model

Contents

6.1 Introduction

A few researchers have considered the Ellis model, either analytically or numerically, in the context of the lubrication approximation. For example, Kheyfets and Kieweg (2013) used the lubrication approximation with the Ellis rheology in different flow configurations including spreading down a vertical wall with surface tension and gravity. Weidner and Schwartz (1994) studied a tear film with the Ellis rheology, Braun, Usha et al. (2012) studied the spreading over a curved plane, Hewson, Kapur et al. (2009) and Afanasiev, Münch et al. (2007) withdrew a film of fluid over a substance from the source of the fluid, and Jossic, Lefevre et al. (2009) drained tear substances via blinking with negligible gravity. These flow configurations represented one-dimensional spreading (two-dimensional problem), whereas Charpin, Lombe et al. (2007) used the axisymmetric flow of coating using the centrifugal forces technique (three-dimensional problem).

The previous chapters have considered the identification of the power-law rheological model, which involved the identification of two parameters. This limited parameterization imposes restrictions on the types of rheology that can be identified. In this chapter, we will consider a rheological law with a broader range of applications: the Ellis rheological law.

The Ellis model uses three parameters, namely the zero shear viscosity μ_0, the shear stress that corresponds to half the zero shear viscosity $\tau_{1/2}$, and the shear thinning parameter α. With these three parameters, the Ellis model offers more flexibility in describing the rheology of the fluids.

The parameter identification for the Ellis model is more complex as it involves three parameters instead of two, but it can identify the rheology of a wider range of fluids.

This chapter first includes the mathematical derivation of the lubrication approximation equation and the corresponding expression of the free surface velocity for the Ellis model. Molasses was used as the non-Newtonian fluid in the experiments (see Figure 2.5). Finally, all results obtained are plotted and discussed at the end of this chapter.

6.2 Mathematical derivation of the lubrication approximation for Ellis fluids

In this section, we derive the lubrication approximation based on the Ellis model. The mathematical expression of the Ellis rheological model is given by

$$\frac{1}{\mu} = \frac{1}{\mu_0}\left(1 + \left|\frac{\tau}{\tau_{1/2}}\right|^{\alpha-1}\right). \tag{6.1}$$

Here, μ_0 is the zero shear viscosity, $\tau_{1/2}$ is the shear stress at which $\mu = \frac{\mu_0}{2}$, and α is the shear-thinning parameter. From equation (6.1), it is clear that the fluid viscosity μ depends on these three adjustable parameters. Furthermore, in equation (6.1), the fluid viscosity depends on one variable that is the fluid shear stress, i.e. $\mu = f(\tau)$. This particular functional relationship can be obtained experimentally from the rheometer data as described by Schwartz and Eley (2002). When $\alpha = 1$, the fluid is Newtonian, whereas when $\alpha > 1$ and $\alpha < 1$, correspond to shear-thinning and shear-thickening fluids, respectively Charpin, Lombe et al. (2007).

To leading order, the shear stress in the fluid is defined as

$$\tau = \mu\,\dot{\gamma} \text{ with } \dot{\gamma} = \frac{\partial u}{\partial z}\,.$$

The viscosity is a function of shear stress Schwartz and Eley (2002), such that:

$$\mu = f(\tau). \tag{6.2}$$

Considering an infinitesimal volume element within the fluid, the sum of the forces is equal to zero since fluid does not undergo acceleration in the lubrication approximation framework. The force balance leads to the following mathematical expression Schwartz and Eley (2002):

$$\frac{\partial \tau}{\partial z} = -\frac{\partial p}{\partial x} \ , \ \ \tau = \left(-\frac{\partial p}{\partial x}\right) z. \tag{6.3}$$

Combining equation (6.2) with $\dot{\gamma} = \frac{\partial u}{\partial z}$, the shear rate is given by

$$\frac{\partial u}{\partial z} = \frac{\tau}{f(\tau)}. \tag{6.4}$$

It is clear from equations (6.3) and (6.4) that $f(\tau) = f(z)$. Substituting that into equation (6.4) yields

$$\frac{\partial u}{\partial z} = \frac{\tau}{f(z)}. \tag{6.5}$$

Substituting $\mu = f(\tau) = f(z)$ and $\tau = \left(-\frac{\partial p}{\partial x}\right) z$ into equation (6.1) yields

$$\frac{1}{f(z)} = \frac{1}{\mu_0}\left(1 + \left|\frac{\left(-\frac{\partial p}{\partial x}\right) z}{\tau_{1/2}}\right|^{\alpha-1}\right). \tag{6.6}$$

Substituting equation (6.6) into equation (6.5) and integrating with respect to z (from $z = 0$ to $z = h$) yields an expression of the free surface velocity u_s similar to that obtained by Kheyfets and Kieweg (2013):

$$u_s = \frac{1}{\mu_0}\left[\frac{\left(-\frac{\partial p}{\partial x}\right)h^2}{2} + \left(-\frac{\partial p}{\partial x}\right)\frac{h^{\alpha+1}}{\alpha+1}\left|\frac{\left(-\frac{\partial p}{\partial x}\right)}{\tau_{1/2}}\right|^{\alpha-1}\right]. \tag{6.7}$$

Mass conservation requires that

$$\frac{\partial h}{\partial t} + \frac{\partial Q}{\partial x} = 0, Q = \int_0^h u\, dz. \tag{6.8}$$

Next, the velocity and flux expressions (equations 6.7 and 6.8) are incorporated into the mass conservation equation to obtain a time-dependent partial differential equation, which describes the evolution of the film thickness h and is given by

$$\frac{\partial h}{\partial t} + \frac{\partial}{\partial x}\left[\frac{-p_x}{\mu_0}\left(\frac{h^3}{3} + \frac{h^{\alpha+2}}{\alpha+2}\left(\frac{|p_x|}{\tau_{1/2}}\right)^{\alpha-1}\right)\right] = 0, \tag{6.9}$$

In which the expression of the absolute pressure is the same as that indicated in equation (3.19), given by

$$p = \rho g\, h - \sigma\, \frac{\partial^2 h}{\partial x^2}.$$

Equations (3.19) and (6.9) represent the lubrication approximations for the Ellis model.

In the next sections, we shall compare the lubrication approximation solver with the Navier–Stokes solver in terms of the Ellis model to validate the lubrication approximation equations. The Ellis model cannot be solved by COMSOL with the Navier–Stokes solver because the latter only includes the power-law model and the Carreau model (which was introduced in Chapter 1). A detailed comparison between the Ellis model and the Carreau model is illustrated in Section 6.3.

6.3 Matching the Ellis and Carreau models

By considering $\mu_\infty = 0$ Pa·s as stated by Myers (2005) and Afanasiev, Münch et al. (2007) in the Carreau model's governing equation (equation 1.3), the remaining Carreau rheological parameters can approximately describe the same viscosity curve described by the Ellis model as shown in Figure 6.1. The discrete data in Figure 6.1 is the data obtained from the rheometer. A MATLAB code was developed to identify both the Ellis parameters (α,$\tau_{1/2}$, μ_0) and the Carreau parameters

(n_c, λ, μ_0), which correspond to the molasses data in Figure 2.5. This code solved the non-linear least square problem to fit the rheometer data by varying the three Ellis parameters followed by the Carreau parameters. The results from the data fitting code are the following: $\alpha = 1.6$, $\tau_{1/2}$=271 Pa, and μ_0=37.4 Pa·s for Ellis model; $\mu_0 = 37.4$ Pa·s, $\lambda = 2.94$ s, and $n_c = 0.76$ for the Carreau model. The zero shear viscosity μ_0 is the same in both Ellis and Carreau models as mentioned by (Myers 2005). In Figure 6.1, the Ellis flow curve is obtained by substituting the obtained Ellis rheological parameters of the molasses: $\alpha = 1.6$, $\tau_{1/2}$=271 Pa, and μ_0=37.4 Pa·s into equation (6.1). Subsequently, equation (6.1) is plotted using a MATLAB code, which solves the implicit function of the fluid viscosity that is included in both sides of equation (6.1). As the shear stress in equation (6.1) is expressed in terms of the viscosity and the shear rate is consistent with equation (1.3), both equations were plotted in the same figure. The Carreau flow curve is obtained by substituting the obtained Carreau rheological parameters of the molasses: $\mu_0 = 37.4$ Pa·s, $\lambda = 2.94$ s and, $n_c = 0.76$ into equation (1.3). Finally, the experimental data are the same as that indicated in Figure 2.5 for the molasses.

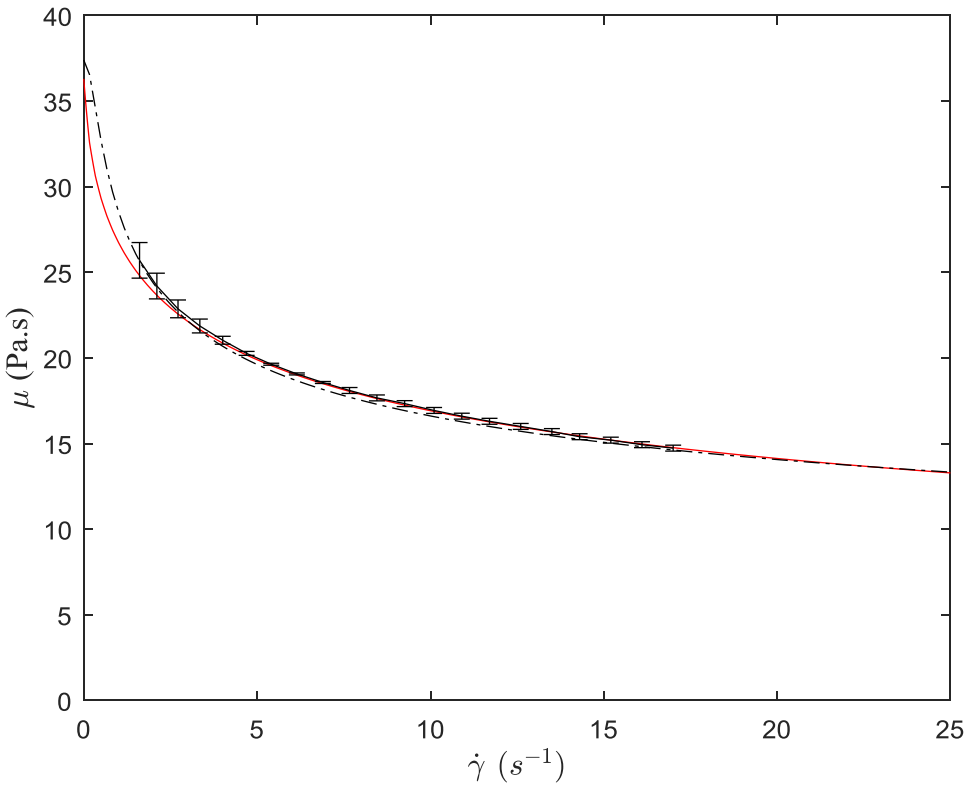

Figure 6.1: Flow curves of three different data for molasses: Ellis data (solid line), Carreau data (dashed dot line), and the experimental data (error bars)

Figure 6.1 shows that the Ellis flow curve and the Carreau flow curve are very similar and fit very well the experimental data.

The match between the Ellis and Carreau models mentioned above was implemented with molasses. We have to perform the same matching process for polyethylene oxide because this fluid is used later to validate the lubrication approximation equations with the Navier–Stokes equations, as will be explained in the next section. Both the Ellis and Carreau rheological parameters of polyethylene oxide was obtained from Myers (2005). The parameters are: $\alpha = 3$, $\tau_{1/2}$= 20 Pa, and μ_0=15.25 Pa·s for the Ellis model; $\mu_0 = 15.25$ Pa·s, $\lambda = 1.18$ s, and $n_c = 0.41$ for the Carreau model.

The Ellis and Carreau flow curves of polyethylene oxide are plotted using the same method as of the molasses, as shown in Figure 6.2.

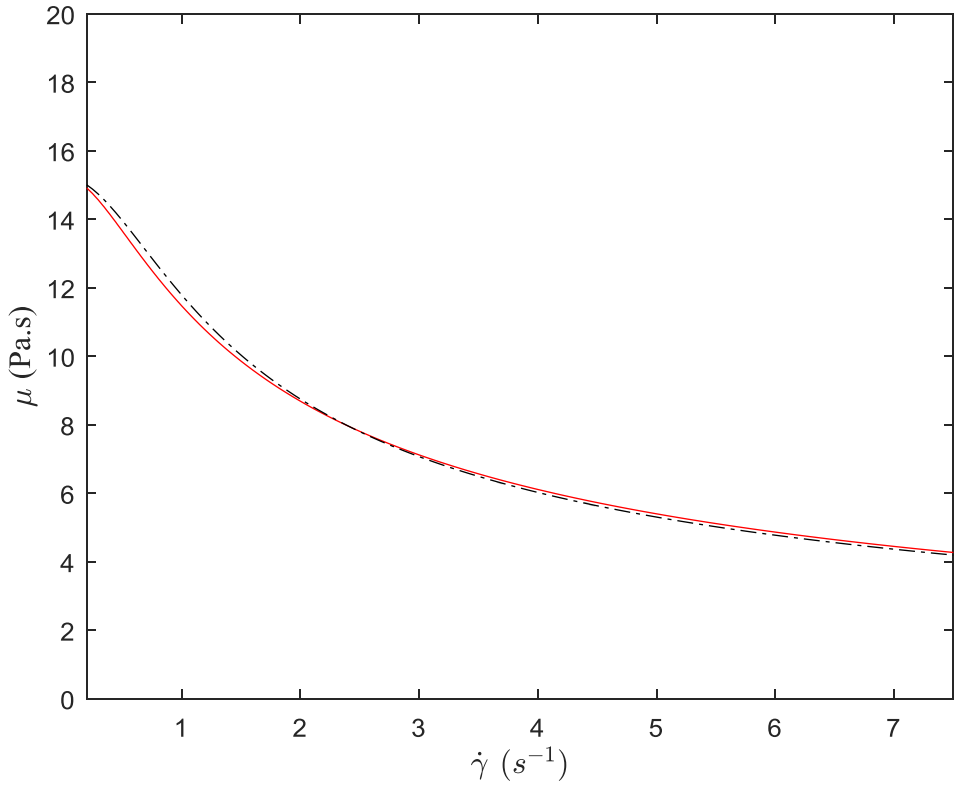

Figure 6.2: Flow curves of three different data for polyethylene oxide: Ellis data (solid line) and Carreau data (dashed dot line)

In Figure 6.2, the compatibility between the two curves is good, which implies that the Ellis rheological parameters can be used to represent the Carreau rheological parameters in terms of the flow curve and vice-versa. Consequently, the Navier–Stokes solver with the Carreau model is used to represent the Ellis model solver. The shear rate range in Figure 6.2 is between 0.2 s^{-1} and 7.5 s^{-1} as indicated by Myers (2005).

6.4 Numerical setup and identification

The equations in the lubrication approximation (equation 6.9 and 3.19) were also solved numerically with COMSOL. Equations (3.19) and (6.9) were rewritten in a standard form for the solver, by matching with the lubrication approximation coefficients:

$$e_a \frac{\partial^2 \boldsymbol{u}}{\partial t^2} + d_a \frac{\partial \boldsymbol{u}}{\partial t} + \nabla . \left(-c \nabla \boldsymbol{u} - \boldsymbol{\alpha u} + \boldsymbol{\gamma}\right) + \boldsymbol{\beta} . \nabla \boldsymbol{u} + a\boldsymbol{u} = \boldsymbol{f}, \boldsymbol{u} = [h, P]^T, \qquad (6.10)$$

where the solution is based on the two dependent variables $h(x,t)$ and $p(x,t)$. The computational domain is a horizontal interval of length 0.916 m divided into 200 quadratic elements, with 0.015 film aspect ratio for the molasses, which was calculated from the height and length scale of the problem, $H_0 = \frac{H_1 + H_g}{2}$ and $L_0 = L_1 + L_g$, respectively, as shown in Figure 2.1 of the tank diagram; the aspect ratio is $\varepsilon = \frac{H_0}{L_0}$ as indicated in Section 3.2 with H_g and H_1 values from Table 2.1 for molasses. A continuously differentiable step function was used to describe the initial free surface condition, i.e. $h(x, t = 0)$.

The numerical setup used to solve the Navier–Stokes equations was the same as that indicated in Section 4.3 with 0.015 fluid film aspect ratio. However, the fluid parameters used was the same as that of polyethylene oxide, as indicated by Myers (2005) and mentioned in Section 6.3. The upstream and downstream values in both finite element models (lubrication approximation and Navier–Stokes) were 0.020 m and 0.008 m, respectively. The validation process was implemented with polyethylene oxide as the non-Newtonian fluid. Figure 6.3 shows the comparison between the lubrication approximation and Navier–Stokes at three different times, namely 0.5 s, 5 s, and 10 s.

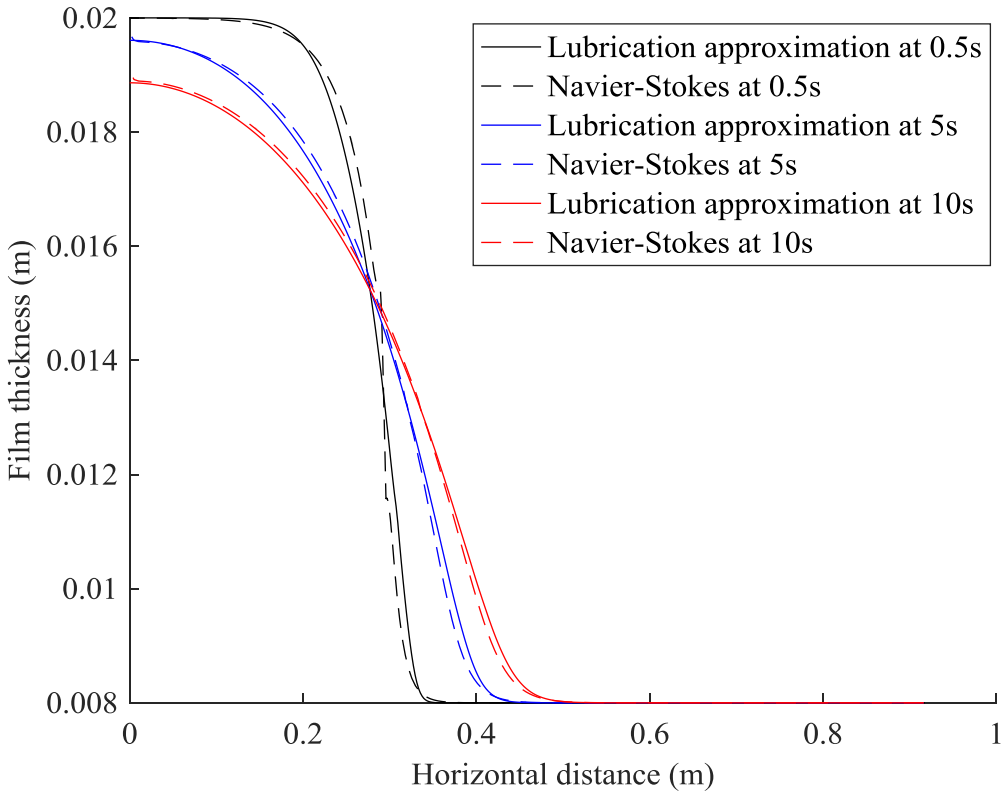

Figure 6.3: Film thickness variation along the tank centreline for the lubrication approximation and the Navier–Stokes solver for polyethylene oxide at three different times

The agreement between both models is good. However, small discrepancy occurred because the lubrication approximation contains several assumptions, yielding an approximation to the Navier–Stokes. The absolute error percentages at 0.5 s, 5 s, and 10 s are 0.75%, 0.51%, and 0.42%, respectively. These errors were calculated according to the following mathematical expression:

$$\delta = \left[\frac{1}{L}\int_0^L \frac{|h(x,t)_{LA} - h(x,t)_{\mathrm{NS}}|}{h(x,t)_{\mathrm{NS}}}\, dx\right], \tag{6.11}$$

where, δ is the absolute error percentage, $h(x,t)_{LA}$ is the film thickness for the lubrication approximation, and $h(x,t)_{\mathrm{NS}}$ is the film thickness for the Navier–Stokes equations.

6.4.1 Identification with synthetic data

Section 4.4.1 described the parameter identification process for power-law fluids using the synthetic data produced by running COMSOL Multiphysics to obtain a free surface velocity distribution.

In this section, synthetic data was created by running COMSOL with the lubrication approximation based on the Ellis model. The Ellis model uses three parameters to capture the non-Newtonian behaviour of the fluid as mentioned in Section 6.2. The grid search to identify the Ellis parameters is more computationally expensive compared to the power-law model. In the grid search above, the lower and upper bounds of the three Ellis parameters were $0.1 \leq \mu_0 \leq 100$, $0.1 \leq \alpha \leq 4$, and $1 \leq \tau_{1/2} \leq 300$. A grid search was then implemented to find the minimum of the objective function. The parametric identification process is illustrated in Figure 6.4 and explained in the subsequent paragraph. In Figure 6.4, the minimum and the maximum subscripts of μ_0, α, and $\tau_{1/2}$ represent the above-mentioned lower and upper bonds of the Ellis parameters.

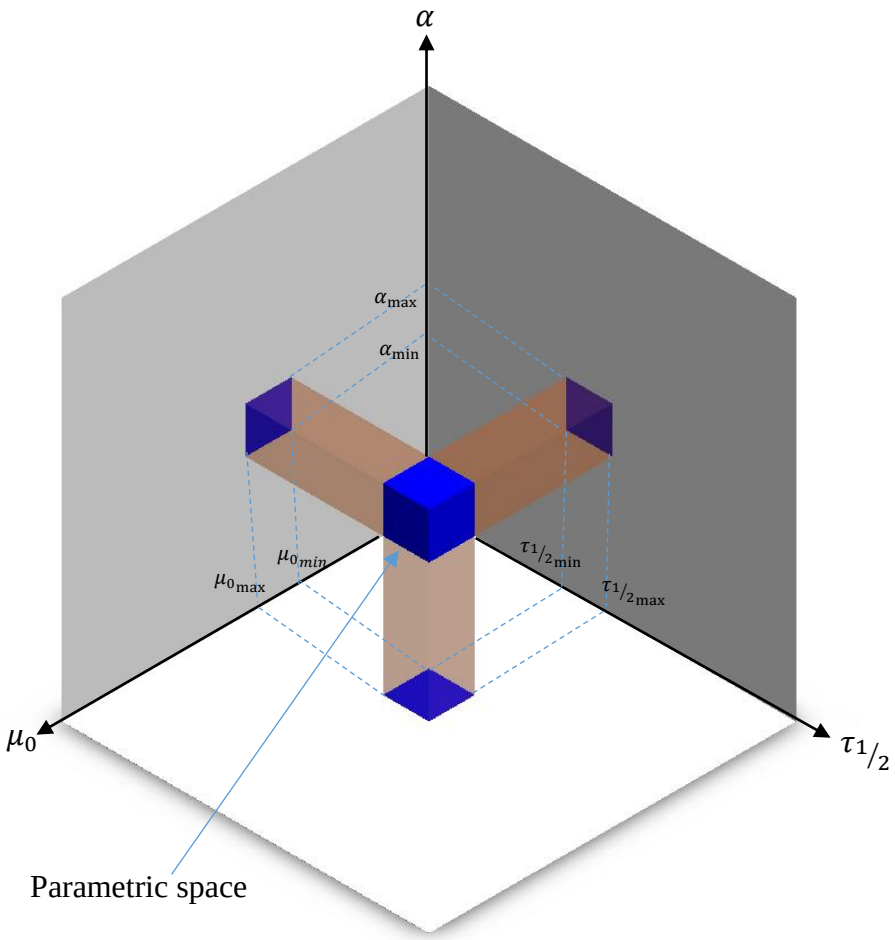

Figure 6.4: Parametric space of the Ellis rheological parameters

To identify the three parameters of the Ellis model, we fixed one of the three parameters by setting it equal to a specific value within the parametric space, which was limited by the upper bound and the lower bound of the Ellis rheological parameters. We then performed an exhaustive grid search with a wide range of the other two parameters to obtain the corresponding minimum OF. The next step was to repeatedly fix the parameter of one of the two parameters explored. This process narrowed down the parametric space until the global minimum of the OF was reached.

The above-mentioned process can be expressed mathematically to give a better understanding: $\alpha \in [\alpha_{min}, \alpha_{max}]$, $\mu_0 \in [\mu_{0_{min}}, \mu_{0_{max}}]$, and $\tau_{1/2} \in [\tau_{1/2_{min}}, \tau_{1/2_{max}}]$. The step-by-step process is described in the following:

Step 1: Select $\alpha = \alpha_1$ from the range above and find μ_{0_1}, $\tau_{1/2_1}$ such that $OF(\alpha_1, \mu_{0_1}, \tau_{1/2_1})$ is minimum.

Step 2: Select $\mu_0 = \mu_{0_1}$ and find α_2, $\tau_{1/2_2}$ such that $OF(\alpha_2, \mu_{0_1}, \tau_{1/2_2})$ is minimum.

Step 3: Select $\tau_{1/2} = \tau_{1/2_2}$ and find α_3, μ_{0_2} such that $OF(\alpha_3, \mu_{0_2}, \tau_{1/2_2})$ is minimum.

Step 4: Select $\alpha = \alpha_3$ and find μ_{0_3}, $\tau_{1/2_3}$ such that $OF(\alpha_3, \mu_{0_3}, \tau_{1/2_3})$ is minimum.

Step 5: Select $\mu_0 = \mu_{0_3}$ and find α_4, $\tau_{1/2_4}$ such that $OF(\alpha_4, \mu_{0_3}, \tau_{1/2_4})$ is minimum.

The steps above were repeated until the global minimum of the objective function was obtained. The results from the final iteration of the parametric search process is shown in Figure 6.5, which includes three minima of OF with one parameter fixed for each of the fluid tested (hydroxylethycellulose and polyethylene oxide). The first comparison was between μ_0 and α, the second was between α and $\tau_{1/2}$, and the third was between $\mu_0$and $\tau_{1/2}$. Consequently, a set of three surfaces were plotted to show the minimum values of the OF for each of the cases.

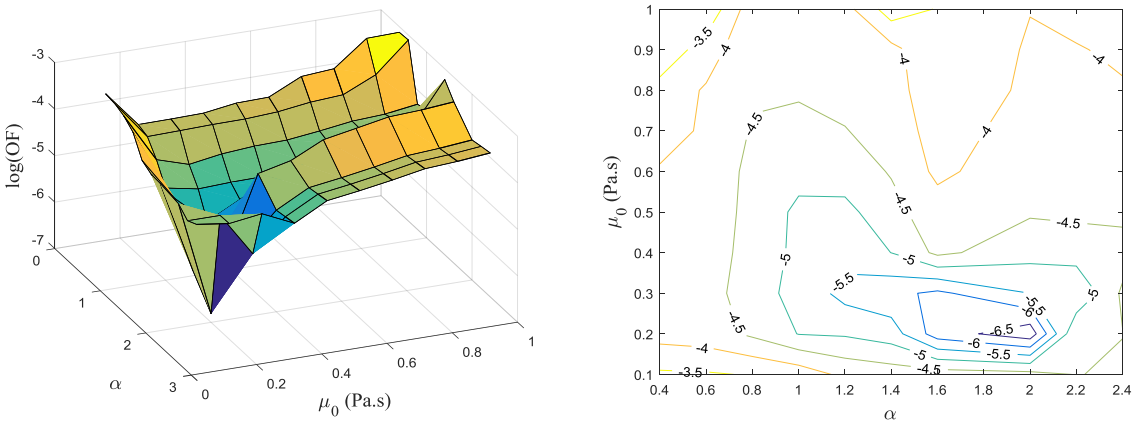

(a)

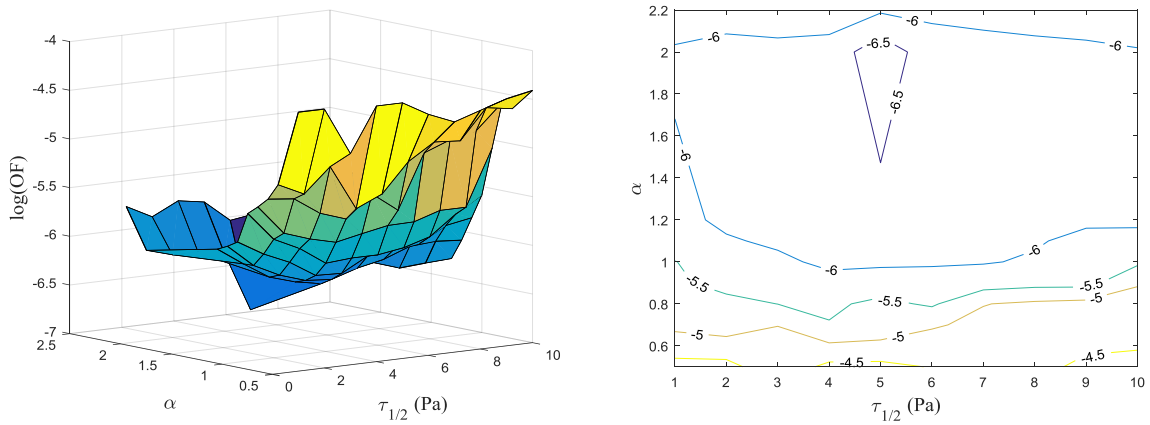
log(OF)
α
$\tau_{1/2}$ (Pa)
α
$\tau_{1/2}$ (Pa)

(b)

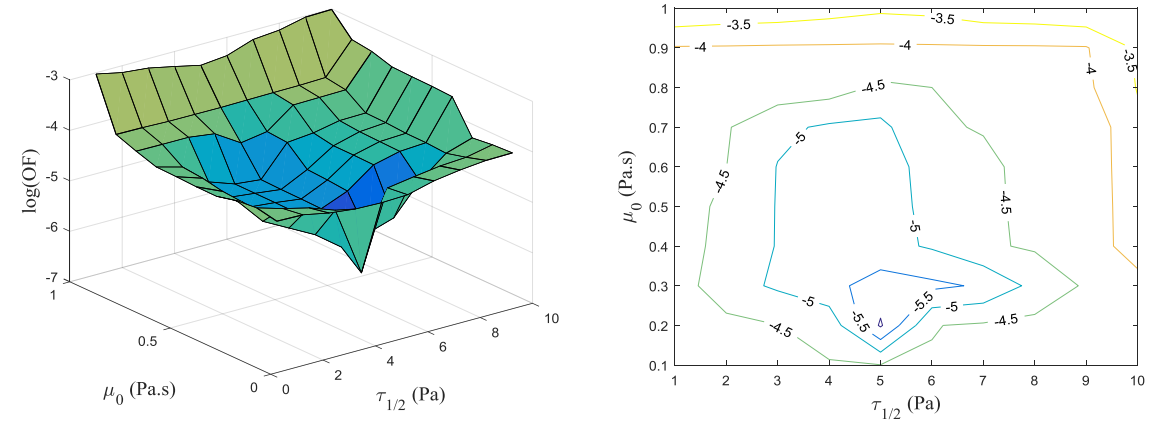
log(OF)
μ_0 (Pa.s)
$\tau_{1/2}$ (Pa)
μ_0 (Pa.s)
$\tau_{1/2}$ (Pa)

(c)

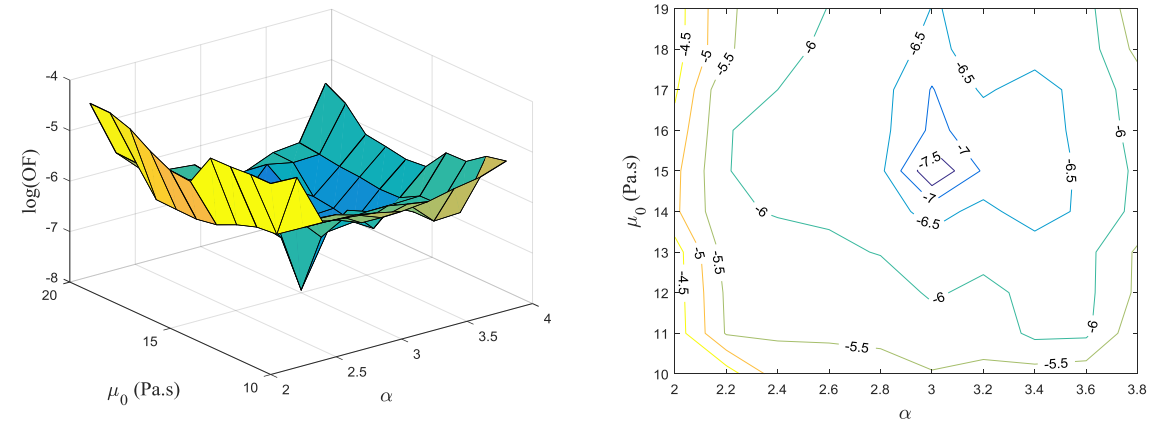
log(OF)
μ_0 (Pa.s)
α
μ_0 (Pa.s)
α

(d)

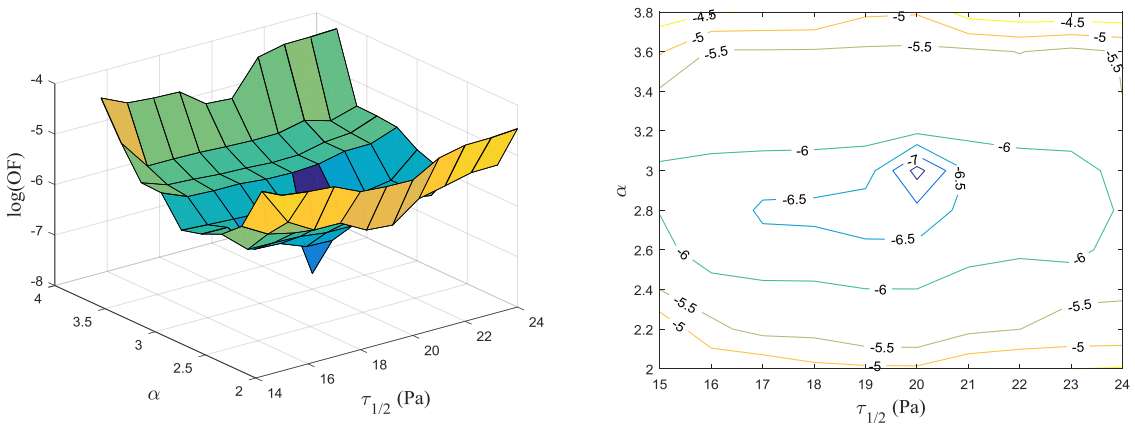

(e)

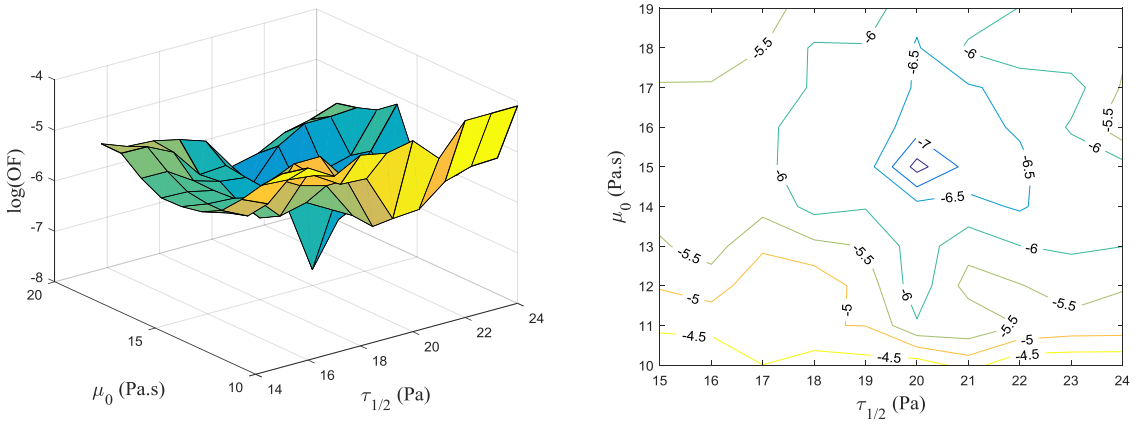

(f)

Figure 6.5: Contour lines and surface plot for the log values of the objective function with respect to the rheological parameters obtained from the exhaustive grid search with synthetic data for two different non-Newtonian fluids, namely (1) hydroxylethycellulose: (a) $\tau_{1/2}$=5 Pa, (b) μ_0=0.22 Pa·s, (c) α=2; (2) polyethylene oxide: (d) $\tau_{1/2}$=20 Pa, (e) μ_0=15.25 Pa·s, (f) α=3

The number of mesh elements used in this parametric study was 229 and the fluid film aspect ratio was 0.0152. A smoothed step function was used to describe the initial free surface level for the dam-break flow configuration. A global minimum of the objective function was found for each

the non-Newtonian fluids above and the rheological parameters corresponding to this minimum are listed in Table 6.1.

Fluid	$\tau_{1/2}\ (Pa)$	$\mu_0\ (Pa.s)$	α
Hydroxylethycellulose (Actual)	5	0.22	2
Hydroxylethycellulose (Reconstructed)	5±1	0.22±0.01	2±0.1
Polyethylene oxide (Actual)	20	15.25	3
Polyethylene oxide (Reconstructed)	20±1	15.25±1	3±0.1

Table 6.1: Actual and reconstructed values for two different non-Newtonian fluids

The sensitivity of our reconstruction algorithm to measurement uncertainty was evaluated by applying noise to the synthetic data for the hydroxylethycellulose and polyethylene oxide fluids. Noise was added to the ideal dataset according to equations (4.3) and (4.4). The identification procedure was then repeated with the noisy dataset.

The new rheological parameters with a range of added noise up to 40% were calculated for both fluids and compared with the synthetic data without noise, with the results shown in Table 6.2.

hydroxylethycellulose				
added noise %	α±0.1	μ_0±0.01 $Pa.s$	$\tau_{1/2}$±1 Pa	$OF_{minimum}\ (\frac{m^3}{s^2})$
0	2	0.22	5	1.53×10^{-7}
2	2	0.23	4	2.36×10^{-7}
3	2.1	0.25	4	2.83×10^{-7}
4	2.1	0.23	5	4.17×10^{-7}
10	2.1	0.23	5	8.71×10^{-7}
20	2.1	0.23	5	6.20×10^{-6}
40	2	0.27	5	2.56×10^{-5}
polyethylene oxide				
added noise %	α±0.1	μ_0±1 $Pa.s$	$\tau_{1/2}$±5 Pa	$OF_{minimum}\ (\frac{m^3}{s^2})$

0	2.7	15.25	20	2.05×10^{-8}
2	2.5	14.25	25	2.31×10^{-8}
3	2.5	14.25	25	2.49×10^{-8}
4	2.5	14.25	25	3.45×10^{-8}
10	2.5	14.25	25	1.5×10^{-7}
20	2.4	14.25	20	5.5×10^{-7}
40	2.7	12.25	45	2.18×10^{-6}

Table 6.2: Ellis model rheological parameters for the synthetic data cases with added noise.

The values of the minimum objective function increased slightly for the higher percentage of added noise cases. We found that the difference between the rheological parameters were insignificant for all the added noise cases except for the largest added noise of 40%. Therefore, our parametric identification procedure is insensitive to relatively high noise levels, indicating that our model is reliable and robust.

6.4.2 Identification with experimental data

The experimental free surface velocity data of molasses indicated in Chapter 5 was used to test the identification process based on the Ellis model. The numerical setup was the same as that indicated in Section 6.4.1. However, in this section, the upper and lower bound of $\tau_{1/2}$ used in the grid search was $1 \leq \tau_{1/2} \leq 500$ to cover the convergence of the calculated objective function. After implementing the grid search, we found that μ_0= 34±1 Pa·s, α = 1.1±0.1 and $\tau_{1/2}$= 290±5 Pa for the molasses. A summary of the results is shown in the following Table (a subset of the data that is close to the solution is shown here).

stage	Constraint		Parameters	OF
1	α	1.2	$\mu_0 \in$ [30,75] in steps of 5 :$\tau_{1/2} \in$ [210,300] in steps of 10	3.94×10^{-9}at μ_0 = 35 and $\tau_{1/2}$ = 290

2	μ_0	35	$\alpha \in [0.8,1.7]$ in steps of 0.1:$\tau_{1/2} \in [210,300]$ in steps of 10	3.776×10^{-9}at α = 1.1 and $\tau_{1/2}$ = 290
3	$\tau_{1/2}$	290	$\mu_0 \in [30,75]$ in steps of 5 :$\alpha \in [0.8,1.7]$ in steps of 0.1	3.776×10^{-9}at μ_0 = 35 and α = 1.1
4	α	1.1	$\mu_0 \in [30,39]$ in steps of 1:$\tau_{1/2} \in [285,330]$ in steps of 5	3.586×10^{-9}at μ_0= 34 and$\tau_{1/2}$ = 290
5	μ_0	34	$\alpha \in [0.9,1.3]$ in steps of 0.1:$\tau_{1/2} \in [285,330]$ in steps of 5	3.586×10^{-9}at α = 1.1 and $\tau_{1/2}$ = 290
6	$\tau_{1/2}$	290	$\mu_0 \in [30,39]$ in steps of 1:$\alpha \in [0.9,1.3]$ in steps of 0.1	3.586×10^{-9}at μ_0= 34 and α = 1.1

Table 6.3: Ellis model rheological parameters obtained for molasses after successive iterations of the identification procedure

The definition of the objective function was described in Section 4.4 and the objective function is given by equation (4.2), which was adopted for the Ellis parameters. The objective function used has dimensions of m^3/s^2. Consequently, the error produced from the objective function is the absolute error. The definition of the objective function was rewritten in the dimensionless form to test both its influence on the results and its effects.

$$OF\left(\mu_0, \tau_{1/2}, \alpha\right) = \sum_{i=1}^{N} 0.5 \int_0^L \left(\frac{u_c^i(x) - u_m^i(x)}{u_m^i(x)}\right)^2 dx. \quad (6.12)$$

Equation (6.12) was used with the same numerical setup indicated in Section 6.4.1 to implement the grid search study and to obtain the Ellis rheological parameters. We found that μ_0= 36±1 Pa·s, α = 1.1±0.1, and $\tau_{1/2}$=305±5 Pa for the molasses, which are close to the results obtained using the normal definition of the objective function (equation 4.2).

We now have the results based on the lubrication approximation solver from two different rheological models for molasses: the Ellis model (Chapter 6) and the power-law model (Chapter 5). The same numerical setup was used for both models (initial condition, boundary condition, mesh size, and aspect ratio). Consequently, a comparison can be made between the free velocity profiles based on the Ellis model, power-law model, and the experimental results from the dam-break flow configuration. Furthermore, the rheometer data (indicated in Figure 2.5 of Chapter 2) was added in this comparison because it represents the true data.

The velocity profile based on the Ellis model was obtained by applying equation (6.7) and by using the reconstructed Ellis rheological parameters from the grid search (μ_0= 34±1 Pa·s, α = 1.1±0.1 and $\tau_{1/2}$= 290±5 Pa). The velocity profile based on the power-law model was obtained by substituting the reconstructed rheological parameters of molasses (n = 0.7±0.1 and k = 16±1 Pa·s^n) into equation (3.18). Finally, the velocity profile based on the rheometer data was obtained by substituting the Ellis rheological parameters of molasses into equation (6.7). To obtain the Ellis rheological parameters of the molasses from the rheometer data, we developed a MATLAB code that identifies the optimal Ellis parameters that best matched the rheometer measurements. Equation (6.1) was used in the MATLAB code with the rheometer data (shear stress and viscosity), which corresponds to the data in Figure 2.5. This code solved the non-linear least square problem to fit the rheometer data by varying the three Ellis parameters. The results from the data fitting code were $\alpha = 1.6$, $\tau_{1/2}$= 271 Pa and μ_0= 37.4 Pa·s It is clear that there are differences between the reconstructed and the true values of the Ellis rheological parameters due to the experimental errors, particles match imperfections and the uncertainty of the used model as described in Section 5.2. The numerical setup used to obtain all three computed velocities above is the same as that indicated in Section (6.4).

Figure 6.6 shows the comparison among the experimental free surface velocity data, the computed free surface velocity based on the power-law model, the computed velocity based on the identified Ellis model, and the computed velocity based on the rheometer data.

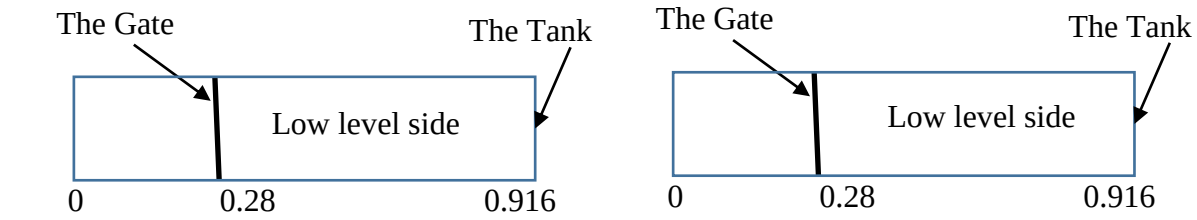
The Gate
The Tank
Low level side
0
0.28
0.916
The Gate
The Tank
Low level side
0
0.28
0.916

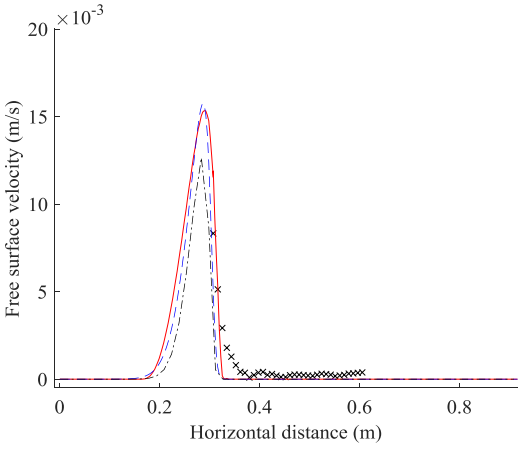
×10-3
Free surface velocity (m/s)
Horizontal distance (m)

(a)

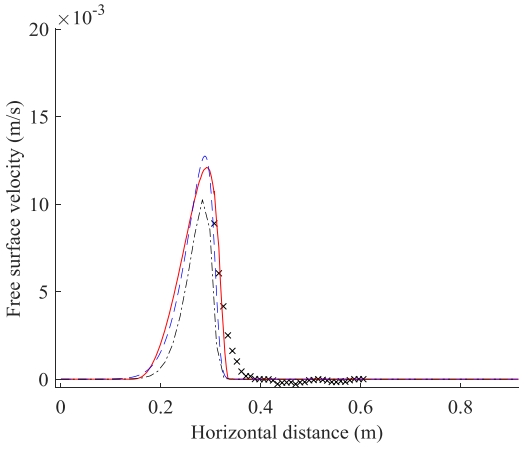
×10-3
Free surface velocity (m/s)
Horizontal distance (m)

(b)

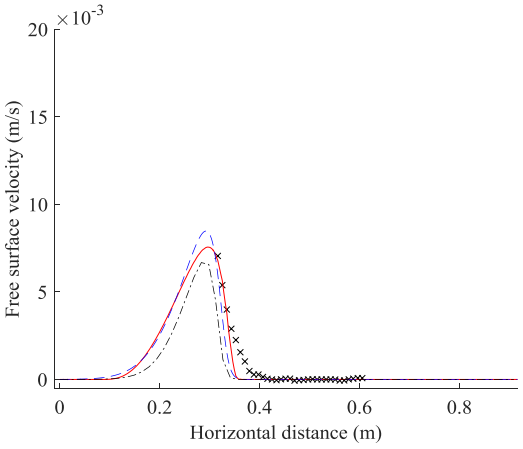
×10-3
Free surface velocity (m/s)
Horizontal distance (m)

(c)

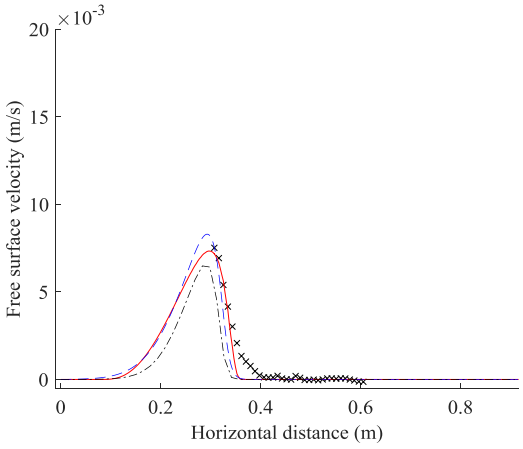
×10-3
Free surface velocity (m/s)
Horizontal distance (m)

(d)

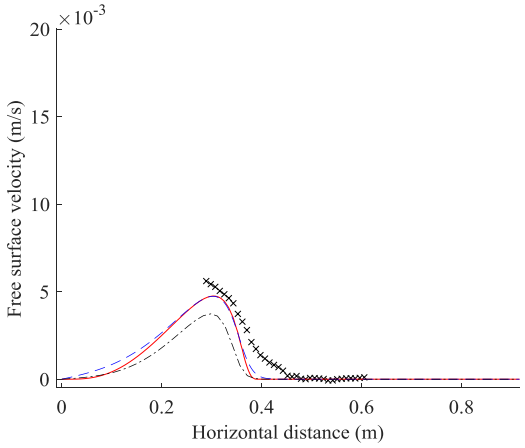

(e)

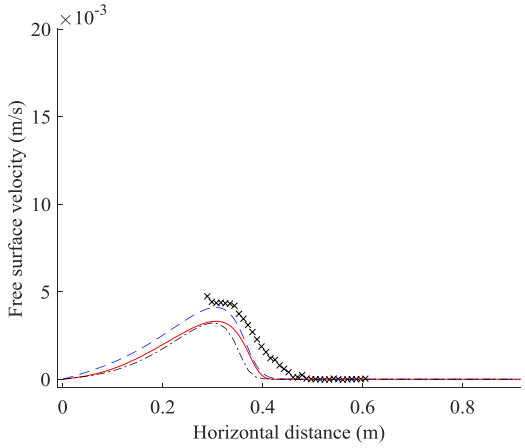

(f)

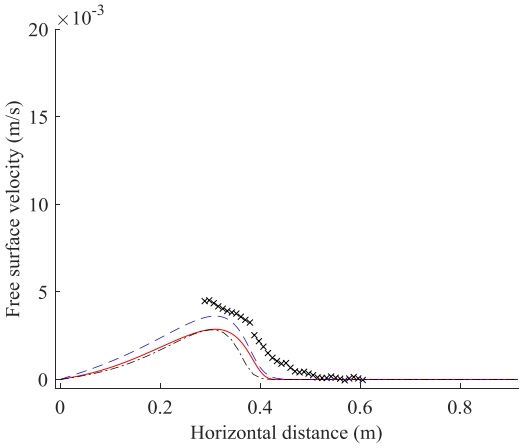

(g)

Figure 6.6: Comparison among the experimental data (crosses), the computed velocity based on the power-law model (solid line), the computed velocity based on the Ellis model (dashed line), and the computed velocity based on the rheometer data (dashed dot line) for molasses at seven different times: (a) 0.4 s, (b) 0.6 s, (c) 1.33 s, (d) 1.4 s, (e) 4.13 s, (f) 5.4 s, and (g) 6.73 s.

Figure 6.6 shows the velocity profiles at different times after the gate is released. The agreement among the velocity profiles is good. The field of view was limited and did not capture the point of maximum velocity (did not reach the peak of the velocity profile) from 0.4 s until 1.4 s due to the slow motion. From 4.13 s to 6.73 s, the computed data under-predicted the experimental data. The

reason for that was the experimental free surface data was decreased in front of the error in terms of the pixel displacement of the particles as indicated in equation (2.2).

The rheometer data represented the true data and could be used to perform further comparison between the lubrication approximation and the Navier–Stokes equations. The purpose of this comparison was to validate the obtained rheological parameters of the molasses. The lubrication approximation equations for the Ellis model were solved and compared with the Navier–Stokes equation for the Carreau model because we can use the rheological parameters of each model to represent the other as indicated in Section 6.3.

To obtain the Carreau rheological parameters of the molasses, we developed a MATLAB code that identifies the optimal Carreau parameters that best matched the rheometer measurements. This code solved the non-linear least square problem to fit the rheometer data by varying the three Carreau parameters. The mathematical expression of the Carreau model used in the MATLAB code was

$$\mu = \mu_\infty + (\mu_0 - \mu_\infty)[1 + \lambda^2\dot{\gamma}^2]^{(n_c-1)/2}, \tag{6.13}$$

where μ_∞ and μ_0 are the limiting viscosities at the low and high shear rates respectively, λ is the characteristic time, $\dot{\gamma}$ is the shear rate, and n_c is the flow behaviour index of the Carreau model. The viscosity μ_0 is from the Ellis data as explained by Myers (2005). Then, by implementing the MATLAB code with $\mu_\infty = 0$ Pa·s for the purpose of simplicity Myers (2005) and Afanasiev, Münch et al. (2007), we found that $\mu_0 = 37.4$ Pa·s, $\lambda = 2.94$ s, and $n_c = 0.76$. These parameters were used in COMSOL to implement the Navier–Stokes solver, with the same numerical set up as indicated in Section 6.4.

The Ellis rheological parameters of the molasses obtained from the rheometer data fitting solution ($\alpha = 1.6$, $\tau_{1/2}$ = 271 Pa, and μ_0 = 37.4 Pa·s) were used to solve the lubrication approximation equation (6.9). First, both the lubrication approximation and the Navier–Stokes models were solved to obtain two film thickness profiles at three different times: 0.5 s, 5 s, and 10 s. Next, we

used equation (6.7), which represents the free surface velocity expression to obtain two velocity profiles at the three times above. The results are shown in Figure 6.7.

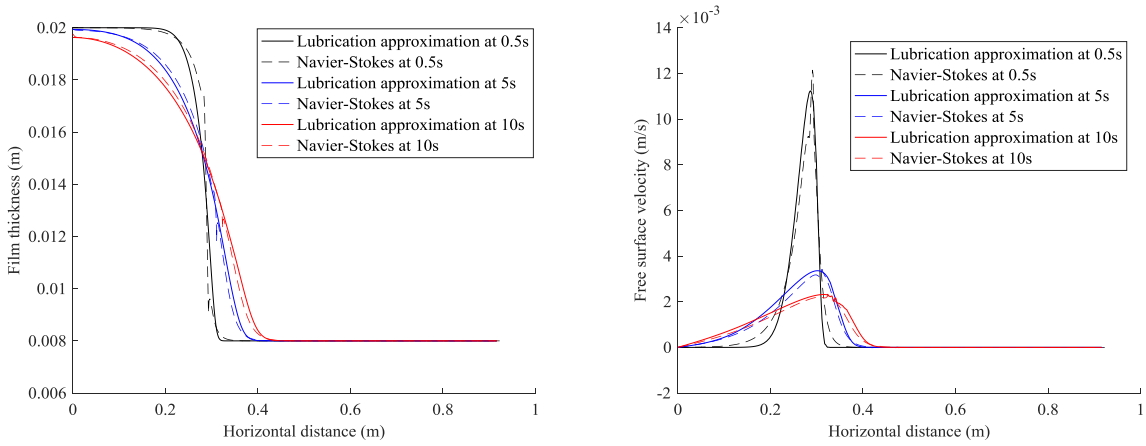

(a) (b)

Figure 6.7: Comparison between the Navier–Stokes equations and the lubrication approximation at three different times of the molasses for two different cases: (a) fluid film thickness as a function of the horizontal distance, and (b) free surface velocity as a function of the horizontal distance

From Figure 6.7, it is clear that the agreement is good in both cases. The small difference between the two models is because the lubrication approximation is an approximation of the Navier–Stokes, in which the inertia terms were neglected and a small film aspect ratio was considered.

Another comparison was implemented using the flow curve, with the viscosity shown as a function of the shear rate. Three data sets are used, namely the rheometer data (Chapter 2 Figure 2.5), the Ellis model data based on the parametric identification as indicated in Section (6.4.2), and the power law data (Chapter 5 Section 5.6).

The rheometer data was plotted by applying equation (6.1) with $\alpha = 1.6$, $\tau_{1/2}$= 271 Pa, and μ_0= 37.4 Pa·s, which was obtained as indicated in Section 6.4.2. The Ellis model data was obtained using equation (6.1) with the reconstructed Ellis rheological parameters μ_0= 34±1 Pa·s, α = 1.1±0.1, and $\tau_{1/2}$= 290±5 Pa, which were reconstructed from the grid search process. Finally, the power-law profile was obtained by applying equation (3.4) and substituting the reconstructed

power-law rheological parameters of molasses: n = 0.7±0.1 and k = 16±1 Pa·s^n (Chapter 5, Section 5.6). The outcome of the comparison is shown in Figure 6.8.

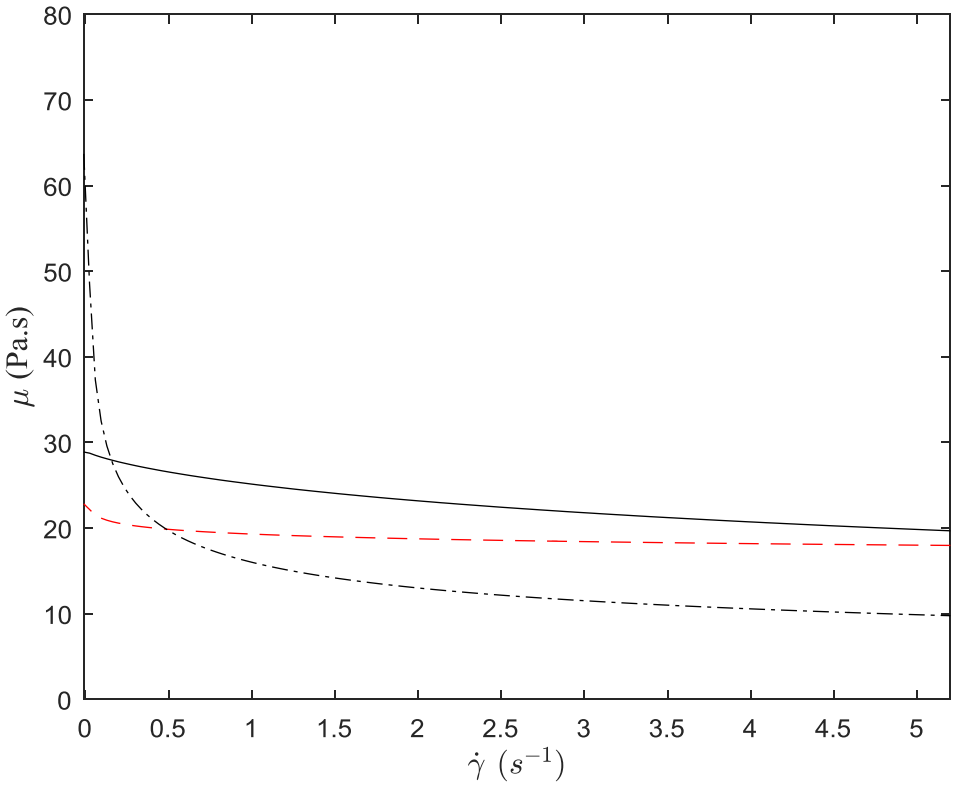

Figure 6.8: Viscosity (Pa·s) as a function of shear rate (s^{-1}) (flow curve) for three different data: the rheometer data (solid line), the Ellis model data based on the reconstructed rheological parameters (dashed line), and the power law data (dashed dot line)

From Figure 6.8, the Ellis model profile is found to be closer to the rheometer profile than that of the power law. Furthermore, the power-law model gives low accuracy for the prediction in low shear rates cases, as also stated by Afanasiev, Münch et al. (2007) and Myers (2005). This suggests that the Ellis model provides a better representation of the molasses rheology because the latter cannot be fitted well with the power law, which has only two parameters. The shear rate range shown in Figure 6.9 represents the shear rate expected in the current experiment.

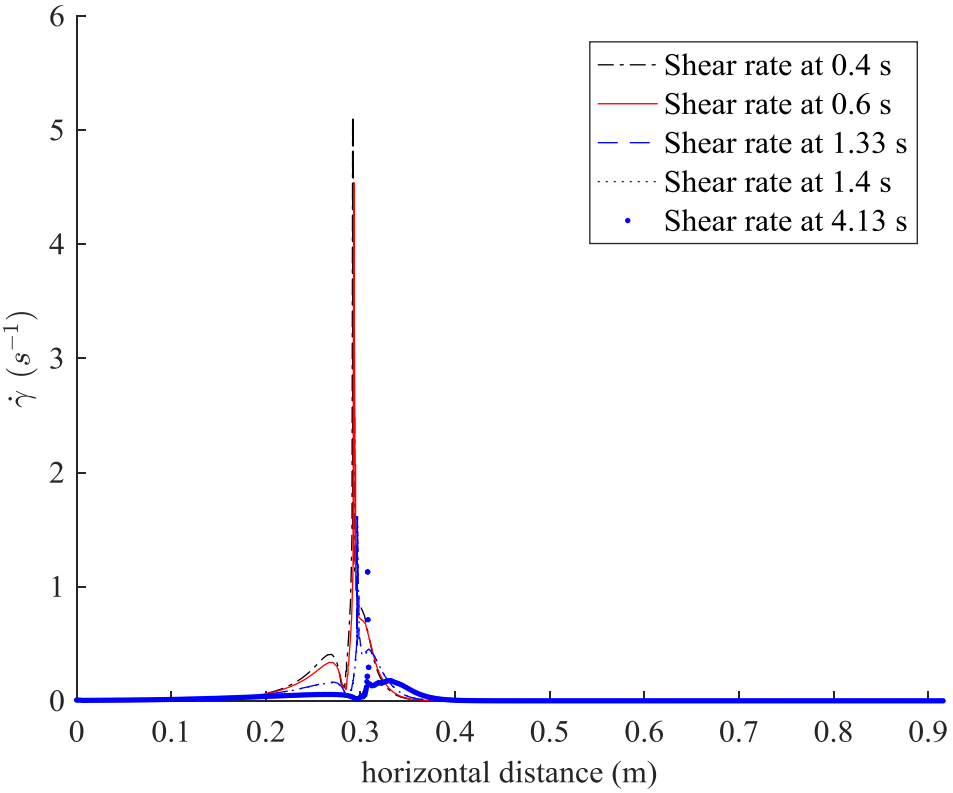

Figure 6.9: Shear rate as a function of horizontal distance of the molasses at five different times

The maximum shear rate of 5.2 s^{-1} at 0.4 s shown in Figure 6.9 was used to represent the shear rate in Figure 6.8. In summary, it is clear from this chapter that the Ellis rheological model parameters for non-Newtonian fluids can be reconstructed by solving the parametric identification problem based on the lubrication approximation. However, a small difference occurred between the obtained rheological parameters and the true rheological parameters due to the experimental and numerical errors (see Section 5.2).

Chapter 7

Comparison of the lubrication approximation and Navier–Stokes solutions

Contents

7.1 Introduction

This chapter compares the solutions obtained from two models: lubrication approximation and Navier–Stokes, for the dam-break classical flow. The former model was based on the lubrication approximation equations, whereas the latter was based on the Navier–Stokes equations. The above-mentioned comparison process allows us to determine whether this approximation is valid for all the ranges of the parameters used, or if it is limited to a specific range. The dam-break classical flow was considered because it allows the comparison with experimental data. Two different aspects are analysed in this chapter. The first aspect is associated with the comparison between the lubrication approximation and the Navier–Stokes using the free surface data obtained from the experiments for both the Newtonian and non-Newtonian fluids as mentioned in Chapter 5 and Chapter 6. The second aspect is related to the comparison process in terms of the dimensionless mathematical forms of the lubrication approximation equations and the Navier–Stokes equations.

The dam-break classical flow was modelled using the full Navier–Stokes equations or the approximation form of the Navier–Stokes equations, which is called the lubrication approximation Piau and Debiane (2005) and Balmforth, Craster et al. (2007). In the past, the dam-break problem has been analysed by Balmforth, Craster et al. (2007) and Ancey, Cochard et al. (2009). The aim of both studies was to measure the position of the fluid front current in a horizontal channel as stated by Balmforth, Craster et al. (2007) or by using an inclined channel as implemented by Ancey, Cochard et al. (2009).

The lubrication approximation equations were derived based on the power-law rheological model (Chapter 3) and the Ellis rheological model (Chapter 6). The lubrication approximation is less computationally expensive than the Navier–Stokes equations and simpler to solve. The dynamics of the thin liquid film was studied by applying the lubrication approximation equations Reynolds (1886). It is well known that the two models mentioned above are widely used but two studies have compared these models, as described by Mahady, Afkhami et al. (2013) and Gaskell, Jimack et al. (2004).

To establish the validity of the approximation in terms of the dimensionless flow parameters and film aspect ratio, the experimental data has been used to confirm the validity of both models.

7.2 Comparison for Newtonian fluids

7.2.1 Silicone compound oil

The computed velocity based on the lubrication approximation is obtained by applying equation (3.18). In this equation, the value of n is set as 1 (Newtonian), the value of k is equal to the viscosity of the silicone oil (0.41 Pa·s) as indicated in Chapter 2 from the rheometer data of silicone compound oil.

As indicated in Chapter 4, COMSOL was used to solve the lubrication approximation equations to obtain the film thickness values and the free surface velocity. The geometry represents an interval divided into quadratic elements, of which the total length was 0.916 m, and the number of quadratic elements was 200 with 0.015 fluid aspect ratio of the silicone oil, which was calculated as indicated in Section 3.2, using H_g and H_1 values of the silicone oil from Table 2.1. A step flow function was used to describe the initial free surface condition of the fluid used.

The other computed free surface velocity was obtained by solving the Navier–Stokes equations for a Newtonian fluid using COMSOL. A finite element technique was employed. The numerical setup used to solve the Navier–Stokes equations is the same as that indicated in Section 4.3, with 0.015 aspect ratio, which was calculated as indicated in Section 3.2, using H_g and H_1 values of the silicone oil from Table 2.1.

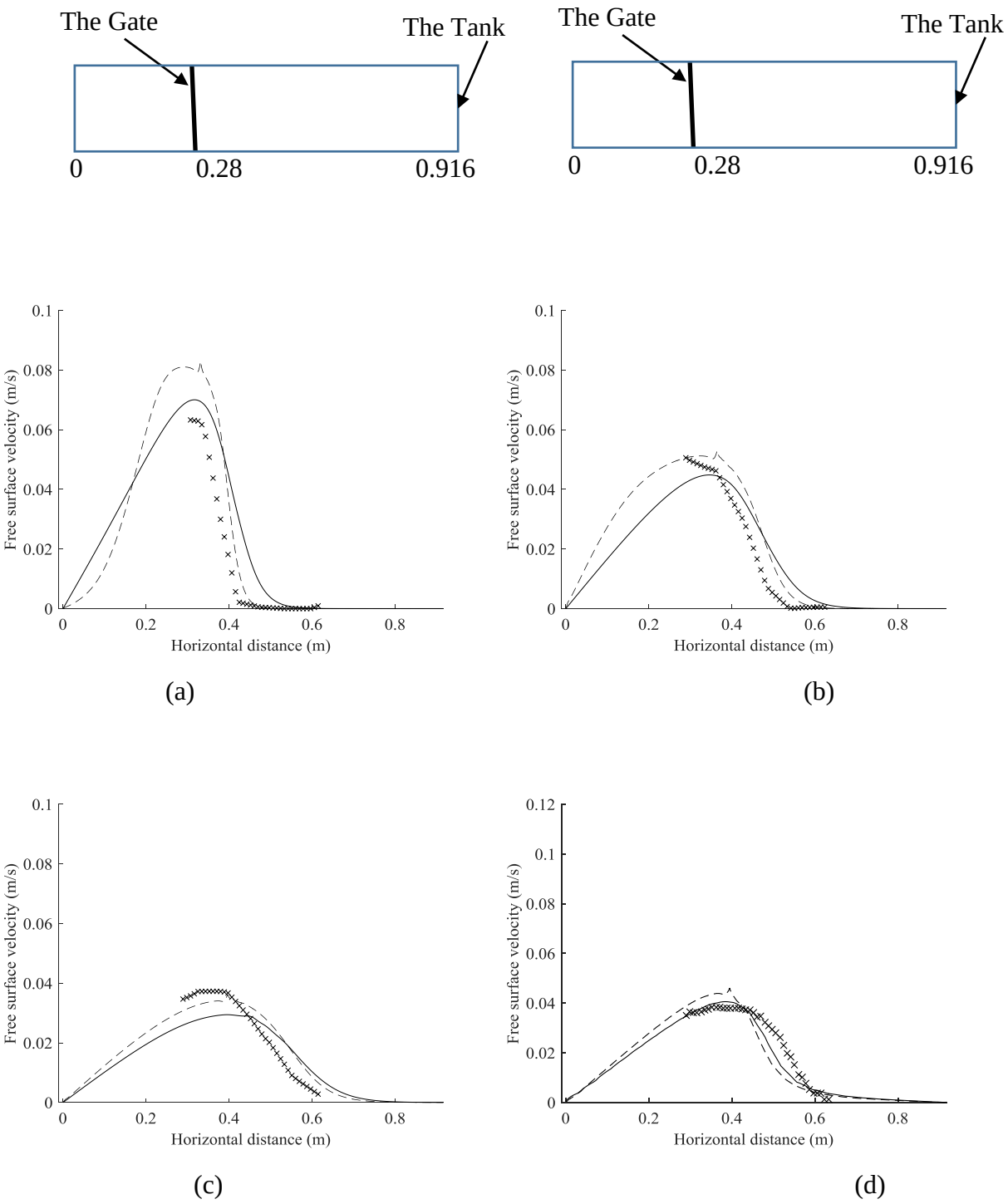

Figure 7.1: Comparison among the experimental data (crosses), the computed velocity based on the lubrication approximation equation with rheometer data (solid line), and the computed

velocity based on the Navier–Stokes equation with rheometer data (dashed line) for a Newtonian fluid (silicone oil) at four different times: (a) 0.43 s, (b) 0.93 s, (c) 1.66 s, and (d) 2.46 s

Figure 7.1 shows the difference between the computed and the measured velocities for a Newtonian fluid. In general, the velocity profiles that are based on the lubrication approximation are under-predicted due to the inertia term being neglected from the Navier–Stokes equations. The difference between the computed velocities based on both the lubrication approximation and the Navier–Stokes is small and is due to the effects of inertia produced from the relatively high aspect film ratio and high fluid slope. However, Figure 7.1 shows a relatively good agreement between the computed and the experimental data of the free surface velocity, and the results obtained were physically reasonable. The agreement provided the required confidence that the COMSOL model (which uses the finite element method) was valid and could be used for further analyses, as will be explained in the next paragraphs.

The above-mentioned comparison process was implemented with aspect ratio 0.015. It is important to analyse the effect of the different aspect ratio values, as shown in Figure 7.2.

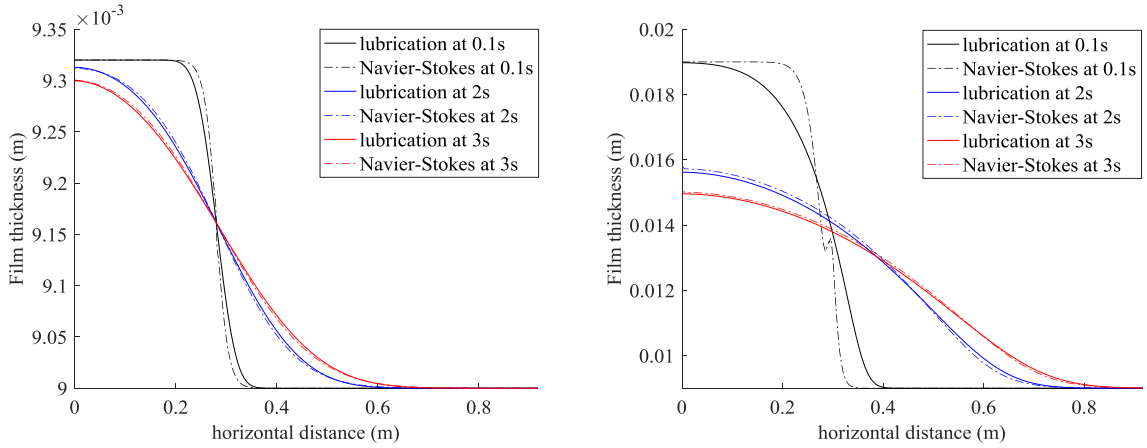

(a) (b)

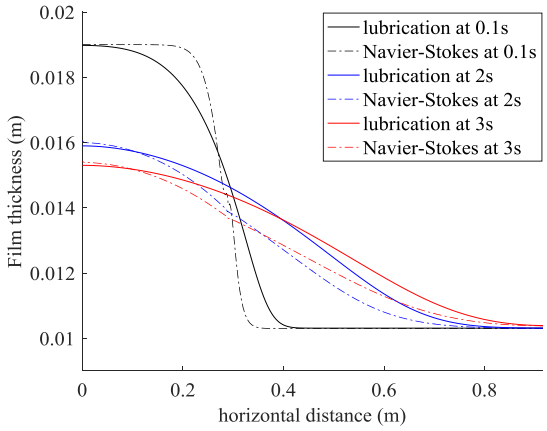

(c)

Figure 7.2: Fluid film thickness as a function of horizontal distance for a Newtonian fluid (silicone oil) at three different aspect ratios: (a) 0.01, (b) 0.015, and (c) 0.016

The agreement between the lubrication approximation and Navier–Stokes improves with a smaller aspect ratio, as shown in Figure 7.2. However, at earlier times, the film thickness profile is influenced by the initial condition of both models used. At aspect ratio 0.016, the agreement was relatively poor; whereas at 0.015 the agreement is poor at the earlier time of 0.1 s but becomes good thereafter.

The comparison above is based on the fluid film thickness. The same comparison can be repeated using the free surface velocity profile instead of the film thickness.

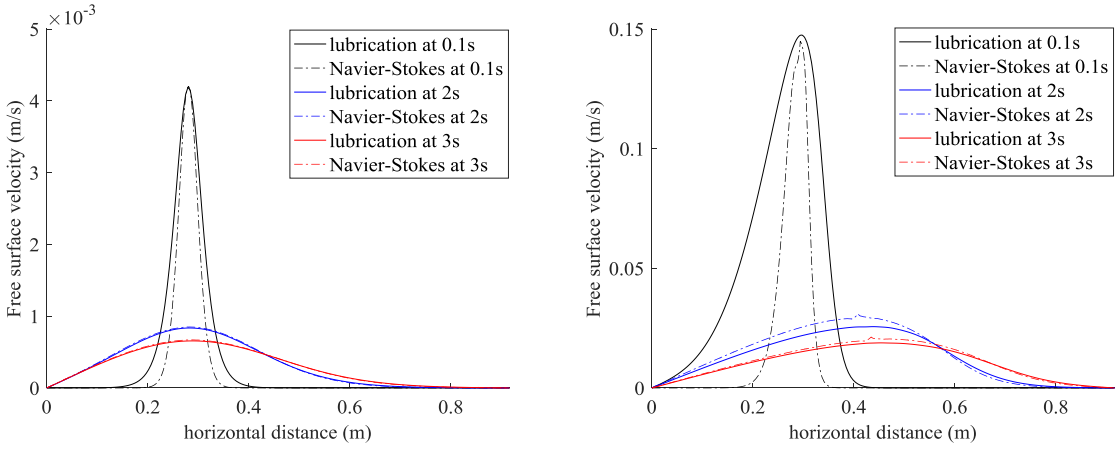

(a) (b)

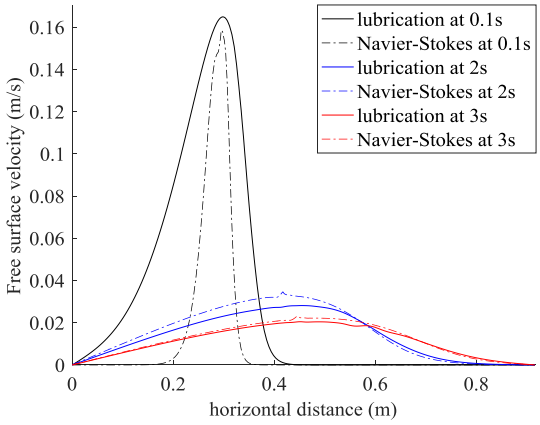

(c)

Figure 7.3: Free surface velocity as a function of horizontal distance for a Newtonian fluid (silicone oil) at three different aspect ratios: (a) 0.01, (b) 0.015, and (c) 0.016

According to Figure 7.3, the error between the two models increases with the increase in the aspect ratio values. This is because the lubrication approximation works better with small aspect ratios Howison, Moriarty et al. (1997).

The rheological parameters of silicone oil were reconstructed by solving the parametric identification problem as indicated in Chapter 5 (n = 0.9±0.1 and k = 0.5±0.1 Pa·s^n). This problem was solved numerically using COMSOL based on the lubrication approximation. The obtained rheological parameters, which were based on the lubrication approximation were compared with those obtained from the rheometer (the true values). The comparison process is implemented with the velocity profile to obtain the relative error percentage between the true values and the measured values. Therefore, both the parametric identification results (n = 0.9±0.1 and k = 0.5±0.1 Pa·s^n) and the rheometer results (n = 1 and k = 0.41 Pa·s^n) of silicone oil were used (results as indicated in Chapter 5). Figure 7.4 shows the comparison between the two computed velocities. The velocity profile based on the lubrication approximation was obtained by substituting the parametric identification results above into the lubrication approximation solver. The velocity profile based on Navier–Stokes was obtained by substituting the rheometer results above into the Navier–Stokes solver. The error between the two profiles represents the true error.

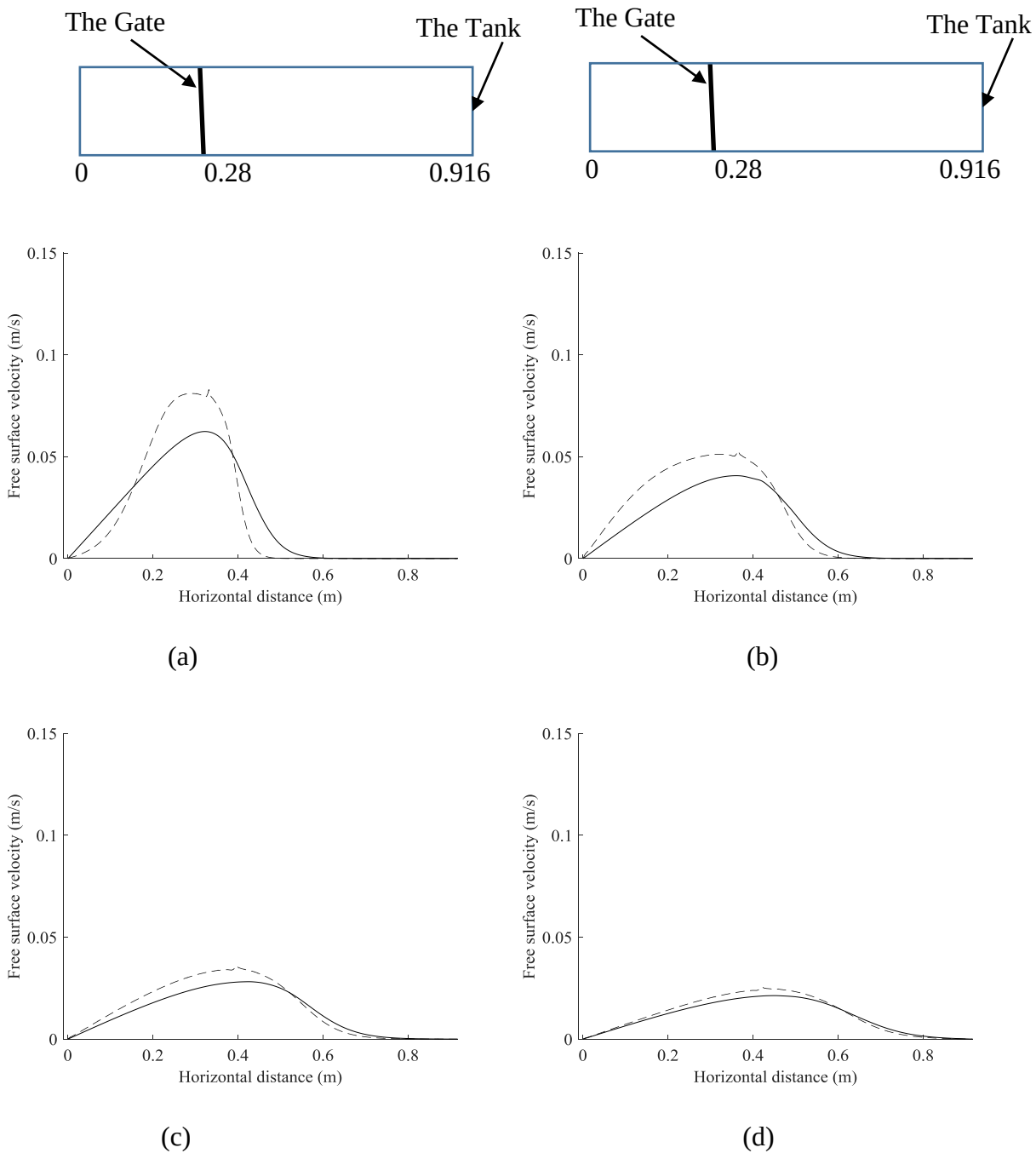

Figure 7.4: Free surface velocity as a function of horizontal distance for a Newtonian fluid (silicone oil) for two models (lubrication approximation based on the identification results (solid line) and Navier–Stokes based on the real results (dashed line)), at four times: (a) 0.43 s, (b) 0.93 s, (c) 1.66 s, and (d) 2.46 s

The relative error percentages between the lubrication approximation and the Navier–Stokes of the four different times mentioned above are shown in Table 7.1.

Time (s)	0.43	0.93	1.66	2.46
Relative error percentage (%)	8.52	11.64	8.30	5.68

Table 7.1: Relative error percentages for silicone oil

The error percentages were calculated by applying the following equation:

$$\delta_u = \left[\frac{1}{L}\int_0^L \frac{|u(x,t)_{LA} - u(x,t)_{\mathrm{NS}}|}{u(x,t)_{\mathrm{NS}}}\, dx\right]. \tag{7.1}$$

In equation (7.1), δ_u is the relative error percentage in terms of the fluid velocity, $u(x,t)_{LA}$ is the computed velocity based on the lubrication approximation and $u(x,t)_{\mathrm{NS}}$ is the computed velocity based on Navier–Stokes.

It is clear that the relative error percentage decreases slightly with increasing time. However, at 0.43 s the error percentage was less than that at 0.93 s due to the difference in the initial condition settings. However, these error percentages are relatively small. Consequently, the agreement between the lubrication approximation and the Navier–Stokes is accepted for the silicone compound oil with the dam-break classical flow experiment.

7.2.2 Aqueous glycerol

In the current work, two different Newtonian fluids were used to reconstruct the rheological parameters, namely silicone compound oil and aqueous glycerol. The relative error percentages were calculated for the silicone oil. Additionally, it is important to check the outcomes obtained from using the aqueous glycerol.

In Figure 7.5, a comparison among the free surface velocity profiles is shown. The experimental data of the aqueous glycerol indicated in Chapter 5 was compared with the computed velocity profiles based on both the lubrication approximation and Navier–Stokes.

The computed velocities were calculated based on the rheometer data of aqueous glycerol (Chapter 2, Figure 2.4: n = 1 and k = 1.14 Pa·s^n). The computed velocity based on the lubrication approximation was plotted using COMSOL. The numerical setup used is the same as that indicated in Section 7.2.1 with aspect ratio 0.019, which was calculated as indicated in Section 3.2 using H_g and H_1 values of the aqueous glycerol from Table 2.1. The velocity profile based on Navier–Stokes was obtained using the Navier–Stokes solver with same numerical setup as that indicated in Section 4.3 with aspect ratio 0.019.

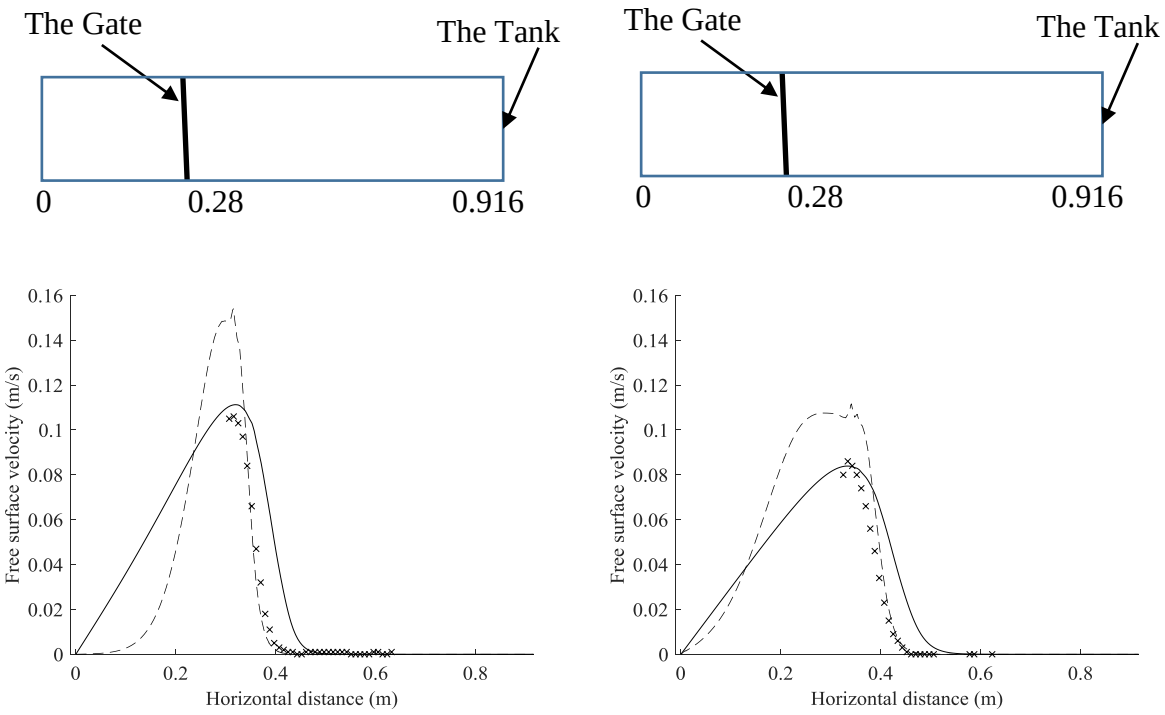

(a) (b)

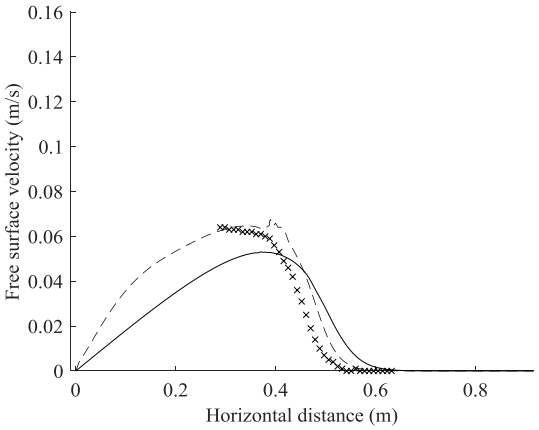

(c)

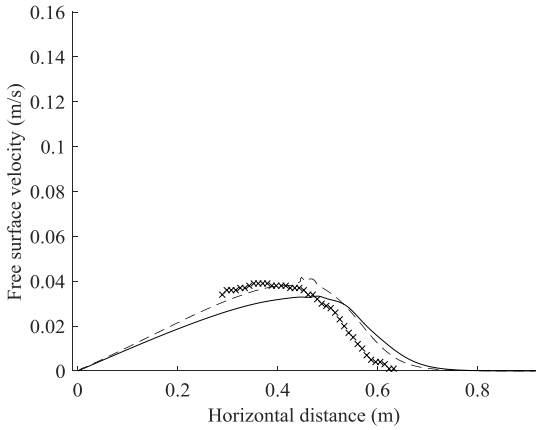

(d)

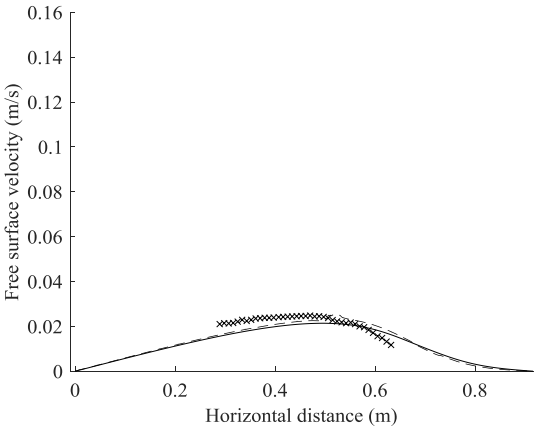

(e)

Figure 7.5: Comparison among the experimental data (crosses), the computed velocity based on the lubrication approximation equation with rheometer data (solid line), and the computed velocity based on the Navier–Stokes equation with rheometer data (dashed line) for a Newtonian fluid (aqueous glycerol) at five different times: (a) 0.29 s, (b) 0.49 s, (c) 0.99 s, (d) 1.96 s, and (e) 3.56 s

Figure 7.6 shows the comparison between the lubrication approximation and the Navier–Stokes using the rheometer data with different aspect ratios for the glycerol used.

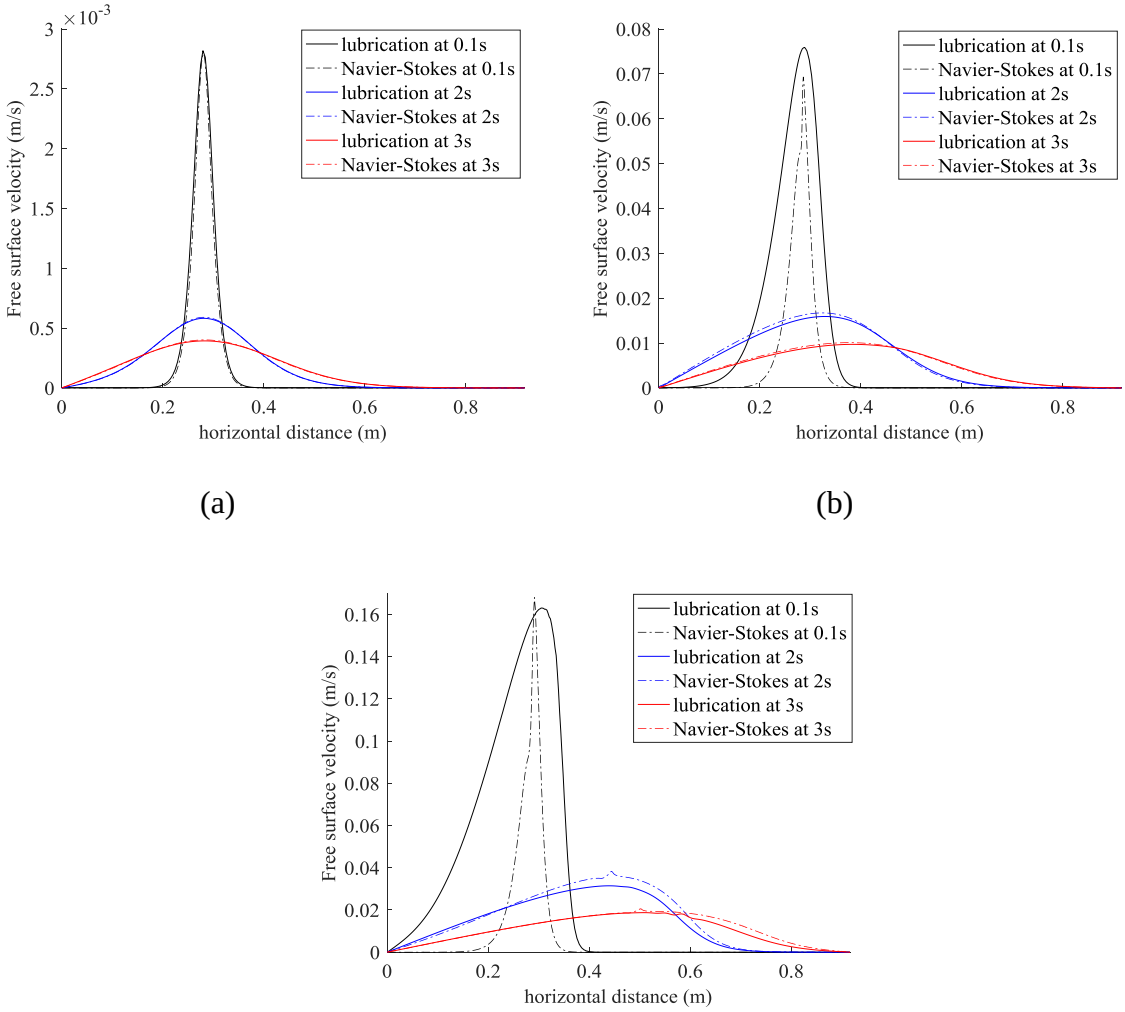

Figure 7.6: Free surface velocity as a function of horizontal distance for a Newtonian fluid (aqueous glycerol) at three different aspect ratios: (a) 0.01, (b) 0.015, and (c) 0.020

The parametric identification technique was used to calculate the rheological parameters of the aqueous glycerol: n = 1.0±0.1 and k =1.3±0.1 Pa·s^n (see Chapter 5 Section 5.4.1). The true values: n = 1 and k = 1.14 Pa·s^n as obtained from the rheometer data in Figure 2.4 of Chapter 2 were used to compare with the measured values. The reconstructed rheological parameters from the identification process of aqueous glycerol were used to find the computed velocity based on the lubrication approximation. The true values of the rheological parameters were used to find the computed velocity based on the Navier–Stokes solver.

The comparison process is implemented with the velocity profile to obtain the relative error percentage between the true values and the measured values. The numerical setup used is same as that indicated in Section 7.2.1. The outcomes of the above-mentioned comparison are shown in Figure 7.7.

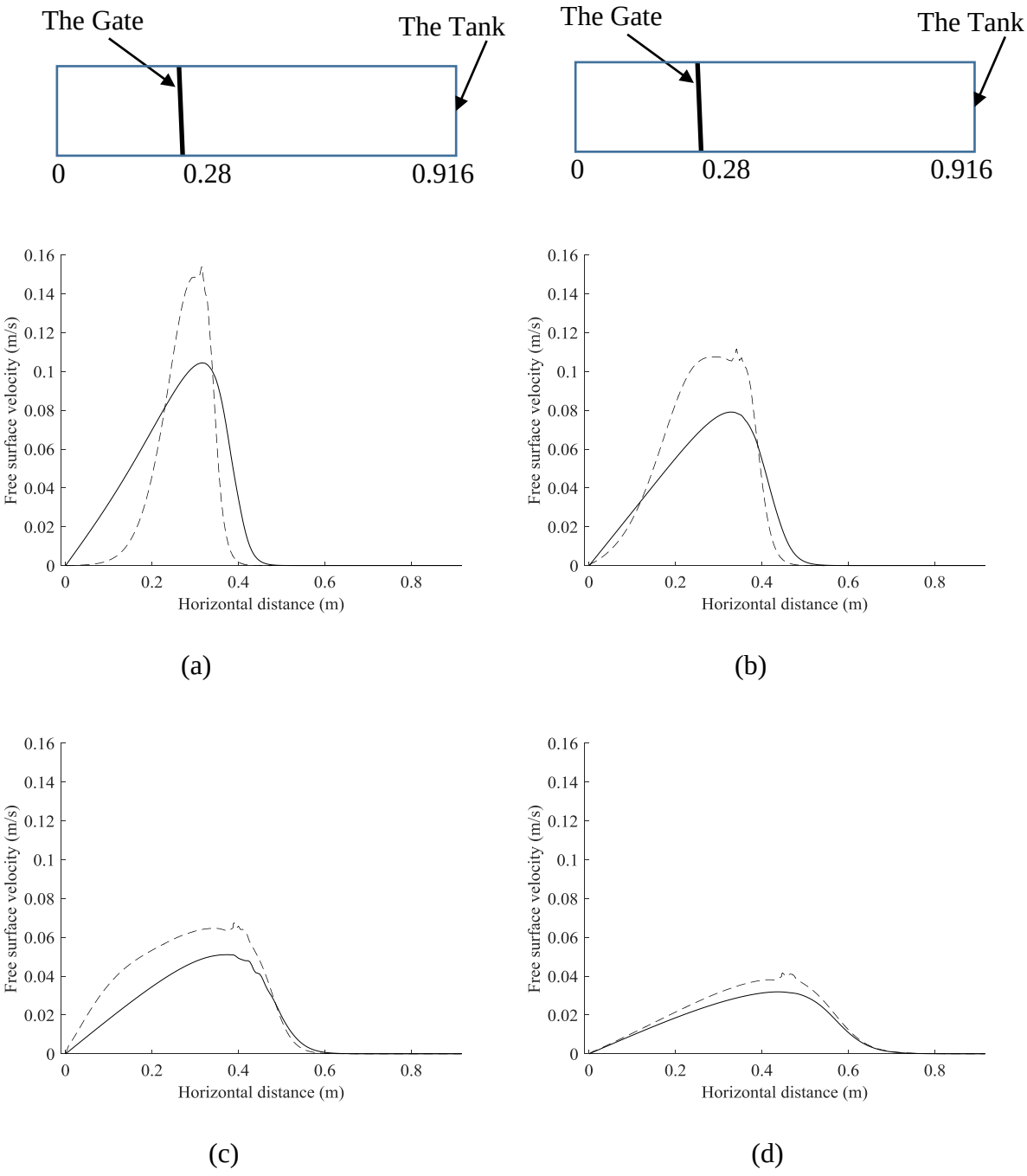

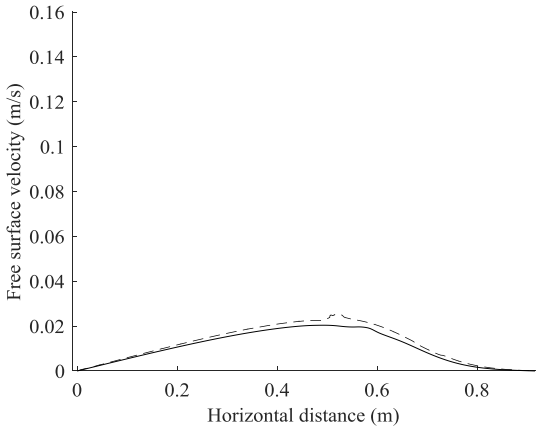

(e)

Figure 7.7: Free surface velocity as a function of horizontal distance for a Newtonian fluid (aqueous glycerol) for two models (lubrication approximation based on the current results (solid line) and Navier–Stokes based on the rheometer data (dashed line)) at five times: (a) 0.29 s, (b) 0.49 s, (c) 0.99 s, (d) 1.96 s, and (e) 3.56 s

From Figure 7.7 and equation (7.1), the error percentages are as shown in Table 7.2.

Time (s)	0.29	0.49	0.99	1.96	3.56
Relative error percentage (%)	8.53	8.32	11.35	6.35	5.98

Table 7.2: Relative error percentages for aqueous glycerol

Similar to Figure 7.4, a disturbance occurred before 0.99 s due to the influence of the initial condition.

It is clear that error values are low, which imply that the lubrication approximation is in good agreement within the 0.019 aspect ratio of the aqueous glycerol.

7.3 Comparison for non-Newtonian fluid (molasses)

In Section 7.2, two different Newtonian fluids were used to perform the comparison between the lubrication approximation and the Navier–Stokes equations. In this section, sugar cane molasses

(see Chapter 2, Figure 2.5) is used as a non-Newtonian fluid. The rheological parameters of the molasses based on Ellis model found using the rheometer were $\alpha = 1.6$, $\tau_{1/2}$=271 Pa, and μ_0=37.4 Pa·s as explained in Section 6.4.2. These parameters were used to calculate the computed velocity profiles for both the lubrication approximation and the Navier–Stokes equations. Consequently, the comparison between the computed and the experimental data based on the true values was implemented as shown in Figure 7.8.

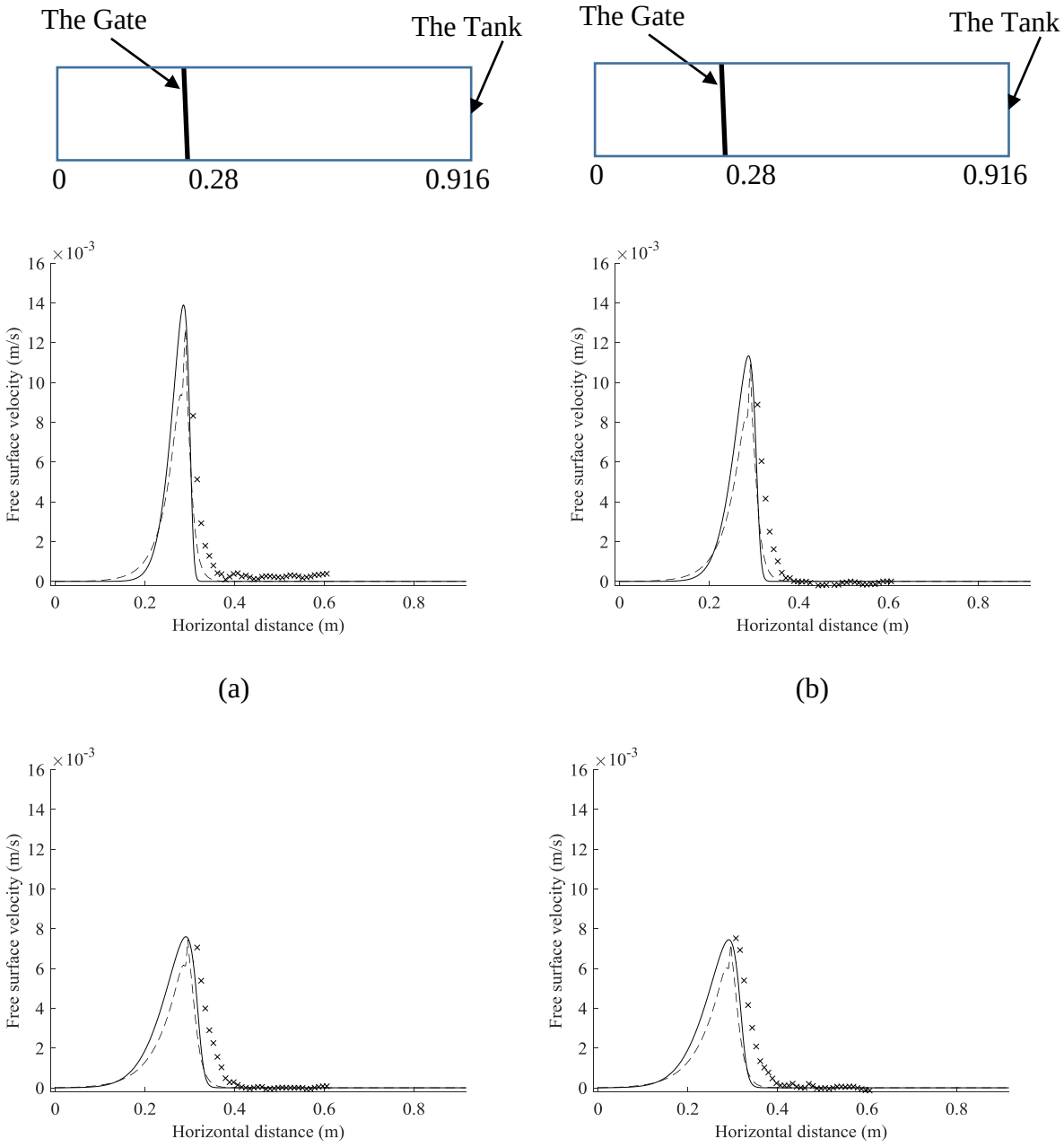

(c)

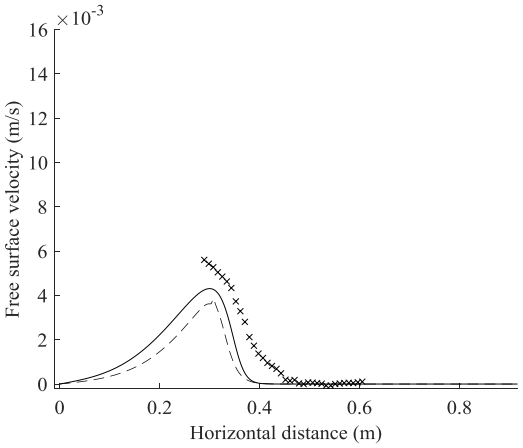

(d)

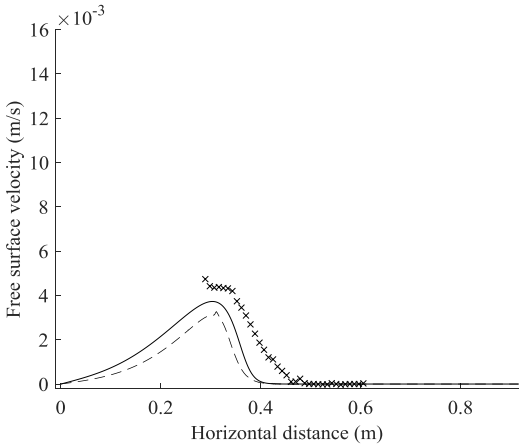

(e)

(f)

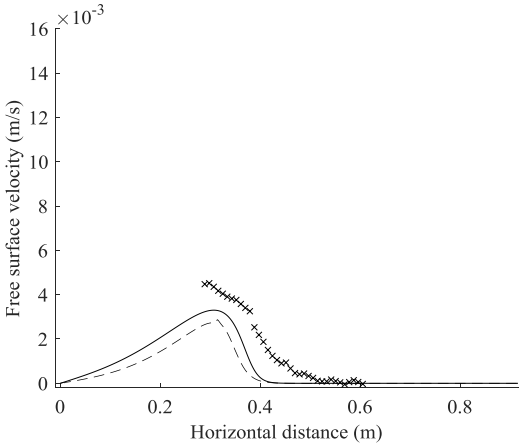

(g)

Figure 7.8: Comparison among the experimental data (crosses), the computed velocity based on the lubrication approximation equation (solid line), and the computed velocity based on the Navier–Stokes equation (dashed line) for a non-Newtonian fluid (molasses) at seven different times: (a) 0.4 s, (b) 0.6 s, (c) 1.33 s, (d) 1.4 s, (e) 4.13 s, (f) 5.4 s, and (g) 6.73 s

The experimental data used in Figure 7.8 were obtained from Chapter 5, Section 5.6 for molasses. In Figure 7.8, it is clear that the compatibility between the computed velocities is good. However, some differences between the experimental and the computed data occurred due to the

experimental error and the assumption made for the lubrication approximation based on the Ellis model.

The error percentages between the computed velocities based on the lubrication approximation and Navier–Stokes in terms of non-Newtonian fluids must be considered. The computed velocity based on the lubrication approximation was calculated by substituting the reconstructed Ellis rheological parameters (μ_0 = 34±1 Pa·s, α = 1.1±0.1, and $\tau_{1/2}$ = 290±5 Pa) into equation (6.7). The computed velocity based on Navier–Stokes was determined by substituting the true rheological parameters ($\alpha = 1.6$, $\tau_{1/2}$=271 Pa, and μ_0=37.4 Pa·s) into equation (6.7). The outcomes of this comparison is shown in Figure 7.9.

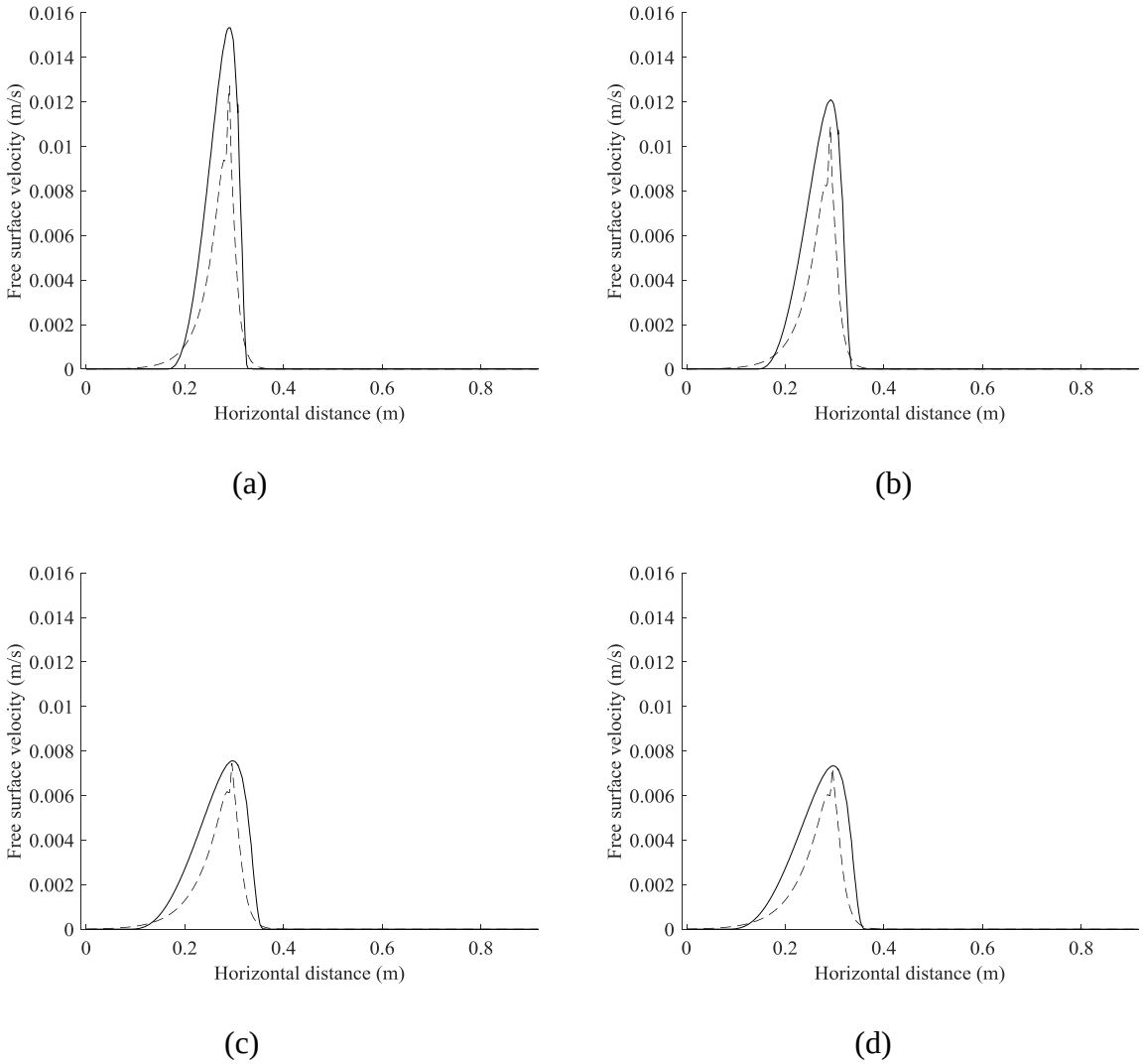

(a) (b)

(c) (d)

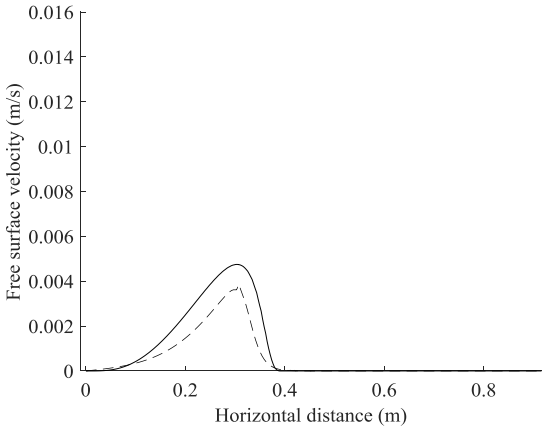

(e)

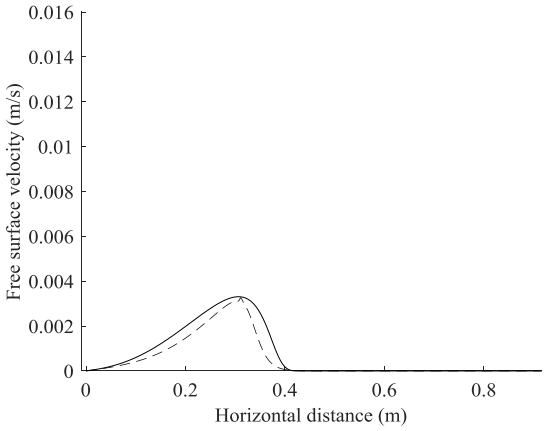

(f)

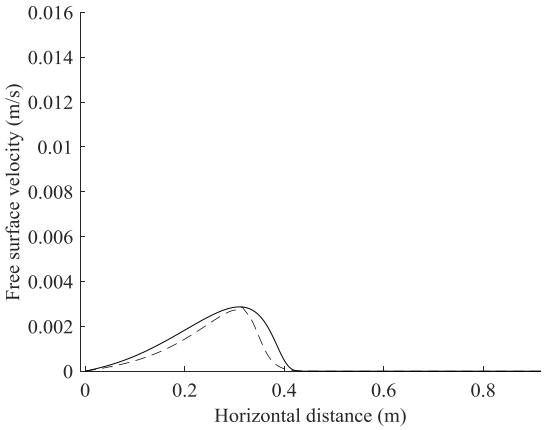

(g)

Figure 7.9: Free surface velocity as a function of horizontal distance for a non-Newtonian fluid (molasses) for two models (lubrication approximation based on the reconstructed results (solid line) and Navier–Stokes based on the rheometer data (dashed line)) at seven different times: (a) 0.4 s, (b) 0.6 s, (c) 1.33 s, (d) 1.4 s, (e) 4.13 s, (f) 5.4 s, and (g) 6.73 s

In Figure 7.9, the error percentages between the lubrication approximation and the Navier–Stokes were calculated according to equation (7.1) and are shown in Table 7.3.

Time (s)	0.4	0.6	1.33	1.4	4.13	5.4	6.73
Relative error percentage (%)	4.41	4.56	5.26	5.34	8.27	5.37	5.35

Table 7.3: Relative error percentages for molasses

Figure 7.10 illustrates the comparison between the lubrication approximation and the Navier–Stokes equations with three different aspect ratios. The numerical setup is the same as that indicated in Section 7.2.1.

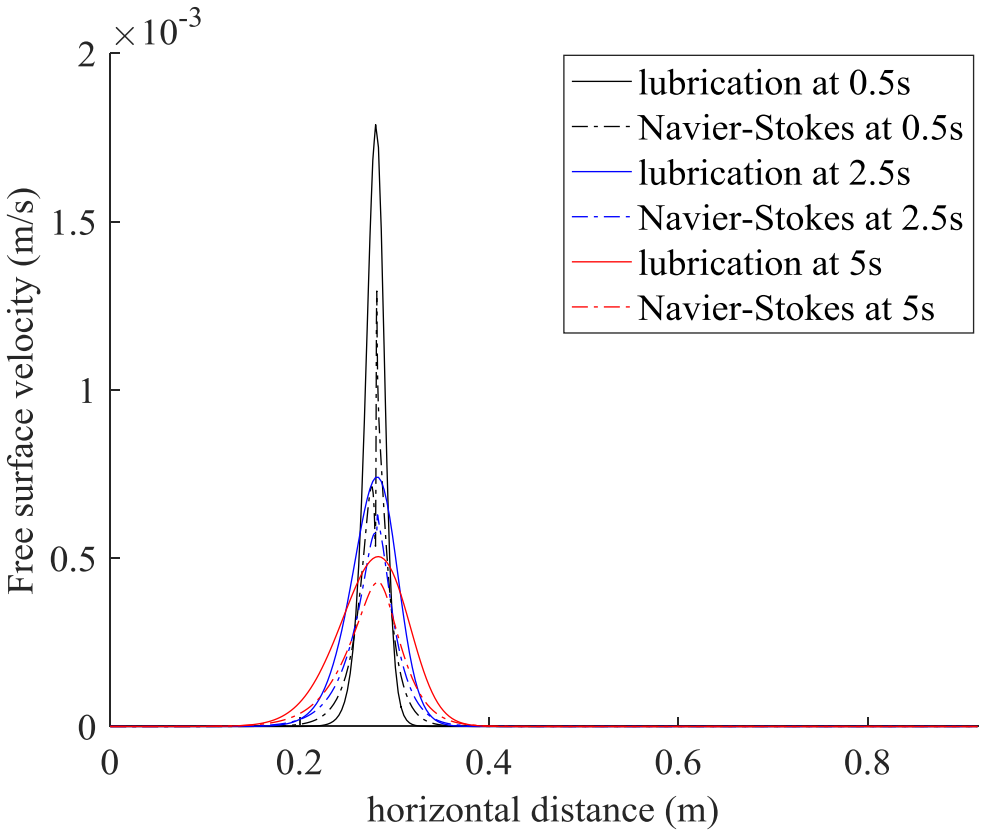

(a)

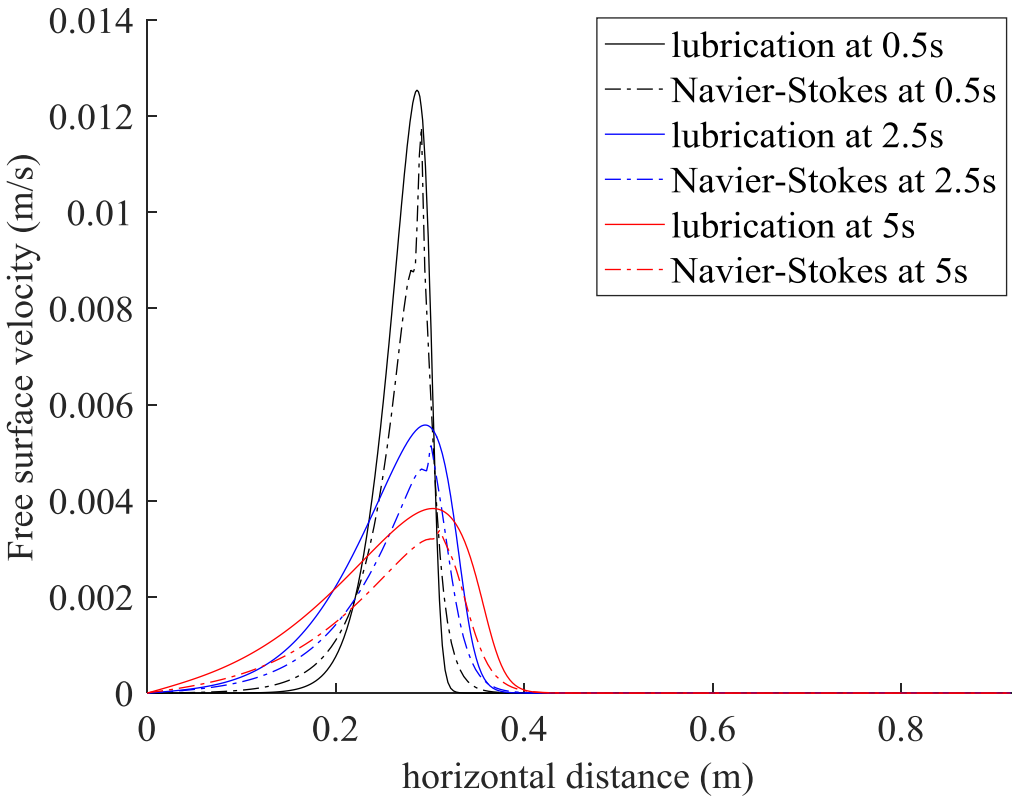
0.014
0.012
0.01
0.008
0.006
0.004
0.002
0
Free surface velocity (m/s)
0
0.2
0.4
0.6
0.8
horizontal distance (m)
lubrication at 0.5s
Navier-Stokes at 0.5s
lubrication at 2.5s
Navier-Stokes at 2.5s
lubrication at 5s
Navier-Stokes at 5s

(b)

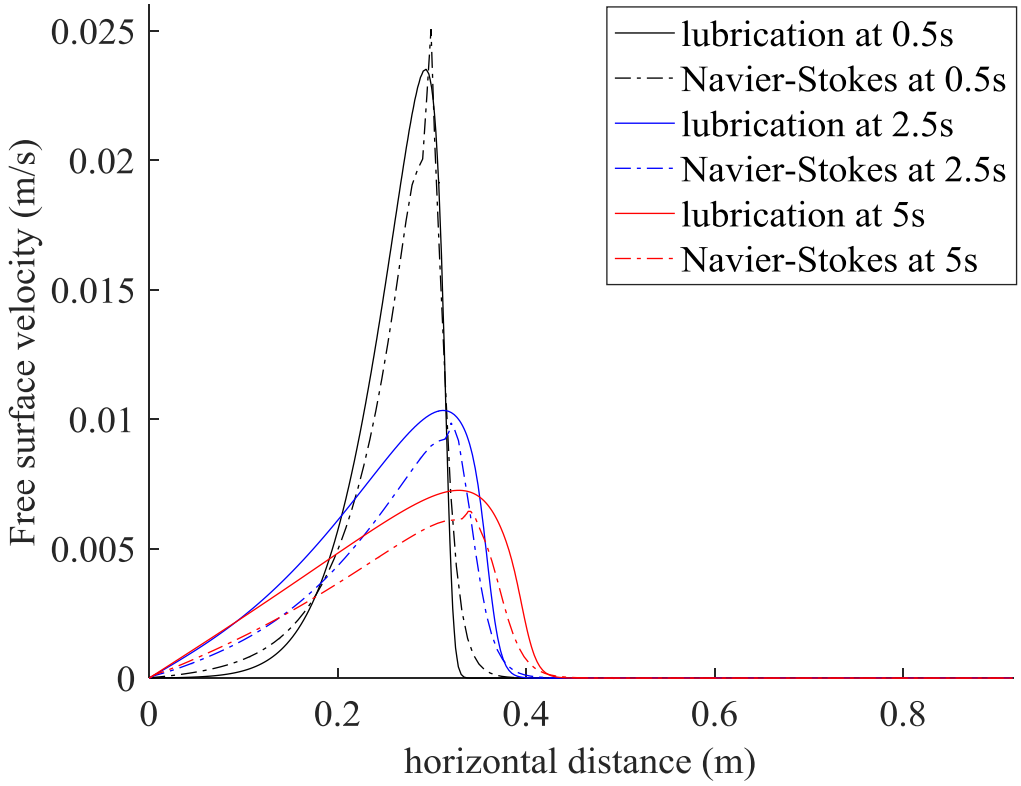

(c)

Figure 7.10: Free surface velocity as a function of horizontal distance of a non-Newtonian fluid (molasses) at three different aspect ratios (a) 0.01, (b) 0.015, and (c) 0.020

In Figure 7.10, it is clear that the agreement is good. However, a small difference between the two models occurred due to the inertia term being neglected in the lubrication approximation.

7.4 Comparison for non-Newtonian fluids with non-dimensionalisation of lubrication approximation and Navier–Stokes

7.4.1 Non-dimensionalisation of the Navier–Stokes equations (power law model)

In both Sections (7.2) and (7.3), the comparison between the lubrication approximation and the Navier–Stokes were carried out with specific Newtonian and non-Newtonian fluids. In this section the dimensionless mathematical technique is implemented to generalize the comparison process.

The height and length scale of the problem are defined as $H_0 = \frac{H_1+H_g}{2}$ and $L_0 = L_1 + L_g$ as shown in the following diagram of the dam-break geometry, and the aspect ratio is $\varepsilon = \frac{H_0}{L_0}$.

Figure 7.11: Sketch of the dam-break problem

The two-dimensional Navier–Stokes equations for an incompressible non-Newtonian fluid can be defined as

$$\rho\left(\frac{\partial u}{\partial t} + u\frac{\partial u}{\partial x} + w\frac{\partial u}{\partial z}\right) = -\frac{\partial p}{\partial x} + \frac{\partial}{\partial x}\left(\mu\frac{\partial u}{\partial x}\right) + \frac{\partial}{\partial z}\left(\mu\frac{\partial u}{\partial z}\right), \tag{7.2}$$

$$\rho\left(\frac{\partial w}{\partial t} + u\frac{\partial w}{\partial x} + w\frac{\partial w}{\partial z}\right) = -\frac{\partial p}{\partial z} + \frac{\partial}{\partial x}\left(\mu\frac{\partial w}{\partial x}\right) + \frac{\partial}{\partial z}\left(\mu\frac{\partial w}{\partial z}\right) + \rho g\,, \tag{7.3}$$

$$\frac{\partial u}{\partial x} + \frac{\partial w}{\partial z} = 0. \tag{7.4}$$

The Navier–Stokes equations must be expressed in terms of dimensionless variables White (2011). Therefore, we need to substitute the dimensionless scale variables in the Navier–Stokes equations, which are given by

$$\tilde{u} = \frac{u}{U_0}, \tilde{w} = \frac{w}{U_0}, \tilde{x} = \frac{x}{L_0}, \tilde{z} = \frac{z}{L_0}, \tilde{t} = \frac{t}{T_0} = \frac{t}{L_0/U_0}, \quad \tilde{p} = \frac{p}{P_0}\,, \tilde{\mu} = \frac{\mu}{\mu_0}\,.$$

After substituting the dimensionless scale variables above into equation (7.2), we obtain

$$\rho\left(\frac{U_0^2}{L_0}\frac{\partial\tilde{u}}{\partial\tilde{t}}+\frac{U_0^2}{L_0}\tilde{u}\frac{\partial\tilde{u}}{\partial\tilde{x}}+\frac{U_0^2}{L_0}\tilde{w}\frac{\partial\tilde{u}}{\partial\tilde{z}}\right)=-\frac{P_0}{L_0}\frac{\partial\tilde{p}}{\partial\tilde{x}}+\frac{U_0}{L_0^2}\frac{\partial}{\partial\tilde{x}}\left(\mu_0\,\tilde{\mu}\frac{\partial\tilde{u}}{\partial\tilde{x}}\right)+\frac{U_0}{L_0^2}\frac{\partial}{\partial\tilde{z}}\left(\mu_0\,\tilde{\mu}\frac{\partial\tilde{u}}{\partial\tilde{z}}\right), \quad (7.5)$$

$$\rho\,\frac{U_0^2}{L_0}\left(\frac{\partial\tilde{u}}{\partial\tilde{t}}+\tilde{u}\frac{\partial\tilde{u}}{\partial\tilde{x}}+\tilde{w}\frac{\partial\tilde{u}}{\partial\tilde{z}}\right)=-\frac{P_0}{L_0}\frac{\partial\tilde{p}}{\partial\tilde{x}}+\frac{U_0\,\mu_0}{L_0^2}\frac{\partial}{\partial\tilde{x}}\left(\tilde{\mu}\frac{\partial\tilde{u}}{\partial\tilde{x}}\right)+\frac{U_0\,\mu_0}{L_0^2}\frac{\partial}{\partial\tilde{z}}\left(\tilde{\mu}\frac{\partial\tilde{u}}{\partial\tilde{z}}\right).$$

Multiplying through by $\frac{L_0}{\rho U_0^2}$, we obtain

$$\left(\frac{\partial\tilde{u}}{\partial\tilde{t}}+\tilde{u}\frac{\partial\tilde{u}}{\partial\tilde{x}}+\tilde{w}\frac{\partial\tilde{u}}{\partial\tilde{z}}\right)=-\frac{P_0}{\rho U_0^2}\frac{\partial\tilde{p}}{\partial\tilde{x}}+\frac{\mu_0}{\rho L_0 U_0}\frac{\partial}{\partial\tilde{x}}\left(\tilde{\mu}\frac{\partial\tilde{u}}{\partial\tilde{x}}\right)+\frac{\mu_0}{\rho L_0 U_0}\frac{\partial}{\partial\tilde{z}}\left(\tilde{\mu}\frac{\partial\tilde{u}}{\partial\tilde{z}}\right).$$

We defined the pressure scale $P_0=\rho U_0^2$ and Reynolds number $Re=\frac{L_0U_0\rho}{\mu_0}$ to obtain the dimensionless Navier–Stokes x-momentum equation, given by

$$\left(\frac{\partial\tilde{u}}{\partial\tilde{t}}+\tilde{u}\frac{\partial\tilde{u}}{\partial\tilde{x}}+\tilde{w}\frac{\partial\tilde{u}}{\partial\tilde{z}}\right)=-\frac{\partial\tilde{p}}{\partial\tilde{x}}+\frac{1}{Re}\frac{\partial}{\partial\tilde{x}}\left(\tilde{\mu}\frac{\partial\tilde{u}}{\partial\tilde{x}}\right)+\frac{1}{Re}\frac{\partial}{\partial\tilde{z}}\left(\tilde{\mu}\frac{\partial\tilde{u}}{\partial\tilde{z}}\right).$$

In terms of the z-momentum, the same procedure is applied and equation (7.3) can be written as,

$$\left(\frac{\partial\tilde{w}}{\partial\tilde{t}}+\tilde{u}\frac{\partial\tilde{w}}{\partial\tilde{x}}+\tilde{w}\frac{\partial\tilde{w}}{\partial\tilde{z}}\right)=-\frac{\partial\tilde{p}}{\partial\tilde{z}}+\frac{1}{Re}\frac{\partial}{\partial\tilde{x}}\left(\tilde{\mu}\frac{\partial\tilde{w}}{\partial\tilde{x}}\right)+\frac{1}{Re}\frac{\partial}{\partial\tilde{z}}\left(\tilde{\mu}\frac{\partial\tilde{w}}{\partial\tilde{z}}\right)+\frac{1}{Fr^2}. \quad (7.6)$$

Finally, when substituting the dimensionless variables into equation (7.4), the following Navier–Stokes continuity expression can be obtained:

$$\frac{\partial \tilde{u}}{\partial \tilde{x}} + \frac{\partial \tilde{w}}{\partial \tilde{z}} = 0. \tag{7.7}$$

7.4.2 Non-dimensionalisation of the lubrication approximation (power law)

The lubrication approximation equations obtained in Chapter 3 are

$$\frac{\partial h}{\partial t} + \frac{n}{2n+1}\left(\frac{1}{k}\right)^{\frac{1}{n}} \frac{\partial}{\partial x}\left[\left|\frac{\partial p}{\partial x}\right|^{\frac{1-n}{n}} \frac{\partial p}{\partial x}\, h^{\frac{2n+1}{n}}\right] = 0, \tag{7.8}$$

$$p = \rho g\, h - \sigma\, \frac{\partial^2 h}{\partial x^2}. \tag{7.9}$$

When substituting the following dimensionless scale variables in the above-mentioned lubrication approximation equations, we can obtain the dimensionless form of the lubrication approximation.

$$\tilde{h} = \frac{h}{H_0} \quad \tilde{x} = \frac{x}{L_0} \quad \tilde{t} = \frac{t}{T_0} \quad \tilde{p} = \frac{p}{P_0}\ .$$

Substituting the dimensionless variables in equation (7.9),

$$P_0 \tilde{p} = -\sigma \frac{H_0}{L_0^2} \frac{\partial^2 \tilde{h}}{\partial \tilde{x}^2} + \rho g H_0 \tilde{h}. \tag{7.10}$$

Dividing throughout by P_0,

$$\tilde{p} = -\sigma \frac{H_0}{P_0 L_0^2} \frac{\partial^2 \tilde{h}}{\partial \tilde{x}^2} + \frac{\rho g H_0}{P_0} \tilde{h}.$$

Multiplying through by $\frac{H_0}{\sigma}$ and defining the pressure scale $P_0 = \frac{\sigma H_0}{L_0^2}$ with the Bond number $Bo = \frac{\rho g {L_0}^2}{\sigma}$ gives

$$\tilde{p} = -\frac{\partial^2 \tilde{h}}{\partial \tilde{x}^2} + Bo \cdot \tilde{h}. \tag{7.11}$$

Then, the dimensionless variables can be substituted into equation (7.8) to obtain the following mathematical expression:

$$\frac{H_0 \partial \tilde{h}}{T_0 \partial \tilde{t}} + \frac{P_0}{L_0^2} H_0^{\frac{2n+1}{n}} \left|\frac{P_0}{L_0}\right|^{\frac{1-n}{n}} \frac{n}{2n+1} \left(\frac{1}{k}\right)^{\frac{1}{n}} \frac{\partial}{\partial \tilde{x}} \left[\left|\frac{\partial \tilde{p}}{\partial \tilde{x}}\right|^{\frac{1-n}{n}} \frac{\partial \tilde{p}}{\partial \tilde{x}} \tilde{h}^{\frac{2n+1}{n}} \right] = 0. \tag{7.12}$$

The term $\left|\frac{P_0}{L_0}\right|$ is always positive because P_0 is positive and L_0 is positive. Therefore,

$$\frac{H_0 \partial \tilde{h}}{T_0 \partial \tilde{t}} + \frac{P_0^{\frac{1}{n}}}{L_0^{\frac{n+1}{n}}} H_0^{\frac{2n+1}{n}} \frac{n}{2n+1} \left(\frac{1}{k}\right)^{\frac{1}{n}} \frac{\partial}{\partial \tilde{x}} \left[\left|\frac{\partial \tilde{p}}{\partial \tilde{x}}\right|^{\frac{1-n}{n}} \frac{\partial \tilde{p}}{\partial \tilde{x}} \tilde{h}^{\frac{2n+1}{n}} \right] = 0\,. \tag{7.13}$$

Multiplying through by $\frac{T_0}{H_0}$,

$$\frac{\partial \tilde{h}}{\partial \tilde{t}} + \frac{T_0 P_0^{\frac{1}{n}}}{L_0^{\frac{n+1}{n}}} H_0^{\frac{n+1}{n}} \frac{n}{2n+1} \left(\frac{1}{k}\right)^{\frac{1}{n}} \frac{\partial}{\partial \tilde{x}} \left[\left|\frac{\partial \tilde{p}}{\partial \tilde{x}}\right|^{\frac{1-n}{n}} \frac{\partial \tilde{p}}{\partial \tilde{x}} \tilde{h}^{\frac{2n+1}{n}} \right] = 0. \tag{7.14}$$

After substituting $P_0 = \frac{\sigma H_0}{L_0^2}$ into equation (7.14), the following expression is obtained:

$$\frac{\partial \tilde{h}}{\partial \tilde{t}} + \frac{n}{2n+1} T_0 \left(\frac{\sigma {H_0}^{n+2}}{k\, {L_0}^{n+3}} \right)^{\frac{1}{n}} \frac{\partial}{\partial \tilde{x}} \left[\left| \frac{\partial \tilde{p}}{\partial \tilde{x}} \right|^{\frac{1-n}{n}} \frac{\partial \tilde{p}}{\partial \tilde{x}}\, \tilde{h}^{\frac{2n+1}{n}} \right] = 0.$$

By defining $T_0 = \frac{2n+1}{n} \left(\frac{k\, {L_0}^{n+3}}{\sigma {H_0}^{n+2}} \right)^{\frac{1}{n}}$,

$$\frac{\partial \tilde{h}}{\partial \tilde{t}} + \frac{\partial}{\partial \tilde{x}} \left[\left| \frac{\partial \tilde{p}}{\partial \tilde{x}} \right|^{\frac{1-n}{n}} \frac{\partial \tilde{p}}{\partial \tilde{x}}\, \tilde{h}^{\frac{2n+1}{n}} \right] = 0. \qquad (7.15)$$

Both equations (7.11) and (7.15) represent the dimensionless lubrication approximation based on the power-law model. Two parameters are needed to describe the lubrication approximation, namely the Bond number (Bo) and the flow behaviour index (n).

The dimensionless lubrication approximation equations and the dimensionless Navier–Stokes equations can be compared using the Reynolds number, Bond number, and Froude number. The Reynolds number represents the ratio of the fluid inertia to viscous forces; the Bond number represents the ratio of the fluid gravity force to the surface tension force; and the Froude number is defined as the ratio of inertia to gravity.

$$\mathrm{Fr} = \frac{\mathrm{U_0}}{\sqrt{\mathrm{g} L_0}}, Bo = \frac{\rho \mathrm{g}\, L_0^2}{\sigma}, \quad \mathrm{Ca} = \frac{\mu_0 \mathrm{U_0}}{\sigma} \text{ and } Re = \frac{L_0 U_0 \rho}{\mu_0}.$$

Thus, $\mathrm{Ca} = \frac{Bo \mathrm{Fr}^2}{Re}$.

To set the velocity scale, we set $\mathrm{Ca} = 1$. Therefore, the velocity is given by

$\mathrm{U_0} = \frac{\sigma}{\mu_0}$ with $\mathrm{U_0} = \frac{L_0}{T_0}$.

Therefore,

$$T_0 = \frac{\mu_0 L_0}{\sigma}. \tag{7.16}$$

When substituting the dimensionless scale variables into the power-law model and using the simplified form of the shear rate (see equation 3.7), the following expression can be obtained:

$$\mu_0 \, \tilde{\mu} = \frac{k}{{T_0}^{n-1}} \left|\frac{\partial \tilde{u}}{\partial \tilde{z}}\right|^{n-1}, \tag{7.17}$$

which leads to $\mu_0 = \frac{k}{{T_0}^{n-1}}$ .Substituting equation (7.16) into (7.17) yields $T_0 = \frac{k\, L_0}{{T_0}^{n-1}\sigma}$; thus $T_0 = \left(\frac{k\, L_0}{\sigma}\right)^{\frac{1}{n}}$ in terms of the Navier–Stokes (${T_0}^{NS}$) and $T_0 = \frac{2n+1}{n}\left(\frac{k\, {L_0}^{n+3}}{\sigma {H_0}^{n+2}}\right)^{\frac{1}{n}}$ in terms of the lubrication approximation (${T_0}^{LA}$). After substituting ${T_0}^{NS}$ into ${T_0}^{LA}$, ${T_0}^{LA}$ is defined by

$${T_0}^{LA} = \frac{2n+1}{n}\frac{{T_0}^{NS}}{\varepsilon^{\frac{n+2}{n}}}. \tag{7.18}$$

The Reynolds, Froude, and Bond numbers can be obtained using the molasses data $\rho = 1450$ kg/m^3, $\sigma = 0.05$ N/m, $n = 0.7$,$k = 28$ Pa·s^n, and $L_0 = 0.916$ m. The values obtained are $Re = 4 \times 10^{-4}$,Fr $= 4.10 \times 10^{-5}$,and $Bo = 2.4 \times 10^{5}$.

The two dimensionless models obtained can be compared. In terms of the dimensionless lubrication approximation (equations 7.11 and 7.15), a COMSOL solver was used to obtain the dimensionless film thickness profile $\tilde{h}$ with the same numerical setup as mentioned in Section 7.2.1. However, the number of mesh quadratic elements was 334 in terms of the lubrication solver and 2891 triangular elements in terms of the Navier–Stokes solver. The outcomes from the comparison process above are shown in Figure 7.12.

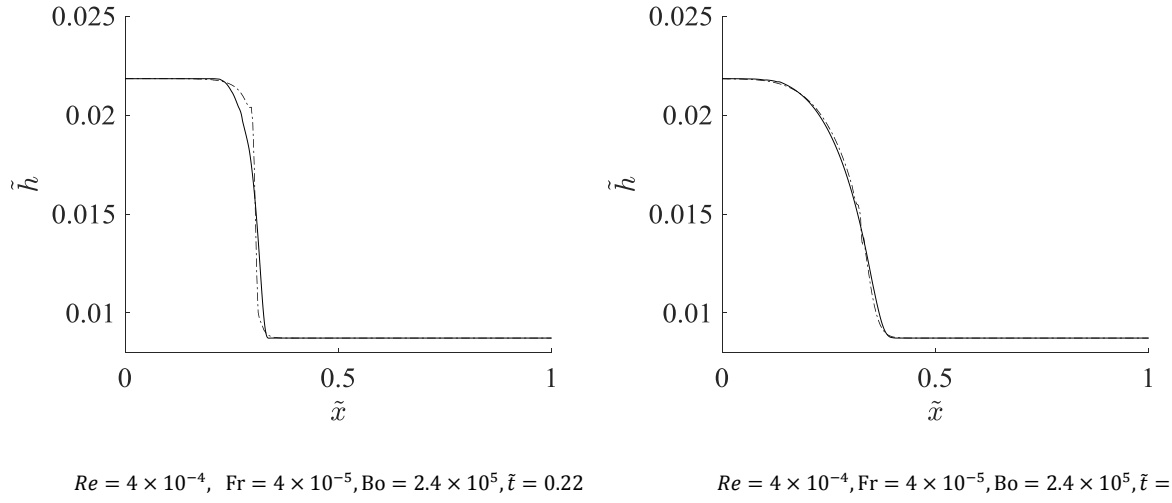

$Re = 4 \times 10^{-4}$, $\mathrm{Fr} = 4 \times 10^{-5}, \mathrm{Bo} = 2.4 \times 10^{5}, \tilde{t} = 0.22$

$Re = 4 \times 10^{-4}, \mathrm{Fr} = 4 \times 10^{-5}, \mathrm{Bo} = 2.4 \times 10^{5}, \tilde{t} = 4.16$

$Re = 4 \times 10^{-4}, \mathrm{Fr} = 4 \times 10^{-5}, \mathrm{Bo} = 2.4 \times 10^{5}, \tilde{t} = 7.44$

$Re = 4 \times 10^{-4}, \mathrm{Fr} = 4 \times 10^{-5}, \mathrm{Bo} = 2.4 \times 10^{5}, \tilde{t} = 743$

Figure 7.12: Dimensionless film thickness as a function of dimensionless horizontal distance in terms of the power-law model at four different dimensionless times. Dashed line represents dimensionless Navier–Stokes solution (NS) and solid line represents dimensionless lubrication approximation (LA), with $\tilde{x}_{NS} = \tilde{x}_{LA}$, $\tilde{h}_{NS} = \varepsilon \tilde{h}_{LA}$, and $\frac{n}{2n+1} \varepsilon^{\frac{n+2}{n}} \tilde{t}_{NS} = \tilde{t}_{LA}$

Figure 7.12 shows a good agreement between the two models. However, at early dimensionless time, a small difference occurred between the two models due to the difference in the initial conditions.

It is important to understand the influence of the dimensionless numbers on the models used. Consequently, four different Reynolds numbers were used to perform the comparison process between the dimensionless lubrication approximation and the Navier–Stokes, namely 0.01, 0.1, 1 and 10 at four dimensionless times 27.5×10^3, 55×10^3, 55×10^4, and 11×10^6 , respectively.

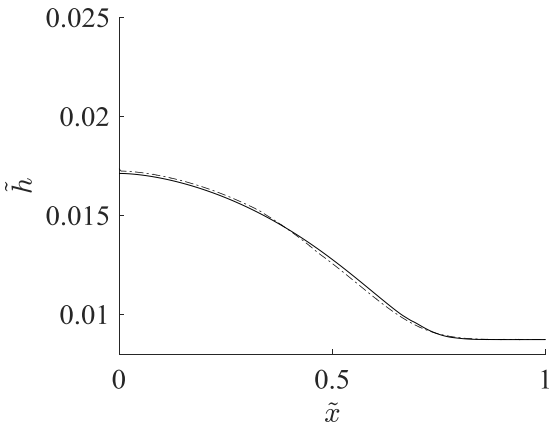

$Re = 10^{-2}, \mathrm{Fr} = 10^{-3}, \tilde{t} = 27.5 \times 10^3$

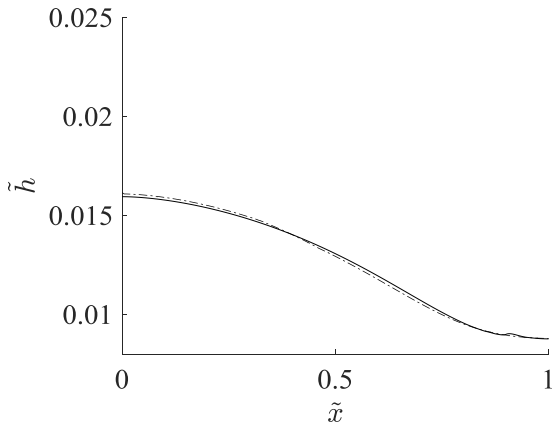

$Re = 10^{-2}, \mathrm{Fr} = 10^{-3}, \tilde{t} = 55 \times 10^3$

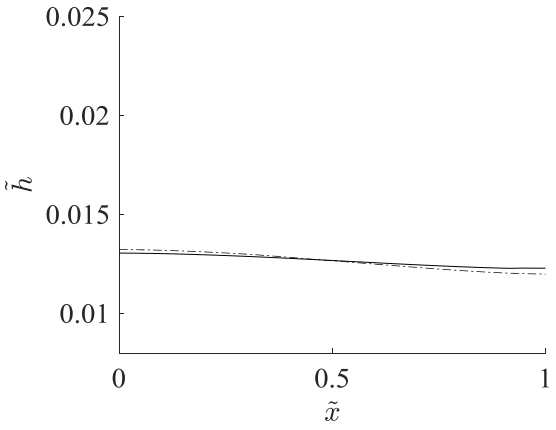

$Re = 10^{-2}, \mathrm{Fr} = 10^{-3}, \tilde{t} = 55 \times 10^4$

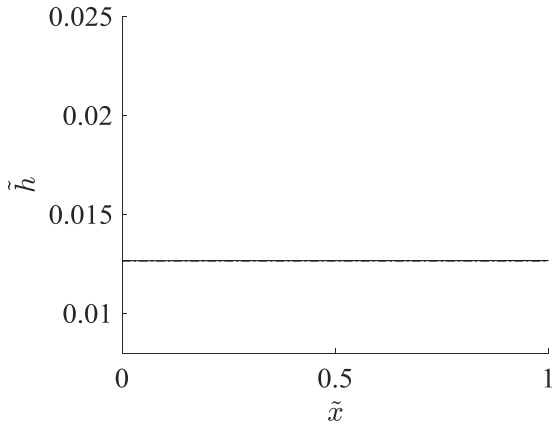

$Re = 10^{-2}, \mathrm{Fr} = 10^{-3}, \tilde{t} = 11 \times 10^6$

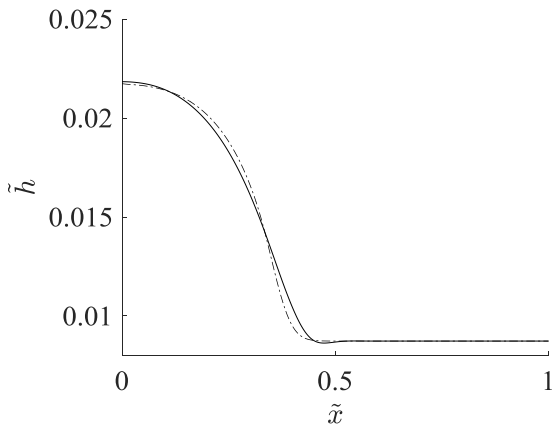

$Re = 0.1, \mathrm{Fr} = 10^{-2}, \tilde{t} = 27.5 \times 10^3$

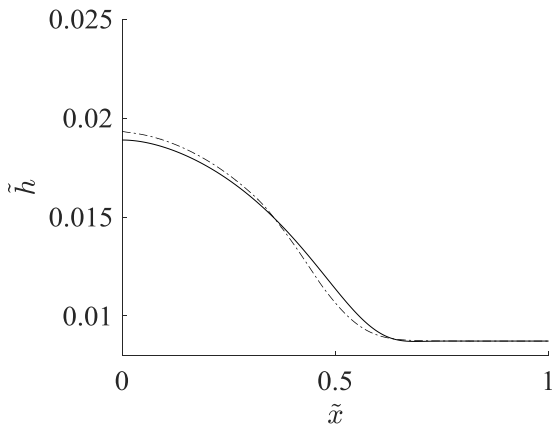

$Re = 0.1, \mathrm{Fr} = 10^{-2}, \tilde{t} = 55 \times 10^3$

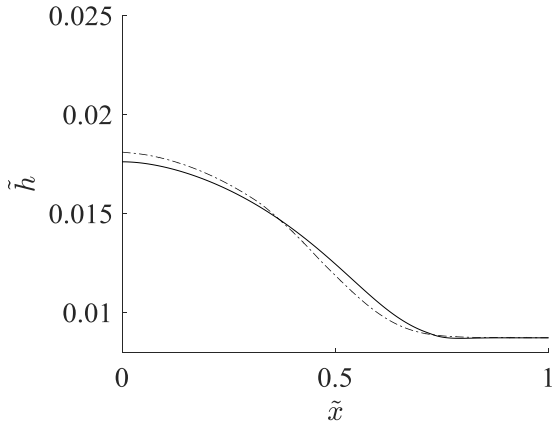

$Re = 0.1, \mathrm{Fr} = 10^{-2}, \tilde{t} = 55 \times 10^4$

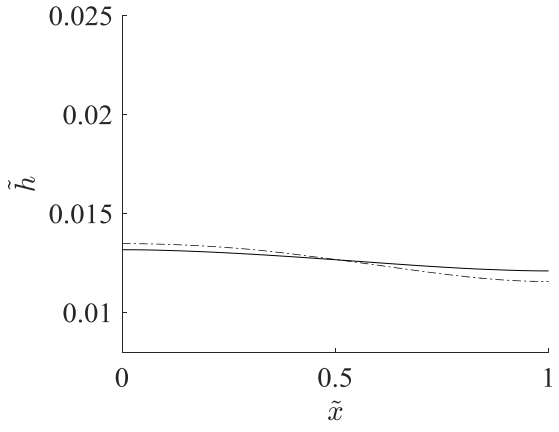

$Re = 0.1, \mathrm{Fr} = 10^{-2}, \tilde{t} = 11 \times 10^6$

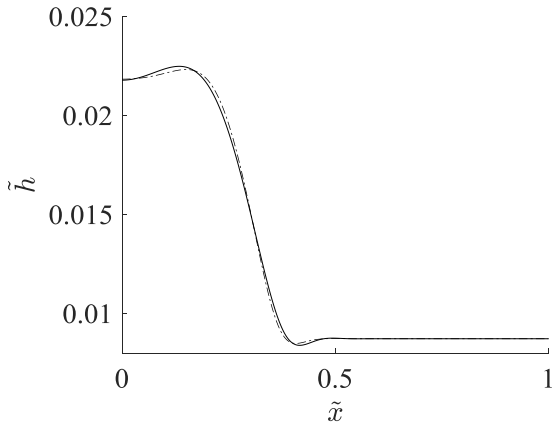

$Re = 1, \mathrm{Fr} = 0.1, \tilde{t} = 27.5 \times 10^3$

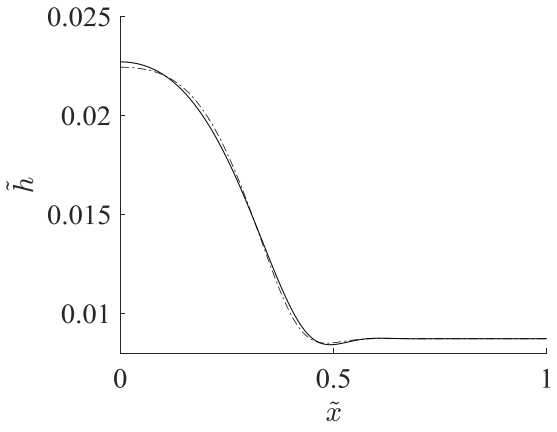

$Re = 1, \mathrm{Fr} = 0.1, \tilde{t} = 55 \times 10^3$

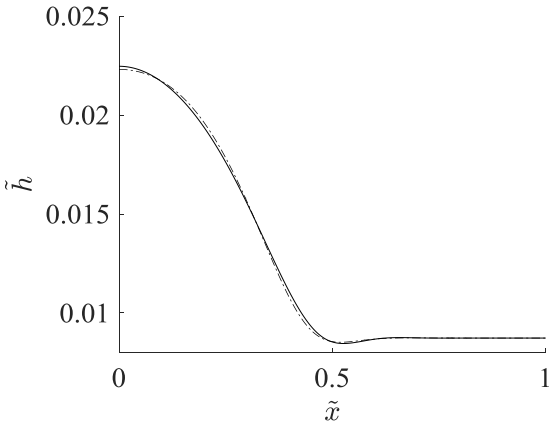

$Re = 1, \mathrm{Fr} = 0.1, \tilde{t} = 55 \times 10^4$

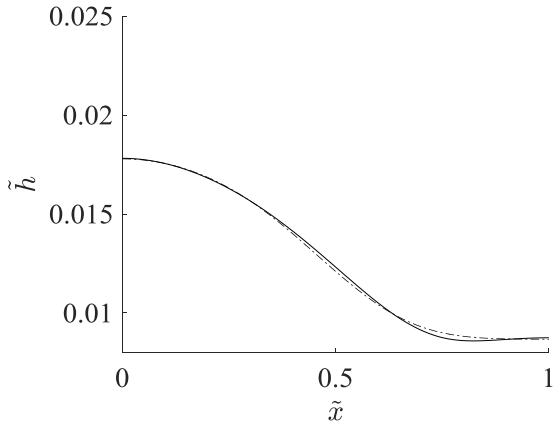

$Re = 1, \mathrm{Fr} = 0.1, \tilde{t} = 11 \times 10^6$

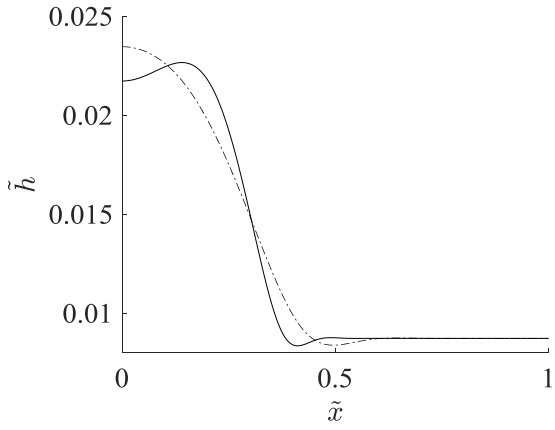

$Re = 10, \mathrm{Fr} = 1.01, \tilde{t} = 27.5 \times 10^3$

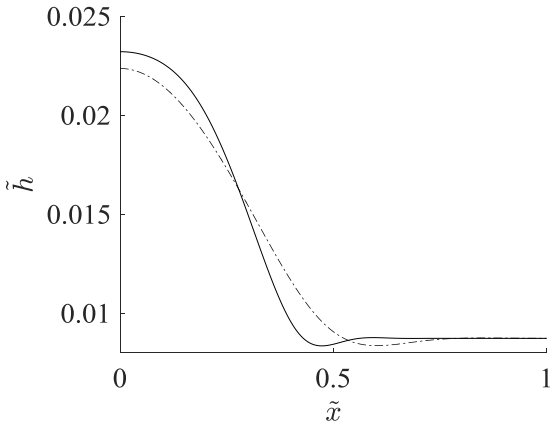

$Re = 10, \mathrm{Fr} = 1.01, \tilde{t} = 55 \times 10^3$

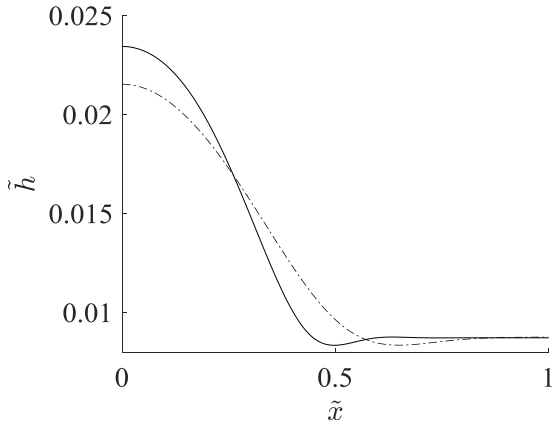

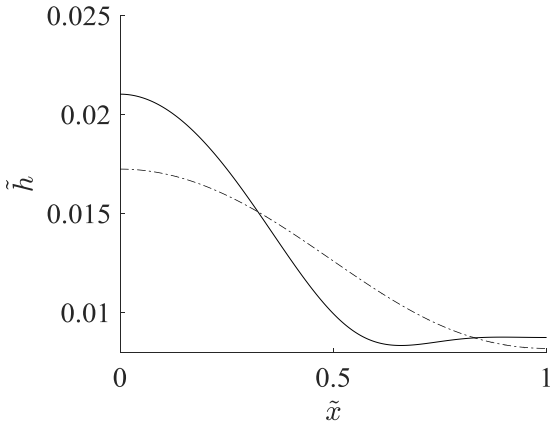

$Re = 10, \mathrm{Fr} = 1.01, \tilde{t} = 55 \times 10^4$ $Re = 10, \mathrm{Fr} = 1.01, \tilde{t} = 11 \times 10^6$

Figure 7.13: Dimensionless film thickness as a function of dimensionless horizontal distance in terms of the Ellis model at four different dimensionless times with four different Reynolds numbers. Dashed line represents dimensionless Navier–Stokes solution (NS) and solid line represents dimensionless lubrication approximation (LA), with $\tilde{x}_{NS} = \tilde{x}_{LA}$, $\tilde{h}_{NS} = \varepsilon \tilde{h}_{LA}$, and $\frac{n}{2n+1} \varepsilon^{\frac{n+2}{n}} \tilde{t}_{NS} = \tilde{t}_{LA}$

Figure 7.13 illustrates the relationship between the dimensionless film thickness with the dimensionless horizontal distance for both the dimensionless lubrication approximation and the dimensionless Navier–Stokes at four different dimensionless times. It is evident that the agreement is poor when the Reynolds number is 10. This implies that more accurate results are obtained at low Reynolds numbers as shown in Figure 7.14.

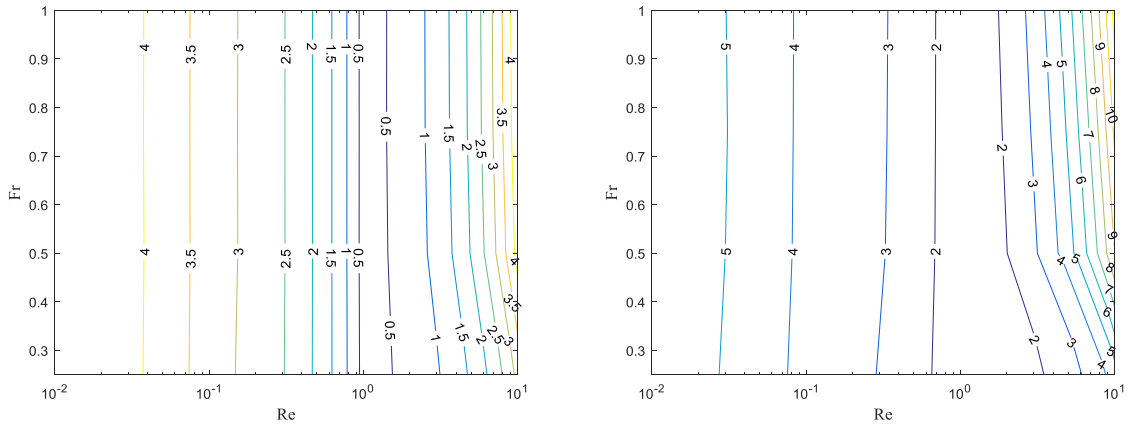

(a) (b)

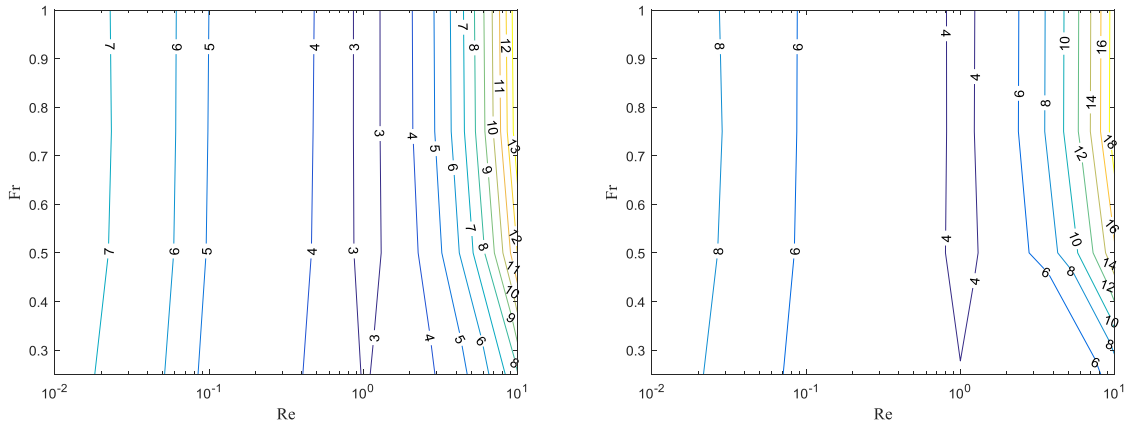

(c) (d)

Figure 7.14: Contours showing the relative error percentages of dimensionless lubrication approximation compared with dimensionless Navier–Stokes at four different dimensionless times: (a) $\tilde{t} = 27500$, (b) $\tilde{t} = 55 \times 10^3$, (c) $\tilde{t} = 55 \times 10^4$, and (d) $\tilde{t} = 11 \times 10^6$ using the power-law model

Figure 7.14 shows the relative error percentage between the dimensionless lubrication approximation and the dimensionless Navier–Stokes equations using the power-law model. The minimum errors occurred around Reynolds number 1.

7.4.3 Non-dimensionalisation of the lubrication approximation (Ellis model)

The dimensionless scale variables mentioned in Section 7.3.2 can be substituted in equation (6.9). Consequently, the dimensionless form of the lubrication approximation based on the Ellis model can be written as

$$\frac{H_0 \partial \tilde{h}}{T_0 \partial \tilde{t}} + \frac{1}{L_0}\frac{\partial}{\partial \tilde{x}}\left[\frac{P_0}{L_0}\frac{-\frac{\partial \tilde{p}}{\partial \tilde{x}}}{\mu_0}\left({H_0}^3\frac{\tilde{h}^3}{3} + {H_0}^{\alpha+2}\frac{\tilde{h}^{\alpha+2}}{\alpha+2}\left(\frac{P_0}{L_0}\frac{\left|\frac{\partial \tilde{p}}{\partial \tilde{x}}\right|}{\tau_{1/2}}\right)^{\alpha-1}\right)\right] = 0. \qquad (7.19)$$

Multiplying through by $\frac{T_0}{H_0}$ yields

$$\frac{\partial \tilde{h}}{\partial \tilde{t}} + \frac{\partial}{\partial \tilde{x}}\left[\frac{-\frac{\partial \tilde{p}}{\partial \tilde{x}}}{\mu_0}\left(\frac{P_0 T_0 {H_0}^2}{{L_0}^2}\frac{\tilde{h}^3}{3} + \frac{P_0 T_0 {P_0}^{\alpha-1} {H_0}^{\alpha+2}}{{L_0}^2 H_0\, {L_0}^{\alpha-1}}\frac{\tilde{h}^{\alpha+2}}{\alpha+2}\left(\frac{\left|\frac{\partial \tilde{p}}{\partial \tilde{x}}\right|}{\tau_{1/2}}\right)^{\alpha-1}\right)\right] = 0\,. \tag{7.20}$$

By defining the pressure scale $P_0 = \frac{\sigma H_0}{L_0^2}$,

$$\frac{\partial \tilde{h}}{\partial \tilde{t}} + \frac{\partial}{\partial \tilde{x}}\left[-\frac{\partial \tilde{p}}{\partial \tilde{x}}\left(\frac{\tilde{h}^3 \sigma\, T_0 {H_0}^3}{3\mu_0 {L_0}^4} + \frac{\tilde{h}^{\alpha+2}\, \sigma^{\alpha} T_0 {H_0}^{2\alpha+1}}{\mu_0\, (\alpha+2) {L_0}^{3\alpha+1}}\left(\frac{\left|\frac{\partial \tilde{p}}{\partial \tilde{x}}\right|}{\tau_{1/2}}\right)^{\alpha-1}\right)\right] = 0. \tag{7.21}$$

After substituting $T_0 = \frac{3\mu_0 {L_0}^4}{\sigma {H_0}^3}$, equation (7.21) can be written as

$$\frac{\partial \tilde{h}}{\partial \tilde{t}} + \frac{\partial}{\partial \tilde{x}}\left[-\frac{\partial \tilde{p}}{\partial \tilde{x}}\left(\tilde{h}^3 + \frac{3\,\tilde{h}^{\alpha+2}\,(\sigma)^{\alpha-1} {H_0}^{2\alpha-2}}{(\alpha+2)\tau_{1/2}{}^{\alpha-1} {L_0}^{3\alpha-3}}\left(\left|\frac{\partial \tilde{p}}{\partial \tilde{x}}\right|\right)^{\alpha-1}\right)\right] = 0\,, \tag{7.22}$$

$$\frac{\partial \tilde{h}}{\partial \tilde{t}} + \frac{\partial}{\partial \tilde{x}}\left[-\frac{\partial \tilde{p}}{\partial \tilde{x}}\left(\tilde{h}^3 + 3\left(\frac{\sigma {H_0}^2}{{L_0}^3 \tau_{1/2}}\right)^{\alpha-1}\frac{\tilde{h}^{\alpha+2}}{(\alpha+2)}\left(\left|\frac{\partial \tilde{p}}{\partial \tilde{x}}\right|\right)^{\alpha-1}\right)\right] = 0\,. \tag{7.23}$$

Therefore equations (7.11) and (7.23) both represent the lubrication approximation based on the Ellis model.

7.4.4 Non-dimensionalisation of the Navier–Stokes equations (Carreau model)

In this section, the Carreau model is considered to obtain the dimensionless form of the Navier–Stokes as explained in Section 6.4. The definition of the Carreau model can be expressed as follows (see Section 1.2):

$$\mu = \mu_\infty + (\mu_0 - \mu_\infty)[1 + \lambda^2 \dot{\gamma}^2]^{(n_c-1)/2}\,.$$

When $\mu_\infty = 0$ Pa·s as stated by Myers (2005) and Afanasiev, Münch et al. (2007), the definition of the Carreau model above becomes

$$\mu = (\mu_0)\left[1 + \lambda^2\left(\frac{U_0}{L_0}\frac{\partial \tilde{u}}{\partial \tilde{z}}\right)^2\right]^{(n_c-1)/2}. \tag{7.24}$$

Substituting equation (7.24) into equation (7.2) yields

$$\rho\left(\frac{U_0^2}{L_0}\frac{\partial \tilde{u}}{\partial \tilde{t}} + \frac{U_0^2}{L_0}\tilde{u}\frac{\partial \tilde{u}}{\partial \tilde{x}} + \frac{U_0^2}{L_0}\tilde{w}\frac{\partial \tilde{u}}{\partial \tilde{z}}\right) = -\frac{P_0}{L_0}\frac{\partial \tilde{p}}{\partial \tilde{x}} + \frac{U_0}{L_0^2}\frac{\partial}{\partial \tilde{x}}\left((\mu_0)\left[1 + \lambda^2\left(\frac{U_0}{L_0}\frac{\partial \tilde{u}}{\partial \tilde{z}}\right)^2\right]^{(n_c-1)/2}\frac{\partial \tilde{u}}{\partial \tilde{x}}\right) +$$

$$\frac{U_0}{L_0^2}\frac{\partial}{\partial \tilde{z}}\left((\mu_0)\left[1 + \lambda^2\left(\frac{U_0}{L_0}\frac{\partial \tilde{u}}{\partial \tilde{z}}\right)^2\right]^{(n_c-1)/2}\frac{\partial \tilde{u}}{\partial \tilde{z}}\right). \tag{7.25}$$

Multiplying through by $\frac{L_0}{\rho U_0^2}$ and defining the pressure scale $P_0 = \rho U_0^2$, equation (7.25) can be written as,

$$\left(\frac{\partial \tilde{u}}{\partial \tilde{t}} + \tilde{u}\frac{\partial \tilde{u}}{\partial \tilde{x}} + \tilde{w}\frac{\partial \tilde{u}}{\partial \tilde{z}}\right) = -\frac{\partial \tilde{p}}{\partial \tilde{x}} + \frac{\partial}{\partial \tilde{x}}\left(\left(\frac{\mu_0}{\rho L_0 U_0}\right)\left[1 + \lambda^2\left(\frac{U_0}{L_0}\frac{\partial \tilde{u}}{\partial \tilde{z}}\right)^2\right]^{(n_c-1)/2}\frac{\partial \tilde{u}}{\partial \tilde{x}}\right) + \frac{\partial}{\partial \tilde{z}}\left(\left(\frac{\mu_0}{\rho L_0 U_0}\right)\left[1 +\right.\right.$$

$$\left.\left.\lambda^2\left(\frac{U_0}{L_0}\frac{\partial \tilde{u}}{\partial \tilde{z}}\right)^2\right]^{(n_c-1)/2}\frac{\partial \tilde{u}}{\partial \tilde{z}}\right). \tag{7.26}$$

With the Reynolds number defined as $Re = \left(\frac{L_0 U_0 \rho}{\mu_0}\right)$, equation (7.26) can be simplified to

$$\left(\frac{\partial \tilde{u}}{\partial \tilde{t}} + \tilde{u}\frac{\partial \tilde{u}}{\partial \tilde{x}} + \tilde{w}\frac{\partial \tilde{u}}{\partial \tilde{z}}\right) = -\frac{\partial \tilde{p}}{\partial \tilde{x}} + \frac{\partial}{\partial \tilde{x}}\left(\frac{1}{Re}\left[1 + \lambda^2\left(\frac{U_0}{L_0}\frac{\partial \tilde{u}}{\partial \tilde{z}}\right)^2\right]^{(n_c-1)/2}\frac{\partial \tilde{u}}{\partial \tilde{x}}\right) + \frac{\partial}{\partial \tilde{z}}\left(\frac{1}{Re}\left[1 + \lambda^2\left(\frac{U_0}{L_0}\frac{\partial \tilde{u}}{\partial \tilde{z}}\right)^2\right]^{(n_c-1)/2}\frac{\partial \tilde{u}}{\partial \tilde{z}}\right). \quad (7.27)$$

The procedure above was repeated to obtain the dimensionless Navier–Stokes z-momentum equation based on the Carreau model:

$$\left(\frac{\partial \tilde{w}}{\partial \tilde{t}} + \tilde{u}\frac{\partial \tilde{w}}{\partial \tilde{x}} + \tilde{w}\frac{\partial \tilde{w}}{\partial \tilde{z}}\right) = -\frac{\partial \tilde{p}}{\partial \tilde{z}} + \frac{\partial}{\partial \tilde{x}}\left(\frac{1}{Re}\left[1 + \lambda^2\left(\frac{U_0}{L_0}\frac{\partial \tilde{u}}{\partial \tilde{z}}\right)^2\right]^{(n_c-1)/2}\frac{\partial \tilde{w}}{\partial \tilde{x}}\right) + \frac{\partial}{\partial \tilde{z}}\left(\frac{1}{Re}\left[1 + \lambda^2\left(\frac{U_0}{L_0}\frac{\partial \tilde{u}}{\partial \tilde{z}}\right)^2\right]^{(n_c-1)/2}\frac{\partial \tilde{w}}{\partial \tilde{z}}\right) + \frac{1}{Fr^2}. \quad (7.28)$$

The dimensionless Navier–Stokes continuity equation is still the same as in equation (7.7). We choose $U_0 = \frac{\sigma}{\mu_0}$ and therefore $Ca = 1$; then we have $U_0 = \frac{L_0}{T_0}$ and hence,

$$T_0 = \frac{\mu_0 L_0}{\sigma}, \text{ in terms of the Navier–Stokes } (T_0{}^{NS}), \quad (7.29)$$

$$T_0 = \frac{3\mu_0 {L_0}^4}{\sigma {H_0}^3}, \text{ in terms of the lubrication approximation } (T_0{}^{LA}). \quad (7.30)$$

Substituting equation (7.29) into (7.30) yields $T_0{}^{LA} = \frac{3}{\varepsilon^3} T_0{}^{NS}$. The Reynolds, Froude, and Bond numbers were calculated in terms of the Ellis parameters of the molasses: ρ = 1450 kg/m^3 , σ = 0.05 N/m, $\mu_0 = 37$ Pa·s, and $L_0 = 0.916$ m. We found that $Re = 0.0485$, $\mathrm{Fr} = 4.51 \times 10^{-4}$, and $Bo = 2.38 \times 10^5$.

Figure 7.15 shows the comparison between the dimensionless Navier-Stokes and the dimensionless lubrication approximation in terms of the Ellis model with the same numerical setup indicated in Section 7.3.2.

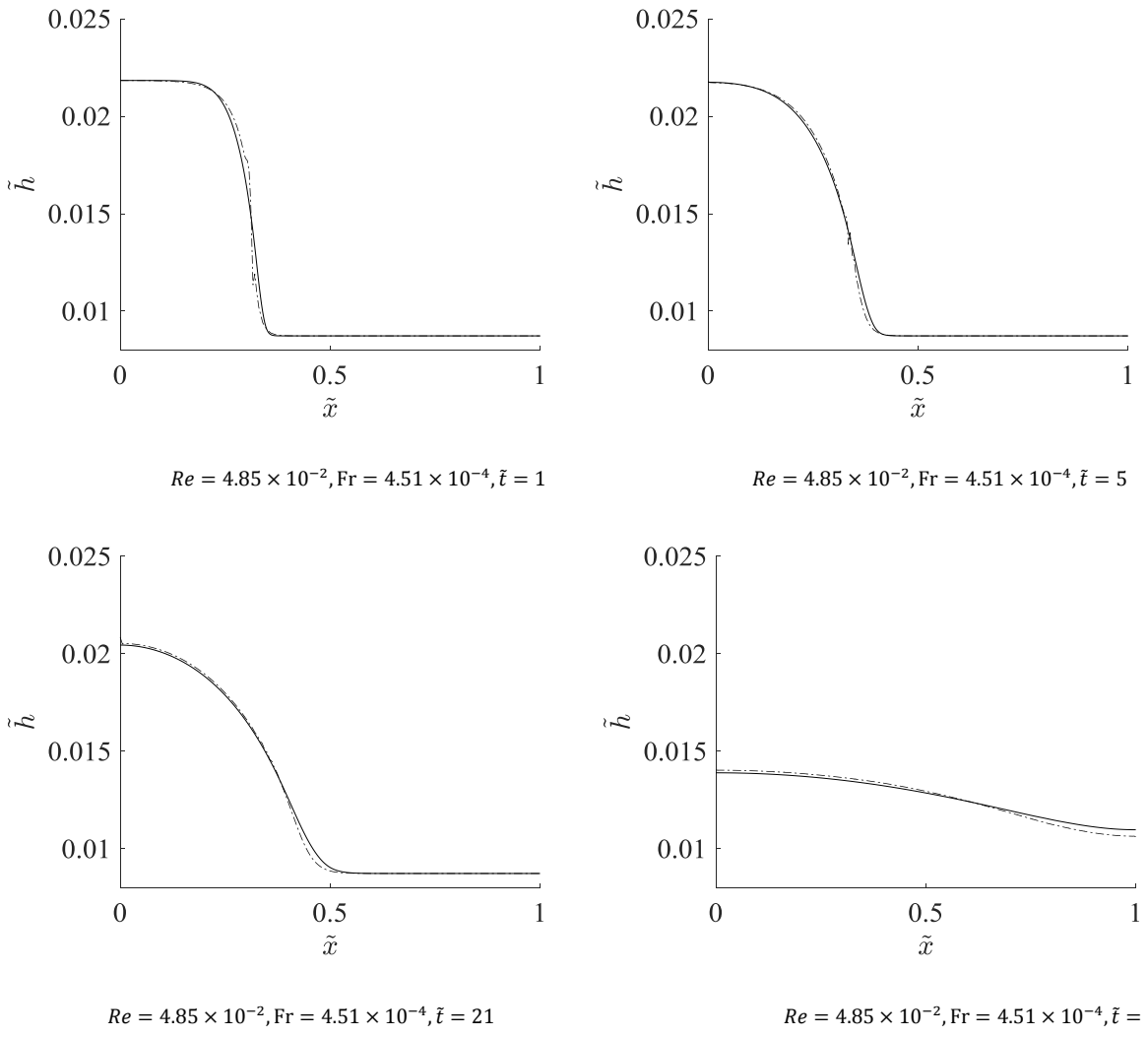

Figure 7.15: Dimensionless film thickness as a function of dimensionless horizontal distance in terms of the Ellis model at four different dimensionless times. Dashed line represents dimensionless Navier-Stokes solution (NS) and solid line represents dimensionless lubrication approximation (LA), with $\tilde{x}_{NS} = \tilde{x}_{LA}$, $\tilde{h}_{NS} = \varepsilon \tilde{h}_{LA}$, and $\frac{3}{\varepsilon^3}\ \tilde{t}_{NS} = \tilde{t}_{LA}$

Similar to Section 7.3.2, four different Reynolds numbers were used to perform the comparison between the dimensionless lubrication approximation and the dimensionless Navier-Stokes, namely 0.01, 0.1, 1, and 10 at four dimensionless times 1, 5, 21, and 600, respectively.

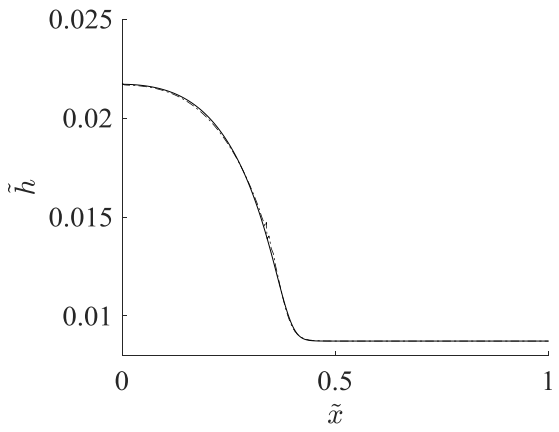

$Re = 10^{-2}, \mathrm{Fr} = 9.2 \times 10^{-5}, \tilde{t} = 1$

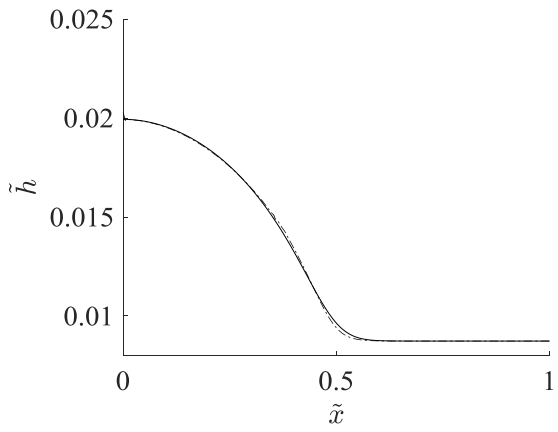

$Re = 10^{-2}, \mathrm{Fr} = 9.2 \times 10^{-5}, \tilde{t} = 5$

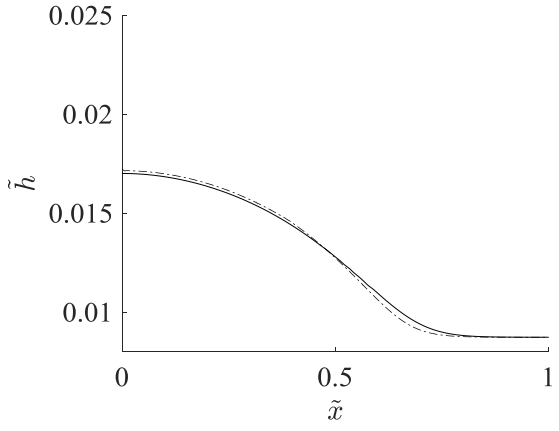

$Re = 10^{-2}, \mathrm{Fr} = 9.2 \times 10^{-5}, \tilde{t} = 21$

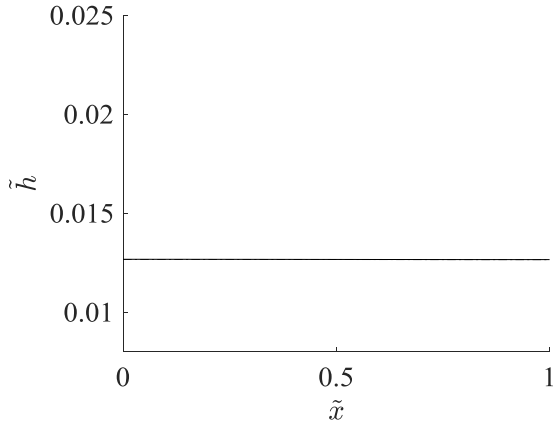

$Re = 10^{-2}, \mathrm{Fr} = 9.2 \times 10^{-5}, \tilde{t} = 600$

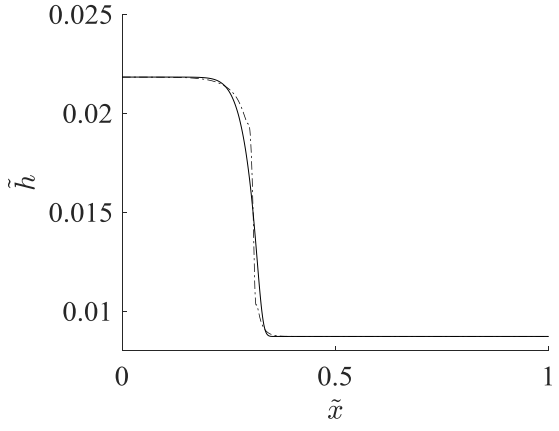

$Re = 0.1, \mathrm{Fr} = 9.2 \times 10^{-4}, \tilde{t} = 1$

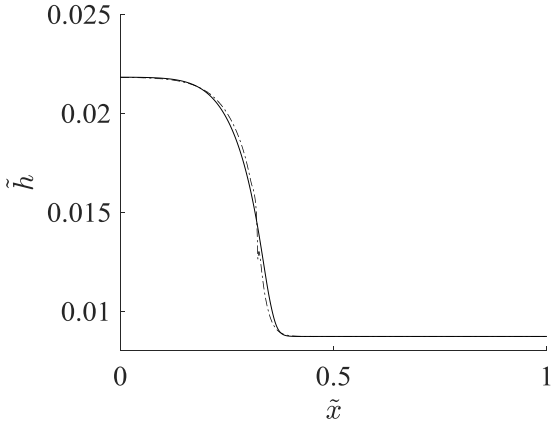

$Re = 0.1, \mathrm{Fr} = 9.2 \times 10^{-4}, \tilde{t} = 5$

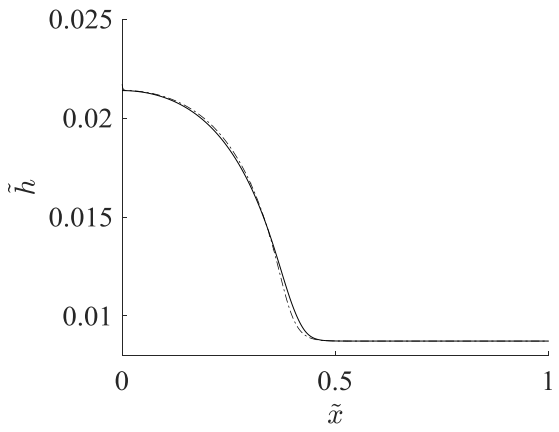

$Re = 0.1, \mathrm{Fr} = 9.2 \times 10^{-4}, \tilde{t} = 21$

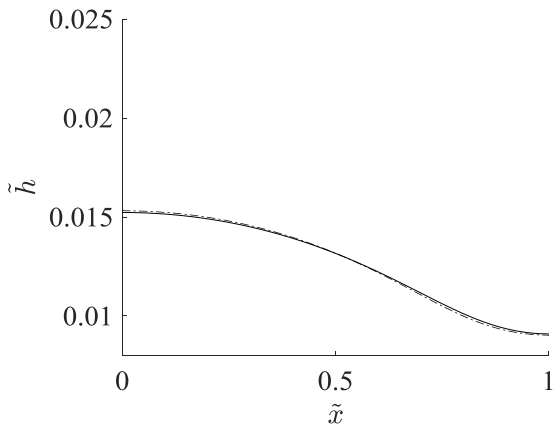

$Re = 0.1, \mathrm{Fr} = 9.2 \times 10^{-4}, \tilde{t} = 600$

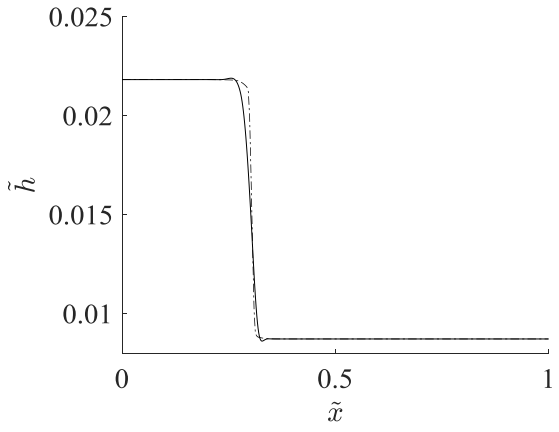

$Re = 1, \mathrm{Fr} = 9.2 \times 10^{-3}, \tilde{t} = 1$

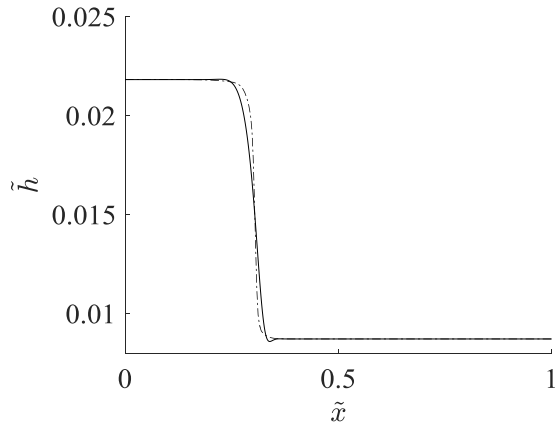

$Re = 1, \mathrm{Fr} = 9.2 \times 10^{-3}, \tilde{t} = 5$

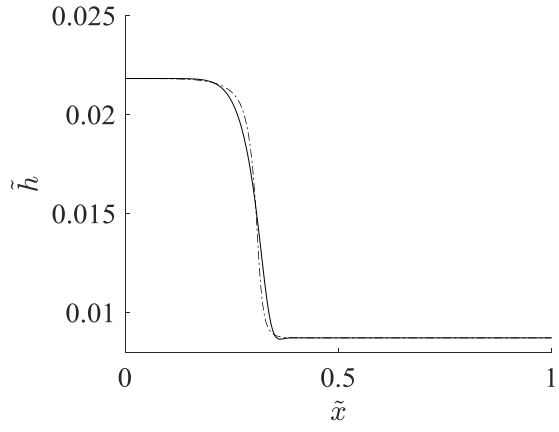

$Re = 1, \mathrm{Fr} = 9.2 \times 10^{-3}, \tilde{t} = 21$

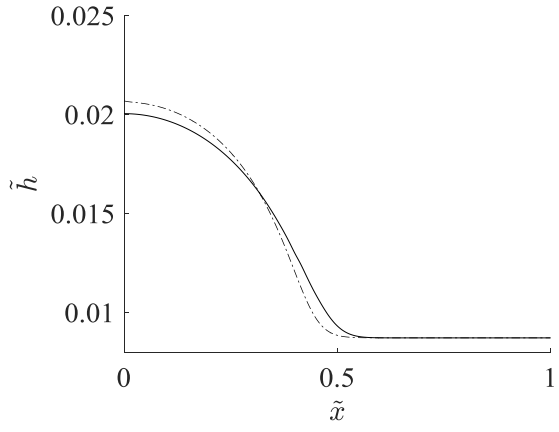

$Re = 1, \mathrm{Fr} = 9.2 \times 10^{-3}, \tilde{t} = 600$

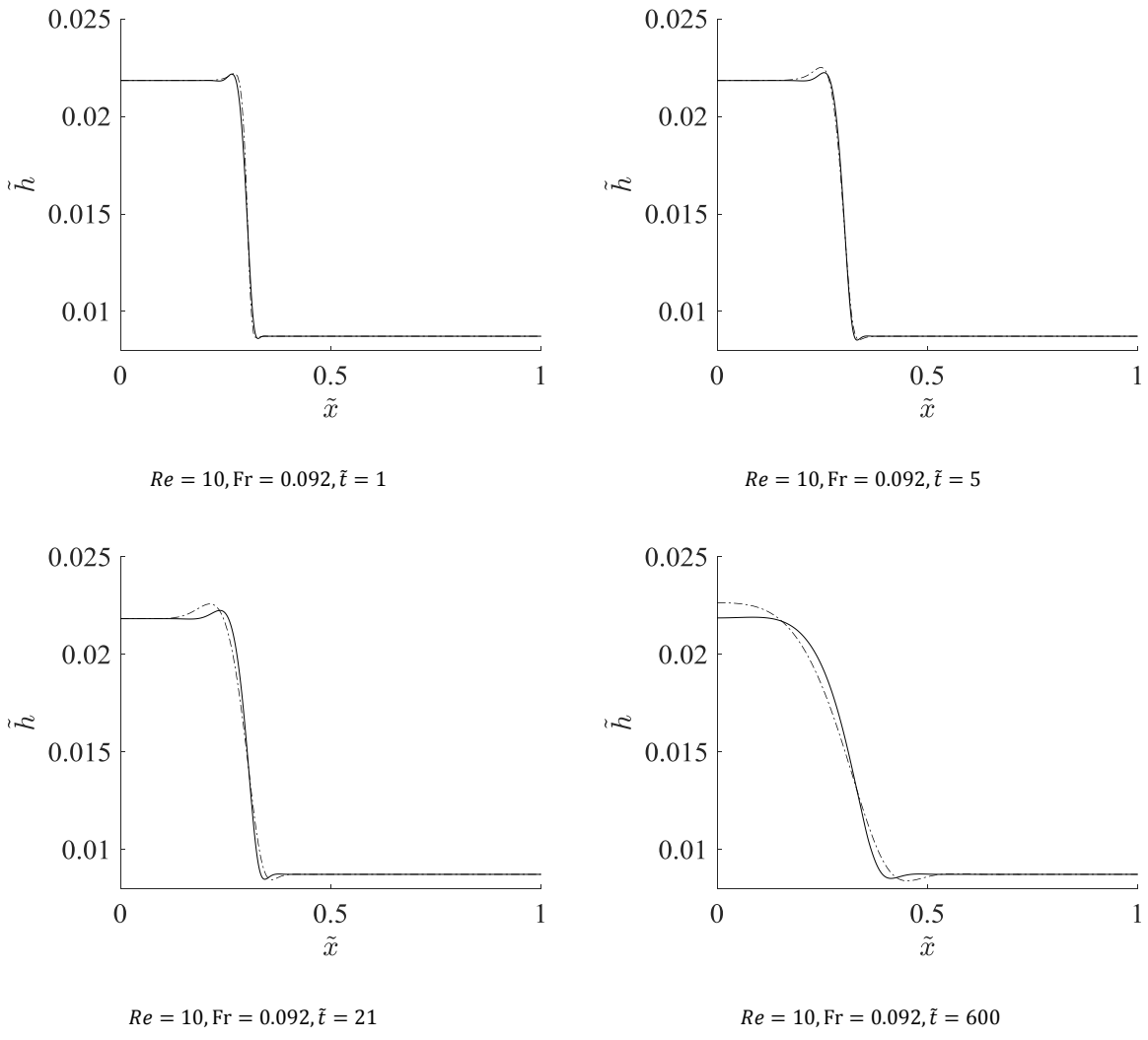

Figure 7.16: Dimensionless film thickness as a function of dimensionless horizontal distance in terms of the Ellis model at four different dimensionless times with four different Reynolds numbers. Dashed line represents dimensionless Navier-Stokes solution (NS) and solid line represents dimensionless lubrication approximation (LA), with $\tilde{x}_{NS} = \tilde{x}_{LA}$, $\tilde{h}_{NS} = \varepsilon\tilde{h}_{LA}$, and $\frac{3}{\varepsilon^3}\,\tilde{t}_{NS} = \tilde{t}_{LA}$

Figure 7.16 shows the relationship between the dimensionless film thickness with the dimensionless horizontal distance for both dimensionless models at four different Reynolds and Froude numbers. It is evident that the agreement between the two dimensionless models is good.

As demonstrated in Section 3.2, the inertia terms are neglected. Consequently, the results in both Figures 7.13 and 7.16 are in agreement with the expectation that the lubrication approximation cannot capture the full levelling dynamics at high Reynolds and Froude numbers. The discrepancy between the two dimensionless models is significant at high Reynolds numbers. The following contour lines provide a clear vision about the effect of the Reynolds number and Froude number on the relative error percentages:

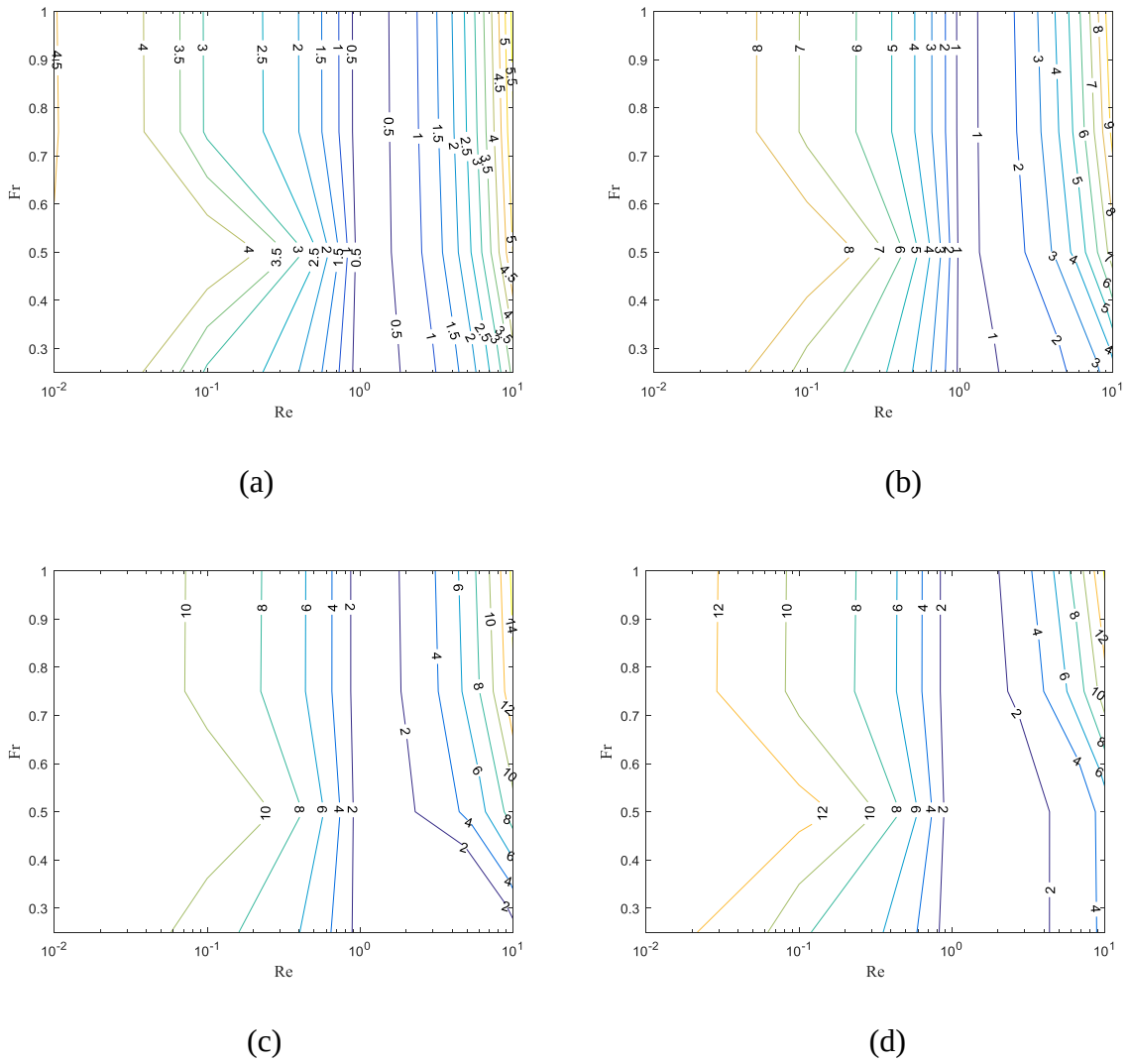

Figure 7.17: Contour lines showing the relative error percentages of dimensionless lubrication approximation compared with dimensionless Navier-Stokes at four different dimensionless times

(a) $\tilde{t} = 3 \times 10^4$, (b) $\tilde{t} = 6 \times 10^4$, (c) $\tilde{t} = 186 \times 10^4$, and (d) $\tilde{t} = 39 \times 10^5$ using the Ellis model

In Figure 7.17, it is evident that the minimum relative error percentages are around $Re = 1$.

Both Figures 7.18 and 7.19 illustrate the effect of changing the aspect ratio ε on the compatibility between the dimensionless Navier-Stokes and the dimensionless lubrication approximation solutions. In terms of the power-law model, the Reynolds and Froude numbers are fixed at $4 \times 10^{-4}$and 4.10×10^{-5}, respectively. The ratio $\frac{H_g}{H_1}$ was also maintained at 2.5. For the Ellis model, $Re = 0.0485$ and $\mathrm{Fr} = 4.51 \times 10^{-4}$ with $\frac{H_g}{H_1}$ ratio of 2.5. Therefore,

$$\varepsilon = \frac{H_0}{L_0} = \frac{H_1 + H_g}{2L_0} = \frac{7H_1}{4L_0} = \frac{0.7H_g}{L_0}. \tag{7.31}$$

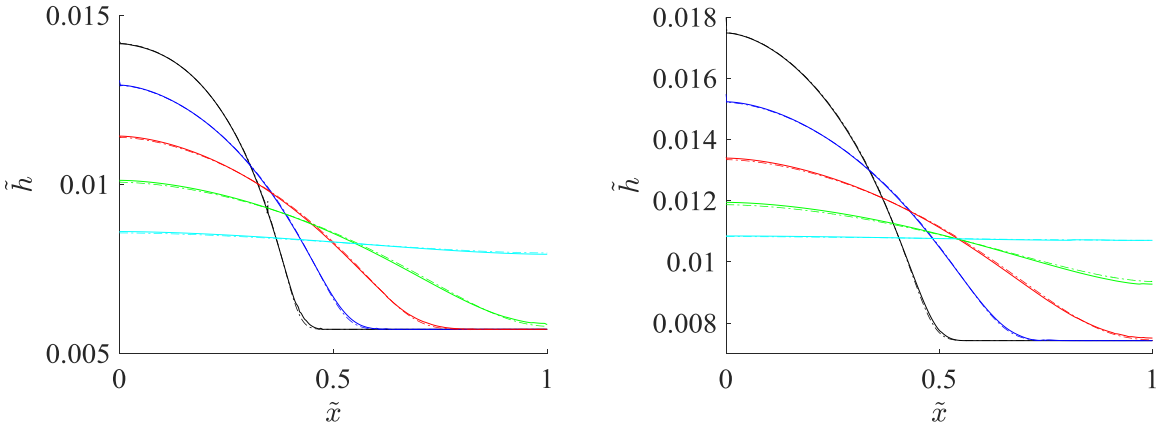

(a) (b)

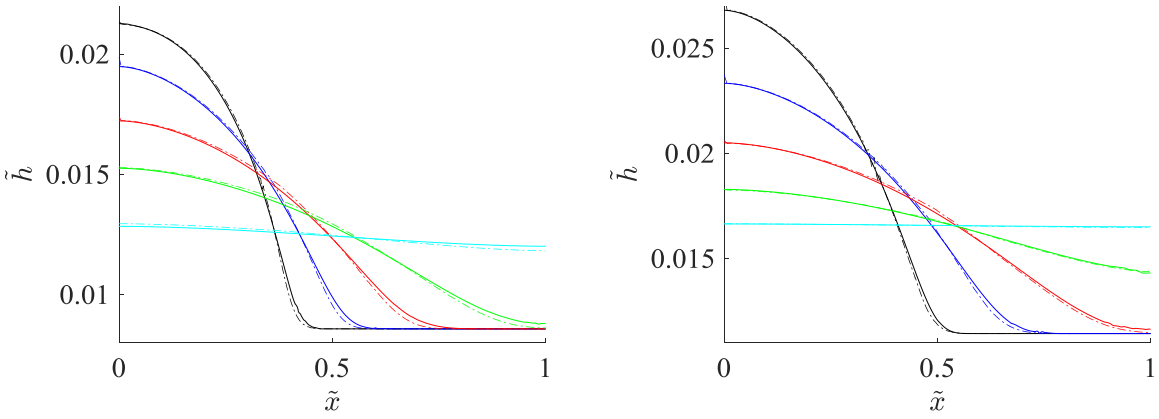

(c) (d)

Figure 7.18: Dimensionless film thickness as a function of dimensionless horizontal distance in terms of the power law model at five different dimensionless time and four different aspect ratios, namely (a) 0.01, (b) 0.013, (c) 0.015 and (d) 0.02. Dashed line represents dimensionless Navier-Stokes solution (NS) and solid line represents dimensionless lubrication approximation (LA)

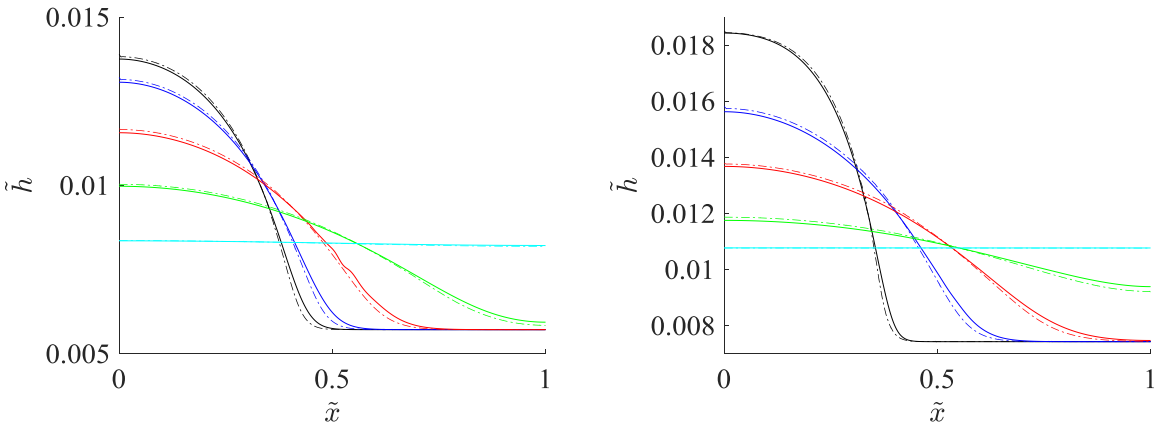

(a) (b)

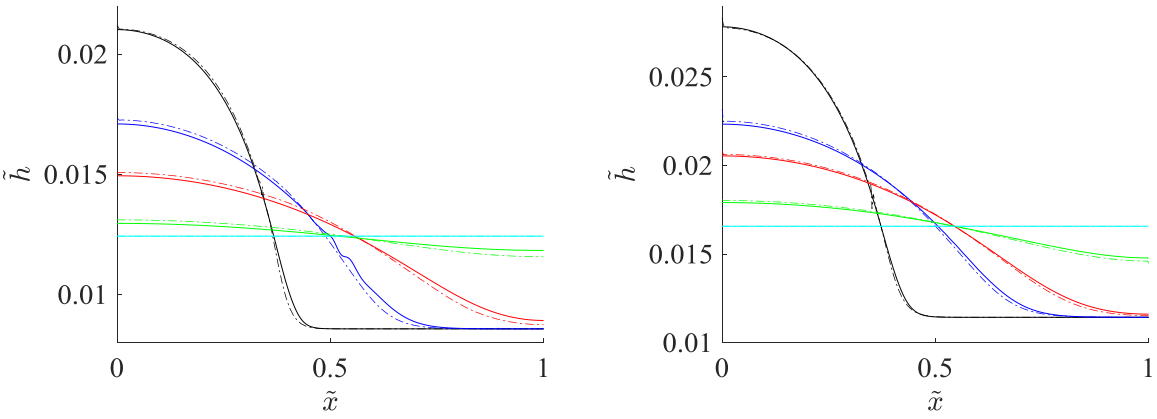

(c) (d)

Figure 7.19: Dimensionless film thickness as a function of dimensionless horizontal distance in terms of the Ellis model at five different dimensionless times and four different aspect ratios: (a) 0.01, (b) 0.013, (c) 0.015, and (d) 0.02. Dashed line represents dimensionless Navier-Stokes solution (NS) and solid line represents dimensionless lubrication approximation (LA)

Figures 7.18 and 7.19 show that the compatibility between the dimensionless lubrication approximation and the dimensionless Navier-Stokes is very good within the range of aspect ratio used. In particular, the relative error percentages calculated by applying equation (6.11) fluctuated between 0.74% and 0.087%, as shown in Figure 7.18, whereas it fluctuated between 1.15% and 0.047%, as shown in Figure 7.19.

In this chapter, we used two different methods to clarify the difference between the lubrication approximation and the Navier-Stokes models. Each method was achieved with the power-law model and the Ellis model. The first method was implemented using the dimensional form for both the lubrication approximation and the Navier-Stokes equations. The second method was implemented using set of scaled variables to non-dimensionalise the mathematical forms of the lubrication approximation and the Navier-Stokes. In terms of the dimensional analysis, we found that the difference between the lubrication approximation and the Navier-Stokes was influenced by the fluid curvature, inertia effects, and the aspect ratio. The lubrication approximation cannot

accurately capture the dynamics of the flow when the inertia effects were significant. When the aspect ratio is high, the lubrication approximation cannot predict the behaviour of the dam-break flow configuration well.

From the standpoint of dimensionless analysis for both the lubrication approximation and the Navier-Stokes, a series of Reynolds, Froude, and Bond numbers were used to clarify the difference between the two models.

The results show that the lubrication approximation can effectively describe the dam-break for fluid flow of thin film and low Reynolds number cases. The higher Reynolds number means higher fluid inertia. Consequently, the lubrication approximation could not accurately describe the dynamics of the flow with high inertia. The influence of inertia decreases with the decreasing value of the Reynolds number.

The ranges of Reynolds number for these flow was 111.5 for silicone oil, 55 for glycerol and 4×10^{-4} for moasses in terms of power-law, while it was 0.048 in terms of Ellis model. These Reynolds number values indicate that the flow region is laminar. Consequently, the lubrication approximation is still valid due to the small inertia term.

Chapter 8

Conclusion

Contents

8.1 Summary

The aim of this thesis was to calculate the rheological parameters of fluids based on the free surface velocity. The purpose was to find a new way to calculate the rheology without using a rheometer. In this work, three different approaches were simultaneously used to reconstruct the rheological parameters of fluids, namely experimental, analytical, and numerical. The work was verified with two rheological models: the power-law model and the Ellis model.

In Chapter 1, the thesis introduced the fundamentals of rheology and the most commonly used rheological models. Both the power-law model and the Ellis model were selected to model the rheology for the dam-break classical flow configuration. The lubrication approximation was used to simplify the complexity of the full Navier–Stokes equations. The rheological parameters were obtained by solving the parametric identification problem by minimizing the objective function, which includes an expression of the computed and experimental free surface velocity. A particle tracking velocimetry (PTV) technique was used to extract the free surface velocity from the experimental data.

In Chapter 2, the dam-break flow configuration that was used to perform the experiments was described. Three fluids were used, namely silicone oil, aqueous glycerol, and molasses. Then the fluid free surface velocity was extracted from the velocity field using the Streams software package.

In Chapter 3, the governing equations for the lubrication approximation were derived and verified. The viscosity in the lubrication approximation was defined according to the power-law rheological model. This was followed by Chapter 4, in which the lubrication approximation and the Navier–Stokes were solved numerically using COMSOL, a finite-element-based scientific computing package. The full Navier–Stokes model was solved using the laminar two phase flow module with a moving mesh. The lubrication approximation was solved using the coefficient form partial differential equation module.

The objective function followed by the parametric identification were both solved numerically. The parametric identification was based on minimizing the mismatch between the measured and computed free surface velocities. Consequently, the optimal rheological parameters corresponding to the minimum of the objective function was found.

The parametric identification was tested by a synthetic dataset created. A clear global minimum of the objective function was apparent at the expected rheological values. The identification was then tested with a noisy synthetic dataset, in which we found that the robustness of the results was good and provided the required confidence that COMSOL modelling for this case was valid, and could be used for further analyses.

After implementing the verifications and tests above, the experimental data was considered in Chapter 5 and the rheological parameters were calculated for both silicone oil and aqueous glycerol. There were a small difference between the reconstructed data and the rheometer data (true data) due to the experimental errors, particle match imperfections and the uncertainty of the used model. We found that both the silicone oil and glycerol were Newtonian, and the results were matched with the power-law model. However, the molasses was poorly represented by the power-law model. One key outcome from the results above is that the power-law model works precisely for Newtonian fluids.

In Chapter 6, the governing equations of the lubrication approximation based on the Ellis model were derived. Both the lubrication approximation and the Navier–Stokes based on the Ellis model were verified and successfully tested with synthetic data and noisy data. We found that the Ellis model works better with molasses when compared with the power-law model. However, still there are differences between the reconstructed and the true values of the Ellis model rheological parameters due to the experimental errors, particles match imperfections and the uncertainty of the used model as described in Section 5.2. In addition, the range of shear rate in the dam-break experiment and that in rheometer experiment does not over lap at low shear rate. That can be account for the parameter fitting discrepancy.

Finally, a comparison of the lubrication approximation and the Navier–Stokes was implemented for both Newtonian and non-Newtonian fluids. The comparison included two different strategies, the dimensional and the dimensionless forms of the lubrication approximation and Navier–Stokes. Both strategies were based on the power-law and the Ellis model. We found that the agreement between both models was very good. It has been found that the lubrication approximation cannot capture the dynamics of the flow at high Reynolds number. Consequently, using the Navier–Stokes solver is suggested in this case.

The results suggest that the fluid rheology can be inferred indirectly by measuring the free surface velocity field with the lubrication approximation assumptions. The fluid rheology can be described by the power-law model and the Ellis model with a variation in accuracy. The Ellis model was more accurate than the power-law model because the Ellis model included three rheological parameters, whereas the power law model included only two. Consequently, the experimental data can be described better with more parameters.

8.2 Suggestions for future work

Both the power-law and the Ellis models do not provide a complete vision of the fluid rheology. In terms of the power-law model, the fluid viscosity is a function of shear rate, whereas for the Ellis model, the viscosity is a function of shear stress. Furthermore, there are many different rheological models that include other variables. For example, the Herschel–Bulkley model includes terms for the yield shear stress, consistency factor, and flow index. The yield shear stress represents the amount of stress that the fluid may be exposed to before it flows Herschel and Bulkley (1926).

The power-law model includes two rheological parameters and the Ellis model includes three. Consequently, selecting a model with a higher number of parameters can describe the rheology of fluid with more accuracy. In addition, the general vision of fluid rheology can be clearer when more parameters are used. The Carreau model includes four rheological parameters and can be used to illustrate the influence of those parameters on the fluid properties. The Ellis model yields very similar results to the Carreau model, although the parameters in the Ellis model are not the same as that of the Carreau model Myers (2005).

In both the cases above, the mathematical expression for the free surface velocity is required. The lubrication approximation is the simple form of the Navier–Stokes, which can be used to calculate the rheological parameters. The validation of the results obtained using the lubrication approximation is applicable with the Navier–Stokes.

The calculation of the rheological parameters of special liquids such as lava leads to a better understanding of the fluid properties. Consequently, the idea of measuring the rheology can be developed by considering many other different types of liquids.

A suitable flow configuration in the experimental work is required for measuring the rheology of fluids. In this thesis, the rheology of silicone oil, aqueous glycerol, and molasses was determined using the dam-break classical flow configuration in the experiment. However, in case of the need to measure the rheology of a small sample of liquid, the dam-break doesn't help and will waste an amount of liquid. Consequently, it is important to use a different flow configuration for different fluids. For instance, the rheology of the xanthan gum could be measured using the gravity currents flow in the experiment Sayag and Worster (2012).

To summarize, the suggestions for future work are as follows:

- Implement more realistic rheology (Herschel–Bulkley model).
- Consider another rheological model that has more rheological parameters (Carreau model).
- Consider more complicated liquids (lava).
- Considering another flow configuration in the experiments.
- Using the Navier–Stokes solver in case of high Reynolds number.

Reference list:

Afanasiev, K., et al. (2007). "Landau-Levich problem for non-Newtonian liquids." Physical Review E - Statistical, Nonlinear, and Soft Matter Physics **76**(3).

Ancey, C., et al. (2009). "The dam-break problem for viscous fluids in the high-capillary-number limit." Journal of Fluid Mechanics **624**: 1-22.

Anna, S. L., et al. (1999). "On controlling the kinematics of a filament stretching rheometer using a real-time active control mechanism." Journal of Non-Newtonian Fluid Mechanics **87**(2): 307 - 335.

Aster, R. C., et al. (2011). Parameter estimation and inverse problems, Academic Press.

Balmforth, N. J., et al. (2007). "Viscoplastic dam breaks and the Bostwick consistometer." Journal of Non-Newtonian Fluid Mechanics **142**(1-3): 63-78.

Bandulasena, H. C., et al. (2011). "An inverse method for rheometry of power-law fluids." Measurement Science and Technology **22**(12).

Barnes, H. A., et al. (1989). An introduction to rheology. New York, U.S.A, Elsevier.

Basilevsky, A. V., et al. (1990). Liquid filament microrheometer and some of its applications In Third European Rheology Conference D.R. Oliver (Ed.),Elsevier Applied Science (1990).

Braun, R. J., et al. (2012). "Thin film dynamics on a prolate spheroid with application to the cornea." Journal of Engineering Mathematics **73**(1): 121 - 138.

Charpin, J. P. F., et al. (2007). "Spin coating of non-Newtonian fluids with a moving front." AMER PHYSICAL SOC **76**(1): 9.

Collyer, A. A. (1973). "Time independent fluids." IOP Publishing **8**(5): 333 - 338.

Corporation, P. C. (2006, 2006). "Silicone oil." Retrieved March, 2016, from http://www.powerchemcorp.com.

Craster, R. V. and O. K. Matar (2009). "Dynamics and stability of thin liquid films." Reviews of Modern Physics **81**(3): 1131 - 1198.

Dark, A. L. (2017). Numerical Modelling of Groundwater Surface Water Interactions with the Double-Averaged Navier-Stokes Equations. Civil Engineering Department. University of Canterbury University of Canterbury. **Ph.D**.

E.Herbert, H. (1982). "propagation of two-dimensional and axisymmetric viscous gravity currents over a rigid horizontal surface." J FLUID MECH **V 121**: 43-58.

Eggers, J. (1997). "Nonlinear dynamics and breakup of free-surface flows." Reviews of Modern Physics **69**(3): 865 - 929.

Engl, H. W., et al. (1996). Regularization of inverse problems, Springer Science & Business Media.

Eswaran, M., et al. (2011). "Experimental measurement of the surface velocity field in an externally induced sloshing tank." Journal of Engineering for the Maritime Environment **225**(2): 133 - 148.

Figliuzzi, B., et al. (2012). "Rheology of thin films from observations." Experiments in Fluids **53**(5): 1289 - 1299.

Fu, S., et al. (2015). "Numerical and experimental comparison of 3D Particle Tracking Velocimetry (PTV) and Particle Image Velocimetry (PIV) accuracy for indoor airflow study." PERGAMON-ELSEVIER SCIENCE LTD **100**: 40 - 49.

Gaskell, P. H., et al. (2004). "Gravity-driven flow of continuous thin liquid films on non-porous substrates with topography." Journal of Fluid Mechanics **509**: 253-280.

H. Ewoldt, R., et al. (2014). "Experimental Challenges of Shear Rheology: How to Avoid Bad Data." Complex Fluids in Biological Systems,: 207-241.

Halfar, P. (1983). "On the dynamics of the ice sheets 2." Journal of Geophysical Research **88**(10): 6043 - 6051.

Hasanoğlu, A. H. and V. G. Romanov (2017). Introduction to Inverse Problems for Differential Equations, Springer.

Heining, C. and M. Sellier (2016). "Direct Reconstruction of Three-dimensional Glacier Bedrock and Surface Elevation from Free Surface Velocity." AIMS microbiology **2**(1): 45-63.

Herschel, W. H. and R. Bulkley (1926). "Konsistenzmessungen von Gummi-Benzollösungen." Kolloid Zeitschrift **39**(4): 291 - 300.

Hewson, R. W., et al. (2009). "A model for film-forming with Newtonian and shear-thinning fluids." Journal of Non-Newtonian Fluid Mechanics **162**(1): 21 - 28.

Howison, S. D., et al. (1997). "A mathematical model for drying paint layers." Journal of Engineering Mathematics **32**(4): 377-394.

Jossic, L., et al. (2009). "The fluid mechanics of shear-thinning tear substitutes." Journal of Non-Newtonian Fluid Mechanics **161**(1): 1 - 9.

Kanemura, T., et al. (2008). "Measurement of free-surface velocity of liquid lithium flow for IFMIF." Elsevier B.V **83**(10): 1529 - 1535.

Kheyfets, V. and S. Kieweg (2013). "Gravity-driven thin film flow of an ellis fluid." Journal of Non-Newtonian Fluid Mechanics **202**: 88 - 98.

Kim, B., et al. (2014). "Inhomogeneous swelling and mechanical properties of polystyrene bead-filled poly(acrylic acid) hydrogels." ROYAL SOC CHEMISTRY **4**(18): 63559 - 63568.

Leal, G. (2007). Advanced transport phenomena: fluid mechanics and convective transport processes, Cambridge ; New York.

Longo, S., et al. (2015). "Non-Newtonian power-law gravity currents propagating in confining boundaries." Environmental Fluid Mechanics **15**(3): 515 - 535.

Mahady, K., et al. (2013). "Comparison of Navier-Stokes simulations with long-wave theory: Study of wetting and dewetting." Physics of Fluids **25**(11): 112103.

Martin, N. and J. Monnier (2015). "Inverse rheometry and basal properties inference for pseudoplastic geophysical flows." European Journal of Mechanics, B/Fluids **50**: 110-126.

Matta, J. E. and R. P. Tytus (1990). "Liquid stretching using a falling cylinder." Non-Newtonian Fluid Mech **35**(2): 215-229.

McGraw, J. D., et al. (2011). "Capillary levelling as a probe of thin film polymer rheology." Soft Matter. Retrieved 17, 7.

McGraw, J. D., et al. (2012). "Self-similarity and energy dissipation in stepped polymer films." Physical Review Letters **109**(12).

McKinley, G. H. and A. Tripathi (2000). "How to extract the Newtonian viscosity from capillary breakup measurements in a filament rheometer." Journal of Rheology **44**(3): 653-670.

Meselhe, E. A., et al. (2004). "Large Scale Particle Image Velocimetry for Low Velocity and Shallow Water Flows." Journal of Hydraulic Engineering **130**(9): 937 - 940.

Miller, K. F. and D. M. Pike (1993). Surface active properites of cane molasses. Proceedings of Australian society of sugar cane technologists**:** 208-213.

Moran, K. and A. Yeung (2004). "Determining bitumen viscosity through drop shape recovery." The Canadian Journal of Chemical Engineering **82**(4): 813 - 820.

Moran, K., et al. (2003). "Shape relaxation of an elongated viscous drop." Journal of Colloid and Interface Science **267**(2): 483-493.

Myers, T. G. (2005). "Application of non-Newtonian models to thin film flow." Physical Review E - Statistical, Nonlinear, and Soft Matter Physics **72**(6).

Nascimento, S. C. C., et al. (2010). "Identification of non-newtonian rheological parameter through an inverse formulation." Journal of the Brazilian Society of Mechanical Sciences and Engineering **32**(2): 187-194.

Noble, P. and J. Vila (2013). "Thin power-law film flow down an inclined plane: consistent shallow-water models and stability under large-scale perturbations." Journal of Fluid Mechanics **735**: 29 - 60.

Nokes, R. (2014). "Streams v2.03 System Theory And Design ": Christchurch: University of Canterbury.

Nokes, R. (2014). "Streams v2.03 Users Guide: Field Objects." Christchurch: University of Canterbury

Oron, A. and S. G. Bankoff (1997). "Long-scale evolution of thin liquid films." Reviews of Modern Physics **69**(3): 931 - 980.

Park, H. M., et al. (2007). "Estimation of rheological parameters using velocity measurements." Chemical Engineering Science **62**(23): 6806-6815.

Piau, J.-M. and K. Debiane (2005). "Consistometers rheometry of power-law viscous fluids." Journal of Non-Newtonian Fluid Mechanics **127**(2-3): 213-224.

Renbaum-Wolff, L., et al. (2013). "Viscosity of α-pinene secondary organic material and implications for particle growth and reactivity." Proceedings of the National Academy of Sciences **110**(20): 8014 - 8019.

Reynolds, O. (1886). "'On the Theory of Lubrication and Its Application to Mr. Lowe's Experiments,''." Philos. Trans. R. Soc. London **77**: 157-234.

Rignot, E., et al. (2011). " Ice flow of the Antarctic ice sheet." AMER ASSOC ADVANCEMENT SCIENCE **3**(2): 239 - 249.

Rodd, L. E., et al. (2005). "Capillary break-up rheometry of low-viscosity elastic fluids." **15**(1): 12 - 27.

Sayag, R. and M. G. Worster (2012). "Axisymmetric gravity currents of power-law fluids over a rigid horizontal surface." Journal of Fluid Mechanics **716**: R51-R511.

Schlichting, H. (1979). "Boundary-layer theory, 7th. editon." McCraw-Hill Book Co., Ncw York.

Schwartz, L. W. and R. R. Eley (2002). "Flow of architectural coatings on complex surfaces; theory and experiment." Journal of Engineering Mathematics **43**(2): 153 - 171.

Sellier, M. (2016). "Inverse problems in free surface flows." Acta Mechanica **227**(3): 913–935.

Sellier, M., et al. (2017). Rheometry based of free surface velocity for the dam-break problem. ACIS, Australia Department of Mechanical Engineering, University of Canterbury.

Sellier, M., et al. (2015). "Estimating the viscosity of a highly viscous liquid droplet through the relaxation time of a dry spot." Journal of Rheology **59**(3): 733-750.

Sellier, M. and S. Panda (2016). "Unraveling surfactant transport on a thin liquid film." Wave motion: 1-19.

Sellier, M. and S. Panda (2017). "Unraveling surfactant transport on a thin liquid film." ELSEVIER SCIENCE BV **70**: 183 - 194.

Sochi, T. (2010). "Computational techniques for modeling non-newtonian flow in porous media." International Journal of Modeling, Simulation, and Scientific Computing **1**(2): 239 - 256.

Sochi, T. (2010). "Non-Newtonian flow in porous media." Polymer **51**(22): 5007 - 5023.

Sokoray-Varga, B. and J. Józsa (2008). "Particle tracking velocimetry (PTV) and its application to analyse free surface flows in laboratory scale models." Periodica Polytechnica: Civil Engineering **52**(2): 63 - 71.

Spurk, J. and N. Aksel (2008). Fluid Mechanics. Springer-Verlag Berlin Heidelberg (2008).

Steffe, J. F. (1996). Rheological methods in food process engineering. USA, Freeman press.

Wazer, V. and J. R (1963). Viscosity and flow measurement: a laboratory handbook of rheology, Interscience Publishers.

Weidner, D. E. and L. W. Schwartz (1994). "Contact-line motion of shear-thinning liquids." Physics of Fluids **6**(11): 3535 - 3538.

White, F. M. (2011). Fluid mechanics. New York, N.Y. , McGraw Hill, 2011.

Whittaker, C. (2013). Modelling Of Tsunami Generated By The Motion Of A Rigid Block Along A Horizontal Boundary. Civil Department. University of Canterbury, Canterbury. **Ph.D**.

Winkelmann, R., et al. (2011). "The Potsdam Parallel Ice Sheet Model (PISM-PIK) – Part 1: Model description." The cryosphere **5**(3): 715-726.